THE UNIVERSITY OF CALGARY

The Seismic Characterization of Meteorite Impact Structures

by

Michael James Mazur

A THESIS SUBMITTED IN PARTIAL

FULFILLMENT OF THE REQUIREMENTS FOR

THE DEGREE OF MASTER OF SCIENCE

DEPARTMENT OF GEOLOGY AND GEOPHYSICS

CALGARY, ALBERTA

AUGUST, 1999

© Michael James Mazur 1999

National Library of Canada
Acquisitions and Bibliographic Services
395 Wellington Street
Ottawa ON K1A 0N4
Canada

Bibliothèque nationale du Canada
Acquisitions et services bibliographiques
395, rue Wellington
Ottawa ON K1A 0N4
Canada

Your file Votre référence

Our file Notre référence

The author has granted a non-exclusive licence allowing the National Library of Canada to reproduce, loan, distribute or sell copies of this thesis in microform, paper or electronic formats.

L'auteur a accordé une licence non exclusive permettant à la Bibliothèque nationale du Canada de reproduire, prêter, distribuer ou vendre des copies de cette thèse sous la forme de microfiche/film, de reproduction sur papier ou sur format électronique.

The author retains ownership of the copyright in this thesis. Neither the thesis nor substantial extracts from it may be printed or otherwise reproduced without the author's permission.

L'auteur conserve la propriété du droit d'auteur qui protège cette thèse. Ni la thèse ni des extraits substantiels de celle-ci ne doivent être imprimés ou autrement reproduits sans son autorisation.

0-612-49711-9

Canada

University of Calgary

Abstract

The Seismic Characterization of Impact Structures

by Michael James Mazur

This thesis examines the seismic characteristics of three possible impact craters and one confirmed impact structure. Using established seismic methods and impact crater scaling relations, an investigation of these features is undertaken. The largest structure examined here is the 24-km diameter Steen River impact feature in northwestern Alberta, Canada. This astrobleme has been imaged by more than 130 seismic lines to date. The second largest structure studied in this thesis is the 3.5-km Hotchkiss structure located approximately 300-km south of the Steen River impact structure. The three seismic lines imaging this feature clearly show many of the diagnostic features of a complex impact feature. The Muskingum structure in Ohio, USA is approximately 1.3 km across and possibly represents an impact crater within the simple-to-complex transition zone. The 2-km diameter Puffin structure is apparent on a 3-D seismic dataset acquired in the Timor Sea off the coast of northwestern Australia. Interpretation of this structure is inherently complex and indefinite due to extensive faulting in the area and due to the proximity of several kimberlite pipes to the study area.

TABLE OF CONTENTS

LIST OF FIGURES ..... **VI**

LIST OF TABLES ..... **IX**

ACKNOWLEDGMENTS ..... **X**

GLOSSARY ..... **XI**

INTRODUCTION TO THE STUDY OF IMPACT STRUCTURES **1**

1.1 THE HISTORY OF IMPACT CRATER STUDIES 1
1.2 TERRESTRIAL IMPACT CRATER STUDIES 3
1.3 IMPACT CRATER TYPES 5
1.4 ECONOMIC IMPORTANCE OF IMPACT STRUCTURES 8
1.5 OTHER CRATER-LIKE FEATURES 9

PHYSICS OF IMPACT CRATERING **11**

2.1 STRESSES, LIMITS, AND HUGONIOT CURVES 11
2.2 THE THREE STAGES OF IMPACT 15
2.3 VERTICAL AND OBLIQUE IMPACTS 16
2.4 STRUCTURED TARGETS 18
2.5 SCALING OF CRATER DIMENSIONS 20

SIMPLE IMPACT STRUCTURES **23**

3.1 PUFFIN 3-D, NW AUSTRALIA 23
3.1.1 Geological Setting *23*
3.1.2 Seismic Data Interpretation *24*
3.1.3 Impact Crater Morphometry *25*
3.1.4 Other Possible Explanations *28*
3.1.5 Concluding Remarks *29*
3.2 MUSKINGUM, OHIO 46
3.2.1 Geological Setting *46*
3.2.2 Geophysical Characteristics *47*
3.2.3 Seismic Data Interpretation *47*
3.2.4 Morphometry *48*
3.2.5 Other Possible Explanations *51*
3.2.6 Age of the Muskingum Strucutre *52*
3.2.7 Concluding Remarks *53*

COMPLEX IMPACT STRUCTURES **65**

4.1 HOTCHKISS, ALBERTA 65
4.1.1 Geological Setting *65*
4.1.2 Geophysical Characteristics *66*
4.1.3 Seismic Data Interpretation *68*
4.1.4 Morphometry *70*
4.1.5 Concluding Remarks *72*
4.2 STEEN RIVER, ALBERTA 84
4.1.1 Geological Setting *84*

4.1.2 Interpretation of the Seismic Time Sections *85*
4.1.3 Observations *86*
4.1.4 Time-to-depth Conversion using Petrosys *87*
4.1.5 Depth Conversion using GeoStat *89*
4.1.6 Visualization of the Results *92*
4.1.7 Concluding Remarks *92*

SUMMARY **155**

FUTURE WORK **157**

6.1 PHYSICAL AND NUMERICAL MODELING 157
6.2 EXAMINATION OF OTHER CIRCULAR FEATURES 157

APPENDIX **158**

BIBLIOGRAPHY **162**

INDEX **164**

LIST OF FIGURES

Figure 1.2.1 Location map of identified terrestrial impact structures 4
Figure 1.3.1 Schematic of a complex impact crater 7
Figure 1.3.2 Schematic of a simple impact structure 7
Figure 1.3.3 Schematic of the rim of a small impact crater 7
Figure 1.5.1 Schematic of a kimberlite pipe 10
Figure 1.5.2 The 'Blue Hole of Belize' 10
Figure 2.1.1 Plot illustrating the concept of the Hugoniot elastic limit 14
Figure 2.3.1 Effect of obliquity of impact on crater morphology 17
Figure 2.4.1 The morphology of craters formed in a layered geology 19
Figure 2.4.2 Lunar crater with a low bench 19
Figure 2.5.1a Scaling parameter diagram (uneroded crater) 22
Figure 2.5.1b Scaling parameter diagram (eroded crater). 22
Figure 2.5.2a Pre-erosional schematic of a complex crater 22
Figure 3.1.1. Puffin structure basemap 30
Figure 3.1.2 Australian kimberlite pipe location map 30
Figure 3.1.3 North West Shelf well location map 31
Figure 3.1.4 Basin subdivision map 31
Figure 3.1.5 Stratigraphy of the Cenozoic 32
Figure 3.1.6 Uninterpreted Puffin structure, Line 594 33
Figure 3.1.7 Line 594 interpreted 34
figure 3.1.8 Oliver sandstone time structure 35
Figure 3.1.9. Puffin time structure of the 'event horizon' 36
Figure 3.1.10 Structure-to-Oliver isochron 37
Figure 3.1.11 Miocene-to-Oliver isochron 38
Figure 3.1.12 Time slice at 736 ms 39
Figure 3.1.13 Downrange-to-crossrange diameter ratio vs angle of impact 40
Figure 3.1.14 Depth/diameter ratio vs impact angle 40
Figure 3.1.15 Atmospheric breakup of a meteoroid 41
Figure 3.1.16a Clustered projectile crater 42
Figure 3.1.16b Clustered projectile crater, 45° impact angle 42
Figure 3.1.17 Target/projectile density and contact time vs D/d 43
Figure 3.1.18 Variation of crater depth with water depth 44
Figure 3.1.19 Solution collapse feature 45
Figure 3.2.1 Location of the Muskingum structure 54
Figure 3.2.2 Cambrian/Ordovician stratigraphic column for Eastern Ohio 55
Figure 3.2.3 Seismic line base map 56
Figure 3.2.4 Correlation of synthetic seismograms 57
Figure 3.2.5 Line FM1, uninterpreted 58
Figure 3.2.6 Line FM2, uninterpreted 59
Figure 3.2.7 Line FM1, interpreted 60

Figure 3.2.8 Line FM2, interpreted 61
Figure 3.2.9 Line FM1, interpreted 62
Figure 3.2.10 Line FM2, interpreted 63
Figure 4.1.1 Location map for the Hotchkiss structure 74
Figure 4.1.2 White Valley seismic line, uninterpreted 75
Figure 4.1.3 Stratigraphic column for the Hotchkiss area. 76
Figure 4.1.4 Correlation of the seismic data with synthetics 77
Figure 4.1.5 Line 2, uninterpreted 78
Figure 4.1.6 Line 2, interpreted 79
Figure 4.1.7 Faults as interpreted on line 2 80
Figure 4.1.8 Line 3, interpreted 80
Figure 4.1.9 Line 1, interpreted 81
Figure 4.1.10 Hotchkiss formation diagram 82
Figure 4.1.11a Pre-erosional stratigraphic uplift measurements 83
Figure 4.1.11b Post-erosion stratigraphic uplift measurements 83
Figure 4.2.12 Stratigraphic uplift measurement for the Hotchkiss structure 83
Figure 4.2.1a. Location map of the Steen River structure 94
Figure 4.2.1b. Base map of the Steen River area 96
Figure 4.2.2. Seismic line 96G80-20 with synthetic seismogram 97
Figure 4.2.3. Seismic line 96G80-09 with synthetic seismogram 98
Figure 4.2.4. An example of data and tie quality, Steen River 99
Figure 4.2.5. An example of data and tie quality, Steen River 100
Figure 4.2.6. Contoured time structure of the Cretaceous unconf. 101
Figure 4.2.7. Contoured time structure of the Slave Point 102
Figure 4.2.8. Contoured time structure of the Keg River 103
Figure 4.2.9. Contoured time structure of the Precambrian 104
Figure 4.2.10. SE region of the Slave Point time horizon 105
Figure 4.2.11. Pseudo-depth structure of the Slave Point 105
Figure 4.2.12. Cretaceous unconformity depth structure, Petrosys 106
Figure 4.2.13 Slave Point depth structure as calculated using Petrosys 107
Figure 4.2.14 Cretaceous unconformity depth structure, Petrosys 108
Figure 4.2.15 Slave Point depth structure as calculated using Petrosys 109
Figure 4.2.16 Keg River depth structure as calculated using Petrosys 110
Figure 4.2.17 Precambrian depth structure as calculated using Petrosys 111
Figure 4.2.18 Input seismic data for the Slave Point horizon 112
Figure 4.2.19 Slave Point time structure plotted using Matlab 113
Figure 4.2.20 Histogram of input seismic data for the Slave Point horizon 114
Figure 4.2.21 Cross-plot for the Slave Point horizon 115
Figure 4.2.22 The well-to-well variogram for the Slave Point horizon 116
Figure 4.2.23 The kriged well data of the Slave Point horizon 117
Figure 4.2.24 Kriging error as calculated for the Slave Point horizon. 118
Figure 4.2.25 The cross-validation plot, Slave Point 119
Figure 4.2.26 The kriging result for the Cretaceous unconformity 120
Figure 4.2.27 Expected error in the kriging result, Cretaceous unconf. 121

Figure 4.2.28 Kriging result for the Keg River horizon 122
Figure 4.2.29 Expected error for the Keg River kriging result 123
Figure 4.2.30 Precambrian kriging result 124
Figure 4.2.31 Expected error for the Precambrian kriging result 125
Figure 4.2.35 Kriging with external drift, Slave Point 126
Figure 4.2.36 Kriging with external drift error, Slave Point 127
Figure 4.2.37 Kriging with external drift cross-validation plot, Slave Point 128
Figure 4.2.38 Anisotropic kriging with external drift, Cretaceous unconf. 129
Figure 4.2.39 Kriging with external drift error, Cretaceous unconformity 130
Figure 4.2.40 Anisotropic kriging with external drift, Keg River 131
Figure 4.2.41 Anisotropic kriging with external drift error, Keg River 132
Figure 4.2.42 Anisotropic kriging with external drift, Precambrian 133
Figure 4.2.43 Anisotropic kriging with external drift error, Precambrian 134
Figure 4.2.44 25 km trend in the seismic data, Slave Point 135
Figure 4.2.45 The 'residual' Slave Point time structure 136
Figure 4.2.46 Depth to the Slave Point, single velocity function 137
Figure 4.2.47 6-direction seismic-to-seismic variogram, Slave Point 138
Figure 4.2.48a Isotropic covariance map, Slave Pt 139
Figure 4.2.48b Anisotropic covariance map, Slave Point 139
Figure 4.2.49 Anisotropic seismic-to-seismic variogram, Slave Point 140
Figure 4.2.50 Isotropic collocated cokriging result, Slave Point 141
Figure 4.2.51 Anisotropic collocated cokriging result, Slave Point 142
Figure 4.2.52 Isotropic collocated cokriging error, Slave Point 143
Figure 4.2.53 Anisotropic collocated cokriging error, Slave Point 144
Figure 4.2.54 Isotropic cokriging cross-validation plot, Slave Point 145
Figure 4.2.55 Anisotropic cokriging cross-validation plot, Slave Point 146
Figure 4.2.56 Collocated cokriging result, Cretaceous unconformity 147
Figure 4.2.57 Collocated cokriging error, Cretaceous unconformity 148
Figure 4.2.58 Collocated cokriging result, Keg River 149
Figure 4.2.59 Collocated cokriging error, Keg River 150
Figure 4.2.60 Collocated cokriging result, Precambrian 151
Figure 4.2.61 Collocated cokriging error, Precambrian 152
Figure 4.2.62 VRML image of the Slave Point 153
Figure 4.2.63 VRML image of the Slave Point 154

LIST OF TABLES

Table 1.4.1 Oil and gas in North American impact craters 8
Table 2.1.1 Hugoniot elastic limits 14
Table 2.5.1 Scaling relations derived from lunar crater morphometry 20
Table 3.1.2 Dimensions of the Puffin structure 27
Table 3.3.1 Summary of the acquisition parameters, Muskingum 47
Table 3.2.2 Dimensions of the Muskingum structure 51
Table 4.1.1 Summary of the acquisition parameters, Hotchkiss 67
Table 4.1.2 The processing flow for line #1, Hotchkiss 67
Table 4.1.3 The processing flow for line #3, Hotchkiss 68
Table 4.1.5 Dimensions of the Hotchkiss structure 72
Table 4.2.1. Oil and gas production, Steen River 85
Table 4.2.2. Conversion factors used for pseudo-depth calculations 87
Table 7.1.1 Known Terrestrial Impact Structures 158

ACKNOWLEDGMENTS

As is always the case with a thesis such as this, there are many people who contributed greatly. Without them, this work would not have been possible. I would to thank my supervisor Dr. Rob Stewart for his guidance and insight into the problems discussed in this thesis. I would also like to thank Dr. Alan Hildebrand for teaching me a great deal about the geology of impact craters.

This work would not have been possible without the generous donations of seismic data by BHP Petroleum Pty Ltd., Gulf Canada Ltd., CGAS Exploration, Pulse, and Shell Canada Ltd. Not only did Gulf Canada generously provide access to their Steen River seismic dataset but they also provided summer work space and use of their Landmark and Petrosys software packages.

Interpretation of this data was performed using SeisWorks 2-D and 3-D interpretation software donated by Landmark Graphics Corporation. The geostatistical methods used in the Steen River study were made possible by using the GeoStat software package from Hampson-Russell Software Services Ltd.

For their generous financial support, I would like to thank the CREWES Project sponsors and, as well, the Geological Survey of Canada. Special thanks are also extended CREWES Project staff Henry Bland and Colin Potter for solving the many hardware and software issues that arose during this work.

Finally, I would like to thank my wife, Tina, for her enthusiasm towards life and for helping me through difficult times.

GLOSSARY

σ Poisson's Ratio

ρ Density

HEL. Hugoniot Elastic Limit

K Bulk Modulus

KED Kriging with External Drift

P-Wave Seismic compressional (pressure) wave

S-Wave Seismic shear wave

TWT Two-way time

WCSB Western Canadian Sedimentary Basin

Chapter 1

INTRODUCTION TO THE STUDY OF IMPACT STRUCTURES

1.1 The history of impact crater studies

The history of impact crater studies can be traced to the investigations of Galileo when he first turned his telescope toward the moon in 1609. Shortly thereafter in 1610, he published Sidereus Nuncius in which he mentioned circular spots on the surface of the moon. These spots, he reasoned, must be depressions since their rims were lit before their floors as the terminator swept across them. Many of these structures, he also noted, had mountains at their center and some were floored with a dark material that looked similar to the dark areas he called maria (Latin for 'seas'). The first suggestion as to the origin of these structures appears to have come in Robert Hooke's 1665 book, Micrographia, which suggests a volcanic origin. Although he considered an impact origin, the idea was dismissed as interplanetary space was thought to be empty. In 1787, William Herschel lent support to the notion of lunar volcanism by reporting his observation of what he thought was a lunar eruption. It wasn't until 1829 that it was suggested by Gruithuisen that the lunar craters had been created by past impacts. This suggestion was not taken seriously and it wasn't until 1893 that G.K. Gilbert showed experimentally that the moon's craters could be due to impact. By performing low-velocity experiments using various slurries and powders he concluded that impact could be the mechanism responsible only in the case of a vertical impact. The idea of impact craters was again rejected since it was known that nearly all observed lunar craters were circular but craters produced by experiment were circular only for vertical impacts. Refuting this idea, E.J. Öpik suggested in 1916 that the impact of high velocity meteroids would result in circular craters for most angles of incidence. This work was followed by Alfred Wegner's 1920 publication, *The origin of lunar craters*, supporting the impact hypothesis. Then in 1924 and 1930, A.C. Gifford published papers comparing impacts to explosions. He noted that the kinetic energy per unit mass of a meteorite striking at a speed of 2 miles per second was equivalent to the

craters formed in such a manner, he suggested, should be circular regardless of the impact angle. Nearly 20 years later, R.S. Dietz used geological techniques to describe lunar features and concluded that they must be of impact origin. Then in 1954, after examining high-quality photographs taken with large telescopes, Gerard Kuiper published an influential paper supporting the impact origin. It wasn't until the 1960's, however, that extraterrestrial collisions were considered to be significant events in the history of the Earth. Recognition of the geological significance of impacts was a result of both the exploration of the solar system by humans and robotic spacecraft and our ability to definitely identify terrestrial impact structures using petrological and geochemical techniques (French, 1999). In the decades that followed, scientists have realized that extraterrestrial impacts have significantly affected the Earth's surface, crust, and geological history (French, 1999).

1.2 Terrestrial impact crater studies

The study of terrestrial impact features appears to have begun in 1906 when D.M. Barringer argued that Meteor Crater, Arizona was caused by the impact of a large, high speed iron meteorite. As he was interested in mining the area, Barringer immediately staked a claim and set about to exploit the large meteoritic mass that he thought lay beneath the crater floor. After drilling several holes, Barringer and B.C. Tilghman published their findings in two separate papers. In these papers, Tilghman discussed impact mechanics and correctly surmised an impact velocity between 9 and 42 miles per second. His assumption that meteoritic material must still lie below the surface, however, was incorrect.

In 1922, Barringer's son suggested an impact origin for several small craters in Odesa, TX. Five years later, I.A. Reinvaldt described the Kaalijarv crater in Estonia as being of an impact origin. In the same year, 1927, L. Kulik led an expedition to the site of the 1908 explosion near Tunguska River where they found 2000 km^2 of fallen trees. In 1931, the Henbury craters in central Australia were recognized as impact features by A.R. Alderman. In 1936, J.D. Boon and C.C. Albritton showed that previously described crytovolcanic structures could be explained as the scars of ancient meteorite impacts. R.S. Dietz restudied the Kentland structure in 1947 and discovered fractures in the rock that caused it to break into striated cones. These cones (now known as shattercones) had first been recognized by W. Branca and E. Fraas at Steinham Basin in Germany but it was Dietz who argued that they could only occur near impact structures. In 1961, E.M. Shoemaker showed that shattercones could be created around small-scale impacts in dolomite. A few years later, Dietz announced the existence of shattercones around the Sudbury structure and around the Vredefort Dome. Discovered in 1953 and 1961 respectively, coesite and stishovite are extremely high-pressure phases of quartz that have only been observed around impact craters. Consequently, their presence makes an excellent diagnostic indicator of impacts.

To date, more than 150 impact features have been identified on Earth (Figure 1.2.1). As one would expect, the distribution is broad, with a greater number of the discoveries in areas with well-developed research infrastructure.

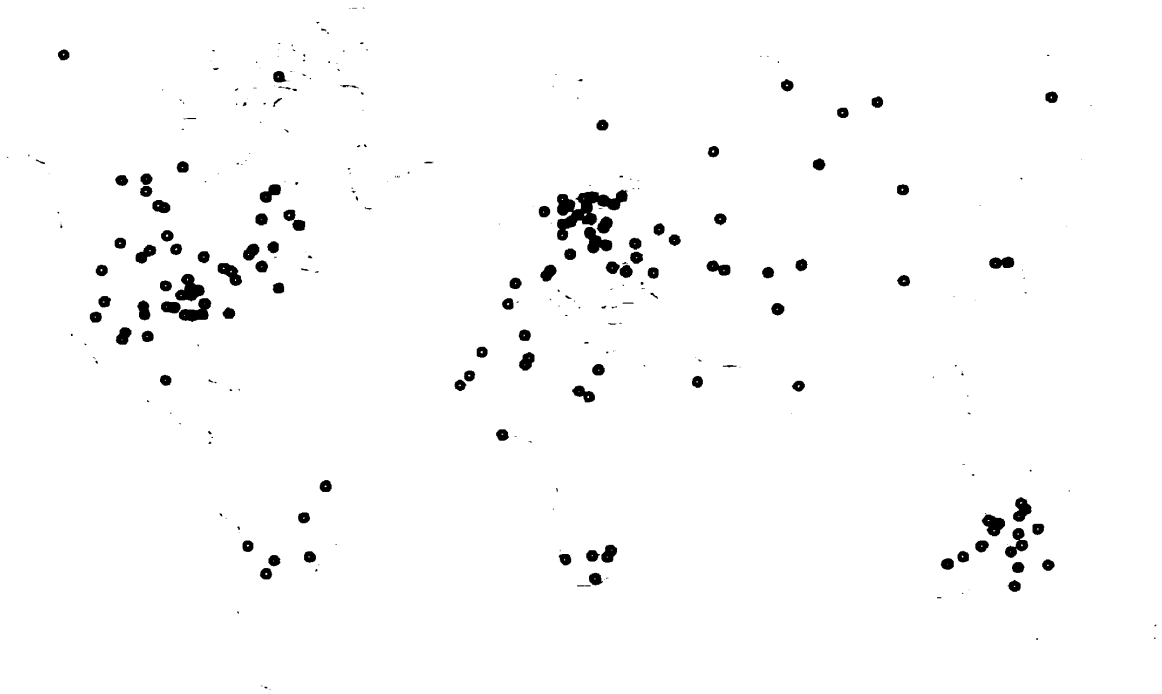

Figure 1.2.1 Location map of identified terrestrial impact structures. (Geological Survey of Canada website)

1.3 Impact crater types

Characterized by their size and morphology, impact craters are classified as either simple or complex. A 'simple crater' (Figure 1.3.1) is distinguished by a bowl-shaped cavity partially filled with an allochthonous (displaced and rotated crater-fill units) breccia lens. Ideally, simple craters have a circular raised rim and an interior profile that is nearly parabolic. Simple impact craters also tend to have a well-defined rim and are regular in shape when formed by a projectile moving in excess of a few kilometers per second. Slower moving projectiles tend to form irregularly-shaped structures with a poorly defined rim. The rim-to-floor depth is roughly one-fifth of the rim-to-rim diameter, and the rim height is about 4 percent of the total diameter (Melosh, 1989). The maximum diameter of such a crater is dependent on the surface gravity of the impacted body and the strength of the impacted rocks. On the Earth, this limit is approximately 4-km in igneous rock and 2-km in sedimentary rock. Beyond this limit, the morphology of an impact crater changes dramatically. The formation of a central uplift and slump blocks arranged within an annular synform characterizes a 'complex crater' (Figure 1.3.2).

Complex craters are much shallower in proportion to their diameter than simple craters and appear to represent collapsed simple craters. The material making up the central peak is composed of rocks that originated below the crater floor. The total amount of stratigraphic uplift is roughly 8 percent of the crater's final diameter (Melosh, 1989). In both types of craters, an ejecta blanket is present. Often, overturned stratigraphic features are noticed around the rim of impact structures or on top of the innermost slump blocks.

As crater size increases, the central peak of a complex crater changes to a concentric ring of peaks. The inner ring of these peak-ring craters is approximately half the rim-to-rim diameter. The peak to peak-ring transition diameter scales in the same manner as the simple to complex transition diameter, inversely with the gravitational acceleration.

Both simple and complex craters exhibit a raised rim structure that is due to both ejecta deposits and structural uplift of the underlying preimpact surface. This uplift is greatest at the rim crest and disappears at approximately ***1.3 to 1.7 crater radii*** from the center (Melosh, 1989). As the crater grows, strong radial forces tend to push/displace the rock

units upwards. Another mechanism for rim uplift can be the injection of subhorizontal breccia dikes into the crater wall (Figure 1.3.3).

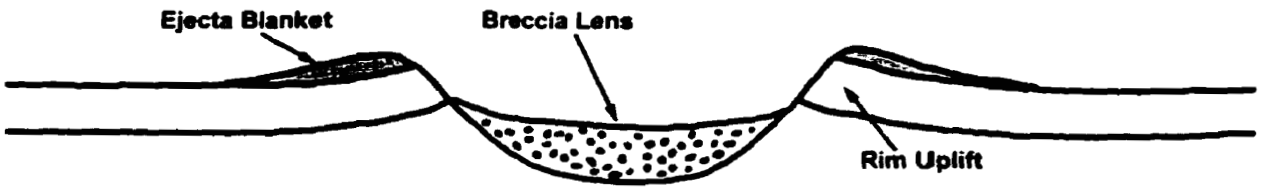

Figure 1.3.1 Schematic of a simple impact structure.

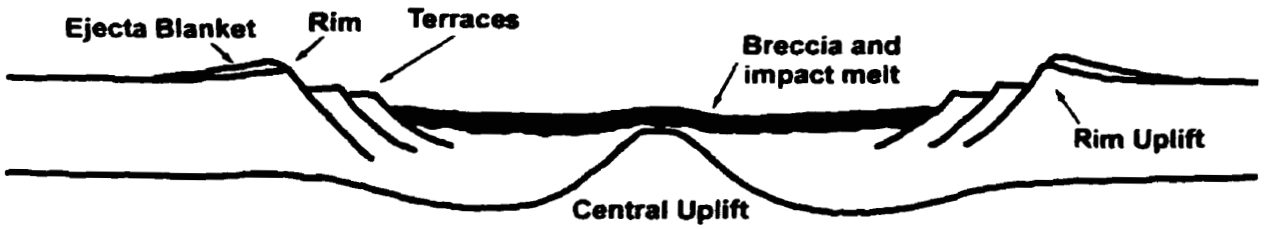

Figure 1.3.2 Schematic of a complex impact crater.

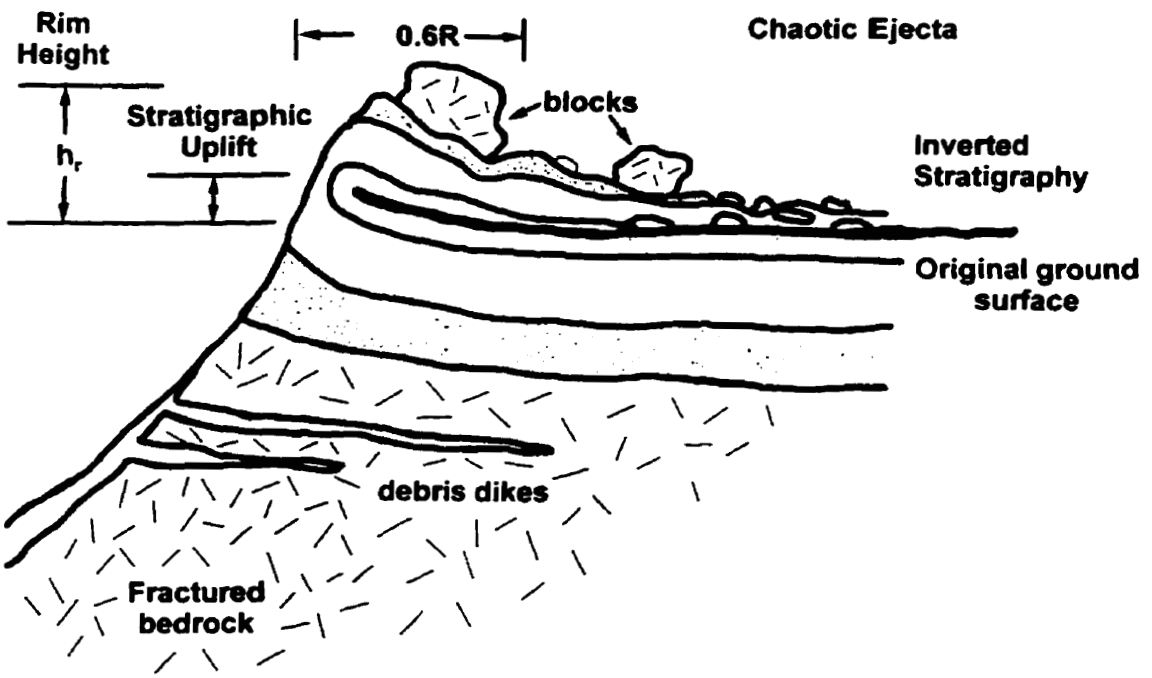

Figure 1.3.3 This schematic of the rim of a small impact crater illustrates the stratigraphic uplift and the effect of injected debris dikes. The stratigraphic uplift is confined to about 1.6x the radius (R) of the crater's center. Also, note the inverted stratigraphy and the large blocks that lie on the rim deposits. (from Melosh, 1989)

1.4 Economic importance of impact structures

Of the more than 150 known impact craters on the Earth, approximately 25% have been associated with economic deposits at one time or another. Of these, 17 are being actively exploited (Grieve and Masaytis, 1994). In some cases, the deposits are world class such as the Cu-Ni deposits at Sudbury, Ontario. Based largely on North American reserves (≈$5 billion annually) and the gold and uranium deposits of the Vredefort structure in South Africa (≈$7 billion annually), the annual revenue from impact-related reserves is estimated at over $12 billion (Grieve and Masaytis, 1994). This estimate, however, does not include revenues generated from the extraction of building material (e.g. cement and lime) from Ries, Germany (≈$70 million annually) or from hydroelectric generation from the Manicouagan reservoir in Quebec (≈$200 million annually).

Table 1.4.1 Hydrocarbon production associated with several impact craters in North America (adapted from Isaac and Stewart, 1993).

Impact Feature	Diameter (km)	Age (MY)	Hydrocarbon Accumulation
Ames Hole, Oklahoma	8	450	$7x10^6m^3$ (50MMbbl) in estimated reserves from crater rim and floor
Avak, Alaska	12	3-100	37BCFG reserves in slump block traps
Calvin, Michigan			600MMbbl oil
Newporte, North Dakota	3.2	500	Oil shows and some production from raised rim
Red Wing Creek, North Dakota	10	200	$6.4x10^6m^3$ to $11x10^6m^3$ (40-70MMbbl) in recoverable reserves from the central uplift
Steen River, Alberta	25	97.5	72BCFG proven reserves
Tookoonooka, Australia	55		Potential for stratigraphic traps
Viewfield, Saskatchewan	2.4	Triassic/Jurassic	$3.2x10^6m^3$ reserves from raised rim

1.5 Other crater-like features

Grouped in the category of crypto-explosion structures, impact craters share many of the characteristics of other features such as those created by magmatic intrusion or collapse. This section discusses diatreme intrusions such as kimberlite pipes and collapse features caused by salt dissolution.

Kimberlite pipes are thought to originate when hot molten kimberlite magma ascends rapidly towards the surface. Upon breaching the surface, a crater closely resembling an impact crater may be created. The initial eruption results in the formation of brecciated material around the rim and on the floor of the crater. The continuing eruption consists of pyroclast production and in rare cases, kimberlitic lavas (Mitchell, 1986). The volume of the pyroclastics is small and they are generally confined to thinly bedded tuff rings and the crater itself (Mitchell, 1986). Subsequent erosion of the structure results in the deposition of epiclastic kimberlites onto the crater floor. Underlying the crater facies is a 1-2 km long carrot-shaped stalk. They generally have a vertical axis and steeply dipping sides (80°-85°) (Mitchell, 1986). On seismic data, these structures tend to appear as poor, washed-out data areas. The poor-data areas extend to great depths in the section and are seldom larger than 1-km in diameter. Due to the relatively low-energy nature (compared to an impact) of these events, horizontal stratigraphy is often present at the surface. Impact generated craters, on the other hand, often exhibit signs of rim uplift and overturned stratigraphy.

Dissolution features can occur in any rock that has a substantial amount of minerals that are easily soluble in brine or fresh water. Generally, they are found to occur in calcareous rocks or evaporites. For dissolution to occur, the solvent must pass through the rocks and must be relatively unsaturated with the minerals in question. The majority of dissolution collapse features are either isolated sinkhole type events, or are linear in form (Jenyon and Fitch, 1985). In an area that contains a substantial thickness of limestone and where stress has been applied, solution collapse features can be frequent (Jenyon and Fitch, 1985).

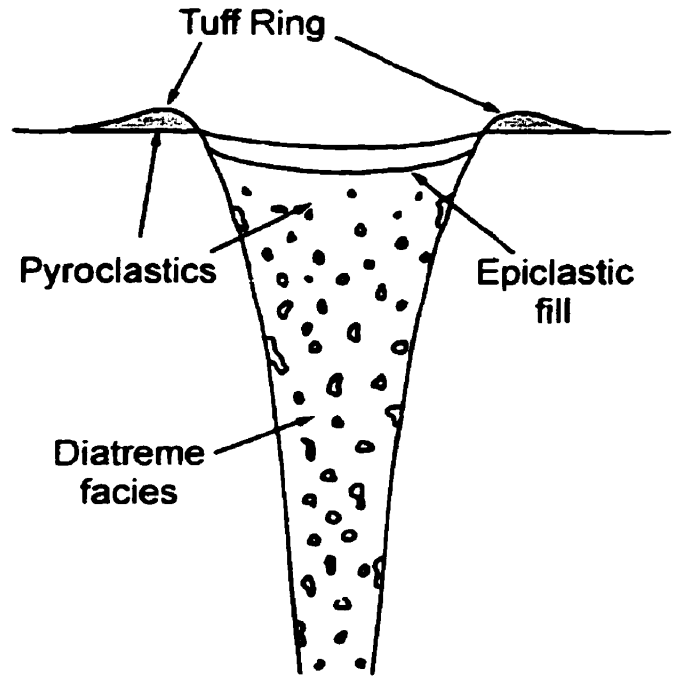

Figure 1.5.1 In general, a kimberlite pipe resembles a simple impact structure. A diagnostic feature is the carrot-shaped diatreme stalk that extends to great depths.

Figure 1.5.2 The Blue Hole of Belize is a well-known sinkhole that is 300 m in diameter by about 130 m in depth. This feature is circular and exhibits what might be mistakenly interpreted as rim uplift on seismic data.

Chapter 2

PHYSICS OF IMPACT CRATERING

2.1 Stresses, Limits, and Hugoniot Curves

What follows is an introduction to basic seismic theory. A more detailed treatment of these concepts can be found in Aki and Richards (1980) and Melosh (1989). To examine the stresses generated during a hypervelocity impact, we must first review the basic wave equation for the inelastic pressure wave,

$$\frac{\partial^2 P}{\partial t^2} = c_B^2 \frac{\partial^2 P}{\partial x^2} \tag{2.1.1}$$

where P is the pressure at time t, c_B is given by $\left(K_o/\rho_o\right)^{\frac{1}{2}}$, K_o is the isentropic bulk modulus, ρ_o is the density of the medium through which the waves are traveling and x is a distance along the direction of propagation. For a weak pressure wave, the pressure P is given as,

$$P = \rho_o u_L c_B \tag{2.1.2}$$

Equation 2.1.1 can also be rewritten in terms of the longitudinal wave velocity, u_L as,

$$\frac{\partial^2 u_L}{\partial t^2} = c_B^2 \frac{\partial^2 u_L}{\partial x^2} \tag{2.1.3}$$

In practice, waves generated by impact will be elastic in nature. That is, they will consist of both a longitudinal pressure (P) wave and transverse shear (S) waves. Thus, we have three separate equations that can be written as,

$$\frac{\partial^2 u_L}{\partial t^2} = c_L^2 \frac{\partial^2 u_L}{\partial x^2} \tag{2.1.4a}$$

$$\frac{\partial^2 u_{T_1 T_2}}{\partial t^2} = c_T^2 \frac{\partial^2 u_{T_1 T_2}}{\partial x^2} \tag{2.1.4b}$$

where u_{T1} and u_{T2} are the orthogonal transverse particle velocities and c_L and c_T are given by,

$$c_L = \left[\left(K_o + {}^{4\mu}/_{3}\right)/\rho\right]^{1/2} \tag{2.1.5a}$$

$$c_T = \left({}^{\mu}/_{\rho_o}\right)^{1/2} \tag{2.1.5b}$$

Equation 2.1.4a represents the longitudinal P wave component and equation 2.1.4b describes the motion of the two orthogonal components of the transverse shear wave. The stresses can now given as,

$$\sigma_L = -\rho_o u_L c_L \tag{2.1.6a}$$

$$\sigma_P = \left(\frac{\upsilon}{1-\upsilon}\right)\sigma_L \tag{2.1.6b}$$

where σ_L is the longitudinal stress, σ_P is the stress component perpendicular to the direction of propagation and ν is Poisson's ratio given by,

$$\upsilon = {}^{1}/_{2}(3K_o - 2\mu)/(3K_o + \mu) \tag{2.1.7}$$

In the case of the transverse wave, the stress is pure shear and can be written as,

$$\sigma_S = \rho_o u_T c_T \tag{2.1.8}$$

Shear waves can probably be neglected during the early stages of crater formation, however, as the stresses involved are much larger than the strengths of known solids (Melosh, 1989).

Solids can typically resist large compressive stresses, however their resistance to stress differences is limited. In equation 2.1.6b we see that the longitudinal stress, σ_L, is $(1-\upsilon)/\upsilon$ times larger than the perpendicular stress, σ_P. As the strength of a disturbance increases, so does the particle velocity and stress in an elastic wave. The stress difference, $\Delta\sigma$, increases and will eventually reach a point beyond which plastic or irreversible distortions occur. The stress difference at which this plastic flow is observed is called the yield stress, -Y. A plot of the maximum shear stress ($\tau=-(\sigma_L-\sigma_P)/2$) versus mean pressure ($P=-(\sigma_L+2\sigma_P)/3$ is given in Figure 2.1.1. Notice how ductile failure of the rock occurs at a maximum shear stress of Y/2 giving a value for the longitudinal stress at this point of,

$$\sigma_L = -\left(\frac{1-\upsilon}{1-2\upsilon}\right)Y \tag{2.1.9}$$

which is the negative of the Hugoniot limit (σ_{HEL}),

$$\sigma_{HEL} = \left(\frac{1-\upsilon}{1-2\upsilon}\right)Y \tag{2.1.10}$$

Given in Table 2.1.1 are the Hugoniot elastic limits for several different rocks and metals.

Table 2.1.1 Given are the Hugoniot elastic limits for a selection of crystals, rocks, and metals. (Melosh, 1989)

Material	Hugoniot Elastic Limit (GPa)
Single Crystals:	
Periclase (MgO)	2.5
Feldspar	3
Quartz (SiO_2)	4.5-14.5
Olivine (Mg_2SiO_4)	9
Corundum (Al_2O_3)	12-21
Rocks:	
Halite	0.09
Blair Dolomite	0.26
Vermont Marble	0.9
Westerly Granite	~3
Lunar Gabbroic Anorthosite	3.5
Granodiorite	4.5
Metals:	
Armco Iron	0.6
SAE 1040 Steel	1.2

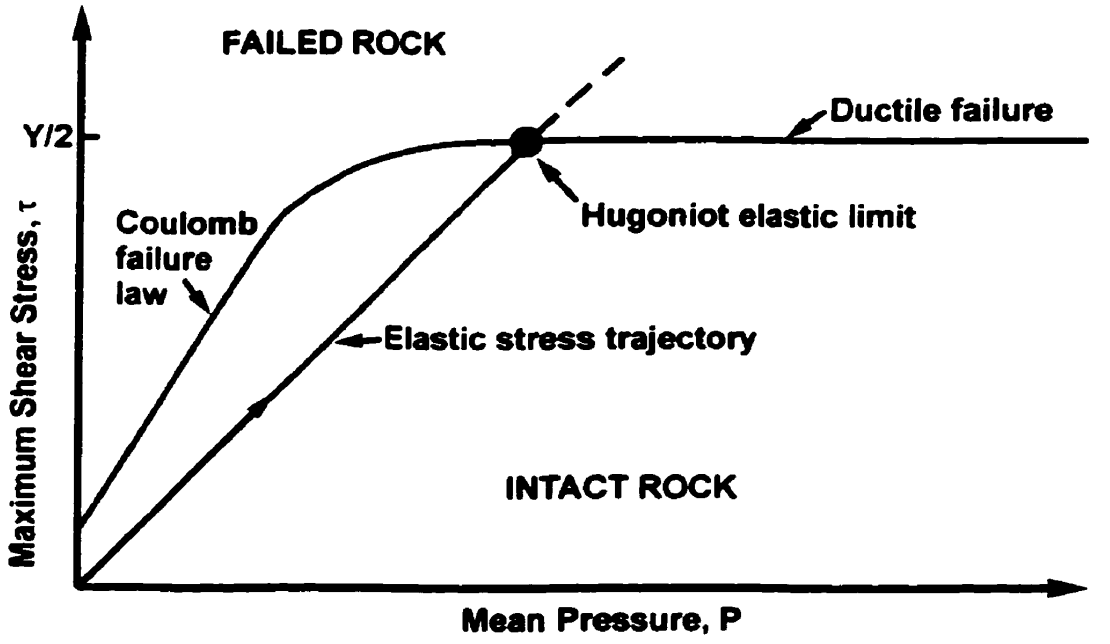

Figure 2.1.1 A plot of the maximum shear stress versus the mean pressure illustrates that the Hugoniot elastic limit is reached at a maximum shear stress of Y/2. Beyond this limit, ductile failure occurs. (Melosh, 1989)

2.2 The three stages of impact

During the impact of a hypervelocity projectile, it has been noted that there are three separate stages in the development of the crater (Gault et al., 1968). These three stages are known as the contact, excavation, and modification stages.

The first stage begins with the initial contact of the projectile with the planetary surface. As the projectile strikes, material is compressed, pushed out of the way, and accelerated to a large fraction of the projectile velocity. Deceleration of the projectile results in the generation of a shock wave as material in the contact zone between the projectile and target is strongly compressed. This shock wave propagates outwards from the point (points in the case of an irregular impactor) of initial contact. Propagating through both the target and projectile, the shock waves initially develop pressures on the order of hundreds of GPa (Melosh, 1989). Consequently, both projectile and target either melt or vaporize upon unloading from these high pressures. After the projectile has been decelerated, the contact and compression stage is finished with the result being the transfer of most of the projectile's kinetic energy to the target. Depending on the size, composition, and velocity of the projectile, this stage lasts anywhere from approximately 10^{-3} s for a 10-m silicate traveling at 10 km/s to more than a second for the very largest impacts (Melosh, 1989).

Immediately after the contact stage comes the excavation stage. This stage is characterized by an expanding, nearly hemispherical shock wave that shocks the target as it passes through it. The shock wave accelerates material and initiates an excavation flow by the interference of rarefaction waves propagating downwards from the surface. The subsequent excavation occurs roughly out to the limits of the brecciation (Hildebrand et al., 1998). An ejecta curtain forms blanketing the nearby terrain in a pattern that can be diagnostic of the initial conditions of impact. Depending on the crater size, this stage can take several minutes to complete. The result of this stage is a bowl-shaped transient cavity many times larger than the projectile that created it.

Following the excavation stage is the modification stage. This stage is characterized by the collapse of the transient cavity. In a small crater, loose material will slide down the

walls of the crater forming the breccia lens. As crater size increases, slump terraces form around the edge of the crater as well as a central uplift in the interior.

2.3 Vertical and oblique impacts

Hypervelocity experiments have shown that craters resulting from high-velocity impacts tend to be circular down to very low angles of incidence. This change in the circularity of craters with obliquity of impact was studied extensively by Gault and Wedekind in 1978. They defined the measure of circularity as D_t/D_c, where D_t is the maximum dimension of the crater measured along the path of the trajectory, and D_d is the maximum dimension of the crater at right angles to the trajectory path. Using aluminum and pyrex spheres with velocities of 3.6 km/s to 7.2 km/s, their experiments show that, for quartz sand targets, hypervelocity impact craters are circular for angles of impact greater than about 10° above horizontal. Their results indicate that this is irrespective of the projectile type or impact velocity. At angles less than 10°, however, the craters become elongated along the projectile flight path (figure 2.3.1).

Given in figure 2.3.2 is the relationship between the depth-to-diameter ratio and obliquity of impact for craters in quartz sand. From trajectory angles of $\theta=90^\circ$ to 30°, a slow decrease in the depth-to-diameter ratio is observed. Below 30° incident angle, however, a sudden decrease of the depth-to-diameter ratio after ricochet and elongation takes place.

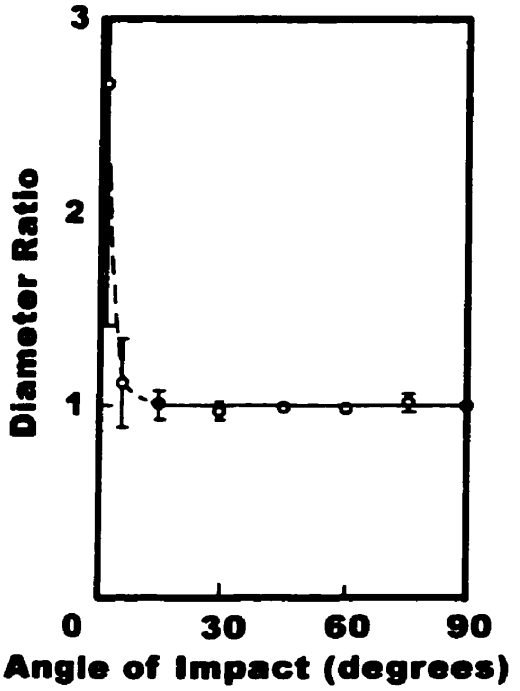

Figure 2.3.1 The effect of obliquity of impact on the circularity of craters formed in non-cohesive quartz sand. For this investigation, 121 pyrex and aluminum spheres were fired at velocities between 3.6 km/s and 7.2 km/s. (Gault and Wedekind, 1978)

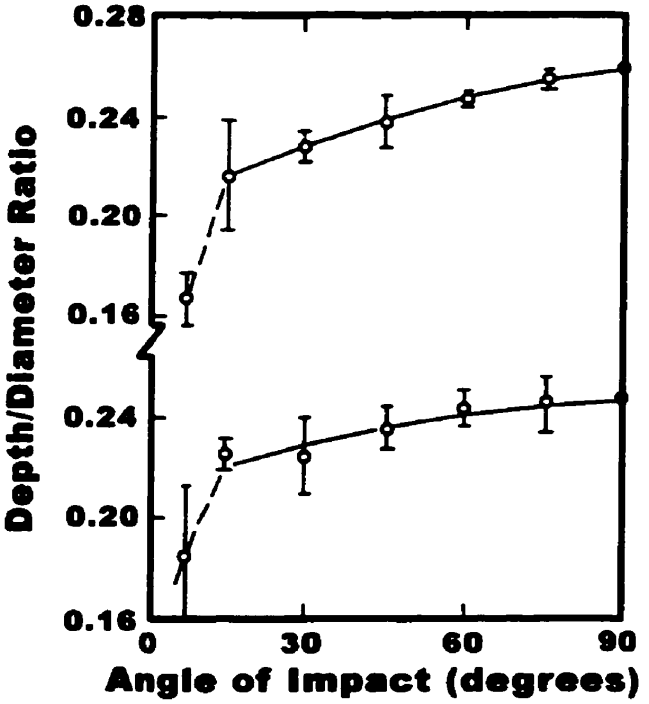

Figure 2.3.2 The variation of crater depth/diameter ratio with impact angle for the conditions of figure 2.3.1. (Gault and Wedekind, 1978)

2.4 Structured targets

When dealing with terrestrial impacts one needs to consider the effects of layering on the morphology of the final crater. Typically, we have a low-velocity near-surface layer overlying stronger, better-consolidated material. The thickness of this surface layer may range from 0 m to more than 100 m and can significantly affect the shape of simple craters.

Based on the work of V.R. Oberbeck and W.L. Quaide (1968), figure 2.4.1 shows how crater morphology can be affected by weak surface layers. Their experiments showed that the final crater morphology is dependent on the ratio between the crater's rim-to-rim diameter, D, and the layer thickness, t_L. The classical bowl-shaped morphology exists only when $D/t_L<4$. When $4<D/t_L<7.5$, a low mound forms in the central portion of the crater. The central mound morphology then gives way to a flat-floor morphology when $8<D/t_L<10$. The flat floor that represents the top of the strong layer, becomes excavated when $D/t_L>10$. The result of this excavation is a concentric crater with a shelf separating the weak layer from the strong half-space. As D/t_L increases beyond this transition, the shelf appears progressively higher up on the crater wall and becomes less noticeable (Melosh, 1989). Assuming a 100 m thick surface layer, we expect to find 'normal' morphology craters up to approximately 400 m in diameter. Between 400 m and 750 m in diameter a central mound develops. At approximately 800 m in diameter, a flat floor should develop and persist until a diameter of about 1000 m. At diameters greater than 1000 m, the simple crater develops a central pit and a low-lying bench.

As evidenced in simple lunar craters (figure 2.4.2), the observed morphology can aid in the estimation of the thickness of the weak surface layer. If a strong layer overlies a weaker layer, however, the only changes in the overall morphology will be larger clumps in the ejecta, blocks on the crater rim, and a more irregular shape in planform (Melosh, 1989).

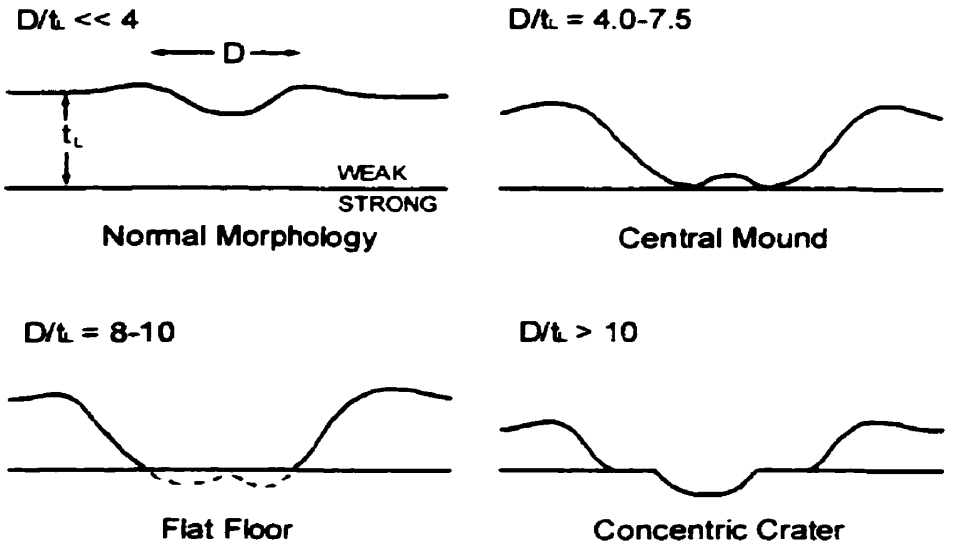

Figure 2.4.1 The morphology of craters formed in a weak layer overlying a stronger layer. (after Melosh, 1989)

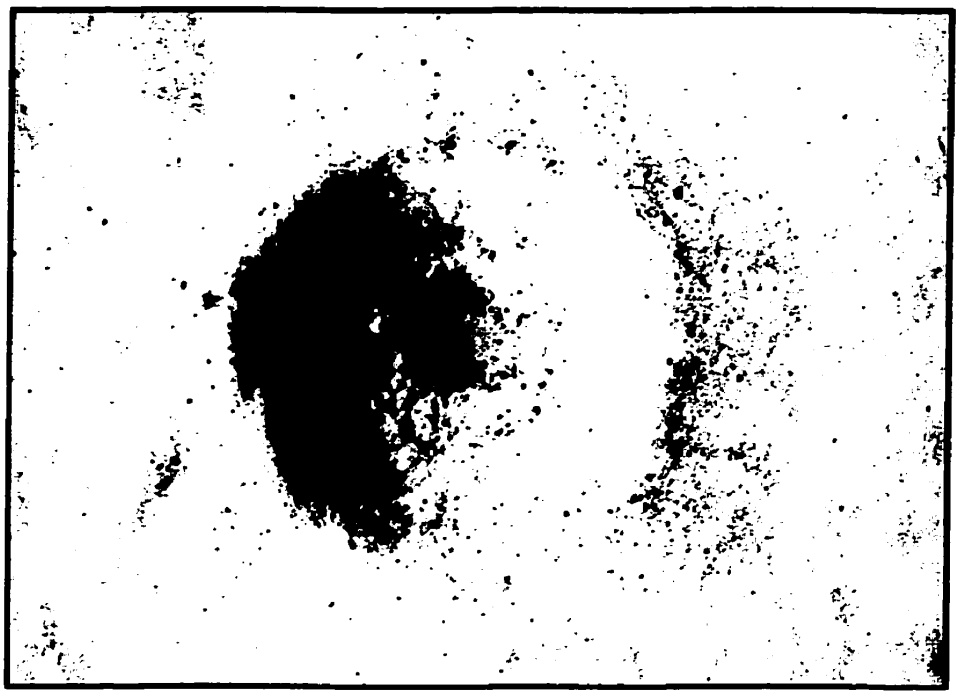

Figure 2.4.2 This lunar crater shows a wide bench low on its wall. This suggests that the surface of the moon in this area consists a 100 m thick weak layer that overlies a more resistant rock unit. The diameter of this feature is about 1.2 km. (Melosh, 1989)

2.5 Scaling of crater dimensions

Many years of lunar and terrestrial crater research have resulted in a number of parametric equations relating various dimensions to the final crater's rim-to-rim diameter. Summarized in Table 2.5.1 and figure 2.5.1a, these equations show that many crater dimensions increase monotonically with rim diameter.

Table 2.5.1 Scaling relations derived from lunar and terrestrial crater morphometry.

Parameter	Dependence on Rim-to-Rim Diameter (D, km)	Diameter Range (km)
Crater Depth	$H=0.196D^{1.01}$ $H=1.044D^{0.301}$	<11 * 11-400 *
Crater Floor Dia.	$D_f=0.19D^{1.25}$	20-140 *
Central Peak Dia.	$D_{cp}=0.31D^{1.02}$	3-200 **
Peak Ring Dia.	$D_{pr}=0.50D$	140-450 ***
Central Peak Height	$h_{cp}=0.0006D^{1.97}$	15-80†
Rim Height	$h_R=0.036D^{1.014}$ $h_R=0.236D^{0.399}$	<21 * 21-400 *
Terrace Zone Width	$W_T=0.92D^{0.67}$	15-350††
Widest Terrace Width	$w=0.09D^{0.87}$	20-200†††

*Pike (1977) from lunar studies
**Therriault et al. (1996) from terrestrial studies
***Wood and Head (1976) from lunar studies
†Hale and Grieve (1982) from lunar studies
††Pike (1976) from lunar studies
†††Pearce and Melosh (1986) from lunar studies

Although these equations were originally developed from lunar studies, several of them can be applied to terrestrial impact crater studies. In the case of a relatively uneroded (Puffin) structure, this thesis makes use of the equations for the crater depth and rim height as they relate to the observed rim-to-rim diameter. When the crater is highly eroded, however, use of these equations becomes difficult. This is because the parameters used in Table 2.5.1 are not expected to remain constant with depth below the surface of the crater (Figures 2.5.1a and 2.5.1b). The Hotchkiss study, for example, measures the central uplift diameter, D_{cp}, to make an estimate of the original crater diameter. Also used in the Hotchkiss study, is an additional equation described by Grieve and Pilkington (1996). This equation shows that the height of the stratigraphic uplift, h_{su}, (figure 2.5.2) is related to the final crater diameter by,

$$h_{su} = 0.086D^{1.03} \qquad (2.5.1)$$

where all distances are in kilometers.

The above lunar scaling relations, however, do not necessarily apply to all terrestrial impact structures. Thus, it would be a worthwhile effort to examine depth-independent parameters to arrive at a set of scaling relations to be used with highly eroded terrestrial craters. An example of such a relation might be that between the widest terrace width and the final crater diameter. Additional studies of seismic data would help show whether the terrace dimensions are truly depth independent. If there is no dependence on depth, careful measurements of terrace dimensions of terrestrial craters could yield a relation that is helpful in further investigations of highly eroded terrestrial craters.

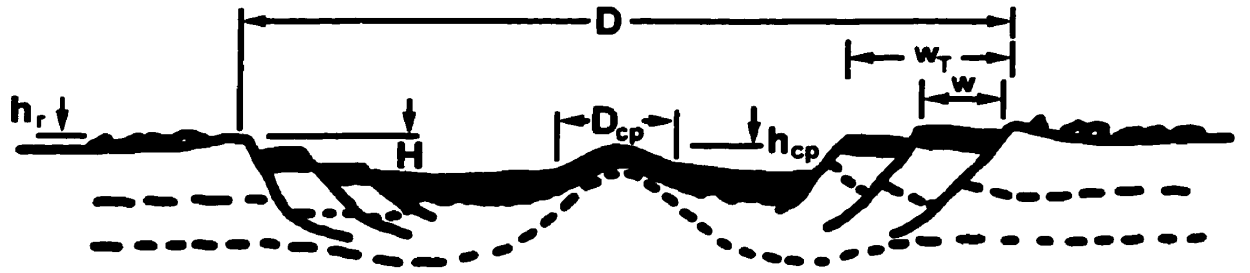

Figure 2.5.1a The scaling relations as given in Table 2.5.1 rely on the parameters shown in this schematic of an uneroded impact crater. (*after* Melosh, 1989)

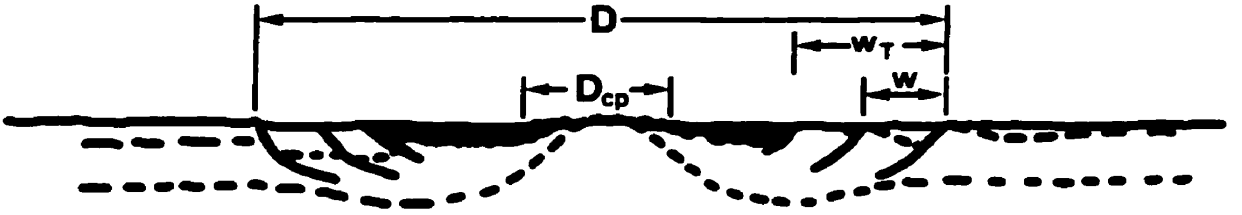

Figure 2.5.1b In the case of a highly eroded crater the number of measurable scaling parameters is limited. Note that only the terrace zone width, w_T, and the width of the widest terrace, w, remain similar to their counterparts in the uneroded case.

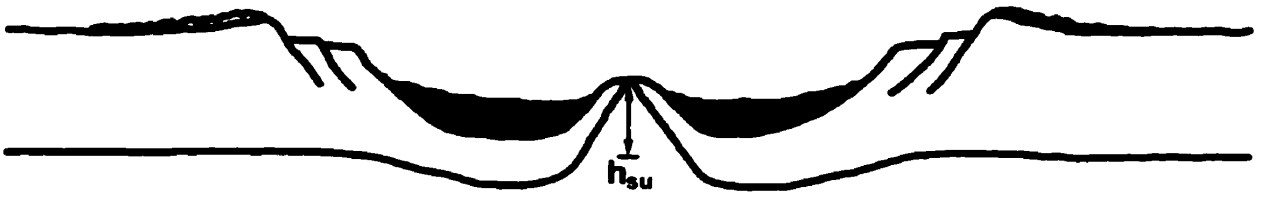

Figure 2.5.2 Pre-erosional schematic of a complex crater shows how the maximum stratigraphic uplift is measured.

Chapter 3

SIMPLE IMPACT STRUCTURES

3.1 Puffin 3-D, NW Australia

Approximately 250-km off the coast of northwestern Australia in the Timor Sea (Figure 3.1.1), a 3-D seismic survey images a small circular feature that exhibits some of the characteristics of a buried impact crater. The feature is approximately 2.0 km in diameter by about 150 m in depth. The depth of burial is about 1500 m in Tertiary carbonates. The structure is observed to be slightly elliptical in shape with a raised rim and a flat floor. Interpretation of the Puffin structure is complicated due to its proximity to a number of kimberlite pipes (Figure 3.1.2) and its placement within a soluble limestone unit. Additionally complicating the interpretation is the presence of large displacement faults and an uplifted lineament directly below the structure.

3.1.1 Geological Setting

The Puffin structure lies on the Ashmore Platform in an area known as the Bonaparte Basin (Figure 3.1.3). Like the other major sedimentary basins in the region, the Bonaparte Basin contains a thick Phanerozoic section that is up to 17,000 m in depth. This section is made up of several superimposed basins whose development can be related to successive cycles of rifting and break-up of the Gondawana supercontinent (Purcell and Purcell, 1988).

The westward-thinning Permian sequence in the area consists mainly of clastics and is thought to directly overly the basement. The clastic sediments of the Triassic range from fine-grained shales at the base to fluvio-deltaic sands at the top. The identifiable depocentres of the Triassic become emphasized in the Jurassic. Consisting of marine shales, the Jurassic sequence fills north-east to south-west trending depocentres but is absent on platform areas (Bradshaw, 1988). The early Cretaceous sediments consist mainly of deltaic sands and marine shales that are unconformably overlain by Cenozoic

carbonates. It is within these Cenozoic sediments that the Puffin structure lies (Figure 3.1.5).

The paleogeographic history of the Cenozoic is characterized by four major cycles. Of Paleocene to Early Eocene age, the first cycle contains several disconformities. Within the Bonaparte Basin, the lithological units comprise the Grebe sandstones and the Hibernia beds. The second cycle is of Middle to Late Eocene age showing no discernible lithological break between the limestones of the Early Eocene and the limestones of Middle and Late Eocene age. The units of this cycle are categorized as the Hibernia beds. During the Late Oligocene to Middle Miocene (cycle 3) there was a progradational building of the North Western Shelf. The end of this cycle is marked by shallow or lagoonal facies. Cycle four began in the Late Miocene and extends to the present time. There are no major breaks in this sequence.

3.1.2 Seismic Data Interpretation

Using SeisWorks 3-D interpretation software, several representative horizons were picked and mapped using many of the lines in the survey (Figure 3.1.6, 3.1.7). Picks were made based on information supplied by BHP Petroleum Pty. Ltd. using the autopicking method when possible. The horizons that will be examined here are those representing the top of the Paleocene, the base of the Miocene, the top of the Oliver sandstone unit (Figure 3.1.8), the 'event' surface (Figure 3.1.9), and a late Miocene reflector. The event surface horizon is thought to represent the surface of the structure after its formation. Also identified are several fault trends thought to have been active at the time of formation of this structure.

The deepest horizon examined is the top of the Paleocene. This reflector is continuous and shows evidence of a substructure anticline. Above the Paleocene, the Grebe sandstone reflector lies sandwiched between the predominantly limestone units of the Hibernia Formation. In the northwest of the study area, erosional truncations give evidence for a basal Miocene unconformity (≈25.5MY old). Lying conformably above the Miocene unconformity is the thin Oliver sandstone member (≈18.5-16.0 MY). Due to the strength and continuity of this reflector, it will be used as the comparison for the isochrons in this

study. Lying directly above the Oliver sandstone member a horizon characterizing the surface of bowl-shaped structure is interpreted. Within the structure, lapout features are observed giving evidence for post-event infill. The seismic character of these features tends to be strong and continuous. Above the structure, a late Miocene event has been picked.

Since the recent to Miocene section consists mainly of parallel reflectors, a great deal of information can be gleaned by examining horizon-to-horizon isochrons. If the structure was formed at a time when the Miocene reflectors were flat, then the structure-to-Oliver (SO) isochron will show the original shape of the structure (Figure 3.1.10). The SO isochron clearly shows a section of uniform thickness (in time) punctuated by a series of WSW-ENE trending faults. The structure is slightly oval in plan view and is observed to have a flat floor and uplifted rim. As a test of the validity of the assumption of reflector horizontality at the time of the event, a late-Miocene-to-Oliver isochron can be examined (Figure 3.1.11).

Estimating the age of this structure can be done in a simple manner if there are assumed to be no major changes in sea level during the mid-Miocene. Under this condition, the average rate of sedimentation can be assumed to be relatively constant. Interpolation between horizons of known age that lie above and below the structure will provide an estimation of the time of the event. Below the structure, the oldest Miocene deposits are about 17 MY old. The reflector characterized as a late Miocene event that lies above the structure is estimated to be about 12 MY old. Since the Puffin structure is located approximately 1/3 of the base-Miocene-to-late-Miocene isochron thickness above the base of the Miocene, and assuming a constant rate of deposition, this translates into roughly 2 MY in time or an age of approximately 15 MY for the Puffin structure.

3.1.3 Impact Crater Morphometry

By applying scaling relations, a better understanding of the Puffin structure can be achieved. Since the diameter of this structure is at the threshold of complex crater formation (2 km in sediments) it is expected that the following relations should apply;

$$H=0.196D^{1.01} \qquad (3.1.1)$$

$$h_r=0.036D^{1.014} \quad (3.1.2)$$

where H is the depth of the simple crater and h_r is the height of the rim above the surrounding plain. For a crater that is 2 km in diameter, the expected final depth is about 395 m while the expected rim height is about 75 m. On the seismic section, we should thus expect a two-way time difference between the top and bottom of the structure of 200 ms (assuming a constant velocity of 4000 m/s). The observed two-way time difference for the Puffin structure is only about 75 ms (or 150 m). One possible explanation for this apparent discrepancy lies in the noncircular shape of the Puffin structure. Its shape closely resembles an ellipse and, as a result, the effects of obliquity of impact and clustered projectiles must be considered.

At incident angles of less than about 10°, hypervelocity impacts tend to result in non-circular craters. In contrast to the apparent point source of the vertical collision, the shock produced in shallow collisions tends to be distributed along a near horizontal line. As a result, it is expected that the final depth of a structure produced in an oblique impact will be less than if the impact were vertical. Using the observed dimensions of the Puffin structure an estimation of the angle of impact can be made. From Figure 3.1.10 the dimensions of the structure are observed to be approximately 2180 m by 1720 m. This gives a diameter ratio of 1.27 which, after the work of Gault and Wedekind (1978), corresponds to an angle of incidence of approximately 5° (Figure 3.1.13). Examining Figure 3.1.14, we see that an incident angle of 5° corresponds to a depth/diameter ratio of between 0.17 and 0.19. From this, the expected depth of the Puffin structure is about 350 m. Since this value is still too large, we must consider another explanation of the anomalous shape.

When a meteoroid enters the Earth's atmosphere, it is subjected to extremely high aerodynamic stresses. At an altitude of 15 km these stresses are on the order of 100 MPa (Melosh, 1989). Since most recovered meteorites typically have crushing strengths between 1 and 500 MPa they are expected to break up upon entering the Earth's atmosphere (Melosh, 1989). Only strong or large meteoroids can survive high-speed travel through the atmosphere without being significantly crushed by aerodynamic stresses. Schematically, the process appears as in Figure 3.1.15. The crater that results from a cluster of meteoroid fragments differs both morphologically and structurally from a crater produced from a solid

meteoroid (Melosh, 1989). These craters tend to be shallow with nearly flat floors. Figures 3.1.16a and 3.1.16b show craters produced in the laboratory by clustered projectiles at impact angles of 90° and 45°. Note that in the case of a clustered projectile the resultant crater is abnormally shallow and is noncircular even at steep angles of impact. Experimentally, Schultz and Gault (1985) have shown that there exist relationships for the depth-to-diameter ratio dependent on the target and projectile densities and the time for the projectile-target contact (Figure 3.1.17). Their results for clustered projectiles into sand indicate the following relation,

$$\log D/d = 0.148 \log [(2r/v)(\delta_t/\delta_p)] + 1.318 \quad (3.1.3)$$

where δ_t and δ_p are the densities of the target and projectile respectively, r is the radius of the projectile, and v is the velocity of the projectile. If we assume a density ratio approximately equal to one (rock impacting into rock), a radius of 50 m (the approximate radius of a rocky meteoroid required to form a 2 km crater), and a velocity of 20 km/s, we find that the depth-to-diameter ratio is approximately equal to 0.1. Using an average diameter of 1.9 km, the depth of the resultant crater is about 190 m.

Since the local environment at the time of the formation of the Puffin structure was shallow marine with water depths of up to 200 m (Bradshaw et al.), a consideration of the effect of a water layer on the final depth of a crater is made. Using the results of small-scale experiments performed by Gault and Sonett (1982) the depth of the transient cavity formed in deep water, d_m, can be calculated from the relation,

$$d_m=0.10E^{0.25} \quad (3.1.4)$$

where E is the impact energy given by $1/2mv^2$. For an impactor of sufficient energy to form the Puffin structure, $E\sim2.5\times10^{17}$ J which gives $d_m\sim2.25$ km. Figure 3.1.18 shows the dependence of final crater depth on the water depth. Using a marine-to-surface crater depth ratio, d_c/d_o, equal to 0.43 (150m/350m) the water depth at the time of formation would have been about 225 m. Since this is close to the expected maximum water depth during the mid-Miocene, the shallow depth can be explained by a marine impact.

Table 3.1.2 Dimensions of the Puffin structure as measured from the seismic data and predicted from crater scaling relations.

Dimension	Measured	Predicted
Diameter	2180 x 1720 m	~2180 x 1720 m *
Depth	150 m	150 m[i] 190 m [ii] 350 m [iii] 400 m [iv]
Rim Height		
Angle of Impact	N/A	<45°

**5° inclined projectile*
[i] 225 m water depth
[ii] *Clustered projectile model*
[iii] *5° inclined projectile*
[iv] *Vertical impact*

3.1.4 Other Possible Explanations

Although the Puffin structure can be explained by the impact of a clustered projectile, consideration of other possible formation mechanisms is appropriate. Due to the circular nature of this structure, the general characteristics of dissolution features and diatreme intrusions must be examined.

As discussed in Chapter 2, diatreme intrusions such as kimberlite pipes can form cryptoexplosive features with characteristics similar to simple impact craters. On seismic data, craters formed by diatremes often exhibit evidence of a carrot-shaped stalk extending to great depths. The seismic reflectors below the Puffin structure, however, are continous and show no signs of intrusion. Additionally, there are no signs of intrusive activity in the area at the time of the formation of this structure.

Karst dissolution features can occur in any rock that has a substantial amount of minerals that are easily soluble in brine or fresh water. Generally, they are found to occur in calcareous rocks or evaporites. For dissolution to occur, the solvent must pass through the rocks and must be relatively unsaturated with the minerals in question. The majority of dissolution collapse features are either isolated sinkhole type events, or are linear in form (Jenyon and Fitch, 1985). In an area that contains a substantial thickness of limestone, and where stress has been applied (e.g., Puffin dataset), solution collapse features can be

frequent (Jenyon and Fitch, 1985). In the case of the Puffin structure, one could surmise that tensional fractures developed over the deeper anticlinal feature thereby providing a circulatory system for water. Dissolution of the underlying carbonates could then occur causing the overlying sediments to collapse gravitationally (Figure 3.1.19). The lack of major subsidence below the Oliver member, however, makes this explanation unlikely. Another explanation, however, is sub-aerial or shallow marine dissolution. If the feature were formed at the surface or at the base of a shallow sea, then collapse of overlying sediments would not occur. The structure would simply fill with sediments possibly creating the proper conditions for differential compaction at a later time. Supporting this theory are lapout features within the structure and an apparent lack of brecciated material. Additionally, the disturbed region of the Puffin structure extends only to the top of the Oliver sandstone member. In the case of sub-aerial or shallow marine dissolution, the insoluble Oliver sandstone sediments should be undisturbed. The lack of a bowl-shaped depression in Figure 3.1.8 illustrates the apparent lack of structure on the Oliver time structure.

3.1.5 Concluding Remarks

The Puffin structure is an anomalous circular feature bearing many of the characteristics of a meteorite impact crater. The seismic time structures and isochrons give evidence for rim uplift, an inner terrace and a broad, flat floor. The Puffin structure's elliptical shape and abnormally shallow profile can be explained by the impact of a clustered projectile about 75 m across travelling at 20 km/s. Although the structure lies in close proximity to several kimberlite pipes, it is thought to be too large to be explained as such. Furthermore, there is no seismic evidence for a carrot-shaped stalk extending to great depths. The dissolution of limestone and subsequent collapse of overlying sediments has also been described as a possible mechanism for the formation of this structure. As there is no observed drape over the rim of the structure this explanation is thought to be incorrect. Sub-aerial or shallow marine dissolution also provides a possible mechanism for the formation of this structure. From the seismic reflection data, the age of the structure is estimated to be approximately 15 MY.

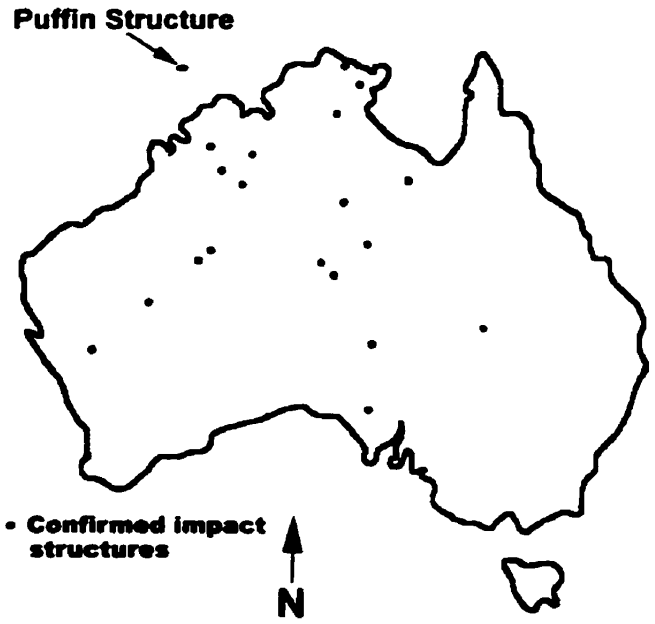

Figure 3.1.1 Australian base map showing the location of the Puffin structure and confirmed impact features on the Australian continent. (modified from Geological Survey of Canada Website, 1997)

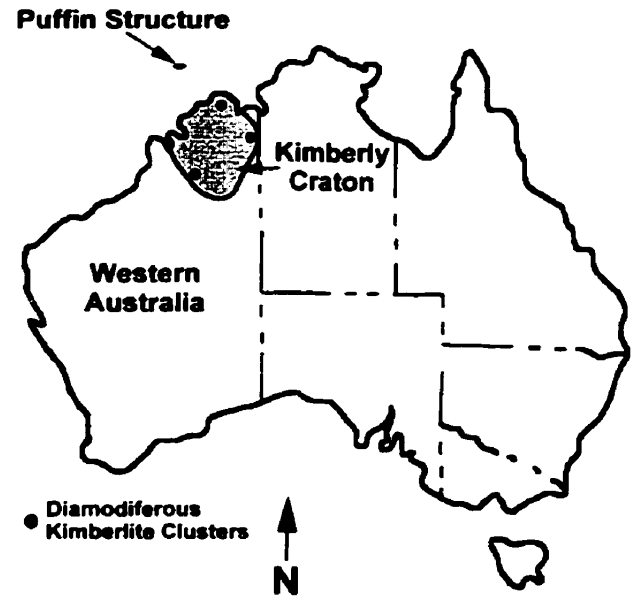

Figure 3.1.2 This map shows the location of the Kimberly Craton and several diamondiferous Kimberlite clusters within the Kimberly province. (after Janse, 1985)

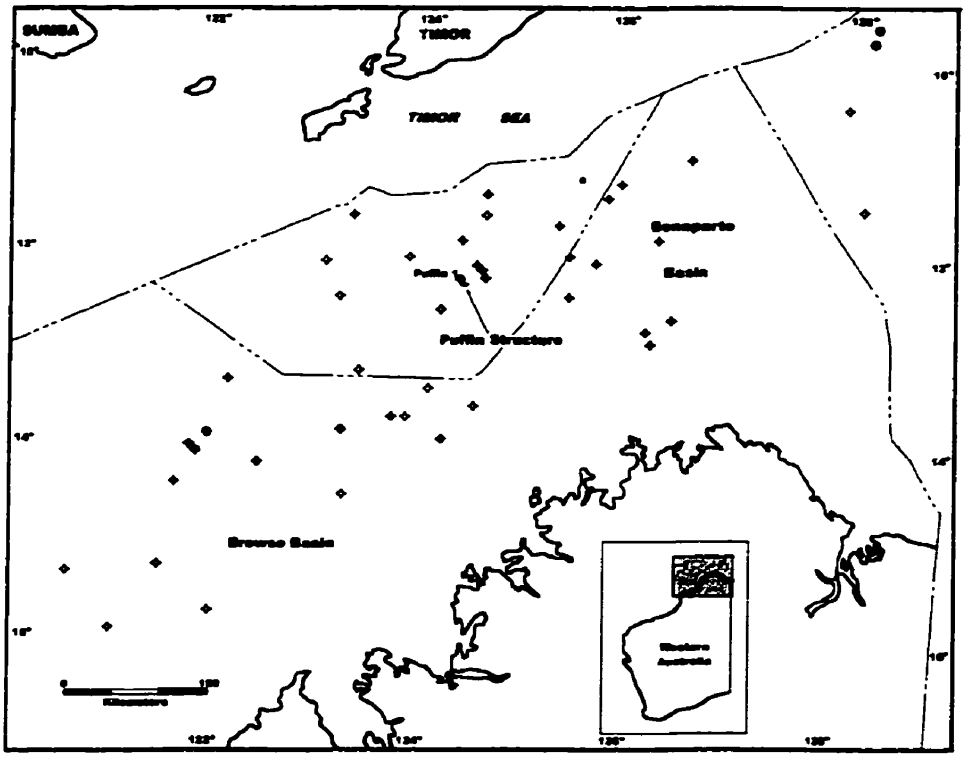

Figure 3.1.3 Location map of the northern part of the North West Shelf showing well locations and the location of the Puffin structure (Apthorpe, 1988).

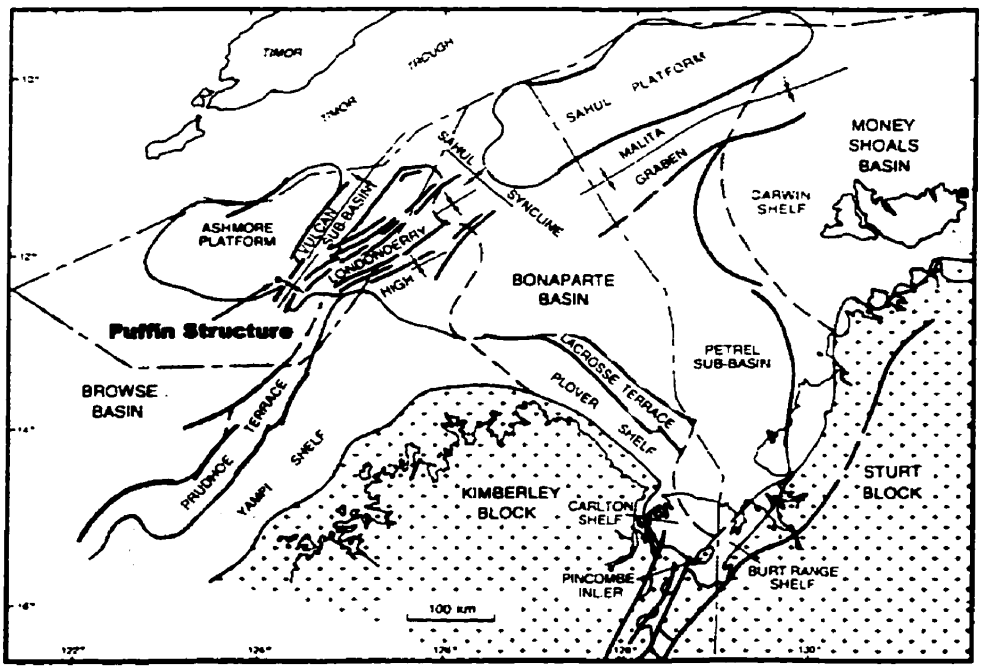

Figure 3.1.4 The Puffin structure lies at the edge of the Vulcan sub-basin on the Ashmore platform. Basin subdivisions for the Bonaparte basin and adjacent basins as given by Mory (1988).

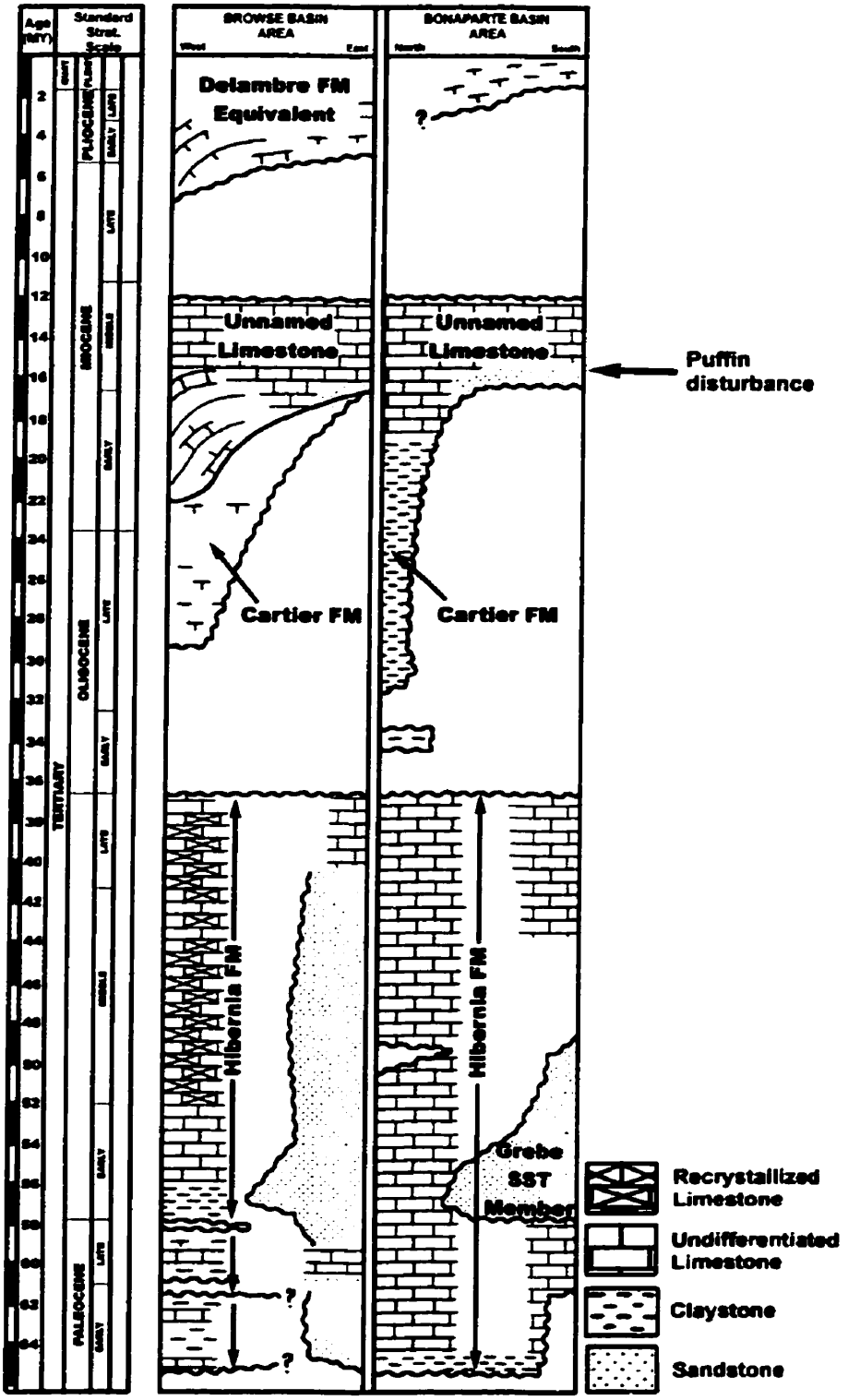

Figure 3.1.5 Stratigraphy of the Cenozoic for the Browse and Bonaparte Basins showing the region of interest (*after* Apthorpe, 1988).

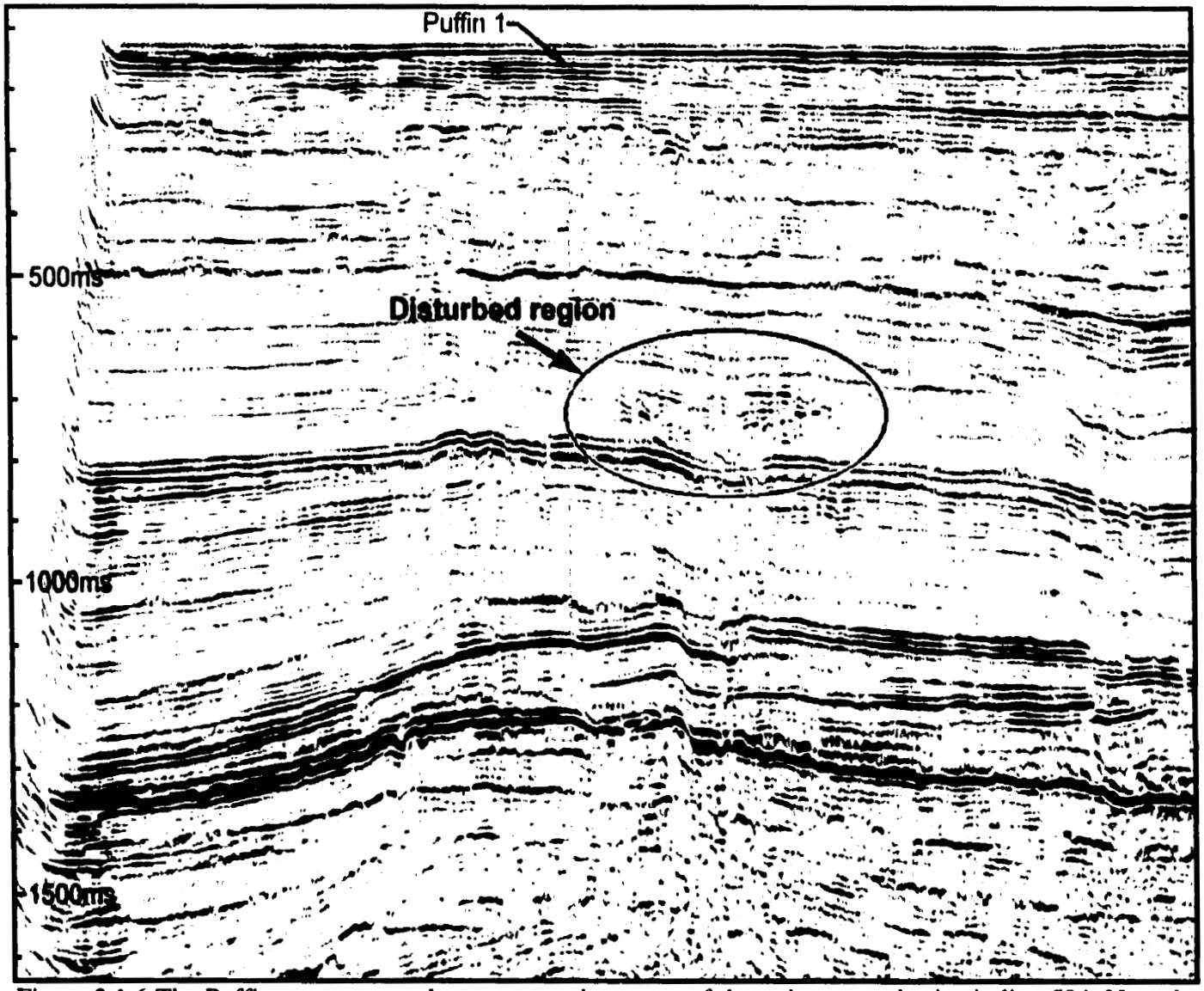

Figure 3.1.6 The Puffin structure can be seen near the centre of the uninterpreted seismic line 594. Note the complexity of the faulting and the anticline below the structure.

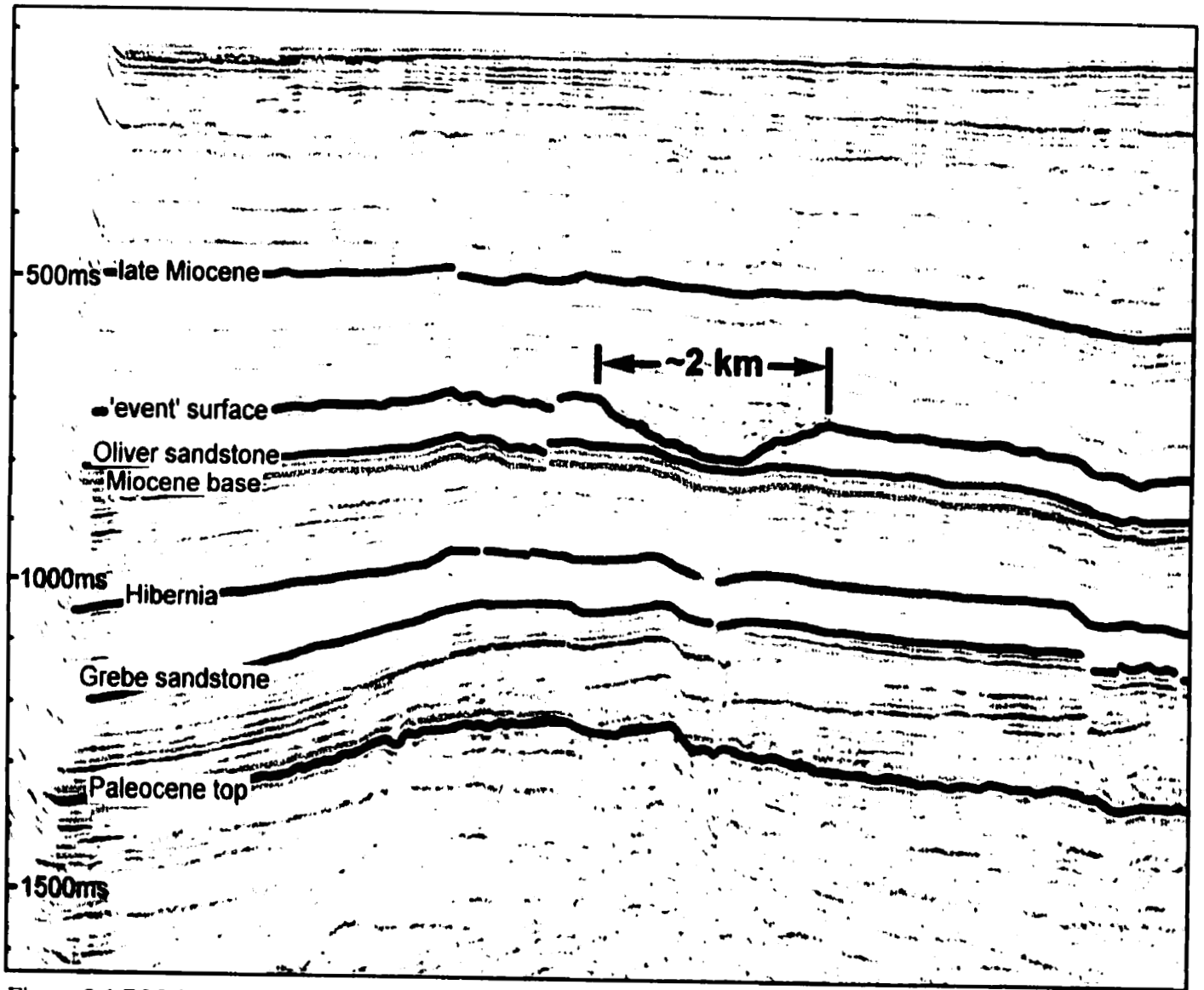

Figure 3.1.7 Major seismic horizons as interpreted on line 594.

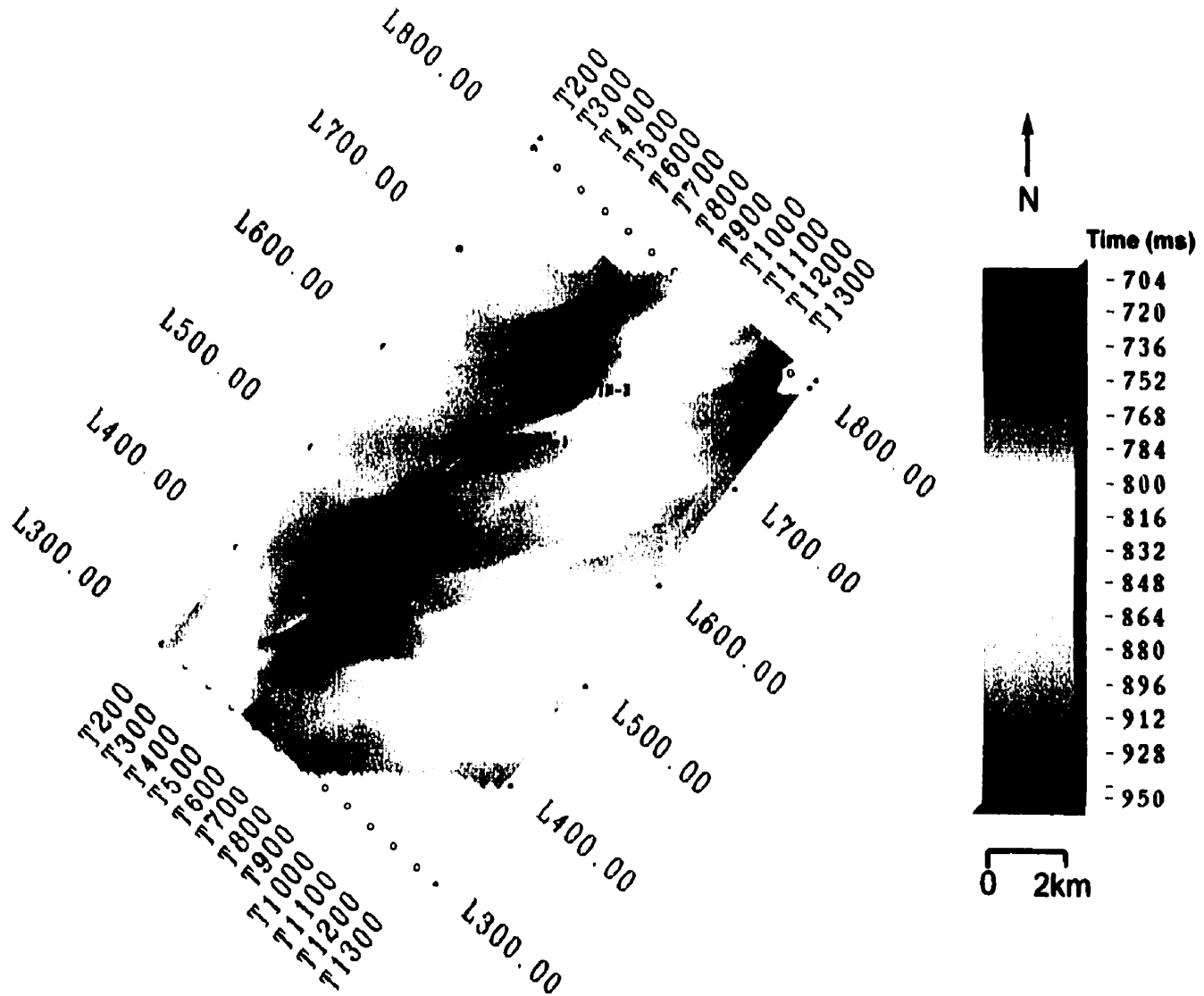

Figure 3.1.8 The Oliver sandstone member is a thin, early Miocene unit lying directly above the base-of-the-Miocene unconformity.

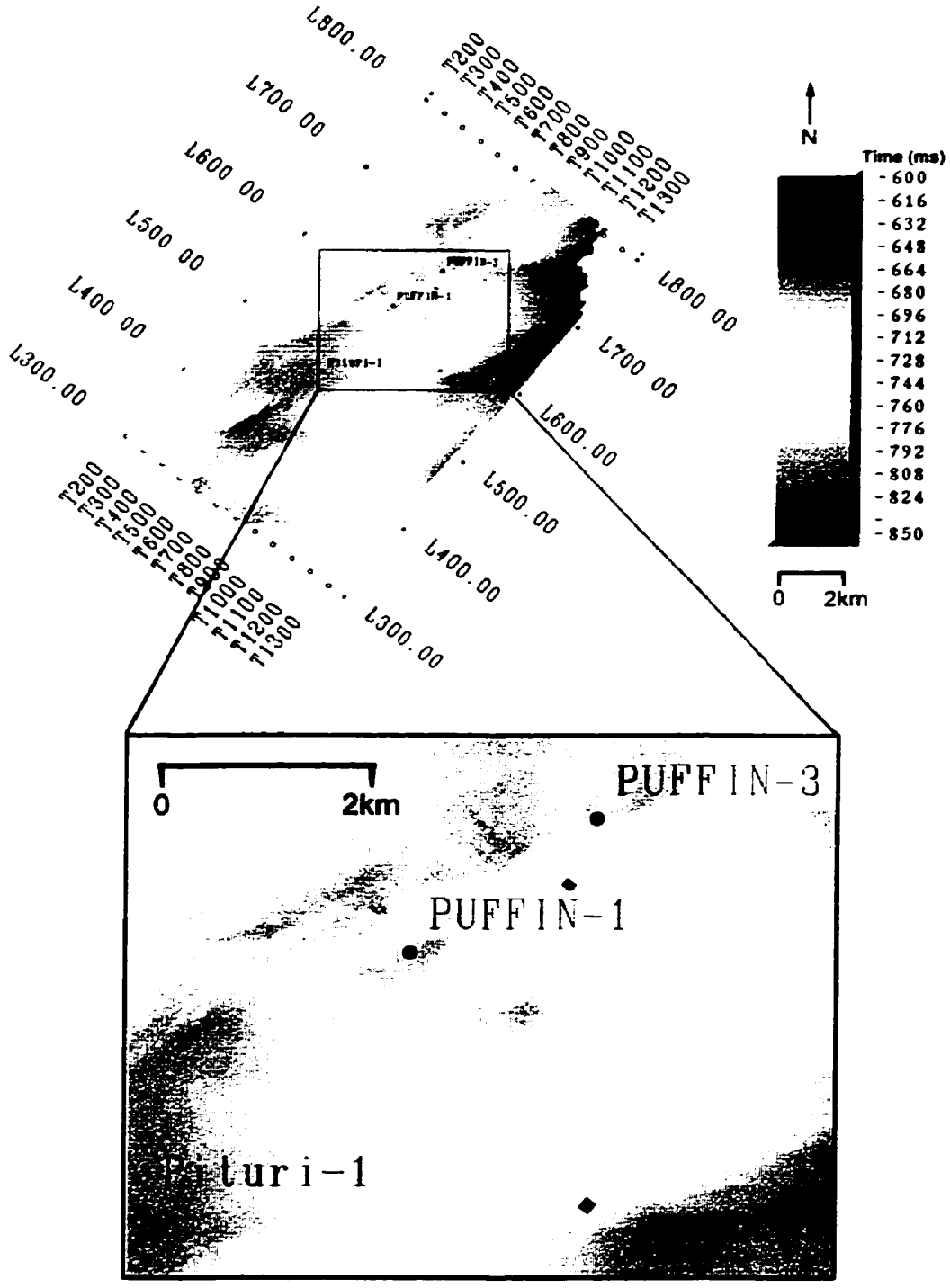

Figure 3.1.9 This time structure of the 'event horizon' shows a nearly circular structure amidst several lineaments.

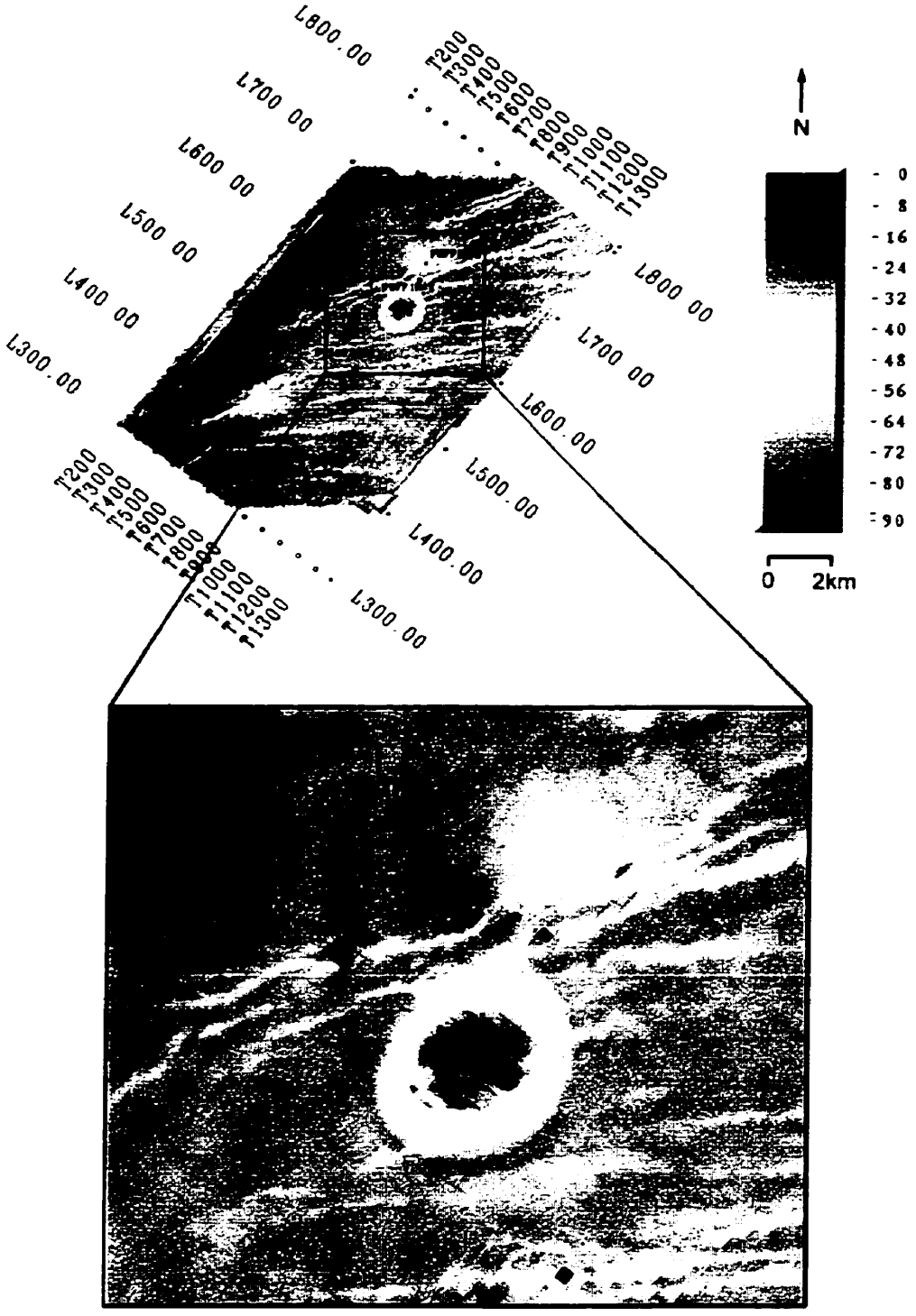

Figure 3.1.10 The structure-to-Oliver isochron shows the structure as it may have appeared at the time of formation. The structure structure can be broadly characterized as an elliptical, flat-floored crater-like feature with apparent rim uplift. Also note the slight raised region towards the NNW.

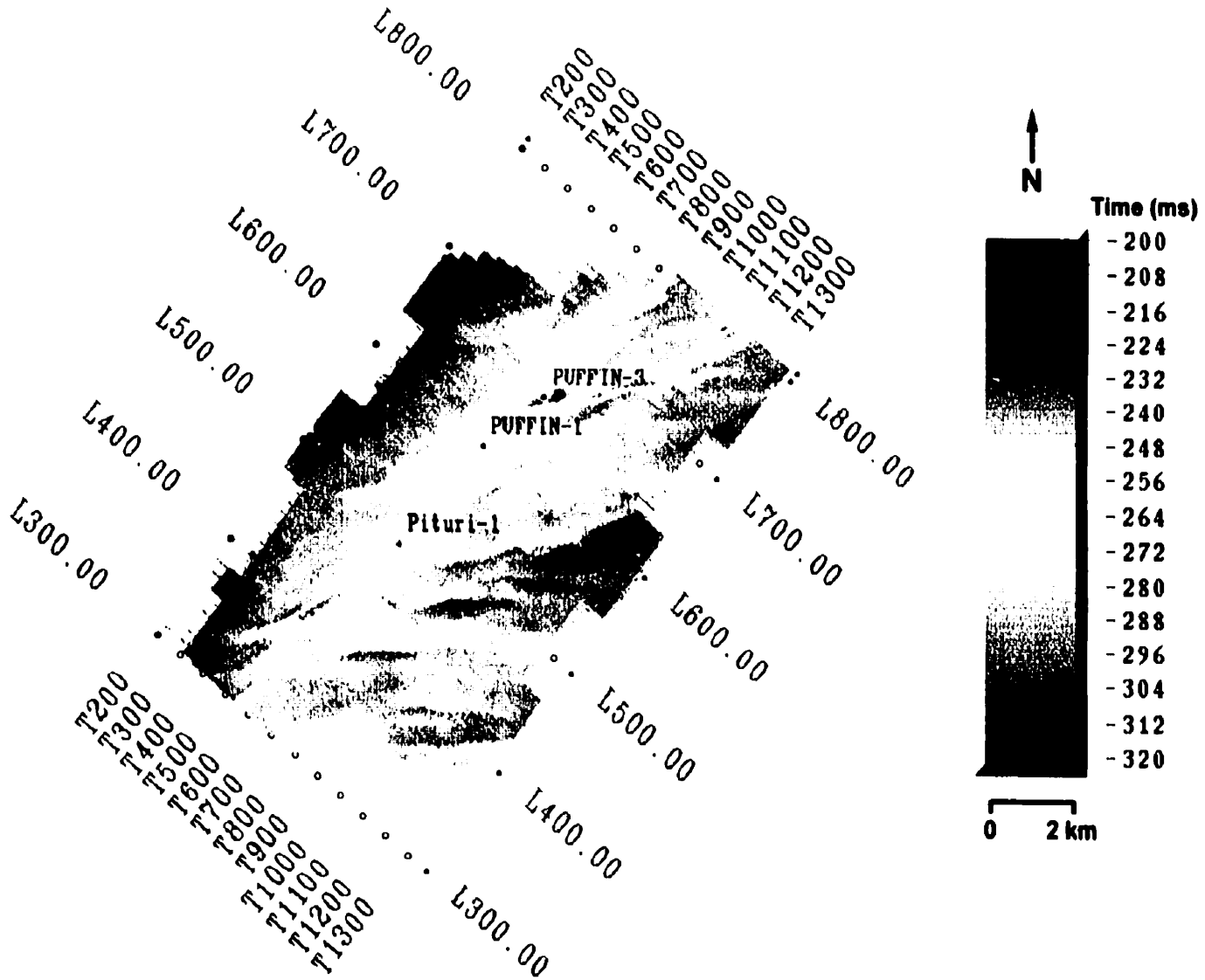

Figure 3.1.11 The late-Miocene-to-Oliver isochron shows a relatively uniform thickness across the area of interest.

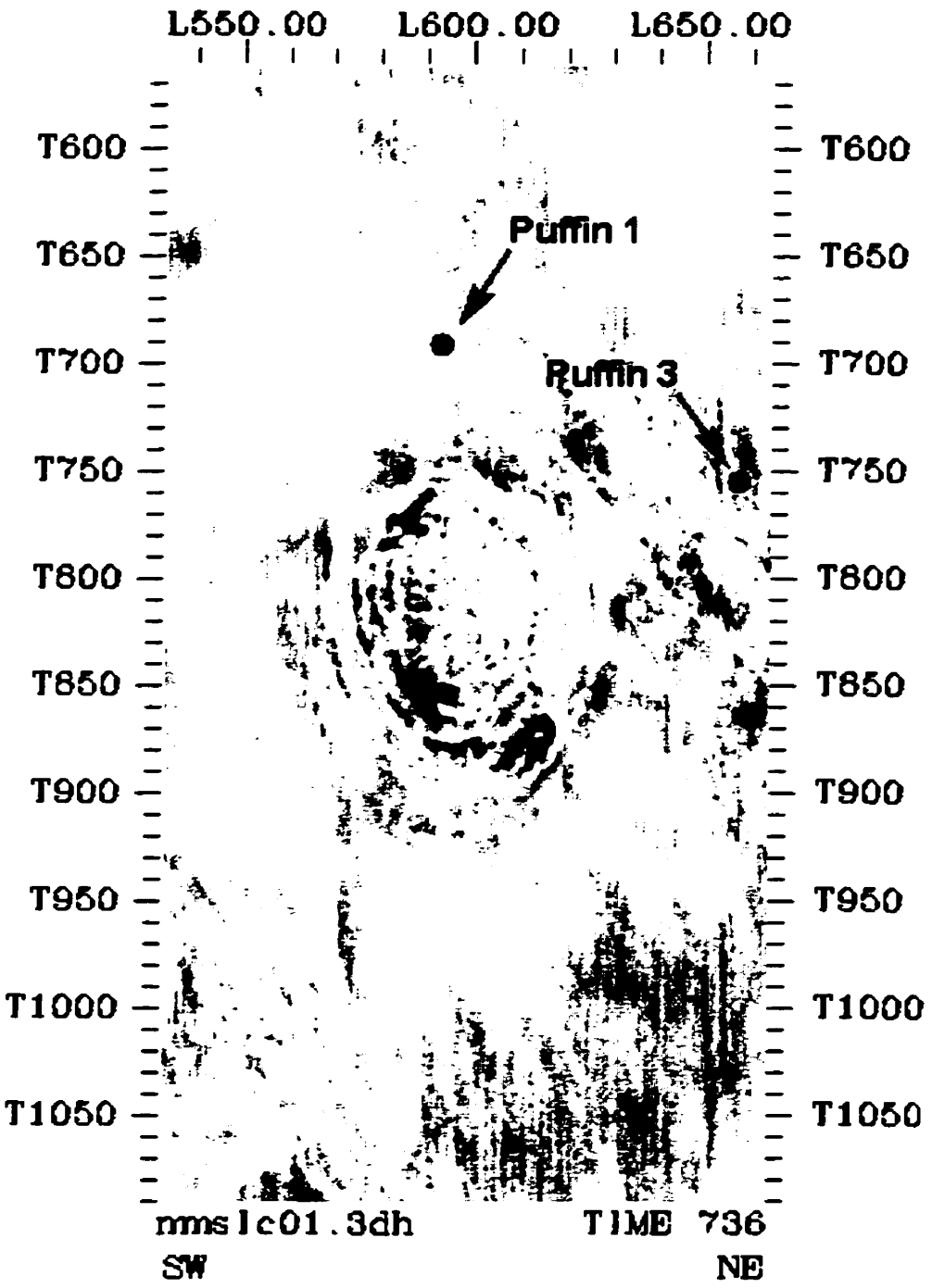

Figure 3.1.12 This time slice taken at 736 ms shows an oval area representing the general shape of the structure being studied here.

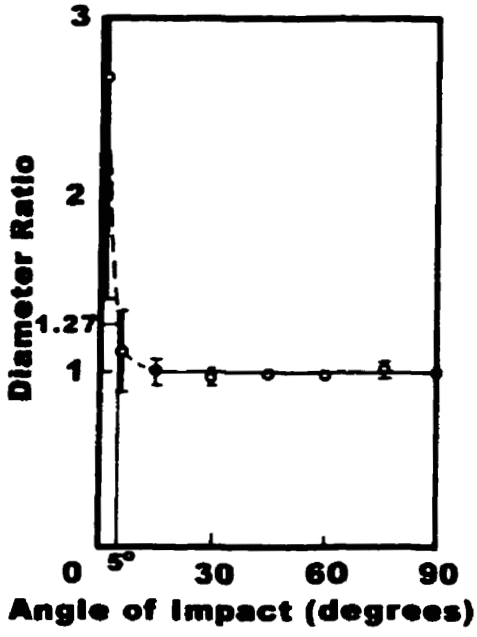

Figure 3.1.13 The ratio of the downrange diameter to the crossrange diameter is a function of the angle of impact. This data is derived from the impact of 121 rounds of pyrex and aluminum spheres fired into noncohesive quartz sand at velocities between 3.6 and 7.2 km/s. Plotting the diameter ratio (1.27) of the Puffin structure allows one to estimate an angle of impact (5°). *After Gault and Wedekind (1978).*

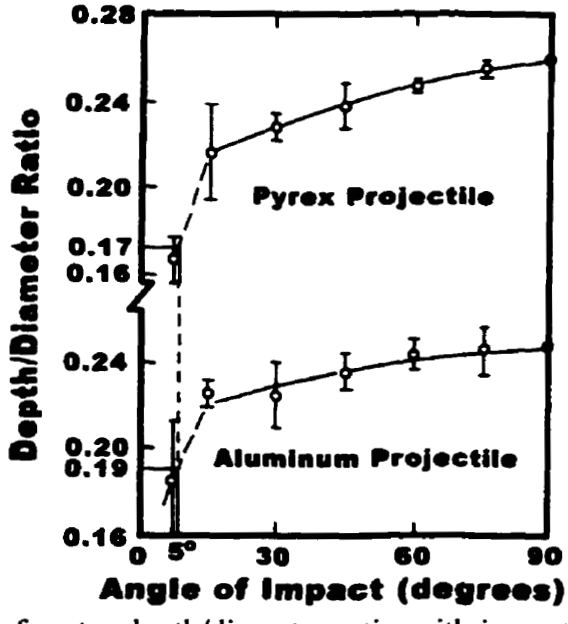

Figure 3.1.14 Variation of crater depth/diameter ratio with impact angle for the conditions given in Figure 3.1.13. Plotting the angle of impact on this figure yields a value for the depth/diameter ratio for the Puffin structure. *After Gault and Wedekind (1978).*

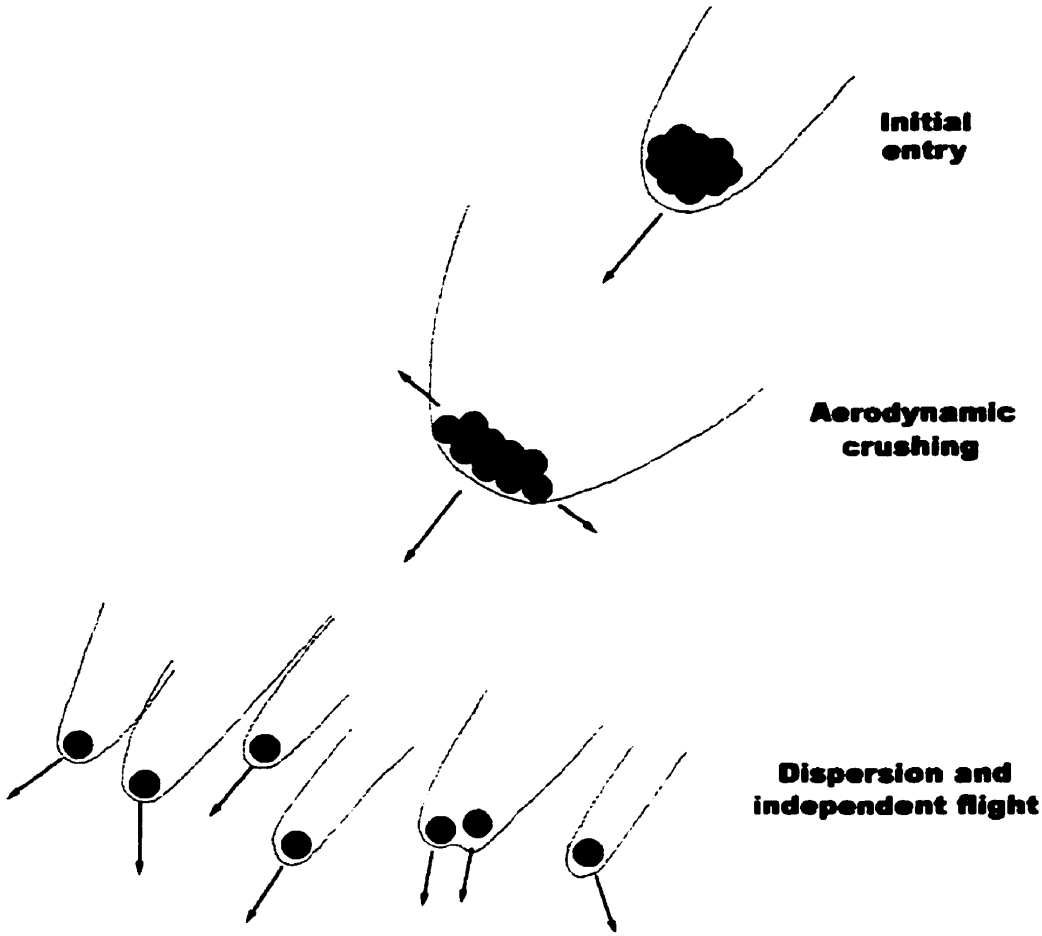

Figure 3.1.15 Schematic of the atmospheric breakup of a meteoroid. Impact can occur at any stage of the breakup. *From Melosh (1989).*

Figure 3.1.16a This crater was produced by a vertical impact of a clustered impactor onto a compacted pumice target. Note the shallow depth and the flat floor. *From Schultz and Gault (1985).*

Figure 3.1.16b This crater was produced by a 45° impact of a clustered projectile onto a pumice target. Note the shallow depth, the flat floor, and the noncircular appearance of the structure. *From Schultz and Gault (1985).*

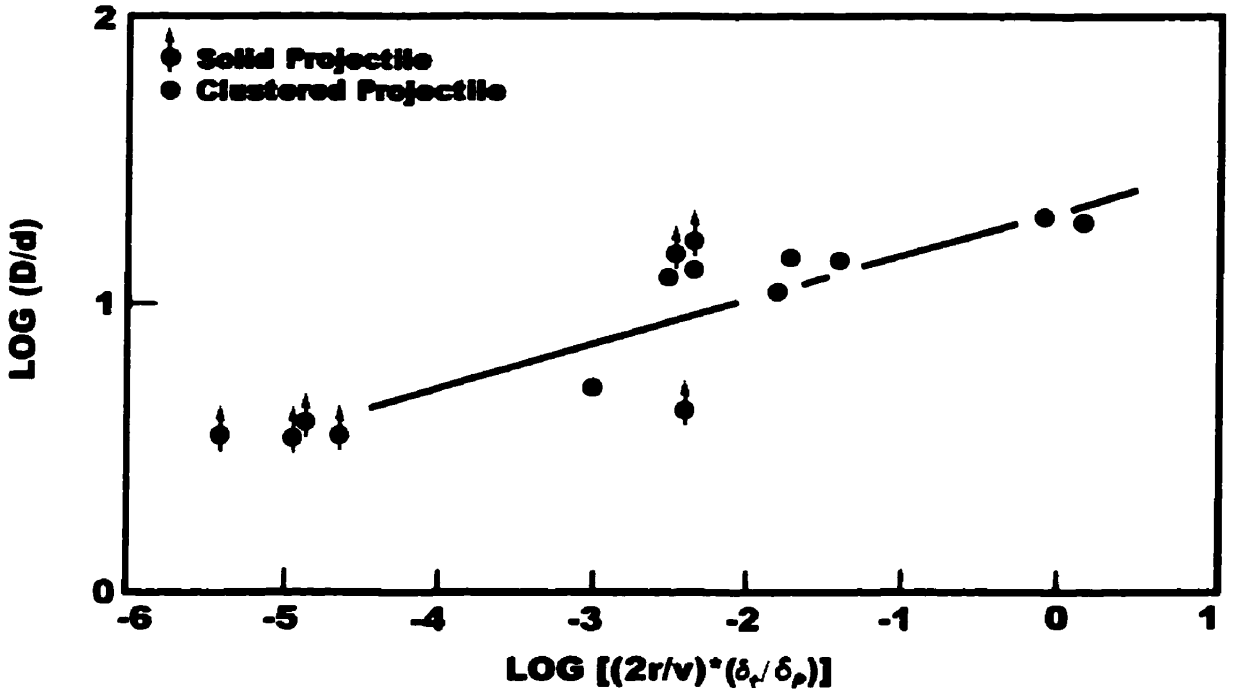

Figure 3.1.17 The combined effects of the target/projectile density (δ_t/δ_p) and the time for projectile-target contact on crater diameter-to-depth ratio. The projectile contact time is given as the projectile diameter (2r) divided by the impact velocity (v).The least squares fit gives: log D/d = 0.148 log [(2r/v)(δ_t/δ_p)] + 1.318 with a correlation coefficient of 0.849. The least squares fit applies only to clustered projectiles. For this experiment the target was sand while the projectiles were solid or clustered. *After Schultz and Gault (1985).*

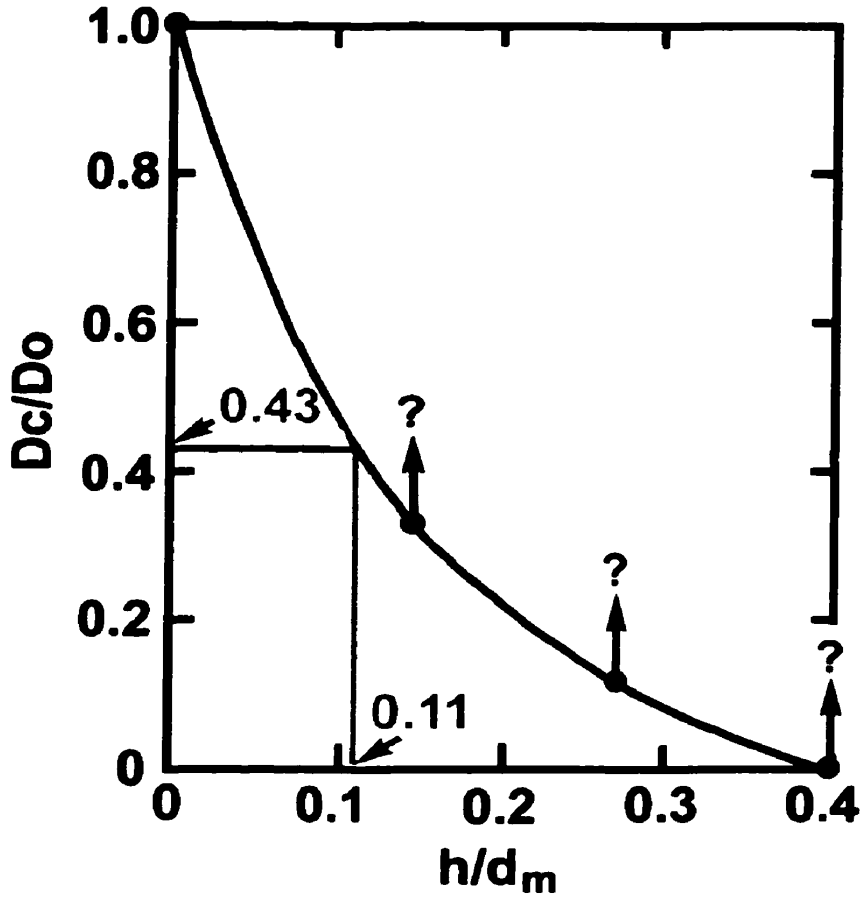

Figure 3.1.18 Variation of crater depth, D_c, formed in a sand floor with water depth, h; D_o is the crater depth for h=0; d_m is the maximum deep-water cavity. (Gault and Sonett, 1982)

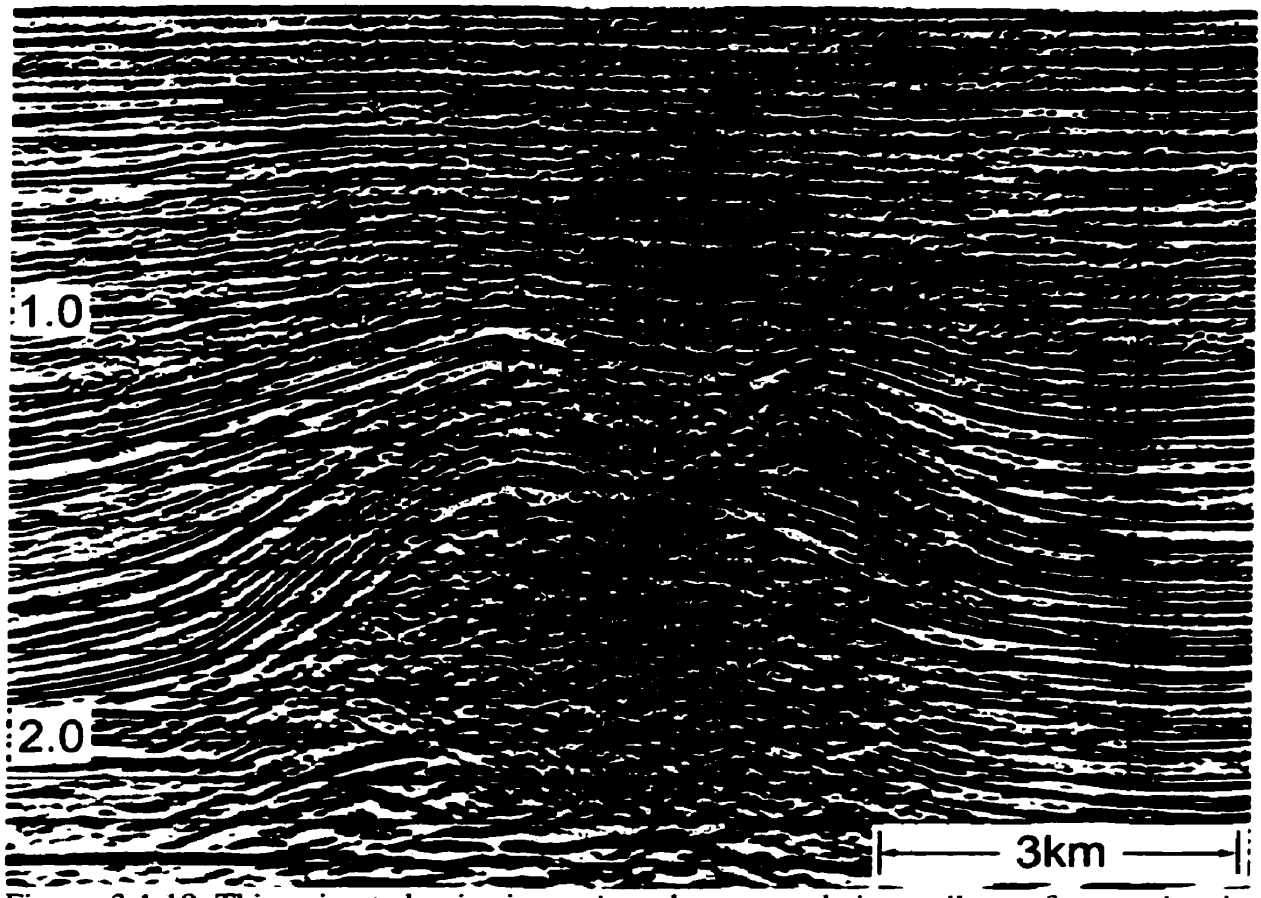

Figure 3.1.19 This migrated seismic section shows a solution collapse feature that is bounded by normal faulting. Tensional fractures developed over the crest of the salt pillow thereby providing a circulatory system for water. The water dissolved some of the halite in the salt pillow resulting in the gravitational collapse of the structure. Continued minor settlement is observed to have taken place over a long period of time as evidenced by small displacements in the shallower section. *From Jenyon and Fitch (1985).*

3.2 Muskingum, Ohio

Buried beneath approximately 1 km of sediments, the Muskingum structure in Ohio, USA exhibits some of the characteristics of a buried impact crater. The limits have been defined by two seismic lines across the structure and several others bordering the feature. At nearly 1300 m in diameter, this feature lacks the diagnostic features of a diatreme intrusion crater. Evidence for rim faults and mounding at the center of the structure suggests that the Muskingum structure is an impact crater that was, at the time of formation, 1450 m in diameter by about 300 m deep. The transient cavity is estimated to have had dimensions of about 1215 m in diameter by 450 m in depth. Correlation of the seismic data with well log data and the use of average erosion rates indicates that the structure is Cambrian-Ordovician in age or about 500 MY old. A more accurate estimation of the event timing is difficult to achieve, however, due to the erosion of the top 150 m of the structure during the Knox unconformity hiatus and a lack of core samples.

3.2.1 Geological Setting

Lying in Cambro-Ordovician sediments in southeastern Ohio (Figure 3.2.1), the Muskingum structure creates an interesting structural disturbance in otherwise flat-lying stratigraphy. Presented in Figure 3.2.2, the Cambrian through Ordovician sediments important to this study can be described beginning in the middle Cambrian with the Rome and Conasauga Formations. Formed as offshore, shallow shelf and prodelta deposits, the Rome and Conasauga Formations are overlain by a series of carbonates. Known as the Knox Dolomites, these sediments accumulated as shallow shelf deposits in the equatorial sea that covered Ohio during the late Cambrian (Hansen, 1997b). Near the end of the Cambrian, the Rose Run sandstone bed was deposited within the Knox Dolomite. Knox deposition continued into the Ordovician with no evidence of a major unconformity at the end of the Cambrian. About 500 MY ago in the early Ordovician, an episode of emergence and erosion formed the widespread Knox unconformity (Hansen, 1997a). After the formation of the Knox unconformity, the seas returned and deposited the thin Wells Creek Formation, which consists of shale, sandstone, siltstone, and dolomite. Ranging from about 6 m in thickness near Knox surface highs to 20 m in thickness near Knox surface lows

(Hansen, 1997a); the Wells Creek formation may be found within the Muskingum structure infill material. Above the Wells Creek Formation, the 100-200 m thick fine-grained limestone unit known as the Black River Group was deposited. Overlying the Black River Group is the Trenton Limestone. Once the most important oil-bearing unit in the United States (Hansen, 1997a), the Trenton Limestone is conformably overlain by the interbedded limestones and shales of the upper Ordovician. These sediments represent a transgressive sequence in which most of the shale-dominated units were deposited in deep, quiet waters and the limestone-dominated units were deposited in shallow, clear waters (Hansen, 1997a).

3.2.2 Geophysical Characteristics

Discovered during regional hydrocarbon surveys, the Muskingum structure is evident on two 2-D seismic lines (Figure 3.2.3). Lines FM1 and FM2 intersect near the center of the structure but only FM1 images the structure from rim to rim. Well control and subsequent correlation (Figure 3.2.4) with the seismic data is established by two wells – Murray #2-1875 and Wagner-Wilcox #3-1976. The Murray #2 well was drilled into the central region of the structure while the other was drilled regionally. Tables 3.3.1 and 3.3.2 list the acquisition parameters for seismic lines FM1 and FM2.

Table 3.3.1 Summary of the acquisition parameters for seismic lines FM1 and FM2.

Acquisition Parameters	
Source	Dynamite – 1/3 lb. x 4 holes Interval: 110 feet
Receiver	Interval: 110 feet
Geometry	12 geophones per group, 10 ft. spacing
Sample Rate	2 ms

3.2.3 Seismic Data Interpretation

Using SeisWorks 2D seismic interpretation software, several representative horizons were picked on seismic lines FM1 and FM2 in order to gain a better understanding of the origin of this structure. Well control and subsequent correlation (Figure 3.2.4) with the seismic data is established by two wells – Murray #2-1875 and Wagner-Wilcox #3-1976.

Observed on seismic lines FM1 and FM2 at about 800 ms TWT, an enigmatic feature disrupts flat-lying sediments (Figures 3.2.5 and 3.2.6). This bowl-shaped structure is defined by the Knox unconformity on the top and the base of the Rose Run sandstone unit on the bottom (Figures 3.2.7 and 3.2.8). The Knox unconformity, which appears at about 820 ms two-way travel time, is an erosional surface separating rocks of the upper Cambrian from those of the Ordovician. Regionally, this unconformity represents a period of extensive erosion. Below the Knox unconformity, the seismic character indicates the presence of the Rose Run sediments. This character is observed to change markedly with the appearance of Knox dolomites at about 920 ms two-way travel time.

Traversing the length of the seismic lines, the Rose Run sediments appear to be regionally flat. At the edge of the structure, however, a small amount of uplift is noted (Figures 3.2.9 and 3.2.10). Within the structure, only the lower portion of the Rose Run unit appears to be continuous. The upper portion of these sediments appears to have been replaced by a possible breccia infill (Figures 3.2.9 and 3.2.10). Below this possible infill, the reflectors of the lower Rose Run are broken and not completely continuous. A possible explanation for the poor seismic imaging in this area is that the rocks have been fractured and brecciated due to the passage of a high-pressure shock wave. Near the center of the structure, the breccia infill appears to form a low mound approximately 30 m high (Figures 3.2.9 and 3.2.10). Above the apparent breccia, a unit with strong, continuous reflectors is observed to lapout against the edge of an excavated cavity. This sandy unit is interpreted as erosional infill from the Knox unconformity hiatus. Above this interpreted sandy infill, subsequent deposits are observed to drape over both the rim of the structure and the central mound, likely as a result of differential compaction. This drape has an amplitude of about 20 m at the Knox unconformity and has disappeared by the base of the Big Lime unit.

3.2.4 Morphometry

An interpretation of the Muskingum structure must necessarily examine the morphological characteristics and compare them to those expected in an impact crater. An important relation that is examined here is that of the depth-to-diameter ratio. In the case of a simple impact structure, the expected rim-floor-depth-to-diameter ratio is about 0.2

(Melosh, 1989). With a present-day diameter of approximately 1.3 km and a floor depth of 150 m (TWT ≈ 50ms, v ≈ 6000 m/s), the Muskingum structure has a current depth-to-diameter ratio of 0.12. Since this value is lies close to the expected range and a period of erosion occurred at the Knox unconformity, an impact origin is plausible.

Apparent on the seismic section is a small amount of uplift associated with the rim of the structure. In section 2.5 the relation between rim height and crater diameter was given as,

$$h_R=0.036D^{1.014} \qquad (3.2.1)$$

where h_R is the measured height of the rim above regional and D is the diameter of the structure. For the Muskingum structure, which has a present-day diameter of 1.3 km, the expected rim height is 47 m. Of course this value neglects the fact that the original crater diameter was likely larger than is observed today. Consequently, the rim height at the time of formation was greater than 47 m. At Meteor Crater, Arizona roughly one-half of the total rim height is due to structural uplift while the other half is due to ejecta deposits. Thus, at the time of foramation, the Muskingum structure would have had at least 24 m of stratigraphic uplift at the rim with an additional 24m of ejecta deposits. The present amount of uplift is observed to be about 5 ms two-way travel time as measured from the rim high point to the adjacent regional low. Using an average velocity of 6000 m/s, this translates into approximately 15 m of current rim uplift. Such a small a value could indicate erosion of the original rim uplift.

As interpreted in figures 3.2.9 and 3.2.10, the inferred present transient cavity depth is about 300 m deep (150 m of breccia overlain by 150 m of sediments). Since the transient crater depth-to-diameter ratio is roughly equal to 1/3 while the final depth-to-diameter is typically close to 1/5, a reasonable estimate of the breccia thickness is about 1/2 the final crater depth. In the case of the Muskingum structure, the inferred breccia is 150 m thick and is overlain by another 150 m of sediments. Therfore a further 150 m of sediments is required above the interpreted top of the crater infill to satisfy the breccia thickness to final crater depth relation. If this structure is an impact crater, the rim height at the time of formation must have been approximately 150 m above the current regional level of the

Knox unconformity. For a rim height of about 50 m, it can be concluded that the surface upon which this structure was formed was 100 m above the current level of the Knox unconformity. Using a value of 1/2.7 for the transient crater depth-to-diameter ratio (Melosh, 1989), the original diameter of the Muskingum structure's transient cavity is about 1215 m. From this value, we can then calculate the original crater diameter using,

$$D_t=0.84D \qquad (3.2.2)$$

where D_t is the transient cavity diameter and D is the final crater diameter (Melosh, 1989). For a transient cavity diameter of 1215 m, the expected final crater diameter is about 1450 m. Figure 3.2.11 shows a schematic of what the Muskingum structure might have looked like shortly after its formation.

The low mounding observed in the central region of the Muskingum structure is consistent with an impact hypothesis. This type of feature is often present in large simple impact structures and is thought to sometimes be the result of the convergence and pileup of high-speed debris streams (Melosh, 1989). Meteor crater in Arizona, for example, shows evidence of a 15-m high mound that is slightly offset from the center of the structure. As discussed in section 2.4, unusual morphologies are also predicted to occur when the target is layered. Central mound morphology, for example, can occur when a weak layer overlies a strong layer and the ratio between the crater diameter and the weak layer thickness is between 4.0 and 7.5. For a crater that is 1450 m in diameter, the thickness of the required weak layer is between 200 m and 365 m. Using an average velocity of 6500m/s for the Rose Run sediments and a two-way travel time thickness of 115 ms, the thickness of this sandy unit is about 375 m. With the addition of the 100 m of sediments that are thought to have existed at the time of formation, the original thickness of this sandy layer was about 475 m giving a diameter-to-weak-layer-thickness ratio of 3.1. Due to the inherent inaccuracies in determining both the original depth of the structure and the thickness of the Rose Run sediments, this value is close to the required value for layering effects to be significant. Since the Rose Run is, in fact, underlain by a stronger carbonate unit, the observed central mound could be due to layering in the target. More likely, however, it is

due to the convergence and pileup of high-velocity debris streams sliding down the crater walls during the modification stage.

Another possible explanation for the apparent central mound might be that this structure represents an impact feature very close to the simple-complex transition diameter in this particular target material. This idea is strengthened by the appearance of several rim faults and apparent parautochthonous breccias (coherent subcrater blocks with little displacement) within a region traditionally thought of as only being occupied by allochthonous breccias. At 1.3 km in diameter, however, the Muskingum structure is smaller than the 2-4 km transition diameter expected for terrestrial craters. A possible solution to this problem may come from studies of Martian impact structures. Studies of Martian craters have revealed that, on average, the simple-to-complex transition occurs at diameters about 2 km smaller than expected under the influence of Martian gravity (Melosh, 1989). The reason for this is likely due to the weakening of Martian surface materials due to the presence of liquid water (Melosh, 1989). It is possible that when the Muskingum structure was formed, the target sediments were highly mobile due to the inclusion of water. The increased mobility could then have facilitated the early collapse of the Muskingum structure into a transitional form at a smaller diameter than would traditionally be expected.

Table 3.2.2 Dimensions of the Muskingum structure as measured from the seismic data and predicted from crater scaling relations.

Dimension	Measured	Predicted
Diameter	1300 m (post-erosion)	1450m (pre-erosion)
Depth to Breccia	150 m	300 m
Rim Height	15 m *	58 m
Central Mound Height	30 m	N/A
Amount of Erosion	N/A	150 m
Transient Cavity Diameter	N/A	1215 m
Transient Cavity Depth	300 m	450 m

*Observed rim height may be a processing artifact.

3.2.5 Other Possible Explanations

Due to the sparse nature of the seismic data over the Muskingum structure, its limits are poorly defined. With the existing data, the best estimate of the planform of the structure is

circular with a diameter of 1.3 km. Although this feature is close to the expected size of a diatreme crater, it lacks evidence of a carrot-shaped stalk extending to great depths below the structure. Consequently, it is not expected that the mechanism responsible for the formation of the Muskingum structure was an explosive diatreme intrusion.

Another possible explanation for this feature might be dissolution. Since the Rose Run sediments are mostly sands, shallow marine erosion during the period of Knox unconformity hiatus is unlikely.

3.2.6 Age of the Muskingum Strucutre

In the absence of core samples, an accurate age for the Muskingum structure initially seems difficult to obtain. If, however, we assume a constant rate of erosion during the Knox unconformity hiatus and make an educated guess of the magnitude of the rate of erosion, a relatively precise age can be determined.

Studies of the present rate of land erosion have shown that the average rate of ground loss in normal-relief terrain is between 20 and 81 mm/1000 years for consolidated rocks (Young, 1969). Apparently, there is little difference in the rates of erosion between rock types, however, unconsolidated sediments are eroded at rates 10-1000 times faster than consolidated rocks (Young, 1969). If we assume that the Muskingum structure was formed on an erosional surface, then the expected time to erode the structure by 100 m to the current level of the Knox unconformity is between 1 MY and 5 MY. Since the oldest sediments found in the overlying Ordovician section are about 500 MY old, we can conclude that the Muskingum structure was formed approximately 3±2 MY prior to the deposition of these rocks. Thus, if we place the end of the Knox unconformity hiatus at about 500 MY ago (Hansen, 1997a), the Muskingum structure is about 503±2 MY old.

This interpretation, however, is only valid if the structure was formed on an erosional surface and if the current rates of erosion can be applied to Cambro-Ordovician times in Ohio. If it was formed on a depositional surface before experiencing subsequent erosion, then we would also need to consider the average depositional rates in the area. Rates which,

at the time of the event, might have differed significantly from the rates of erosion suggested above.

3.2.7 Concluding Remarks

The mechanism that is best thought to describe the formation of the Muskingum structure is that of meteorite impact. Evidence for dissolution collapse of the Rose Run sediments is absent and shallow marine dissolution is unlikely since the Rose Run is predominantly sandstone. The structure lacks a carrot-shaped stalk extending to great depths, ruling out diatreme intrusion as a possible mechanism.

Presently, the structure is approximately 1300 m in diameter with a depth to the top of the inferred breccia of about 150 m. Using the thickness of the inferred breccia infill, the original size of the Muskingum structure is estimated to have been 1450 m in diameter by about 300 m deep (to the top of the breccia lens). The transient cavity is estimated to have been approximately 1215 m in diameter.

The small amount of observed rim uplift and shallow depth indicates that the Muskingum structure underwent an amount of erosion equal to about 150 m during the formation of the Knox unconformity. This idea is also supported by the sand infill within the crater. This infill is thought to represent material eroded from the periphery of the structure at the end of the Knox erosional hiatus.

Further investigation is required to confirm an extraterrestrial origin for the Muskingum structure. Additional seismic data is needed to better describe the shape of structure while deeper well logs would help to better estimate the age of the structure. Drilling chips from well Murray #2 should be examined for any evidence of shock features that might indicate an impact mechanism.

Figure 3.2.1 The Muskingum structure in southeastern Ohio is located in Muskingum county.

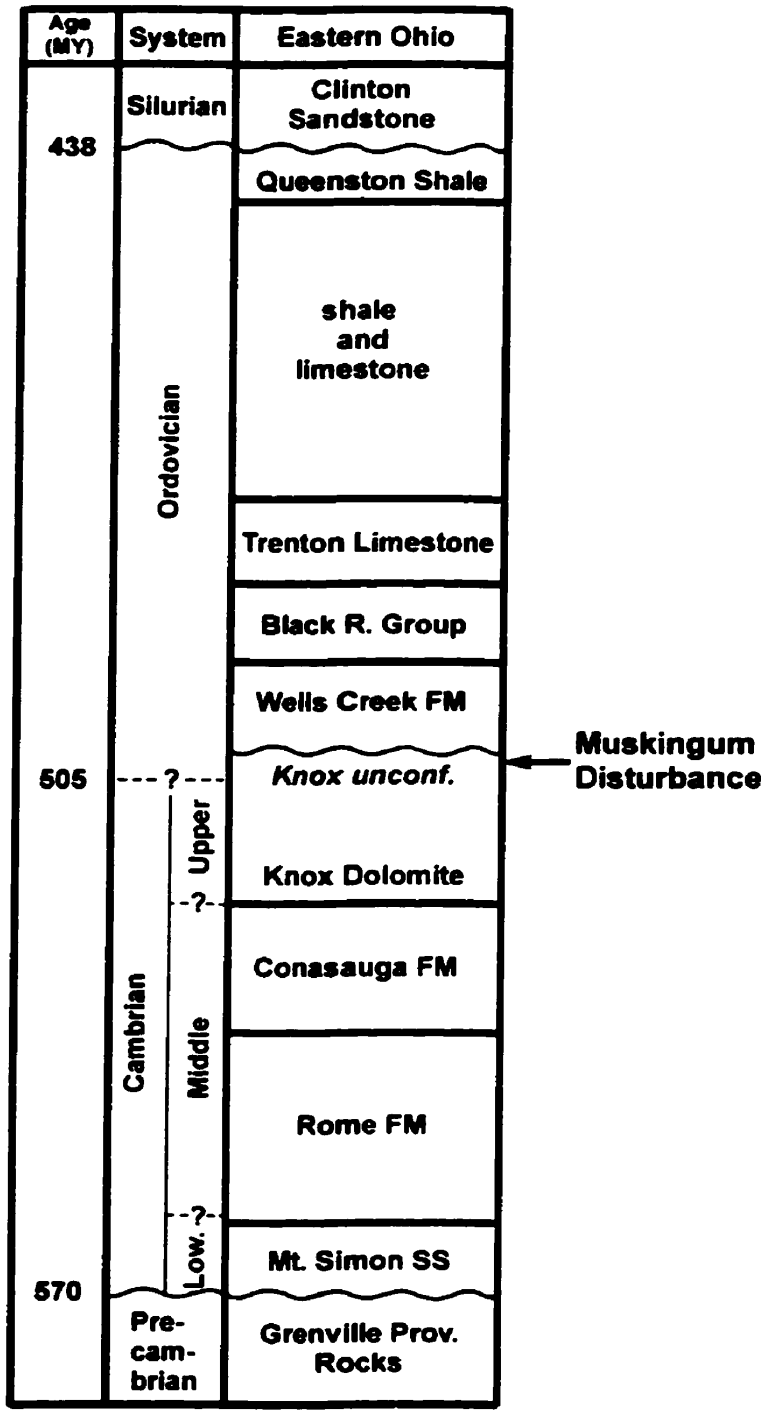

Figure 3.2.2 Generalized Cambrian/Ordovician stratigraphic column for Eastern Ohio including Muskingum county. (After Hansen, 1997a and 1997b)

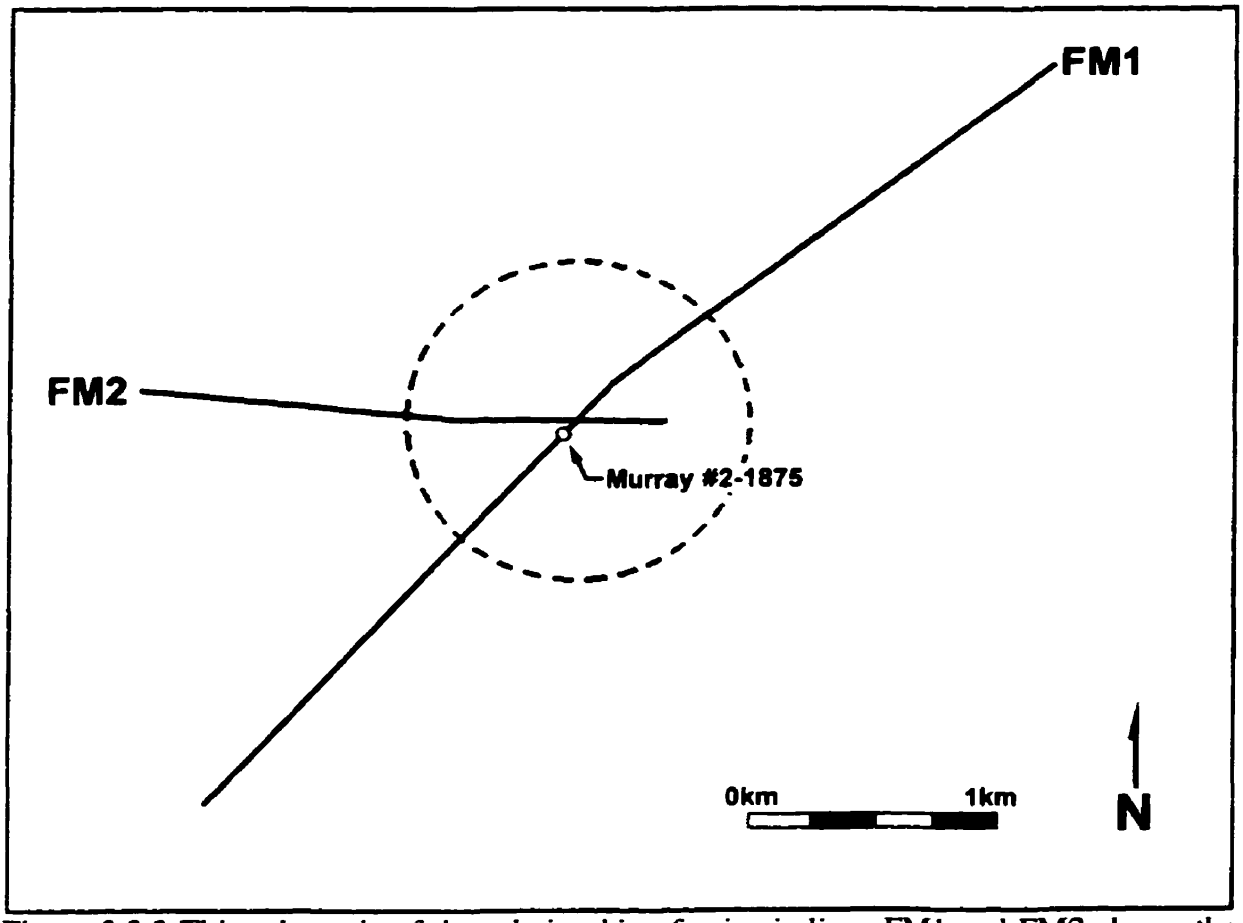

Figure 3.2.3 This schematic of the relationship of seismic lines FM1 and FM2 shows the location of the Murray #2-1875 well (circle) and the estimated position of the crater rim (dotted line).

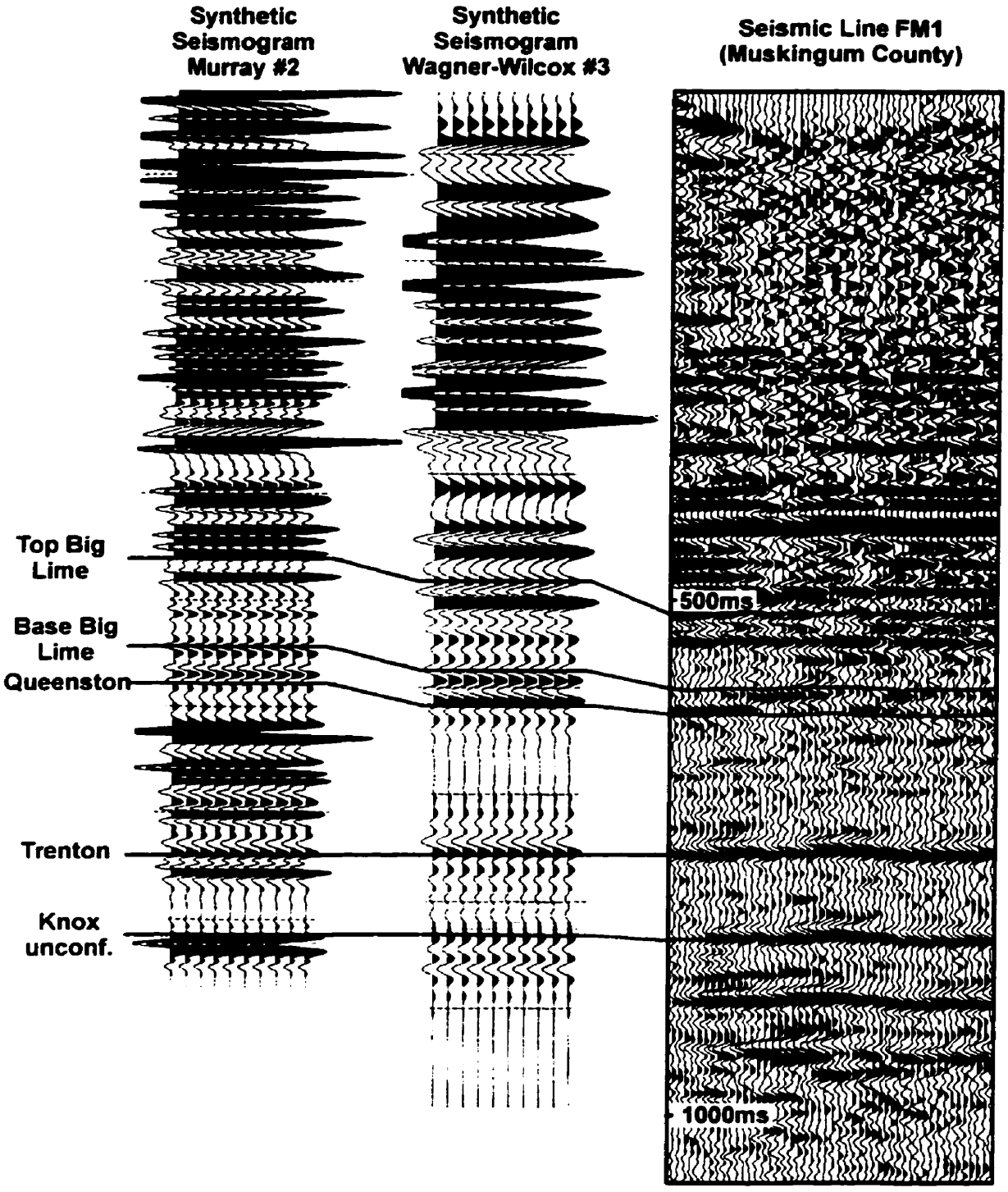

Figure 3.2.4 Synthetic seismograms created from well log sonic and density measurements can be correlated with a section of seismic line FM1.

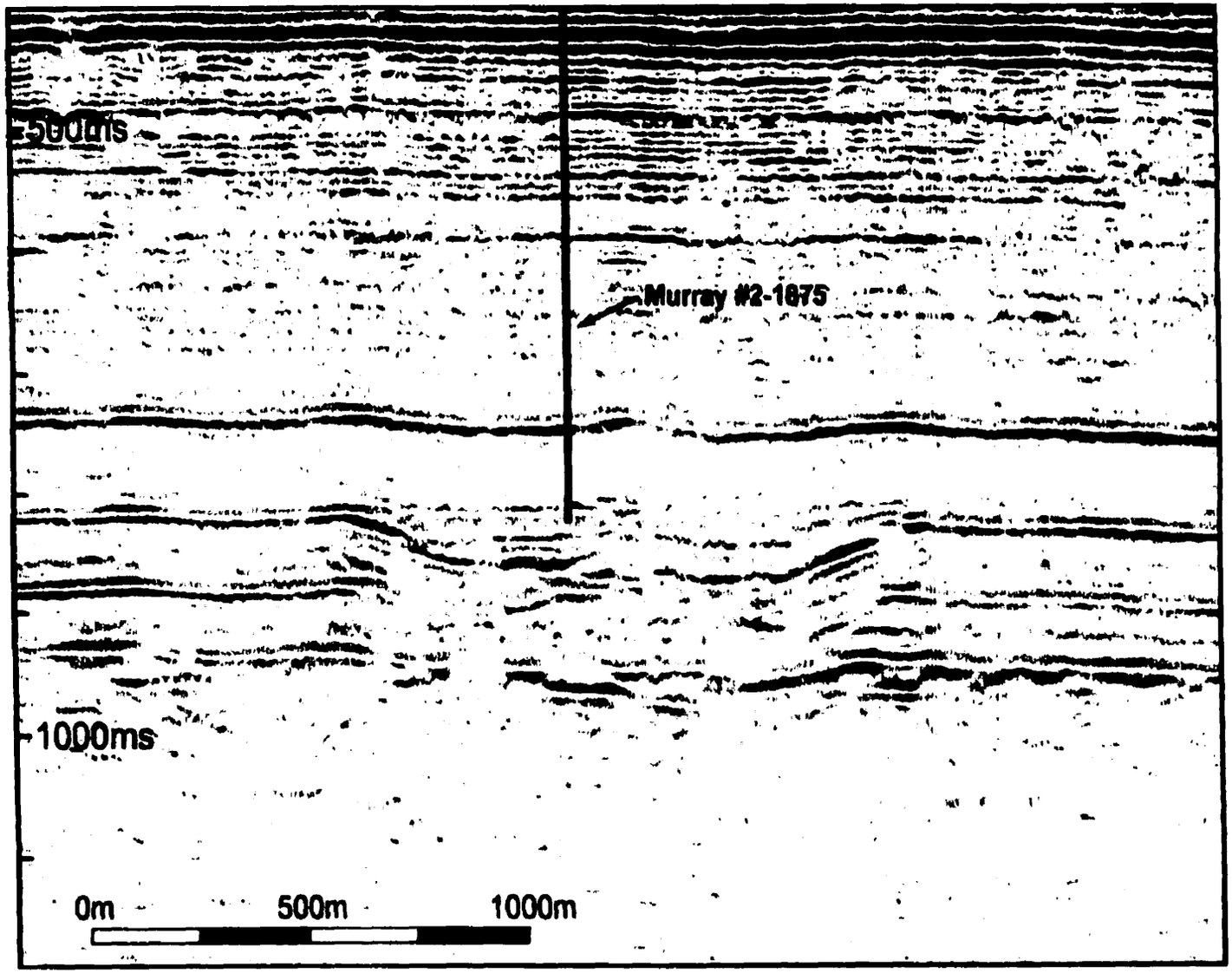

Figure 3.2.5 An uninterpreted 2-D seismic section (line FM-1) acquired across the Muskingum structure. Immediately apparent is an uplifted rim and a central mounded region.

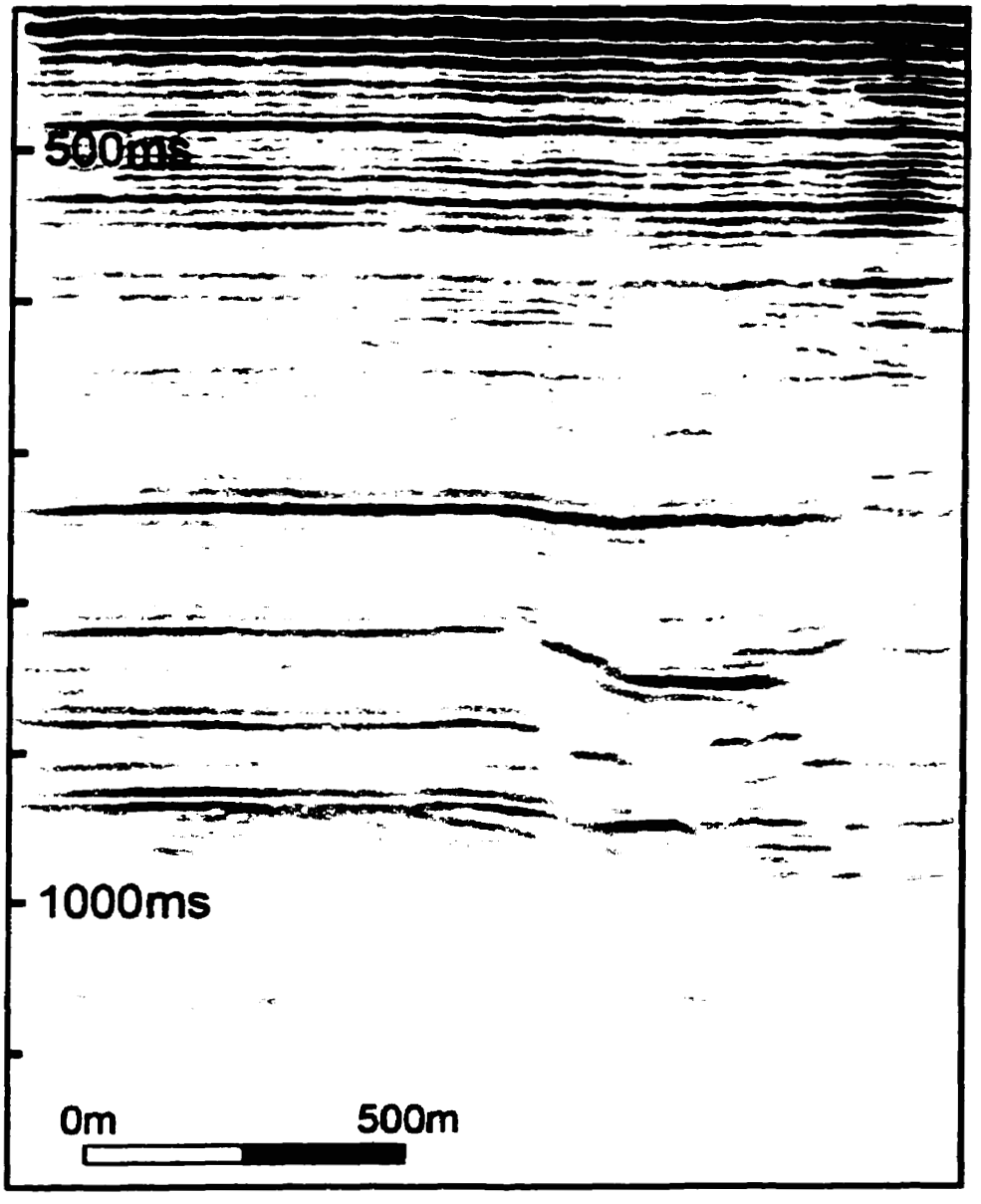

Figure 3.2.6 Line FM2 uninterpreted. Note that the poor quality of the seismic data at the edges of the line is due to the low fold of the data in these regions.

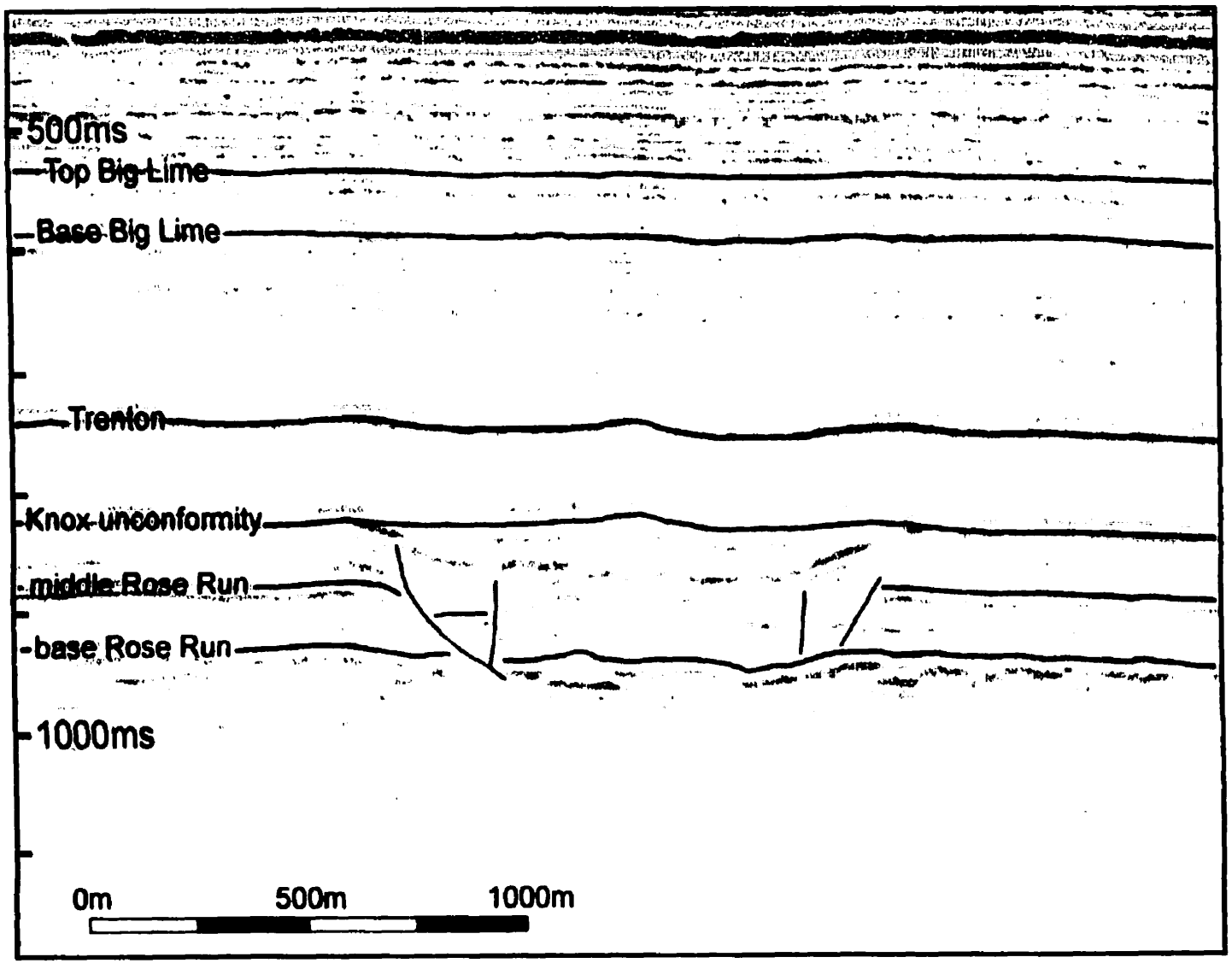

Figure 3.2.7 Seismic line FM1 showing seismic horizon interpretations. Included in this interpretation are horizons identified as 'mid crater' and 'below crater'.

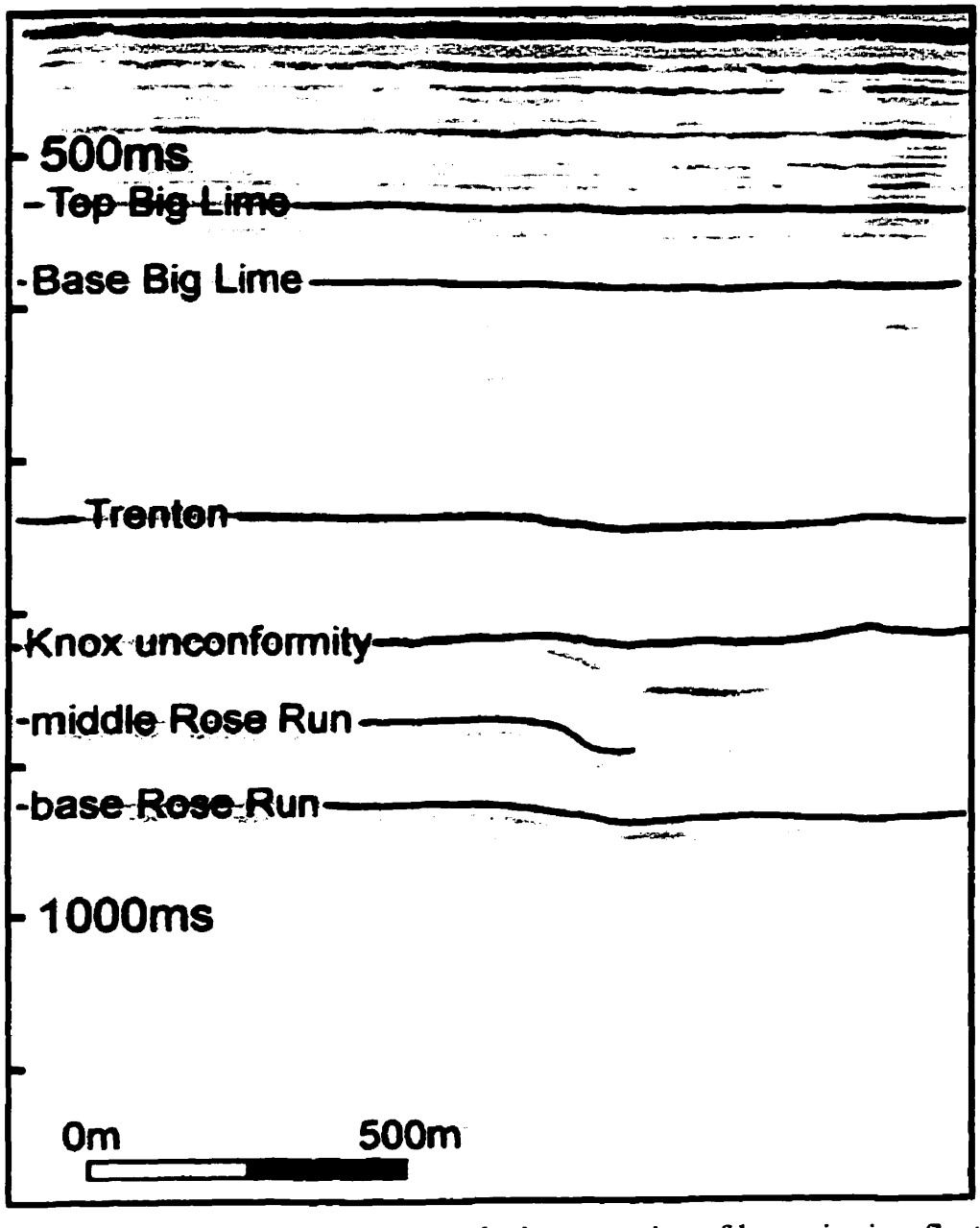

Figure 3.2.8 Seismic line FM2 showing the interpretation of key seismic reflectors.

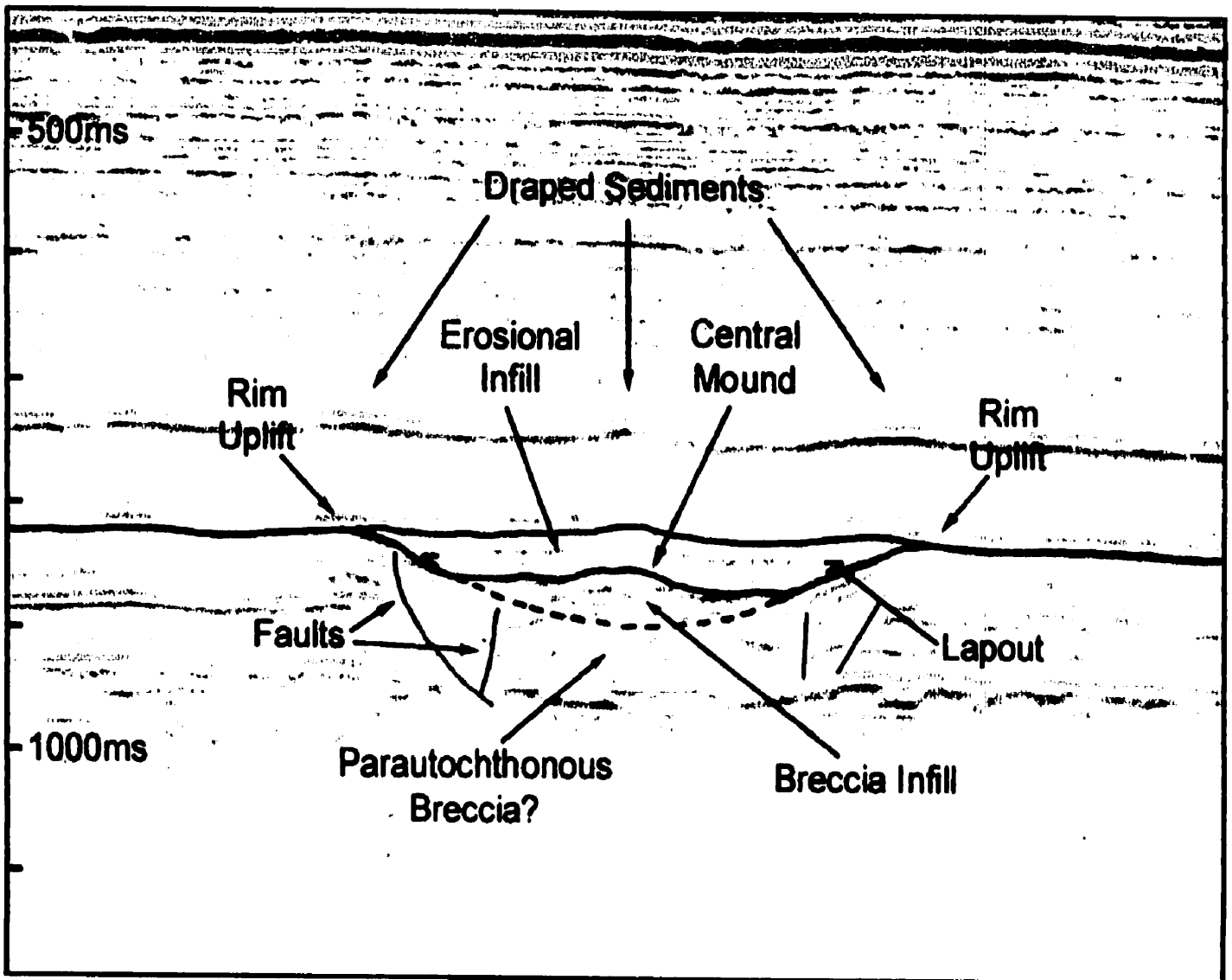

Figure 3.2.9 The Muskingum structure is interpreted on line FM1 as a 1.3 km diameter impact structure in Cambro-Ordovician sandstones. Notice the apparent rim fault, central mound, and the inferred breccias.

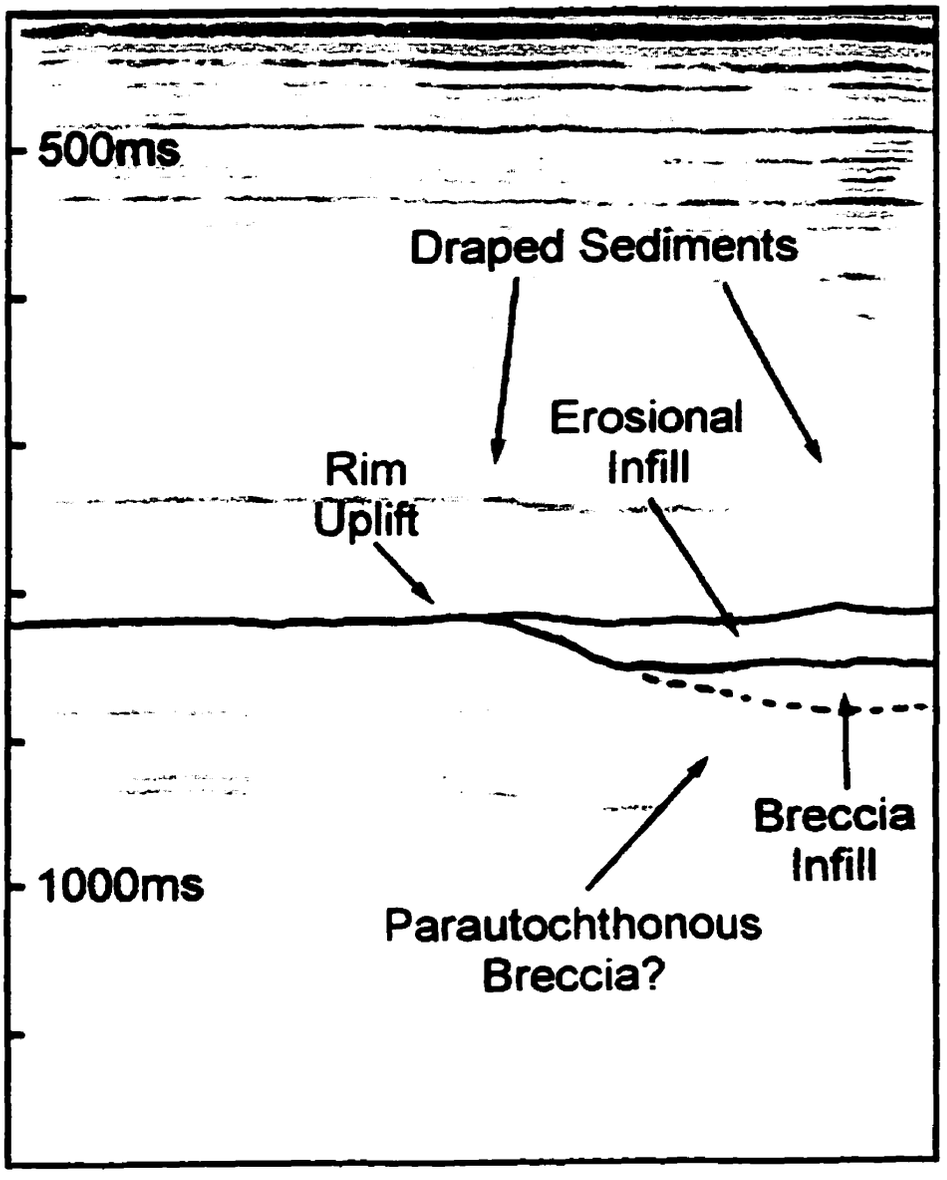

Figure 3.2.10 This interpretation of the Muskingum structure on line FM2 shows evidence of a bowl-shaped structure, brecciated materials, and sediment drape.

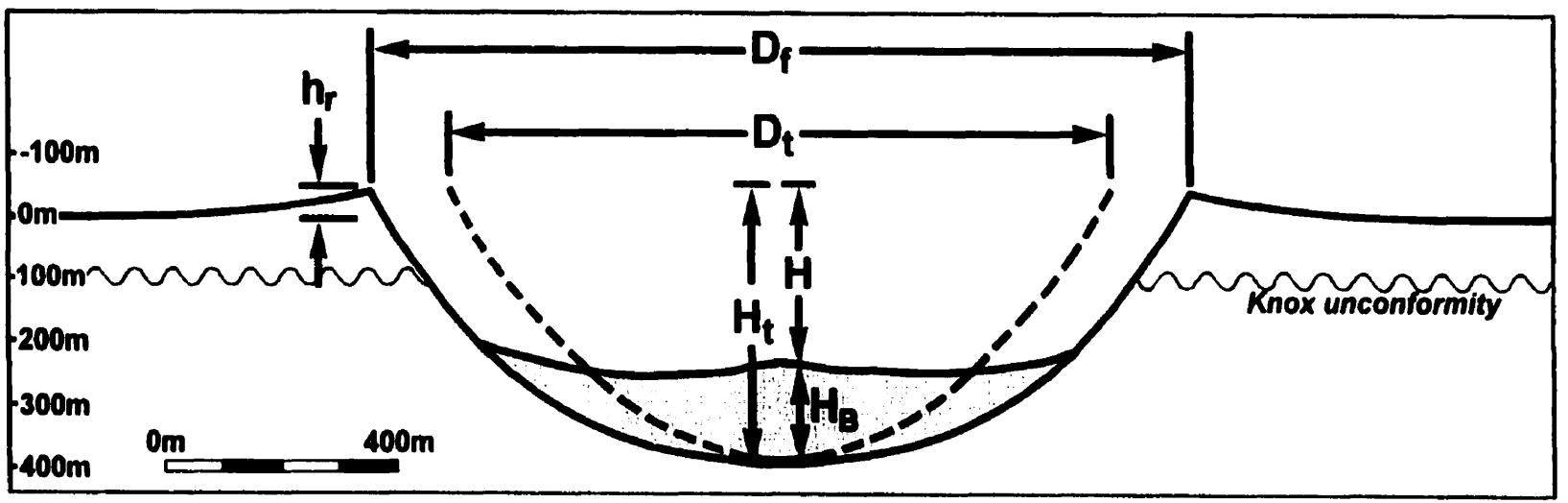

Figure 3.2.11 This schematic suggests that the Muskingum structure was formed in flat-lying sediments approximately 100 m higher than the present-day Knox unconformity. The structure is estimated to have had an original diameter of 1.45 km and a depth of 450 m. D_f and D_t are the final and transient crater depths respectively. H_t is the transient crater depth while H is the final crater depth after the formation of a breccia lens with thickness H_B. The amount of rim uplift, h_r, is estimated to have been about 50 m.

Chapter 4

COMPLEX IMPACT STRUCTURES

4.1 Hotchkiss, Alberta

The Hotchkiss structure in NW Alberta is an enigmatic feature imaged by several 2-D seismic lines (Figure 4.1.1). The appearance of the Hotchkiss structure on seismic data closely resembles that of a complex impact crater such as the White Valley structure in SW Sakatchewan (Figure 4.1.2). Using 2-D seismic data, this study interprets the current extent of the feature and its pre-erosional dimensions. The current size of the area of disturbance is 3.5 km across and 400 m thick. Using scaling relations, the Hotchkiss structure is estimated to have been 4.5 km in diameter and 500 m deep at the time of formation between 120 and 330 million years ago. The transient cavity is estimated to have been about 2.6 km in diameter by about 730 m deep. Subsequent to its formation, the Hotchkiss structure experienced a large amount of erosion. The Gething-Debolt unconformity marks this period of erosion during which an estimated 500 m of the structure was eroded.

It is hoped that a thorough examination of the seismic characteristics of this structure will provide some insight into its origin. If we are correct in postulating an impact origin for this structure then not only should certain diagnostic features be present but crater scaling relations should apply. This chapter examines these features and attempts to reconstruct the initial dimensions of the Hotchkiss feature using well established scaling relations.

4.1.1 Geological Setting

Located in northwestern Alberta, the Hotchkiss structure appears as an anomalous feature affecting Mississippian (Carboniferous) carbonates and shales (Figure 4.1.3). The regional dip of the Precambrian basement is to the southwest. Overlying the structure are Cretaceous sediments with parallel stratigraphy that also show evidence of drape. The

Debolt carbonate unit is terminated by a significant unconformity, referred to here as the Gething-Debolt unconformity. Above this unconformity, the lower Cretaceous Gething sands show evidence of differential compaction in the form of an obvious drape feature. Figure 4.1.3 gives a generalized stratigraphic column of the area. Note the Gething-Debolt unconformity and the absence of more than 200 million years of sediments.

4.1.2 Geophysical Characteristics

Observed on at least three 2-D seismic lines, the Hotchkiss structure was was originally discovered during a regional search for hydrocarbon deposits. The three lines examined as part of this thesis cross one another near the central region, providing enough data to adequately characterize the shape of the structure. Two wells in the area allow for correlation of the seismic data with known geologic units. Tables 4.1.1 through 4.1.2 summarize the acquisition parameters and processing flows for each of the three seismic lines (Note: the processing flow for line 2 is currently unavailable).

Table 4.1.1 Summary of the Acquisition Parameters for the seismic lines of this study.

Acquisition Parameters	
Source	Dynamite • line #1 – 5 lb @ 37 ft • line #2 - ? • line #3 – 1 kg @ 11 m Interval: 61 m
Receiver	Interval: 61 m
Date Shot	Line #1 – 1965 Line #2 – 1995 Line #3 – 1964
Sample Rate	2 ms

Table 4.1.2 The processing flow for line #1

Processing Flow – Line # 1	
Elevation Statics	
CDP Gather	
Gain Recovery	
Frequency Filter	Highpass: 12 Hz, Smoothing: $\cos^2$
Deconvolution	
Velocity Analysis	
Residual Statics	
Velocity Analysis	
NMO Correction and Stack	
Frequency Filter	Bandpass: 12-65 Hz, Smoothing: $\cos^2$
Normalization	
Migration	
Frequency Filter	Highpass: 12 Hz, Smoothing: $\cos^2$
Deconvolution	
Frequency Filter	Bandpass: 12-65 Hz, Smoothing: $\cos^2$
Normalization	

Table 4.1.3 The processing flow for line #3.

Processing Flow – Line # 3	
Refraction Statics	
Deabsorption	
Deconvolution	Wiener
Velocity Analysis	
Residual Statics	
Dip Moveout (DMO)	
NMO Correction and Stack	
Migration	Kirchoff
Deconvolution	Zero-phase Wiener whitening
Filter	Butterworth Bandpass: 15/4 – 75/12
Normalize	

4.1.3 Seismic Data Interpretation

Of three lines over the study area donated for this project, digital data were only available for line 2. As such, all detailed interpretations including morphometric calculations were confined to measurements from line 2. Lines 1 and 3 are presented to show that the Hotchkiss structure is round in plan view and that the features interpreted on line 2 are consistent with the seismic data from the other lines.

Using logs from two wells (06-18-098-06W6 and 14-22-098-07W6) in the immediate study area, an interpretation of several important seismic horizons is made. Synthetic seismograms were created using GMAplus Modeling software with information from the sonic and density logs. A convincing correlation can be made between the synthetic seismograms and the seismic data from line #2 (Figure 4.1.4). Horizons were picked in the area of post-impact sedimentation (Peace River and Spirit River), within the zone of maximum disturbance (Debolt, Pekisko, Banff, Wabamun, and Kakiska), and below the area of disturbance (Moberly, Slave Point, and Muskeg). The unconformity marking the transition from post-impact sedimentation to disturbed material is interpreted as a Gething (≈120 mybp) to Debolt (≈330 mybp) unconformity. Also interpreted on the seismic section are the locations of faults and slump blocks, possible breccia infill, and central uplift material.

An examination of the post-Gething sediments reveals flat-lying stratigraphy with evidence of drape over the central region of the structure (Figure 4.1.5). Continuation of the drape feature to the surface suggests the presence of a smooth topographic feature that is approximately 15-30 m above regional. Re-examining figure 4.1.1 it can be observed that the buried structure does possibly influence drainage patterns and surface topography. Below the annular trough a systematic pull-up of the seismic time horizons is observed throughout the section. It is likely that this pull-up is an indicator of a high lateral velocity contrast between the regional rocks and those filling in the trough region. At the level of the Muskeg, there appear lateral changes in reflector brightness that are correlated with the pull-up region. It is possible that this brightening is due to amplitude versus offset (AVO) effects and is indicative of the presence of gas.

Uniquely identifying this structure as an impact feature is a difficult task since there are no wells penetrating deeply into the disturbed rocks of the structure. Regional evidence of an impact origin is not expected to be present. This assumption is made since the Gething-Debolt unconformity marks a period of erosion that is likely to have removed all ejecta and signs of the ejecta blanket. The only direct evidence of impacted lithologies may be found in the disturbed rocks within the impact structure. Since samples were not available for this study, identification of this feature must rely on its comparison to known examples of impact structures and other suspected cases.

Several unique observations can be made from the appearance of the structure. These observations include an apparent lateral asymmetry of the Wabamun and asym1 horizons and a pushdown of the Wabamun (Figures 4.1.6 and 4.1.7). Although it is expected that some of the pushdown can be explained as a velocity effect, the majority is undoubtedly real due to the lack of similar structure at greater seismic travel times. Asymmetries in the bedding could be explained as a non-spherical release of energy at the time of impact (a condition that might arise in a non-vertical impact). Figures 4.1.8 and 4.1.9 give an interpretation of seismic lines 3 and 1 respectively. Although the quality of the data from these lines is worse than that from line 2, they tend to support the observations made from

line 2. Additionally, these two interpretations help to confirm the nearly circular planform of the structure.

Determining the timing of this event is poorly constrained stratigraphically since the Gething-Debolt unconformity marks a nearly 200 million-year gap in the geological record in this area. To more closely estimate the time at which this structure was formed, an examination of impact crater scaling relations is undertaken. By calculating the original size and shape of the structure, an estimate of the amount of erosion since formation can be made. Using this figure, we can then proceed to better estimate the time of formation.

Interpreting this structure as an impact event allows reconstruction of the events leading up to the formation of the Hotchkiss structure as it is observed today (Figure 4.1.10). If the impactor is assumed to have been a stony object traveling at 20 km/s, we find that the diameter required to create a 5 km crater is about 250m (French, 1999). As the meteoroid crashed into what was likely a shallow sea, the excavation of the transient cavity and start of the central uplift began. Within about 20 seconds, the central uplift was nearly formed and the rim was beginning to collapse (Melosh, 1989). After several minutes the crater had assumed its final shape. Sometime later, a period of erosion occurred introducing a great deal of uncertainty in the determination of the age of the structure.

4.1.4 Morphometry

Using scaling relations, the original dimensions of the structure can be estimated. However, it must be kept in mind that many of the scaling relations have been developed from studies of lunar craters. For the most part, these structures show few signs of erosion unlike the highly eroded Hotchkiss structure. Studies of terrestrial complex craters have shown that the maximum structural uplift (Figure 4.1.11a) of the crater's center, H_{su}, is related to the final crater diameter (Grieve et al., 1981), D, by

$$H_{su}=0.086D^{1.03} \qquad (4.1.1)$$

where all distances are in kilometres and structural uplift is defined as the maximum depth from which lithologies are uplifted at the center of complex impact structures (Grieve et al., 1981). Although this relation has been shown to apply to several terrestrial impact features

(Grieve and Pilkington, 1996), the severe level of erosion in this case means that we can only place a lowere limit on the pre-erosion diameter using this method. The maximum stratigraphic uplift can be estimated by continuing the slope of the central uplift to a peak and then measuring its height above regional (Figure 4.1.12). In doing so, we find a value of 350 m. This gives a maximum original diameter of 3.9 km.

Other relations exist such as a comparison between the central peak diameter, D_{cp}, and the total diameter of the crater (Melosh, 1989).

$$D_{cp}=0.31D^{1.02} \qquad (4.1.2)$$

Measuring the current extent of the central uplift, D_{cp} is found to be about 1.1 km. Using this value in equation 4.1.2 the original rim diameter is found to have been 3.46 km.

Using these two scaling relations, we have shown that the maximum diameter of the original structure is between about 3.46 km and 3.9 km. Another estimate of the pre-erosion diameter of this feature can be made by if the original crater had a roughly parabolic shape. A parabola can then be designed that is tangent to the current dip at the rim. Extrapolation outwards along this parabola to the angle of repose (approximately 30 degrees) will yield an estimate of the pre-erosion diameter. Measurements of the bedding at the rim of the structure yield present dip angles of about 25 degrees, giving a pre-erosion diameter of 4.3 km.

The original depth of the structure can be calculated by using scaling relations deduced from lunar studies (Melosh, 1989). The depth, H, of a complex terrestrial impact feature can be given as,

$$H=0.32D^{0.3} \qquad (4.1.3)$$

Using a midrange estimate of 3.9 km for the original diameter of the structure we find that the initial depth was on the order of 480 m. The height of the rim above the regional levels can also be computed by using the relation (Melosh, 1989),

$$h_r=0.036D^{1.014} \qquad (4.1.4)$$

Using this relation we find a value for the rim height of about 145 m above regional. With these two values, we see that, at the time of formation, the surface was about 335 m above the present-day Gething-Debolt unconformity.

Using the value calculated above for the original crater diameter, an estimate of the dimensions of the transient cavity can be made. Since the transient cavity diameter in the complex crater case is between approximately 0.5 and 0.65 times the final crater diameter (Melosh, 1989), the Hotchkiss transient cavity was about 2.26 km in diameter (using 0.58D). The depth of the transient cavity can then be calculated by using a median value of 0.28 for the transient cavity depth-to-diameter ratio (typically between 0.24 and 0.32 (Melosh, 1989)). The result of this exercise is a transient cavity that is about 2.26 km in diameter by about 630 m deep. Another measure of the diameter of the transient cavity can be made by measuring the distance between the innermost slump blocks. Although this dimension would be more accurately defined as the disruption cavity (limit of brecciation), it still offers a upper limit for the transient cavity diameter. Measured directly from the seismic data this dimension is found to be between 2.3 km and 2.6 km depending on where the inner edges of the slump blocks are picked.

Table 4.1.5 Dimensions of the Hotchkiss structure as measured from the seismic data and predicted from crater scaling relations.

Dimension	Measured	Predicted
Diameter	3.5 km (post-erosion)	4.5 km (pre-erosion)
Depth to Breccia	0 m	500 m
Central Peak Diameter	1.1 km	1.1 km
Stratigraphic Uplift	350 m (by extrapolation)	315 m
Amount of Erosion	N/A	500 m
Transient Cavity Diameter	2.3-2.6 km *	2.26 km
Transient Cavity Depth	N/A	630 m

* Measured dimension is the disruption cavity which is expected to be slightly larger than the transient cavity

4.1.5 Concluding Remarks

The Hotchkiss structure exhibits many of the diagnostic features of a meteorite impact structure. These features include evidence for a central uplift, large-scale faulting at the rim

and in the central uplift, a breccia infill, and a continuation of the disturbance to depths in excess of 1500-m below the top of the feature. The Hotchkiss structure also obeys many of the scaling relationships relating to impact features. At the time of formation between 120 and 330 million years ago, the original size of this structure is estimated to have been 3.9 km in diameter by 480 m in depth. At the end of the modification stage, the transient cavity had a diameter of 2.26 km and was about 630 m deep.

The presence of large displacement faults and structural disturbance within this feature makes the Hotchkiss structure a possible target for hydrocarbon exploration. Areas of interest might be the observed drape over the structure, the breccia infill (if it exists) within the annular synform, and the slump blocks around the rim.

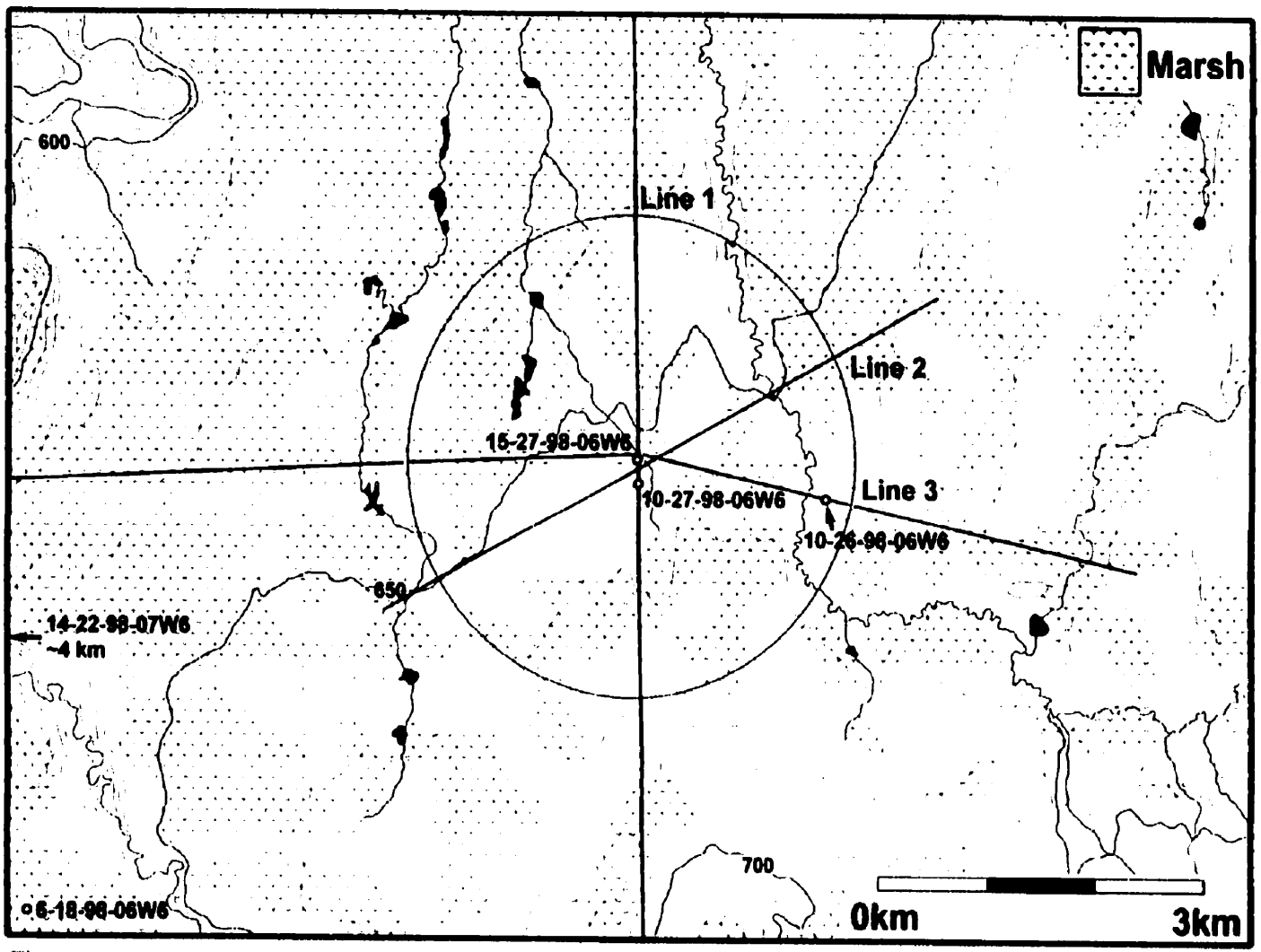

Figure 4.1.1 Location map for the Hotchkiss structure showing approximate location of the seismic lines used in this study. The extent of the Hotchkiss structure is roughly indicated by the red circle. Note the how the streams bordering the eastern and western limbs of the structure as well as the 700 m contour line to the west of the structure appear to be influenced by the subsurface feature.

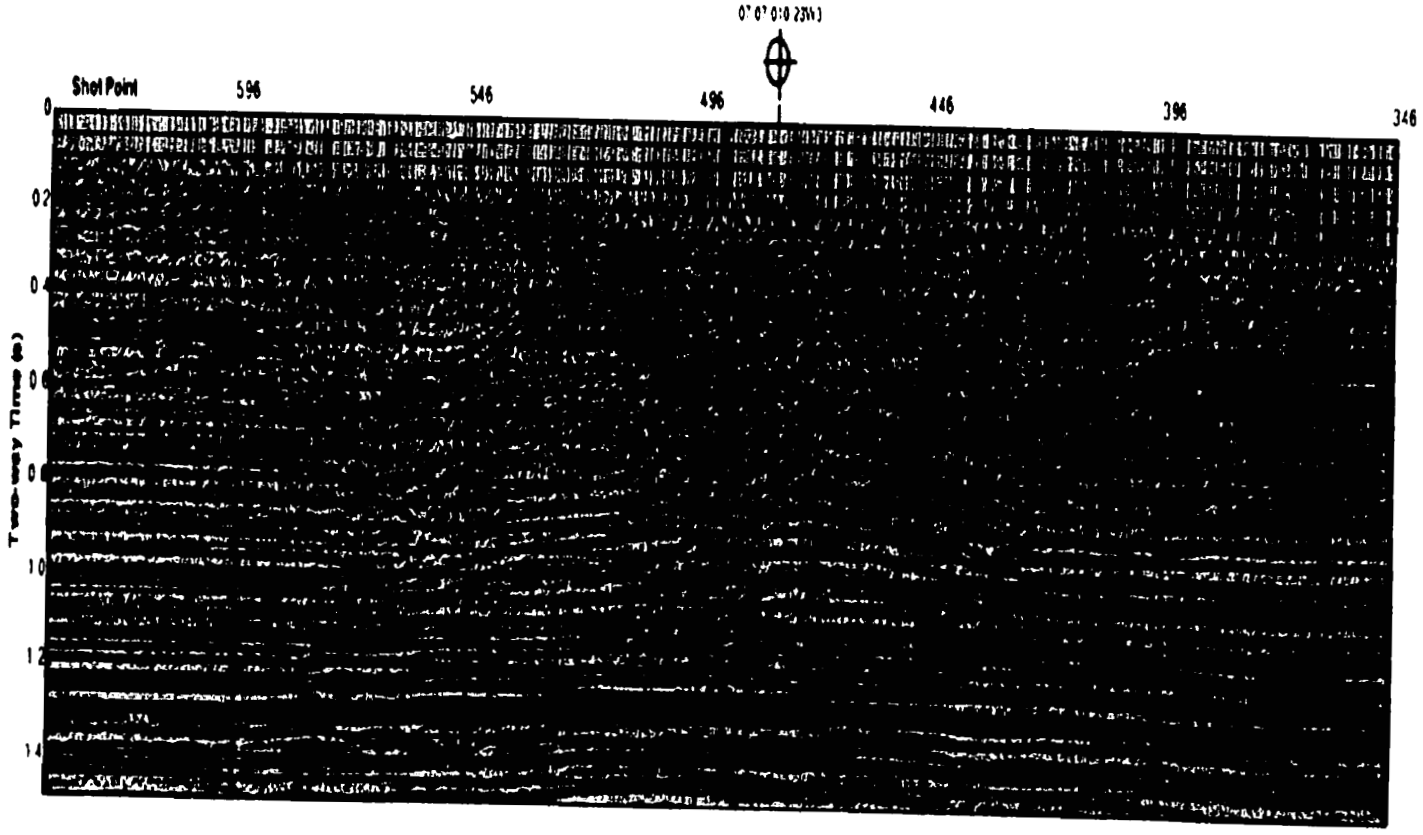

Figure 4.1.2 White Valley seismic line WV-017 showing the uninterpreted section. Notice the asymmetry in the bedding across the structure and the lack of coherent reflections in the central area. (Westbroek, 1995)

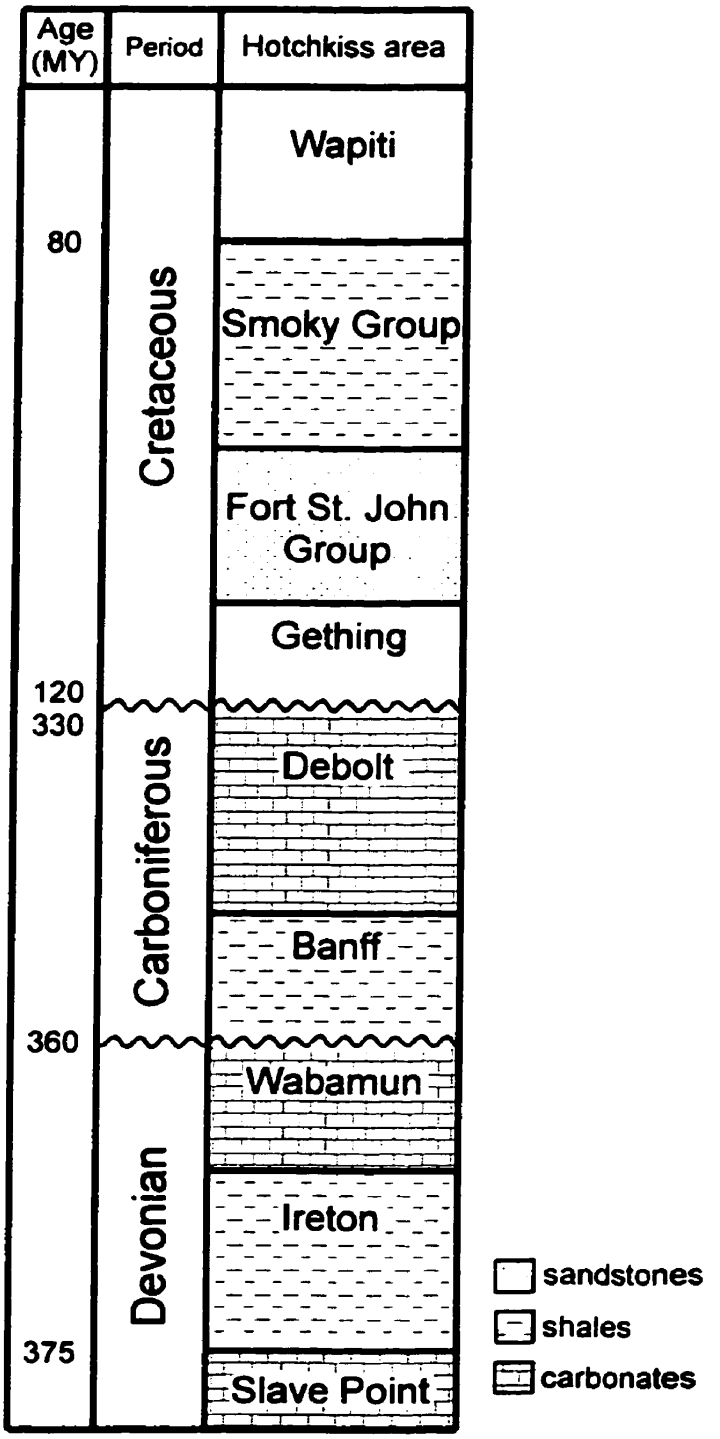

Figure 4.1.3 This simplified stratigraphic column for the Hotchkiss area shows that the Gething-Debolt unconformity represents a major gap in the geologic record in this area.

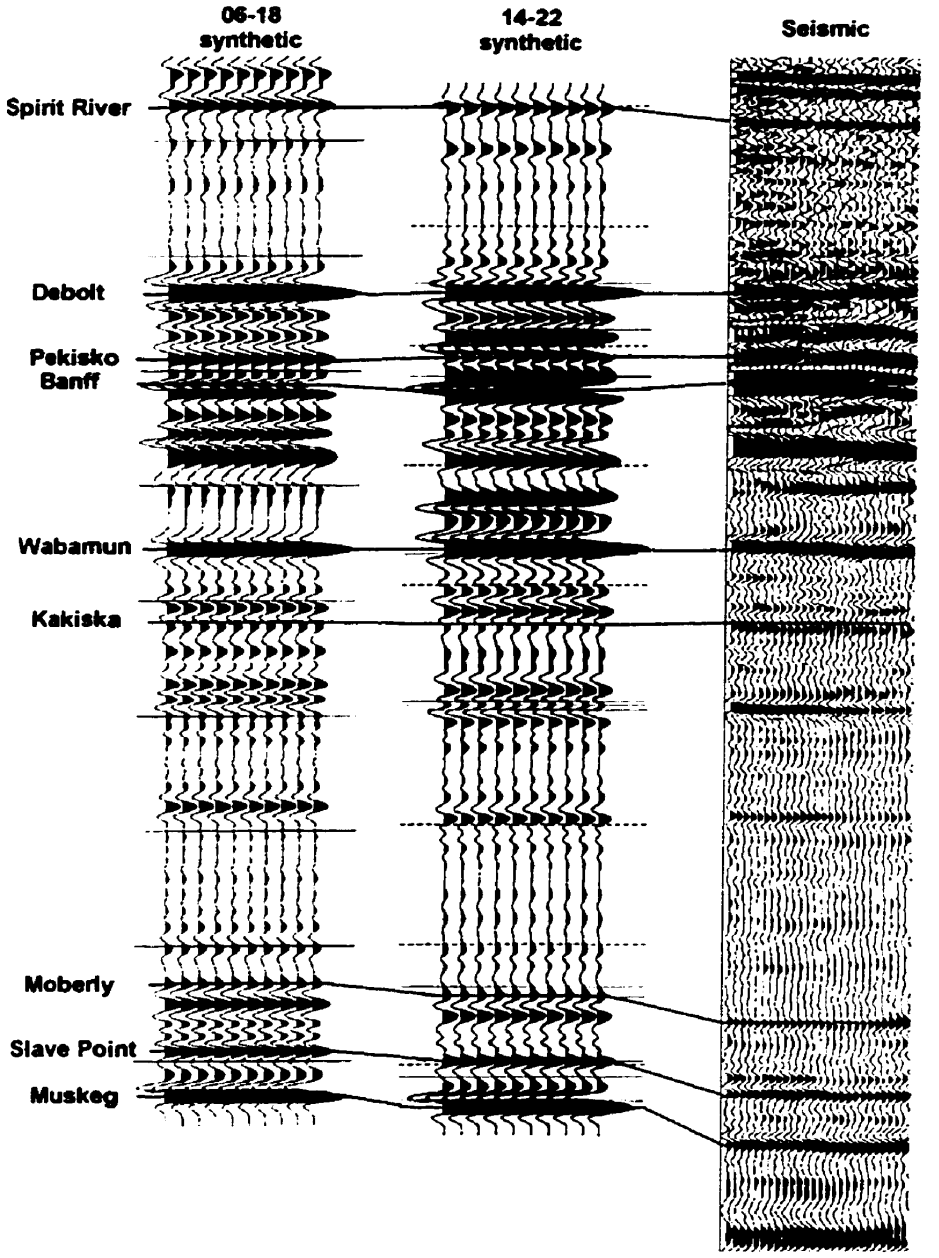

Figure 4.1.4 The correlation of the seismic data with synthetics created using well log data is observed to be good throughout most of the study area.

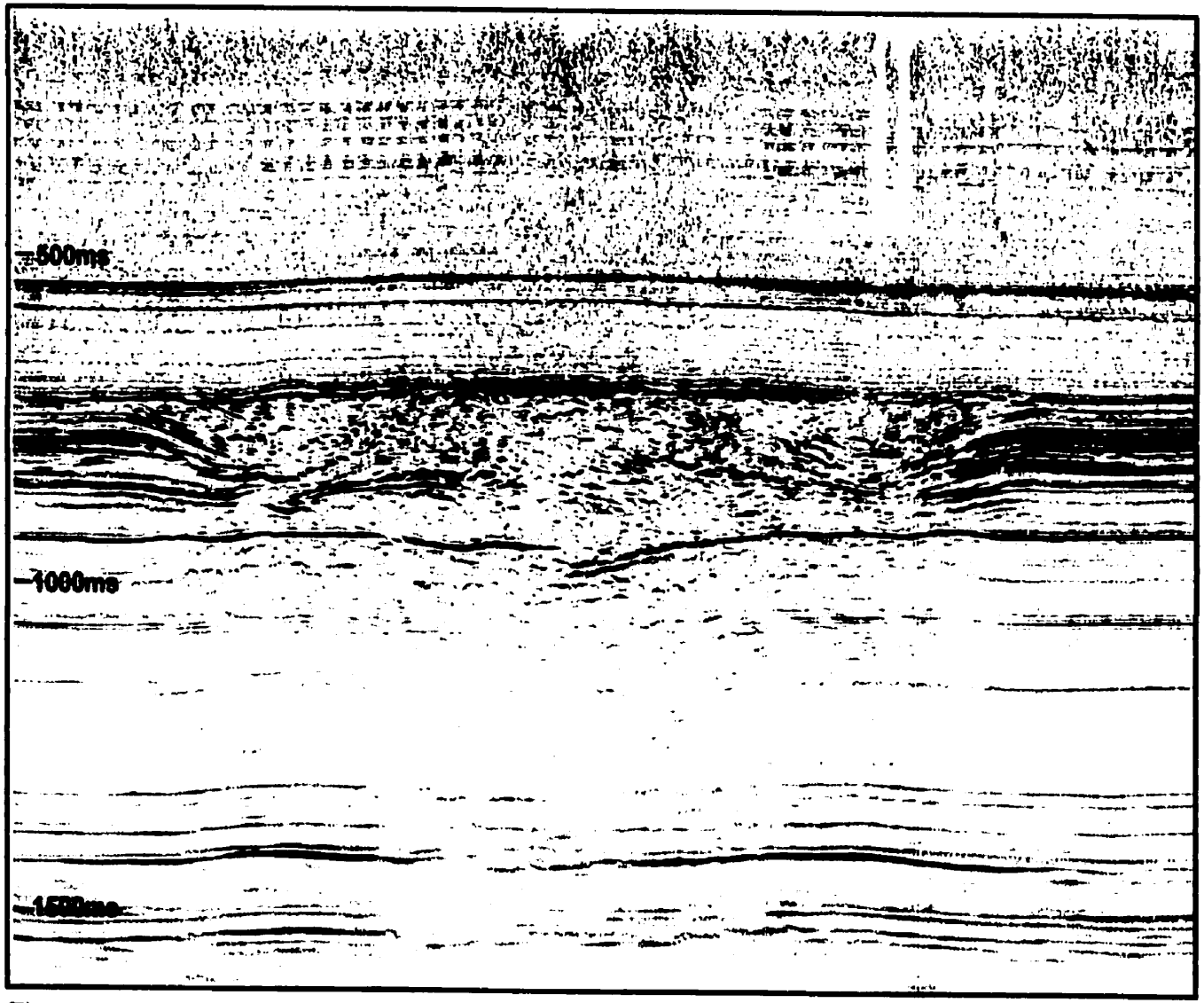

Figure 4.1.5 The Hotchkiss structure as it appears on line #2. The disturbed region in the centre is observed to be different from the regional data due its discontinuous appearance. Note the regions of velocity pull-up directly below the two troughs.

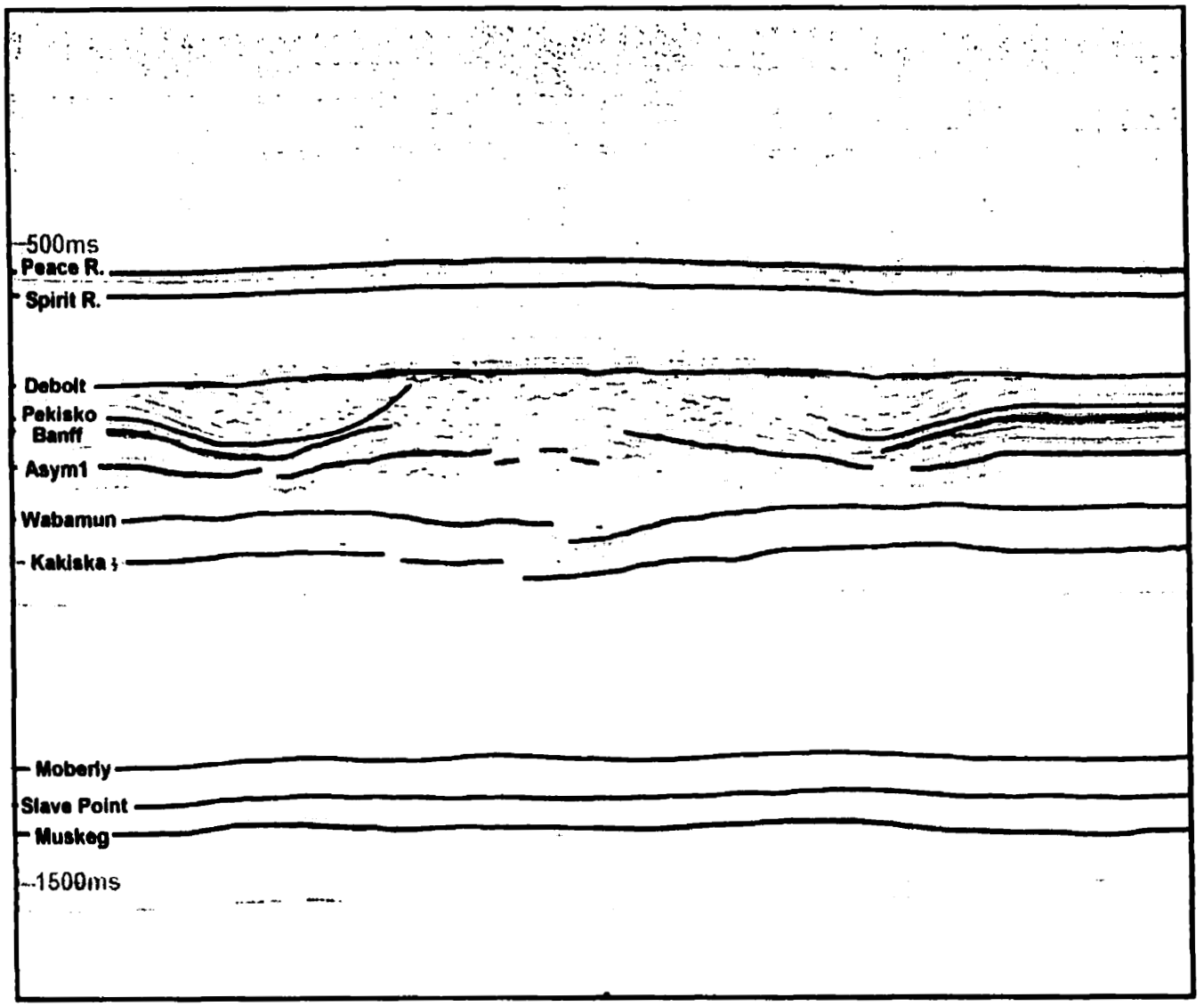

Figure 4.1.6 Interpreted horizons on the Hotckiss seismic line #2. Notice the horizontal asymmetries in the stratigraphy and the velocity pull-up effects.

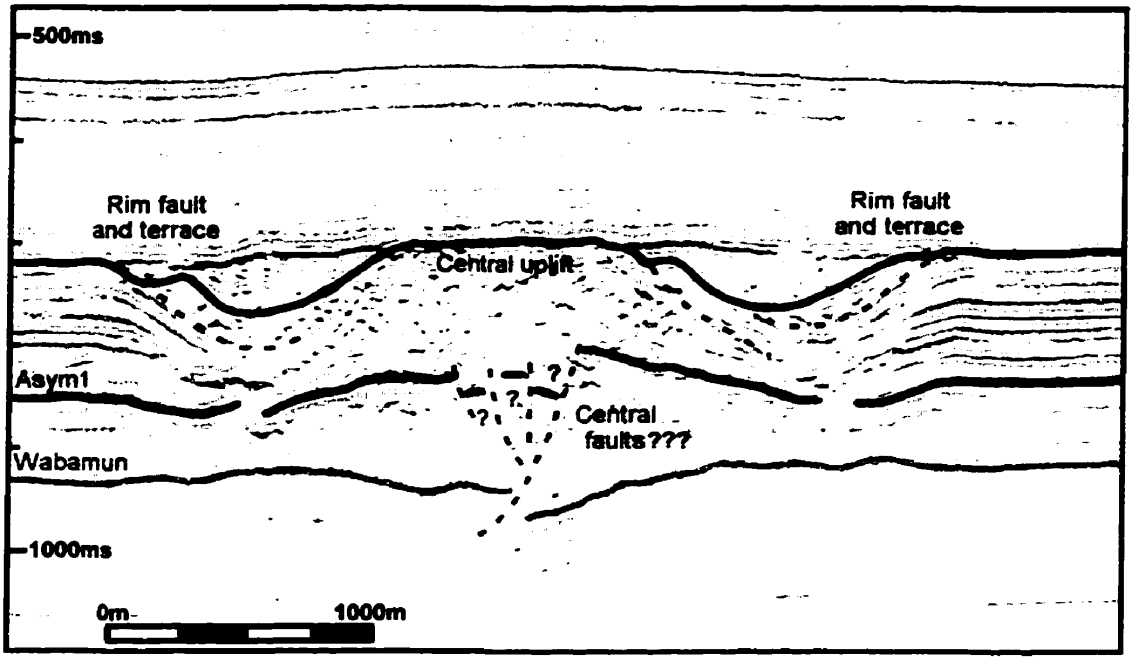

Figure 4.1.7 Shown here are faults as interpreted on seismic line #2. Also shown: a continuous surface representing the general shape of the structure, the Wabamun, and an intermediate asymmetrical horizon.

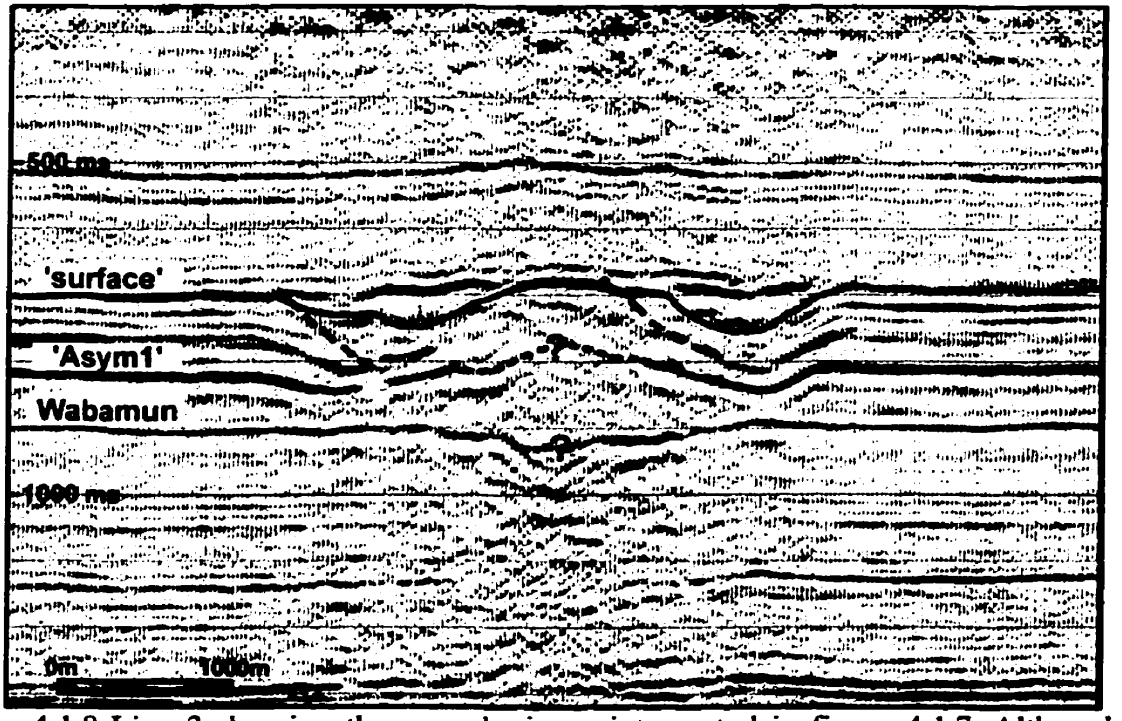

Figure 4.1.8 Line 3 showing the same horizons interpreted in figure 4.1.7. Although the event surface is similar in appearance to that in figure 4.1.7, it is difficult to continue the Wabamun and asym1 horizons into the central uplift. A single rim fault and central uplift fault shown as the dashed black line.

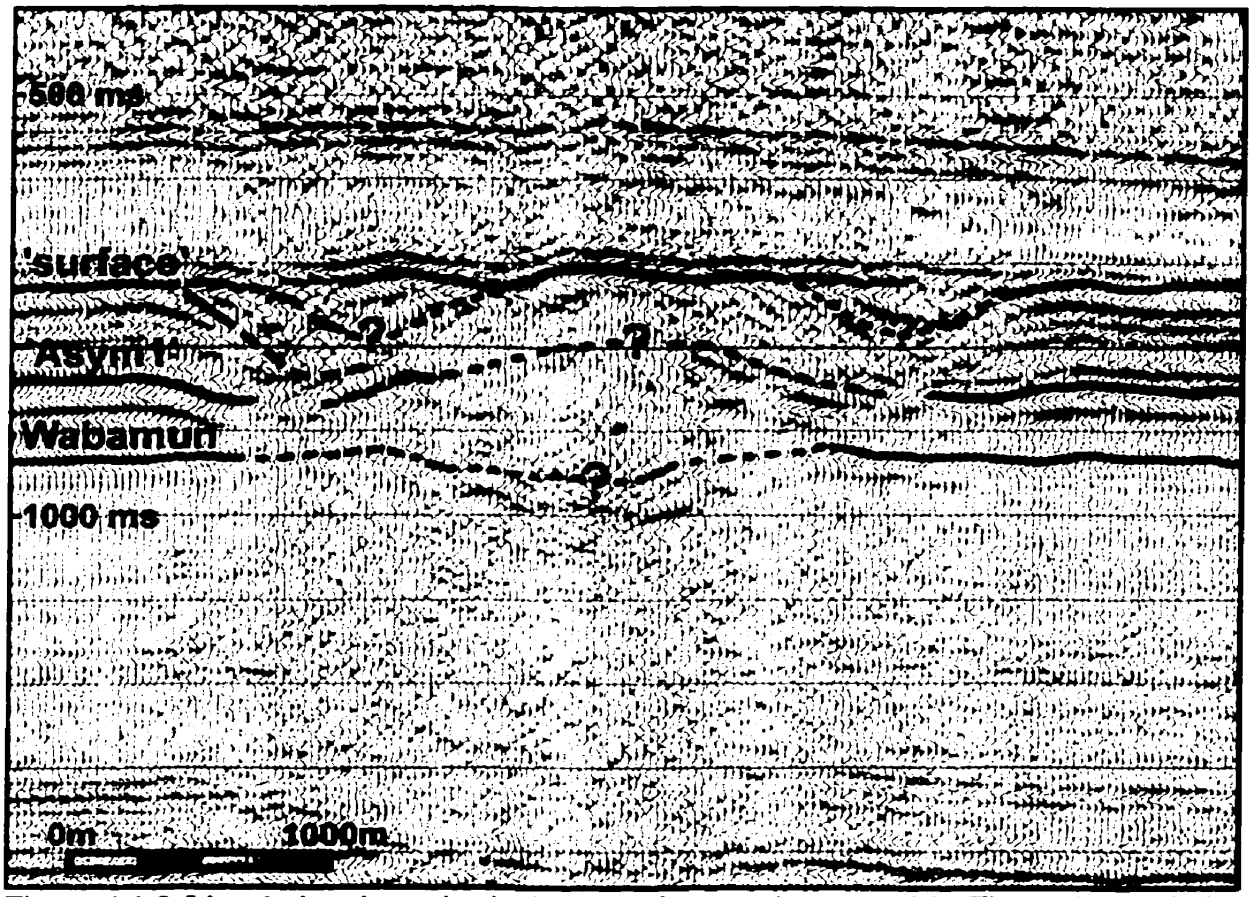

Figure 4.1.9 Line 1 showing seismic the same features interpreted in Figure 4.1.7. Notice the poorer quality of the seismic data in comparison to seismic lines 2 and 3. Interpreting the data within the troughs and central uplift is difficult. A possible rim fault is shown as the dashed black line.

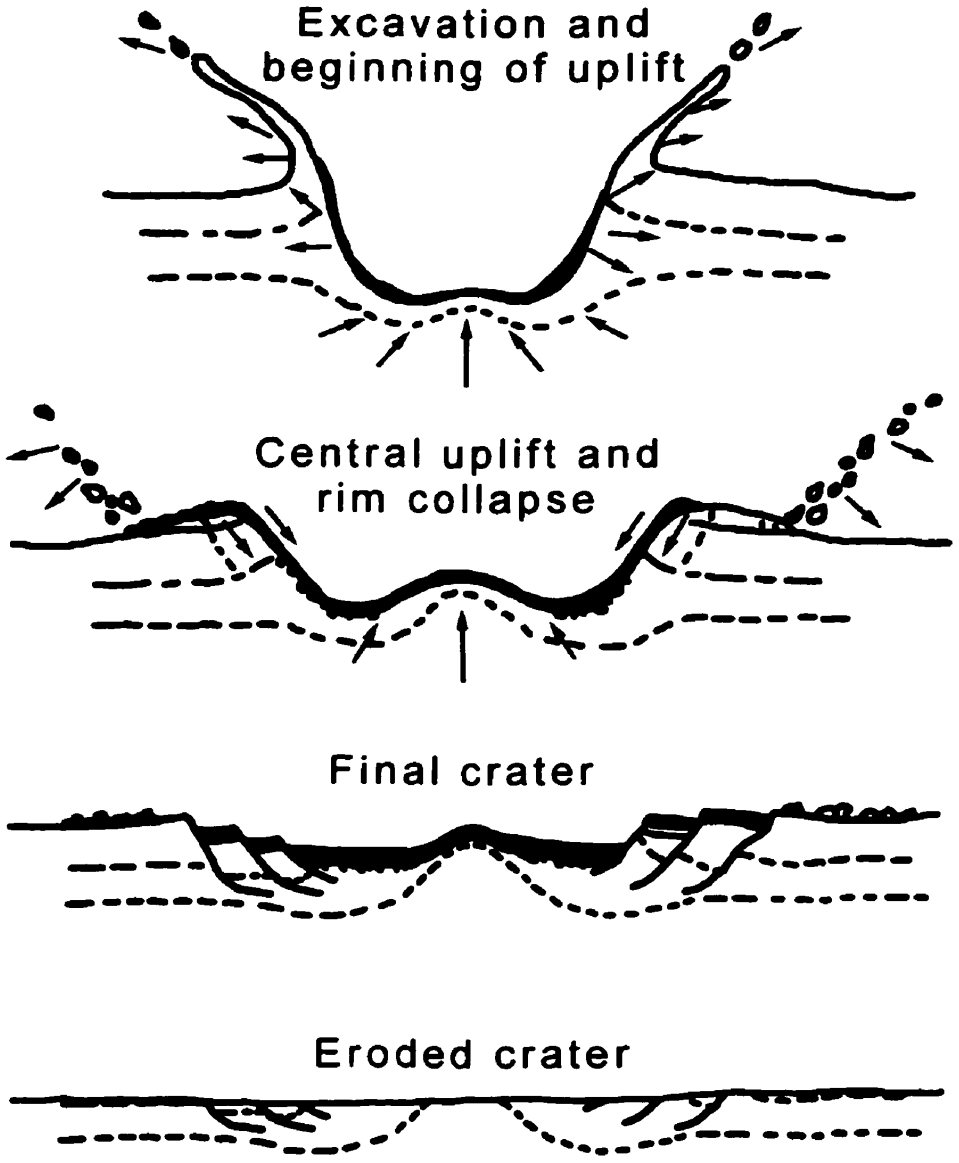

Figure 4.1.10 The Hotchkiss structure may have been caused by the impact of a 250 m stony meteoroid travelling at 20 km/s. The event would have begun with the excavation of the transient cavity which would soon have been accompanied by the start of the central uplift. Within about 20 s the central uplift would have been nearly formed and the rim would then have started to collapse. After the event, the crater experienced approximately 500 m of erosion. (*adapted from* Melosh, 1989)

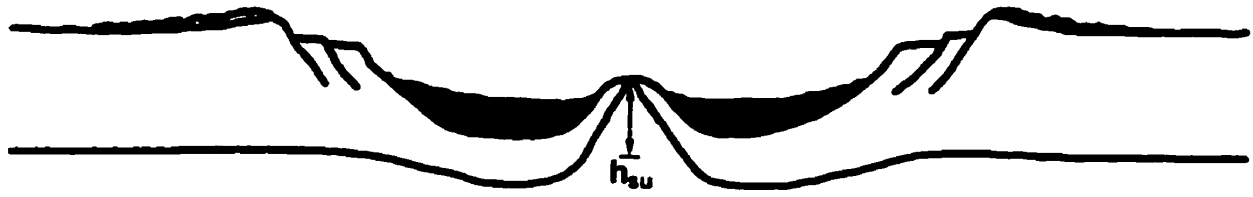

Figure 4.1.11a This pre-erosional schematic of a complex crater shows how the stratigraphic uplift would be measured.

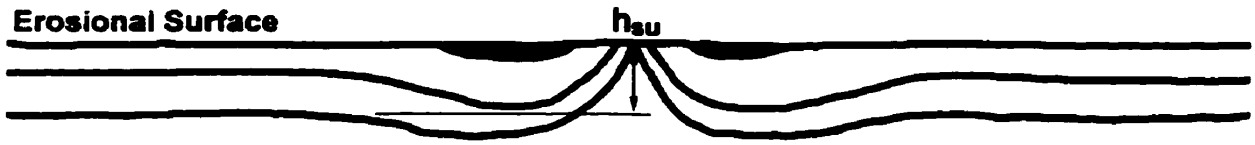

Figure 4.1.11b After erosion, the stratigraphic uplift can be measured by measuring the depth from which the exposed lithologies at the center of the central uplift originate. Note that the presence of erosion means that the observed central lithologies will be older than those observed in the pre-erosional case

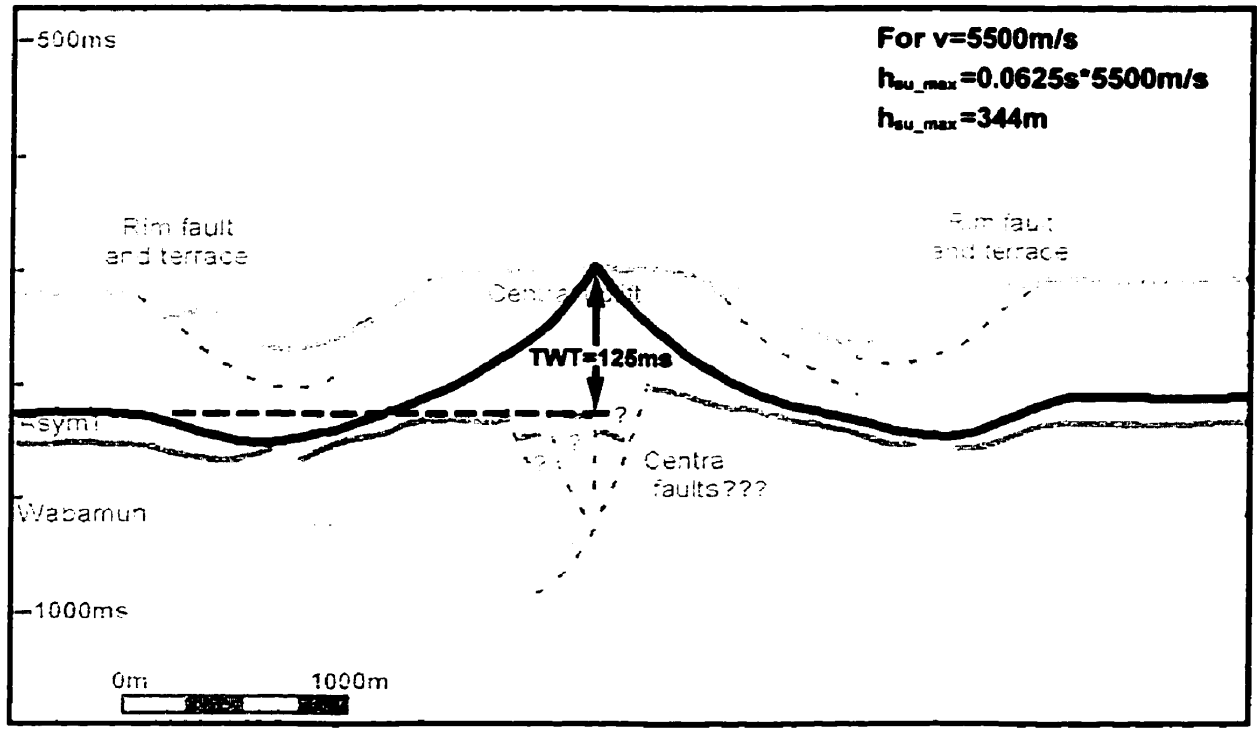

Figure 4.2.12 Applying the procedure as described in figure 4.2.11b yields a value of 344 m for the maximum stratigraphic uplift, h_{su_max}.

4.2 Steen River, Alberta

The Steen River impact structure is located in northwest Alberta (Figure 4.2.1a) approximately 700 km northwest of Edmonton. It is the remnant of the largest known impact crater in Western Canada. The feature is of considerable scientific interest because of its size as well as major economic interest due to its hydrocarbon potential. Due to the remoteness of the area and the lack of sufficient oil and gas infrastructure, the structure has been under-explored until recently. The completion of Gulf Canada's 30 million cubic foot per day gas processing plant in March of 1999 makes the Steen River structure one of the most economically important impact structures in North America. Presently, the crater rim supports about 1000 BOPD petroleum production and hosts ~12 producable gas wells with proven reserves exceeding 72 billion cubic feet of gas. Nearly 25 km in diameter, the heavily eroded crater has been imaged by more than 120 seismic lines (Figure 4.2.1b) over the past 30 years.

Each of the 127 seismic lines has been interpreted to identify seismic horizons of interest and to create contoured time structures. To provide a more conventional picture, the computed time structures are converted to depth. The time-to-depth conversions have been performed using two different techniques. The first method makes use of well information and the Petrosys gridding and contouring routines, while the second method employs GeoStats software (from Hampson Russell Software Ltd.). Using Petrosys, it is possible to tie well information to seismic data to create depth maps of a given structure. This yields a representation of the subsurface for each of the horizons of interest. The GeoStats software allows the production of depth structures as well as plots relating the expected errors associated with the computed depth structures.

4.1.1 Geological Setting

Located in the interior plains of northwest Alberta, the Steen River structure appears as an anomalous feature affecting the crystalline basement. Neither topography nor drainage (Figure 4.2.1b) shows obvious indications of the buried circular feature. The regional dip of the Precambrian basement is to the southwest. The centre of the feature lies about 63 km northwest of the large northeast trending Precambrian lineament known as the Hay River

Shear Zone (Winzer, 1972). Regionally, the pre-Cretaceous sediments are horizontal. The Paleozoic shales at the top of this sequence are terminated by an unconformity. Above this unconformity, the Lower Cretaceous Loon River sandstones and shales show little evidence of the underlying structure. Figure 4.2.1c gives a generalized stratigraphic column of the area. Note the pre-Cretaceous unconformity as well as the thick Devonian carbonate section.

Oil and gas discoveries have been confined to the Slave Point and Keg River Formations and the Sulphur Point and Zama members of the Muskeg Formation (Robertson, 1997). Table 1 gives data for some of the wells in the area that have shown oil or gas.

Table 4.2.1. Oil and gas production is seen in many wells located around the rim anticline. Production values are given as of November, 1996. (Robertson, 1997)

Well #	Date completed	Formation	Oil/Gas	Production	Status
1-28	1968	Keg River	Oil	300 BOPD	producing
9-21	1986	Keg River	Oil	≈200,000 BO	producing
15-13	1987	Sulphur Point	Oil	≈90 BOPD	suspended
14-6	1983	Zama formation	Oil	3530 BO	abandoned
1-28	1968	Slave Point	Gas	10,600 MCFGPD	shut-in
13-17	1979	Slave Point	Gas	3,100 MCFGPD	shut-in
12-28	1984	Sulphur Point	Gas	1,673 MCFGPD	abandoned

4.1.2 Interpretation of the Seismic Time Sections

In total, 127 seismic lines in the region of the Steen River structure have been analyzed. An interpretation, using Landmark's SeisWorks 2D interpretation package, of 17 horizons from the Cretaceous Unconformity to the Precambrian basement rocks has been undertaken. Horizons of interest include the Slave Point, Sulphur Point, Zama, and Keg River. To better understand the structure of this large impact feature, several horizons have also been picked above the Slave Point.

Outside of the Steen River structure (Figure 4.2.2) the seismic horizons are easily picked and lie nearly parallel to one another. Moving into the structure (the right hand side of Figure 4.2.2) the events become more chaotic and difficult to pick. With careful correlation, however, it is possible to pick some of the major horizons of interest. This is typical of every line that crosses from the regionally flat data into the disturbed inner section of the structure.

Good correlation can be seen, for example, between the synthetic seismic data created (with GMA software) from sonic logs and seismic line 96G80-20 (Figure 4.2.2). From this, it is possible to extend our horizon interpretation in a progressive manner around the structure. The quality of the correlation can also be observed in Figure 4.2.3 which shows line 96G80-09 with the synthetic seismogram from well 8-03-121-20W5.

A reasonable correlation of the horizons from line to line can be seen in Figures 4.2.4 and 4.2.5. These lines have all been corrected for misties to the Mississippian unconformity as follows. The lines were correlated (and shifted) to line BVG-001 which itself was datumed during processing to 350m asl. It should be noted that, while the correlation is good, it is not perfect. As such, we should expect some anomalies to result in our time structure maps.

Time contour maps of the area are made from the horizon picks of all of the lines using Petrosys gridding software. Figures 4.2.6 through 4.2.9 give time structure maps of the Cretaceous Unconformity, Slave Point, Keg River, and Precambrian horizons respectively. Also shown on these maps are the seismic pick locations. Close to the pick locations, the gridding algorithm is expected to be accurate. In the regions that are known to be structurally complex (central uplift, slump blocks) but that have no seismic information the gridding algorithm is expected to be inaccurate.

4.1.3 Observations

Reflecting the buried crater, some relief is present on the Cretaceous unconformity (Figure 4.2.6). Note the circular nature of the structure and the location of many wells along the rim. Examining the horizons of economic interest, the general structures and shapes are similar at each horizon (Figures 4.2.7 and 4.2.8). The annular uplift or rim is

observed to be about 24 km in diameter, about 3 km wide, and about 100 m ($\Delta t \approx 20$ ms and $v \approx 5000$ m/s) high. Due to the poor coverage or quality of the data in the interior of the structure, the central uplift is poorly defined.

Timing of the event can be broadly placed sometime Post-Mississippian to pre-Lower Cretaceous due to the structural disturbance observed throughout the Devonian section and its lack in the later sediments. Pinpointing the event timing, however, is difficult due to the approximately 1 km of erosion that took place prior to deposition of the Cretaceous Loon River shale (Hildebrand et al., 1998a).

4.1.4 Time-to-depth Conversion using Petrosys

The Petrosys software system accepts horizon depths (from well information) and seismic structure in time. All of the well information was provided by Gulf Canada Ltd. Depths are given below Kelly Bushing (KB) and, as a result, we first examine the depth structures with respect to KB and then with respect to sea level. Ultimately, the sea level referenced depths are desired as we wish to examine the structure independent of topography. Using Petrosys, gridded two-way traveltime maps were created and displayed with two-way times and depths posted beside each of the wells for which tops had been picked (Figure 4.2.10).

Using the posted values from several of the wells, it is possible to calculate an average conversion factor (Table 4.2.2) in the map area. This conversion factor is used to convert time to depth for the whole structure creating what is termed a 'pseudo-depth' structure (Figure 4.2.11). Differences between each of the known well tops and the corresponding pseudo-depth point are then calculated, gridded, and contoured. By adding this 'difference map' to the pseudo-depth structure a corrected approximation of the structure is created. Depths below KB as picked for each well are given to the right of the well symbols. In the case of no data, the well symbol only is shown.

Table 4.2.2. Conversion Factors Used For Pseudo-depth Calculations

Horizon	Paleo.	Slave Point	Sulphur Point	Muskeg	Keg River	Chinchaga	Precambrian
Conversion Factor	1027	898	977	979	1146	1233	1249

Time-to-depth conversions have been performed for the following horizons: Cretaceous unconformity, Slave Point, Keg River, and Precambrian. In this first pass, all depths are below KB. Figure 4.2.12 illustrates the Cretaceous unconformity as anchored to the well tops of that horizon. In the central region, the horizon appears to dip deeper possibly reflecting the buried annular synform or simply an inaccuracy of the horizon picks. The apparent deeper area in the NW correlates with the NE-SW striking Cameron Hills, so that the apparent structure is a result of our use of KB depth values. Figure 4.2.13 shows the Slave Point depth structure as computed using Petrosys. Clearly evidenced is the outermost rim of the crater, several small peaked areas, and a deep region in the NW. Also evident, is a general correlation between the structural highs and the positions of previously drilled wells.

To gain a better understanding of the true subsurface structure in depth, the results as calculated relative to sea level are presented in Figures 4.2.14 through 4.2.17. The method used is the same as that for Figures 4.2.12 and 4.2.13 except that the horizons have been tied to the picked asl depths. All wells except for five (12-19, 16-19, 3-12, 1-15, 7-32) were used in the calculation. These five wells were deemed to have a negative effect on the minimum curvature gridding algorithm due to their proximity to large displacement faults. The NE-SW striking feature due to the Cameron Hills in the northwest disappears when the depth structures are calculated relative to sea level. It should be noted that depths below sea level are given as negative values while those above sea level are positive numbers.

The first depth structure that will be examined is that of the Cretaceous unconformity. The Cretaceous unconformity depth structure (Figure 4.2.14) dips to the west about 100 m over 40 km. The structure is smooth with a deeper region towards the centre that is probably an artifact of the well top picks.

In examining the remaining maps (Figures 4.2.15 through 4.2.17), we see good definition of the crater rim. It is punctuated by many small structural highs. Most notably, is the high associated with a suspended gas well on the eastern limb of the structure. This high circumscribes a large area on each of the horizons of interest. Smaller highs exist throughout the area in the SE, many of which are drilled. There are, however, several

examples where the well is located ≈1 km away from the nearest structural high. Several wells in the NW corner, while successful, appear to be located slightly SW of their associated major structural highs.

4.1.5 Depth Conversion using GeoStat

The GeoStat program, from Hampson-Russell Software Services Ltd., deals with spatially organized data. It is designed to integrate multiple sets of geological or geophysical measurements using statistical methods. Geostatistical techniques take 'hard', sparse information (well log data) and use it to convert plentiful, less-resolved data (seismic data) into interpolated values. GeoStat is used to analyze input data (well log and seismic data), determine their statistical properties, and then interpolate values on a regular grid. The ultimate goal of GeoStat is to create a map of some desired property. For the purpose of this study, the desired property is that of depth relative to sea level.

Figure 4.2.18 shows the well locations for the Slave Point horizon as posted on top of a shaded contour plot of the gridded time structure (gridded using Petrosys) of the Slave Point horizon using the GeoStat package. Since only 12 colours are available to GeoStat, the plotted contour intervals are large. Consequently, to view the small-scale structure the following plots must be exported to xyz ascii files and then examined using another package such as Matlab. Figure 4.2.19 gives the Slave Point time structure as it appears when plotted using Matlab. A histogram of the input data is examined in Figure 4.2.20. This histogram shows that there are several distinct groups (600 ms, 700 ms, and 750 ms) about which the two-way traveltimes are scattered. Intuitively, this is expected as the 600 ms group corresponds to raised rim data, the 700 ms group corresponds to deeper regional data, and the 750 ms group corresponds to the central area of the structure. Another way of looking at the data is to examine the cross-plot of the dense seismic data versus the sparse well data (Figure 4.2.21). The points of the cross-plot can be seen to be roughly described by a straight line whose slope is a measure of the average (surface to Slave Point) subsurface velocity in the area.

Kriging

The process of kriging allows the creation of a gridded map of sparse data. The first step in this process is to model the well-to-well variogram. The variogram is a mathematical function that measures the spatial continuity of two datasets. Contained within it is information about how well correlated the data points are and if directional continuity patterns exist. Figure 4.2.22 shows the isotropic well-to-well variogram with 20 offsets ranging from 0 to 52 km. Calculated values are shown as black points while the red line defines the modelled variogram. Shown in the background is a bar plot giving the number of wells used in the calculation at each offset.

Kriging of the well log provides an optimally contoured map of the well log data. Shown in Figure 4.2.23, this kriged result illustrates the fit through the well log data. The error in this result is given in Figure 4.2.24. Notice that the error is smallest close to the wells and gets larger further from the wells. By deleting one well at a time from the kriging calculation, we can produce a cross validation plot showing the effect of each well on the calculation. Figure 4.2.25 shows the error associated with each prediction. Note that the error ranges from 0 m to approximately ±50 m. Using this technique depth conversions for other horizons of interest can be made. Shown in figures 4.2.26 through 4.2.31 are depth structures and their associated errors for the Cretaceous unconformity, Keg River, and Precambrian horizons respectively.

Kriging with External Drift

Kriging with external drift (KED) is a simple and efficient algorithm that incorporates a secondary variable (seismic data in this case) into the estimation of the primary variable (well data in this case). By using the secondary (seismic) data to inform the shape of the primary variable mean surface this technique can be more accurate than simple kriging as the resultant KED maps tend to have trends that reflect the secondary variable.

Figure 4.2.32 shows the KED result for the Slave Point horizon. A comparison with figure 4.2.23 illustrates contribution of the seismic attribute to the final map. The KED error for the Slave Point horizon is given in figure 4.2.33 and can be seen to have a

magnitude of about ±35 m throughout the area of interest. Examining the cross-validation plot (Figure 4.2.34) the individual effects of each of the wells on the KED process can be observed. Figures 4.2.35 through 4.2.40 show the results of performing KED on the Cretaceous unconformity, Keg River, and Precambrian horizons respectively.

Cokriging

In order to properly perform time-to-depth conversions geostatistical algorithms require that the dense seismic data be stationary. That is, the data must have a constant mean or average value. A quick inspection of the input data (Figure 4.2.19) however, has shown that the seismic data trends NE to SW and exhibits several features related to the local topographic and subsurface trends. Thus, the input Steen River gridded seismic data set violates the conditions under which geostatistics works best. By removing the trend from the input data, the stationary condition can be met. Figure 4.2.41 displays the trend as produced by smoothing the seismic data using a 25 km smoothing filter. A large smoother is applied to emphasize large scale structure. The result of applying such a filter is taken to represent an approximation of the regional topography and subsurface trends. Subtraction of this trend from the seismic dataset will result in the residual dataset as seen in Figure 4.2.42. We can now see additional short-wavelength anomalies.

All of the subsequent computations compare the dense seismic data with its trend removed and the sparse log tops reduced to asl values. Recall from figure 4.2.21 that the best-fit regression line through the points of the cross-plot had a slope of 0.538552. Corresponding to a velocity conversion factor this value is applied to the seismic data to produce the Slave Point depth structure in Figure 4.2.43.

The next step in this process is to model the seismic-to-seismic variogram. Figure 4.2.44 uses 40 offsets extending from 0 to 52 km at six separate azimuths to compute the seismic-to-seismic variogram. In each case, the solid curve represents the modelled variogram. The interpretation of these results is that the range is longer in the N-S direction than in the E-W direction. The 60° azimuth clockwise from north gives a minimum width while 150° indicates a maximum. Another way of examining the affect of directional anisotropy is to examine the variogram map (Figure 4.2.45a and 4.2.45b). By adjusting the variogram for

anisotropic effects (an anisotropy factor = 0.8 at a principal direction of 160° was found to give the best fit) a much better model variogram can be obtained (Figure 4.2.46).

To produce a map that honors the well data but uses both the seismic data and the variograms to interpolate between the wells, we cokrig the data. Figures 4.2.47 and 4.2.48 give the isotropic and anisotropic collocated cokriging results respectively. Notice the, now evident, circular nature of the structure and the appearance of a rim. The fit of this result is excellent as is evidenced by the errors shown in figures 4.2.49 and 4.2.50. Cross-validation plots are given in figures 4.2.51 and 4.2.52 for the isotropic and anisotropic collocated cokriging results respectively. Figures 4.2.53 through 4.2.58 show the anisotropic collocated cokriging results for the Cretaceous unconformity, Keg River, and Precambrian horizons respectively.

4.1.6 Visualization of the Results

Upon completion of the time-to-depth conversions, several possible methods of displaying the results were examined. The technique that we found the most instructive allows for real-time dynamic visualization of 3-D datasets using commonly available web browsers. Using the gridded xyz depth files created with Geostat and Virtual Reality Machine Language (VRML, pronounced *virmel*), 3-D depth structures were created. These depth structures were then viewed using Netscape with Silicon Graphic's 'Cosmoplayer' VRML plug-in. Figures 4.2.59 and 4.2.60 show two different views of the cokriged Slave Point horizon. Notice the NW-SE trending right-lateral vertical-offset fault bisecting the structure.

4.1.7 Concluding Remarks

The Steen River structure is observed to be a nearly circular impact feature that is approximately 25 km in diameter. The slightly elliptical nature is evidenced by the azimuthal dependence of the variograms as created using GeoStats. Rim uplift is observed to be about 100 m above regional levels while the central region is observed to lie approximately 100 m below regional levels. Additionally, clear anomalous blocks in the rim are visible in the residual seismic maps as well as the final depth images.

Two separate methods for converting the time structures to depth have been examined. The Petrosys method ties the depth structures directly to the well data. This results in a reasonable depiction of the subsurface in depth. The GeoStats method employs various geostatistical techniques to create accurate maps of the subsurface by the methods of kriging, kriging with external drift, and cokriging. The results using the latter method are similar to those using Petrosys, but are thought to provide a better picture of the subsurface especially when the effects of variogram anisotropy are included.

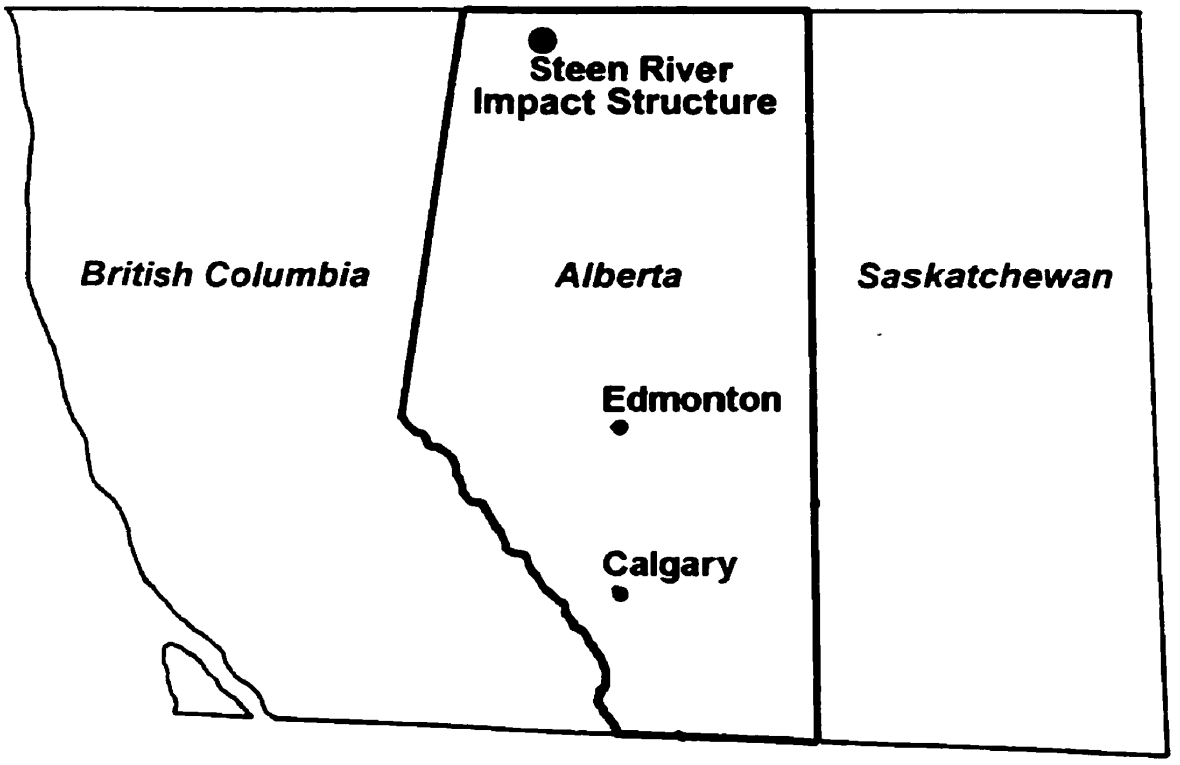

Figure 4.2.1a Location map of the Steen River structure in NW Alberta.

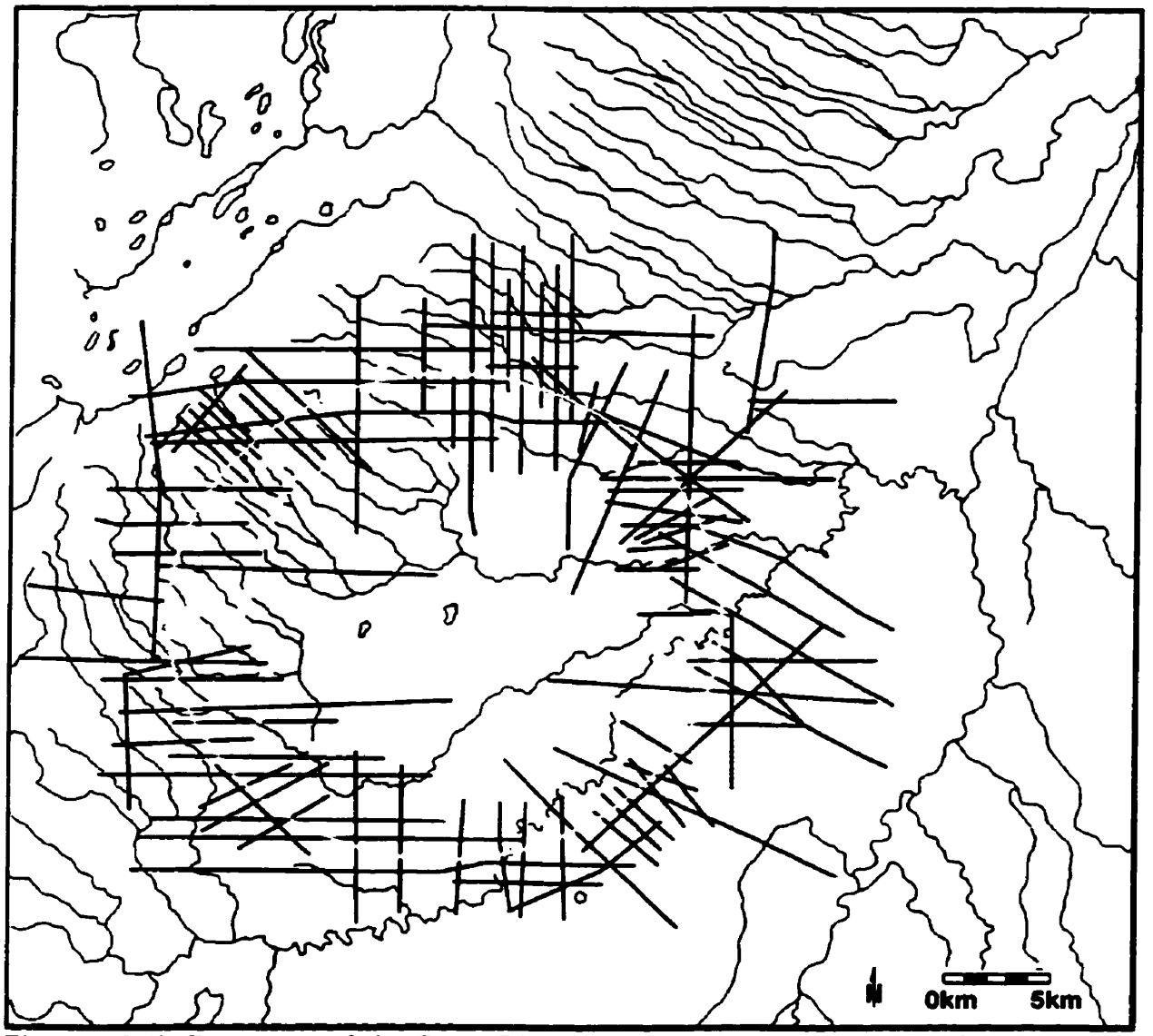

Figure 4.2.1b Base map of the Steen River area showing seismic lines of interest. The drainage pattern provides no indication of the subsurface impact structure whose rim extent is roughly shown by the yellow circle. Seismic lines are shown in black.

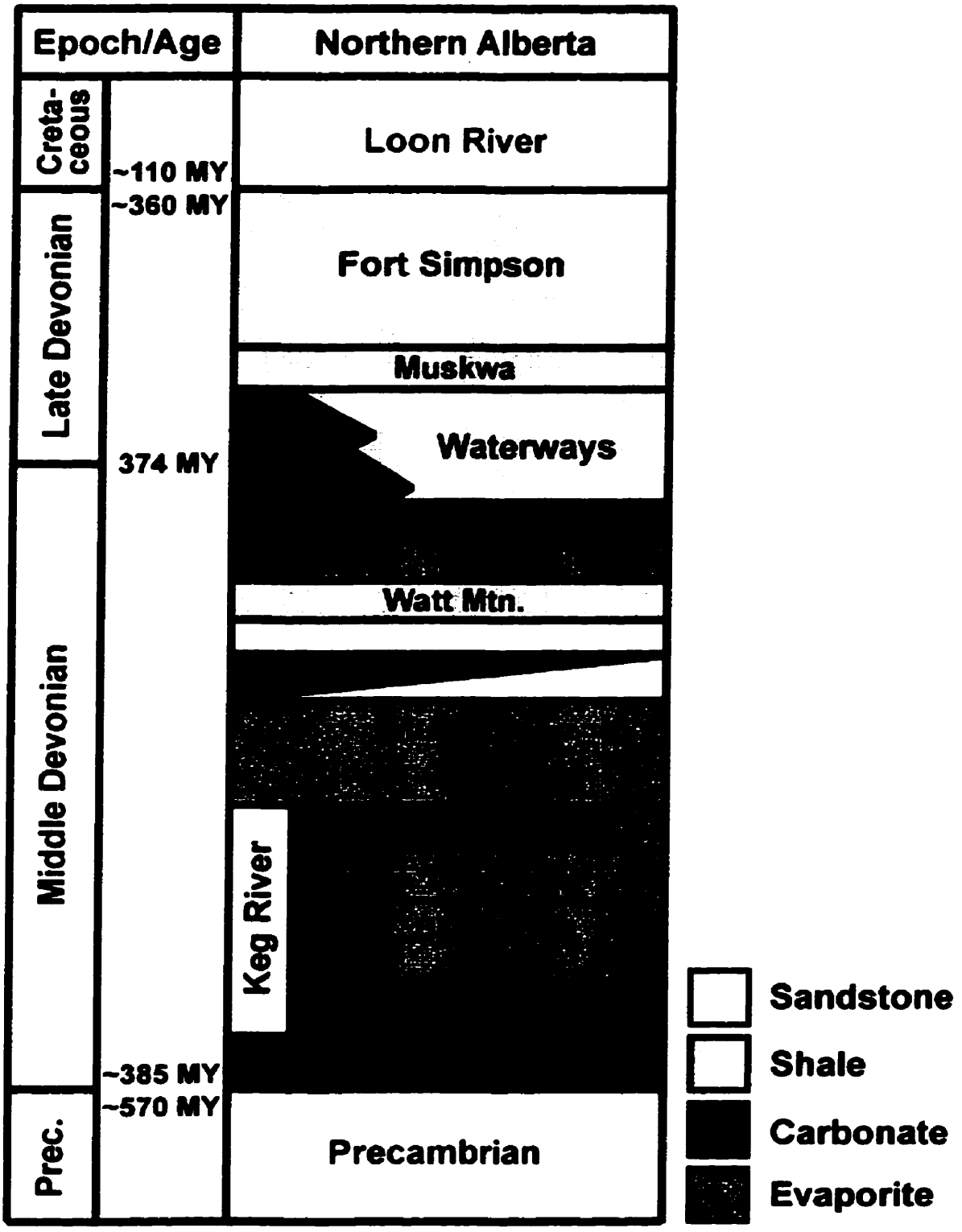

Figure 4.2.1c Generalized stratigraphic column of the Steen River area. (after Hladiuk, 1998)

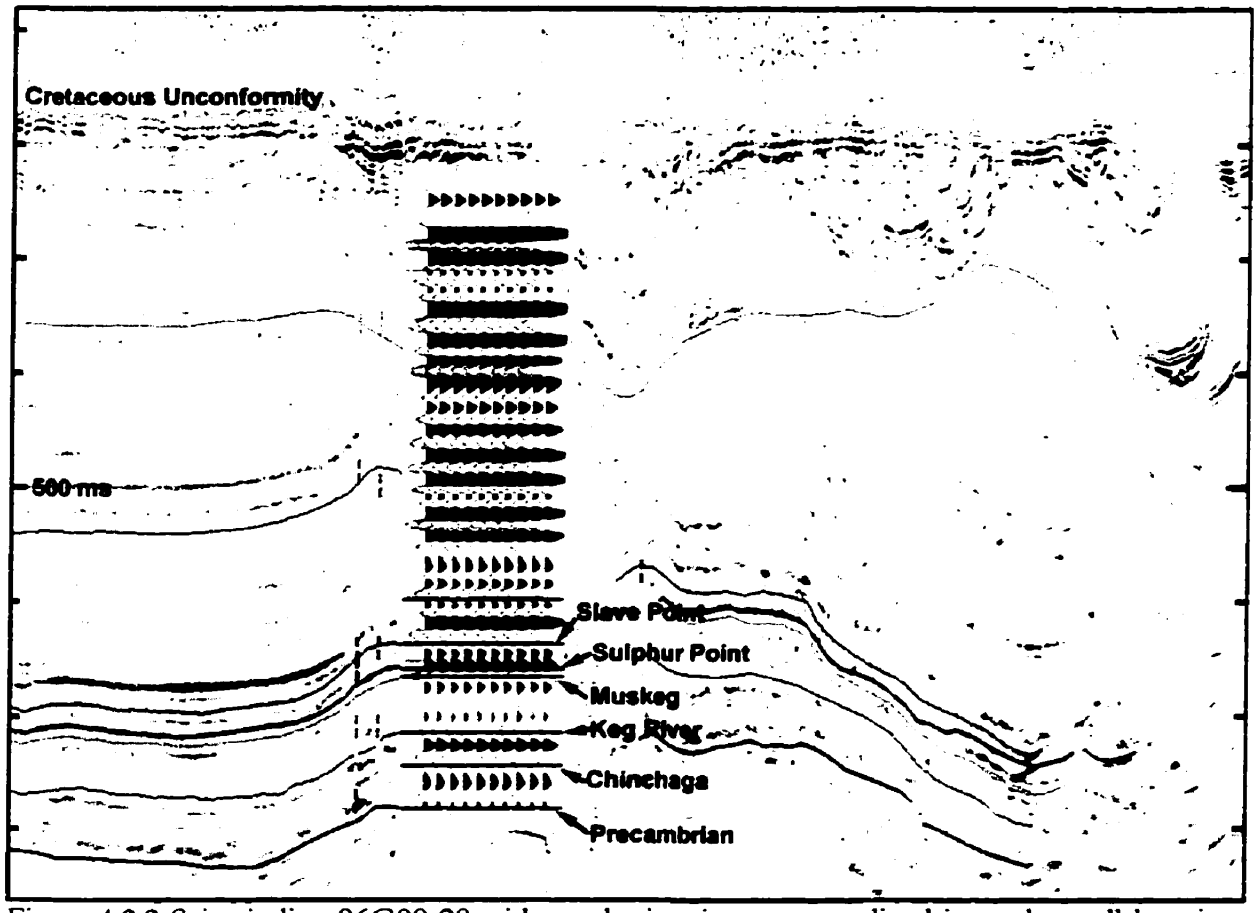

Figure 4.2.2 Seismic line 96G80-20 with synthetic seismogram spliced in at the well location. Observed near the top of the seismic section, the Cretaceous unconformity and its overlying reflectors are continuous throughout most of the section. Note that the correlation is good across the horizons of interest (Slave Point, Keg River, and Precambrian).

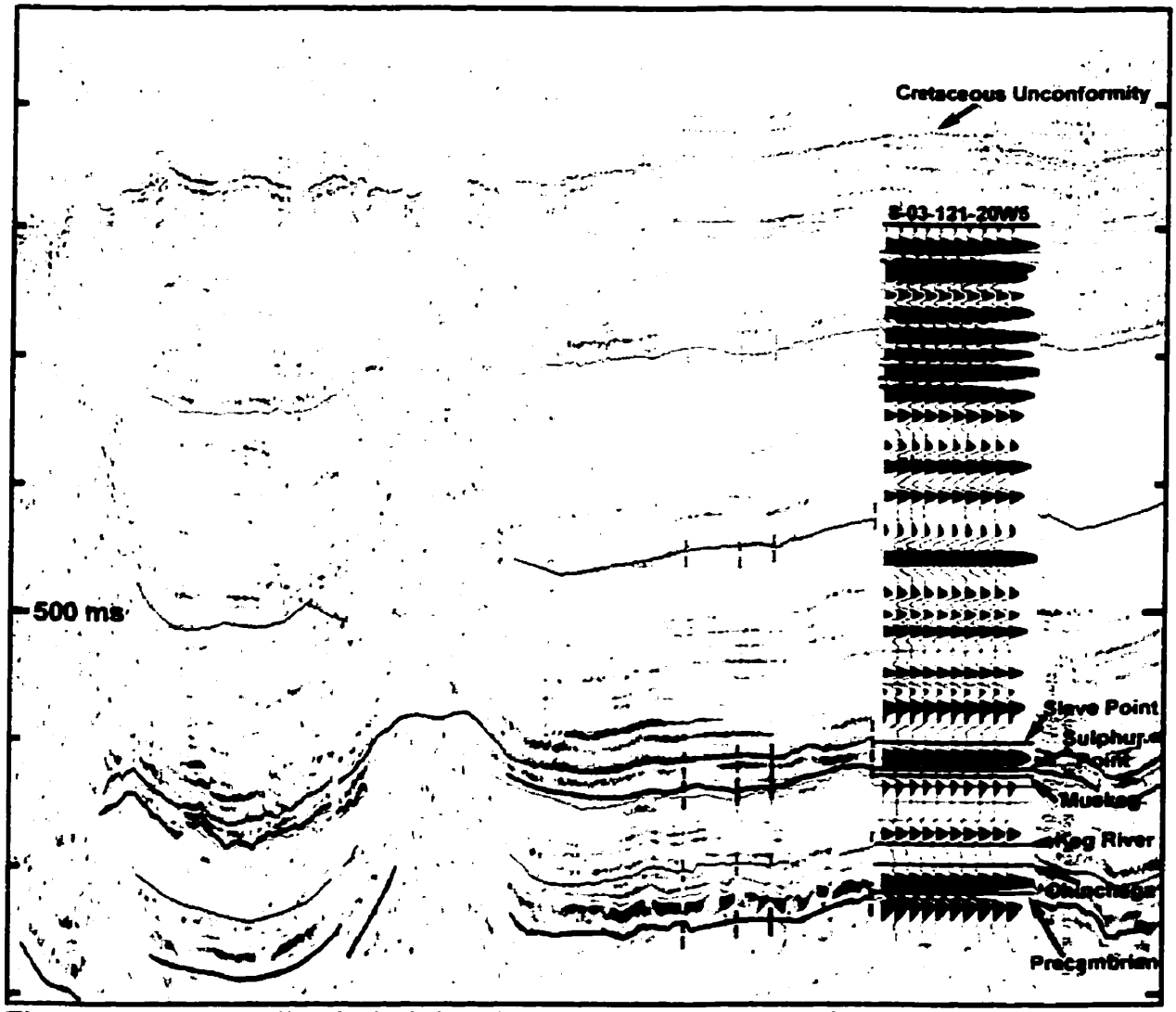

Figure 4.2.3 Seismic line 96G80-09 with synthetic seismogram from well 8-03-121-20W5 spliced in at the well location. Observed near the top of the seismic section, the Cretaceous unconformity and its overlying reflectors are continuous throughout most of the section. Note that the correlation is good across the horizons of interest (Slave Point, Keg River, and Precambrian).

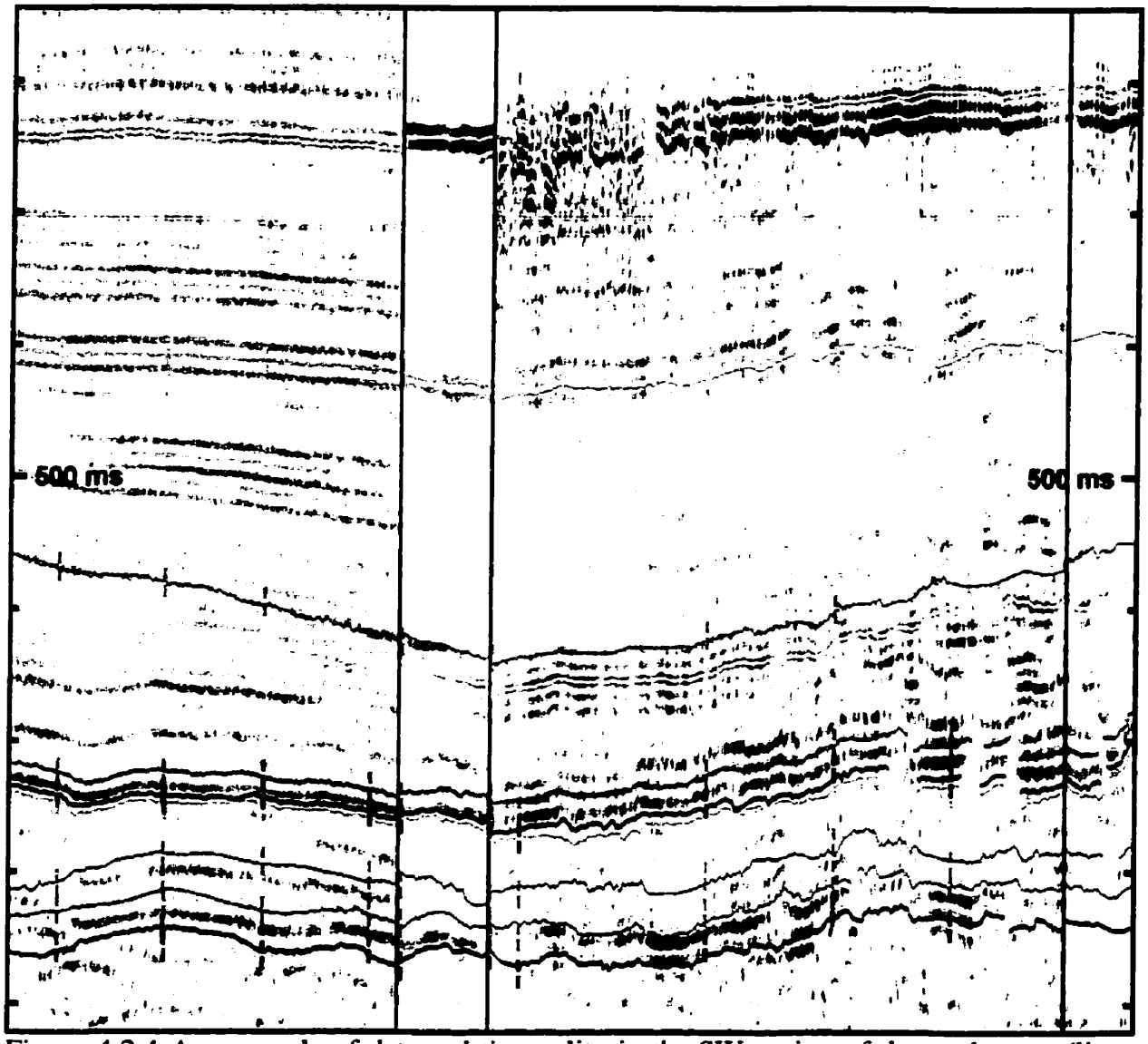

Figure 4.2.4 An example of data and tie quality in the SW region of the study area (lines 8303-07, BHO-002, 66T12-25-AA-PT2, 66T31-4PT2 from left to right)

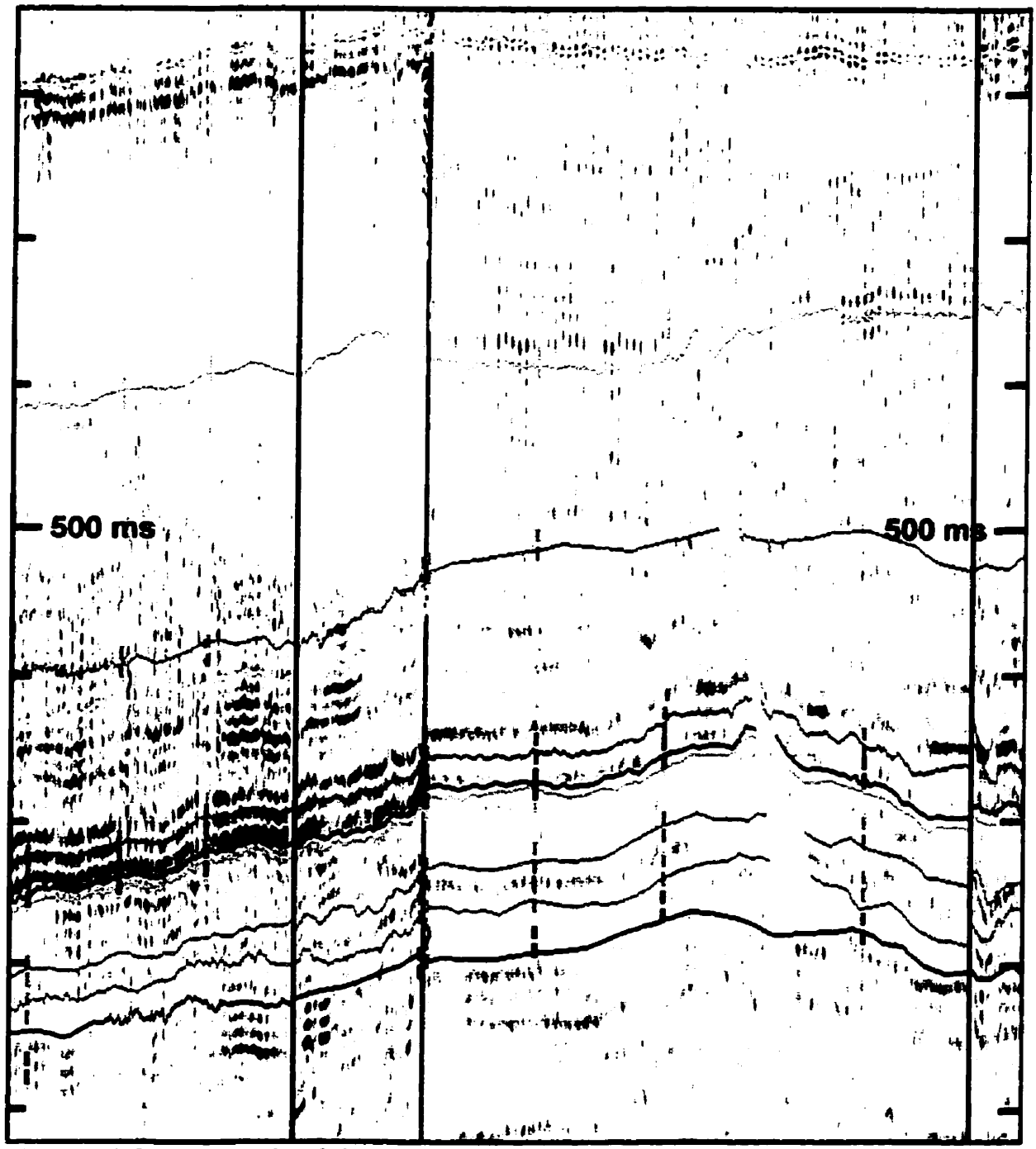

Figure 4.2.5 An example of tie quality in the western region (seismic lines 66T12-25-00, 67T1225-50-12, 8263-01, 67T25-50-14 from left to right)

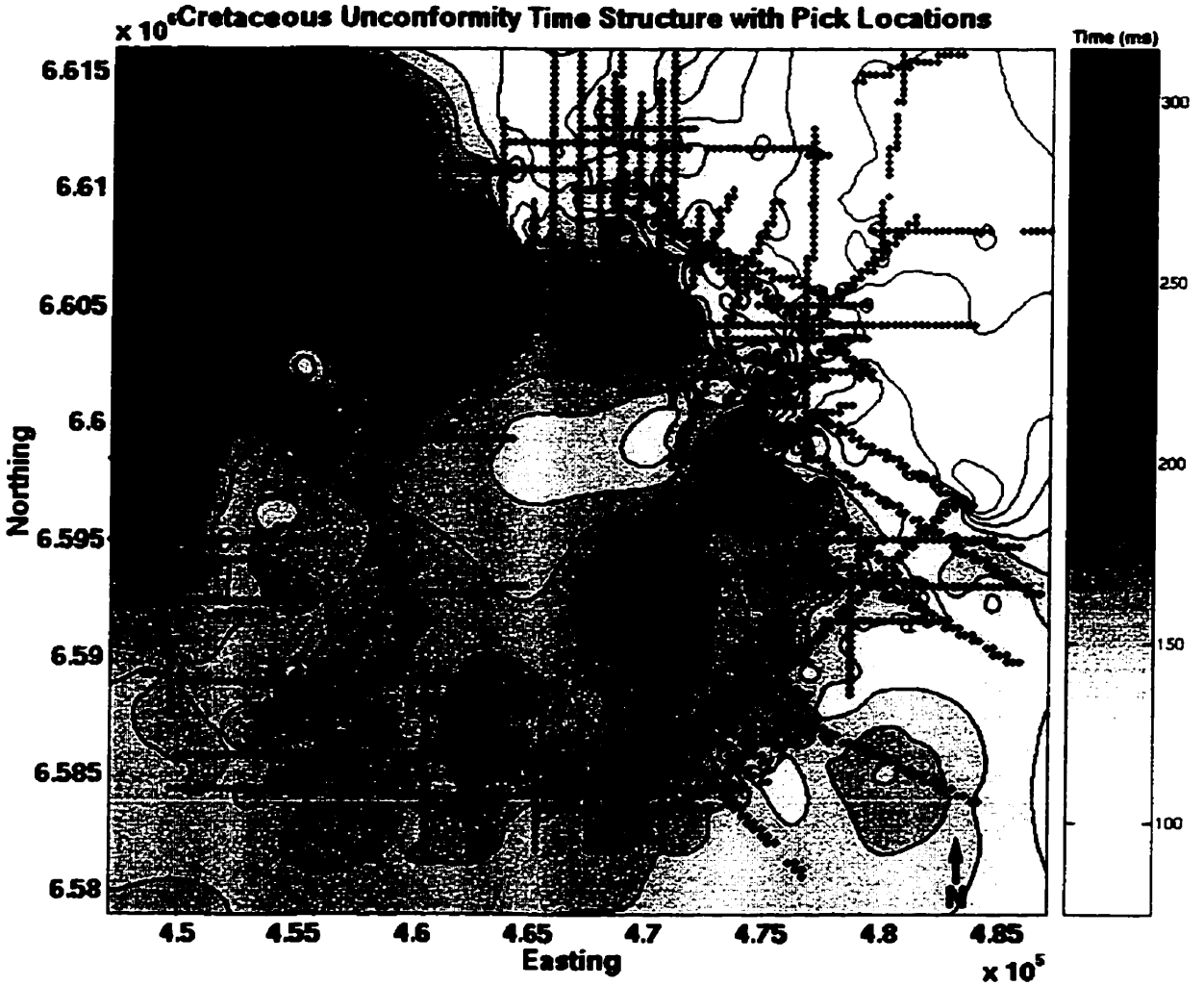

Figure 4.2.6 Contoured time structure of the Cretaceous unconformity showing the locations of the picks (black dots) used in the gridding calculation.

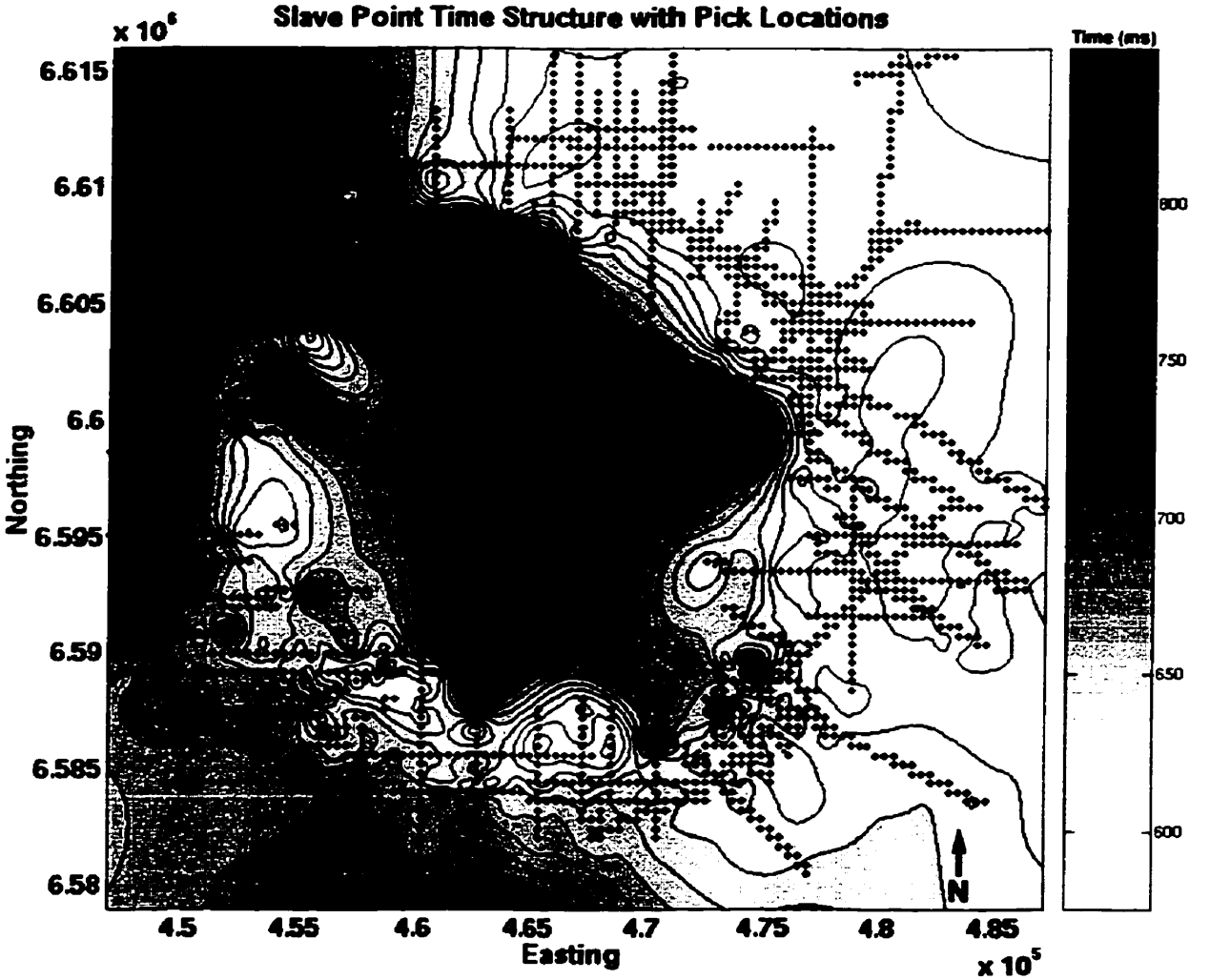

Figure 4.2.7 Contoured time structure of the Slave Point horizon showing the locations of the picks (black dots) used in the gridding calculation.

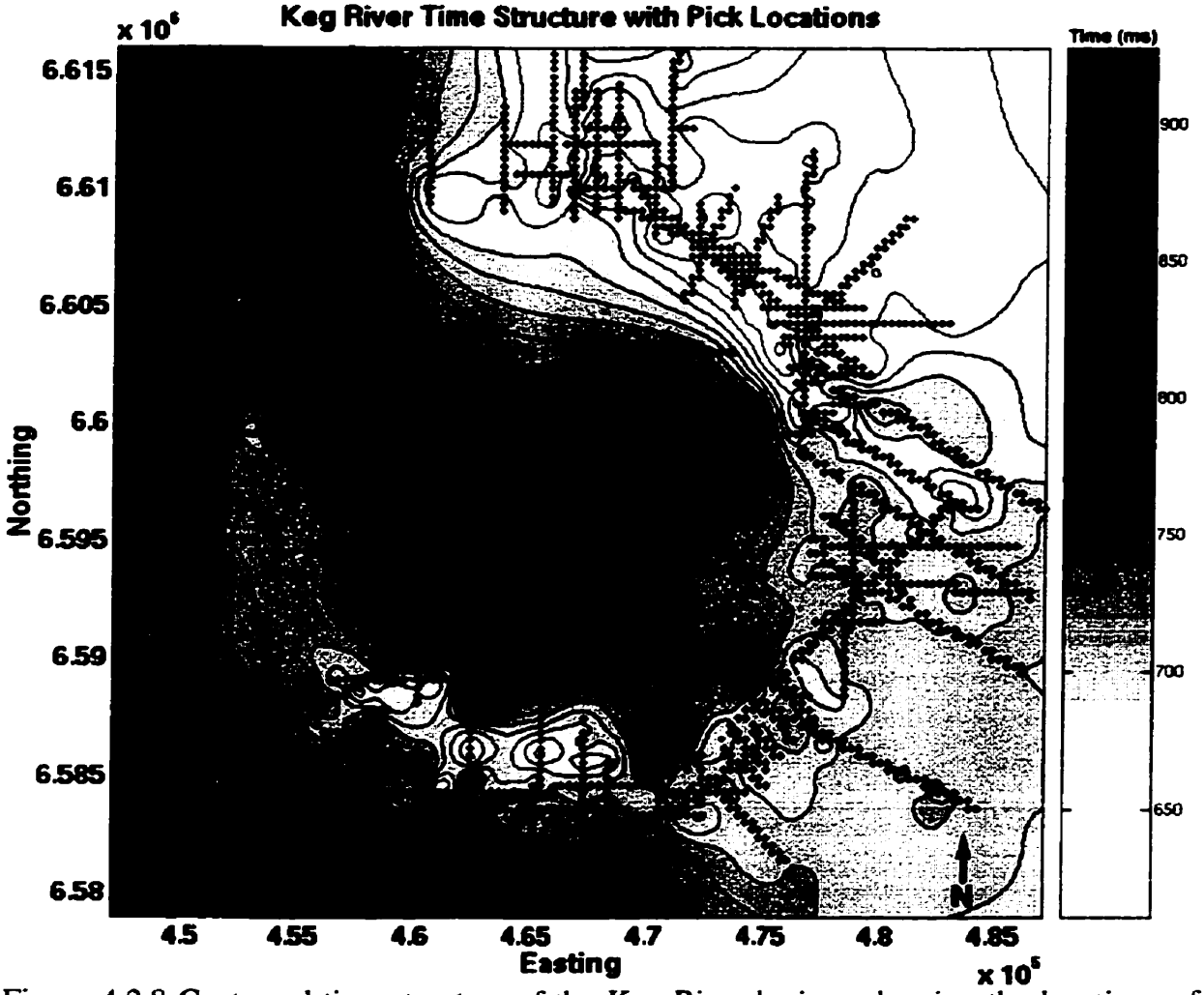

Figure 4.2.8 Contoured time structure of the Keg River horizon showing the locations of the picks (black dots) used in the gridding calculation.

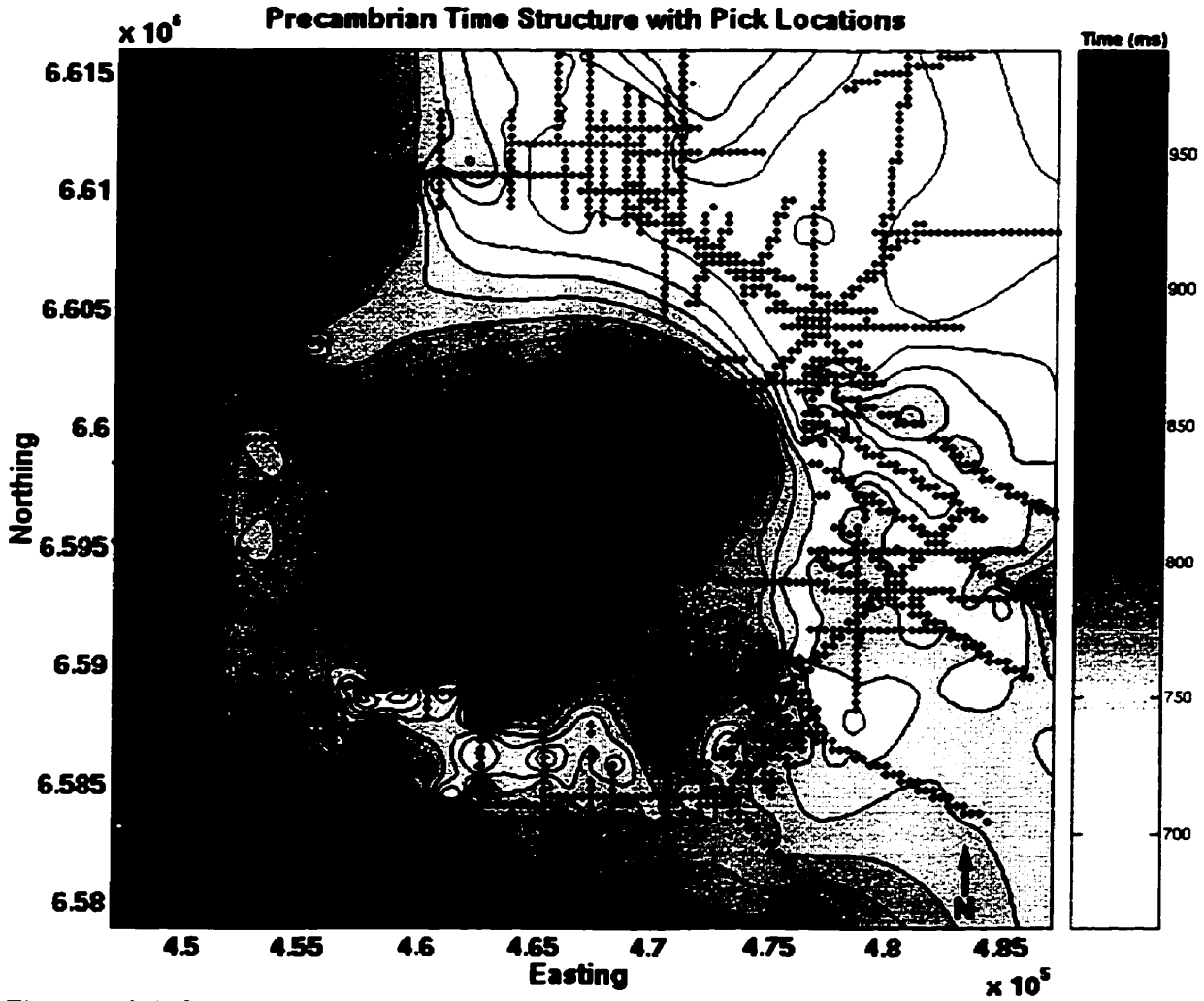

Figure 4.2.9 Contoured time structure of the Precambrian horizon showing the locations of the picks (black dots) used in the gridding calculation.

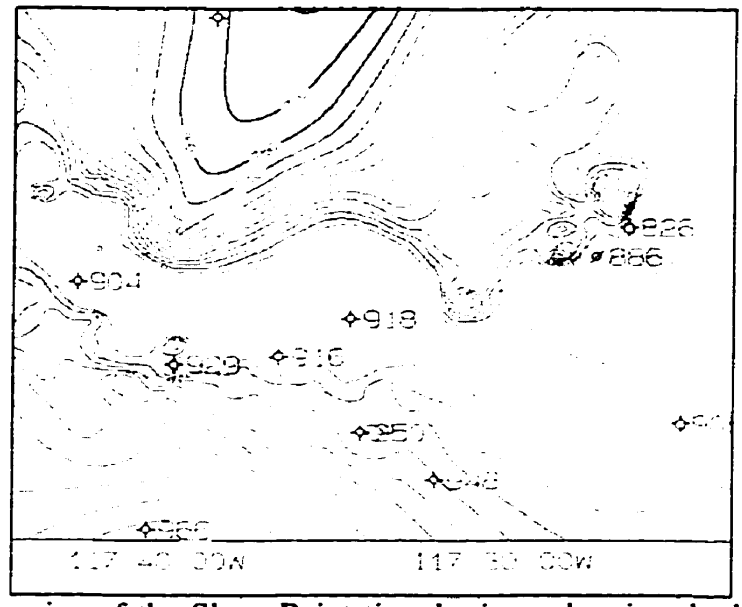

Figure 4.2.10 SE region of the Slave Point time horizon showing the location of several wells and their respective Slave Point tops below KB.

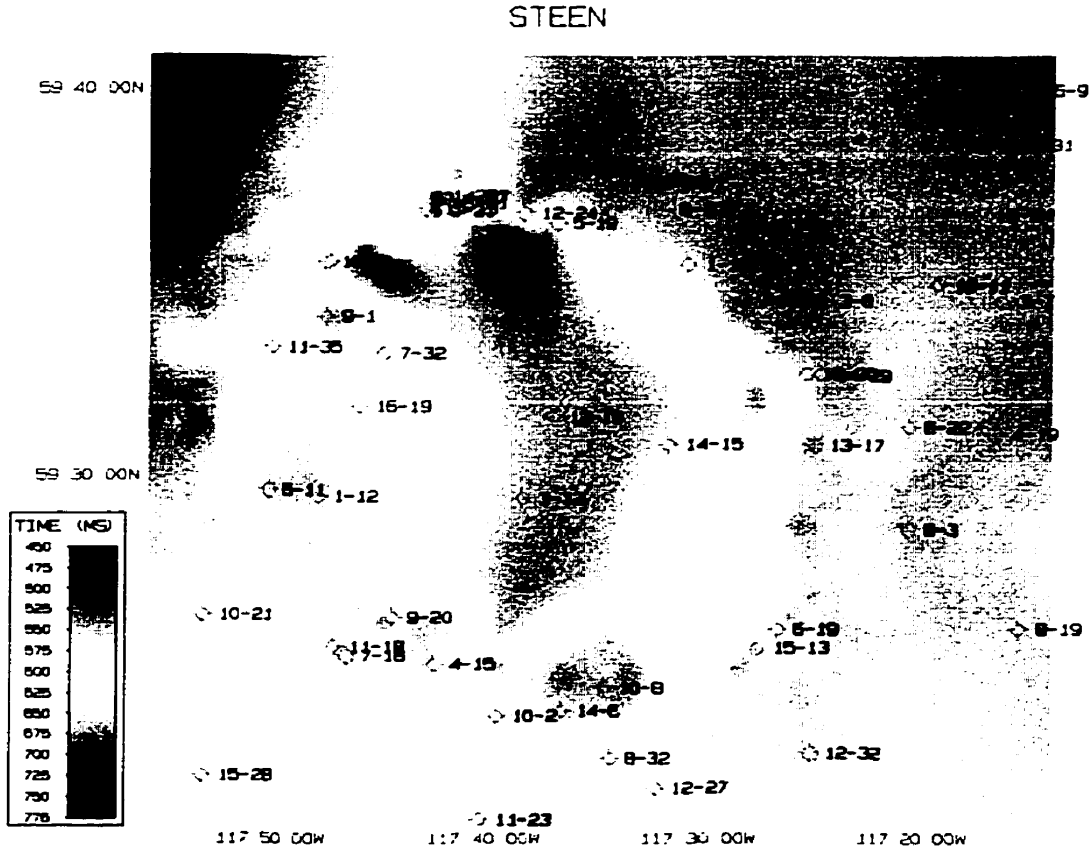

Figure 4.2.11 Pseudo-depth structure of the Slave Point horizon calculated using a single velocity.

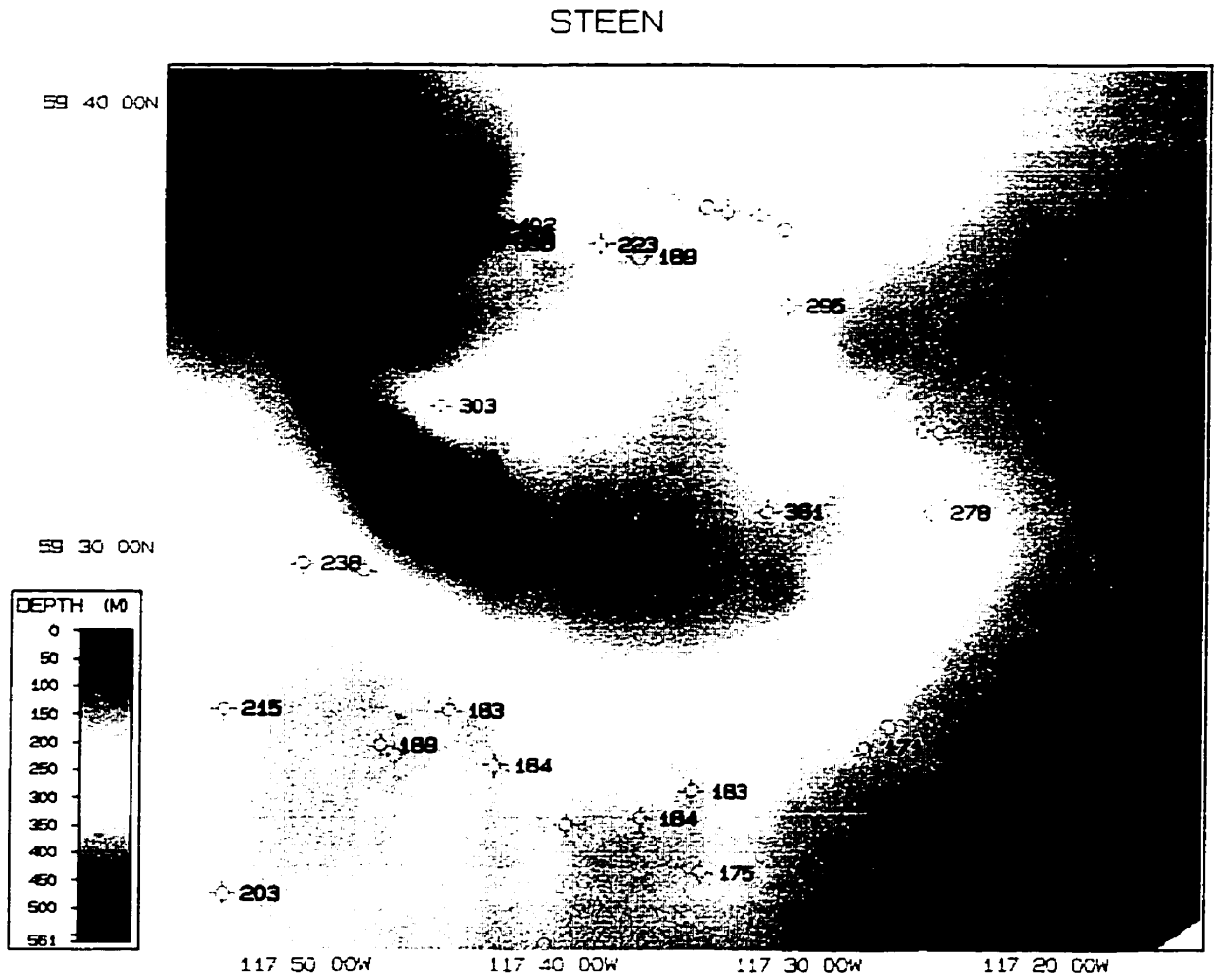

Figure 4.2.12 Cretaceous unconformity depth structure as computed using Petrosys. Depths are given below KB.

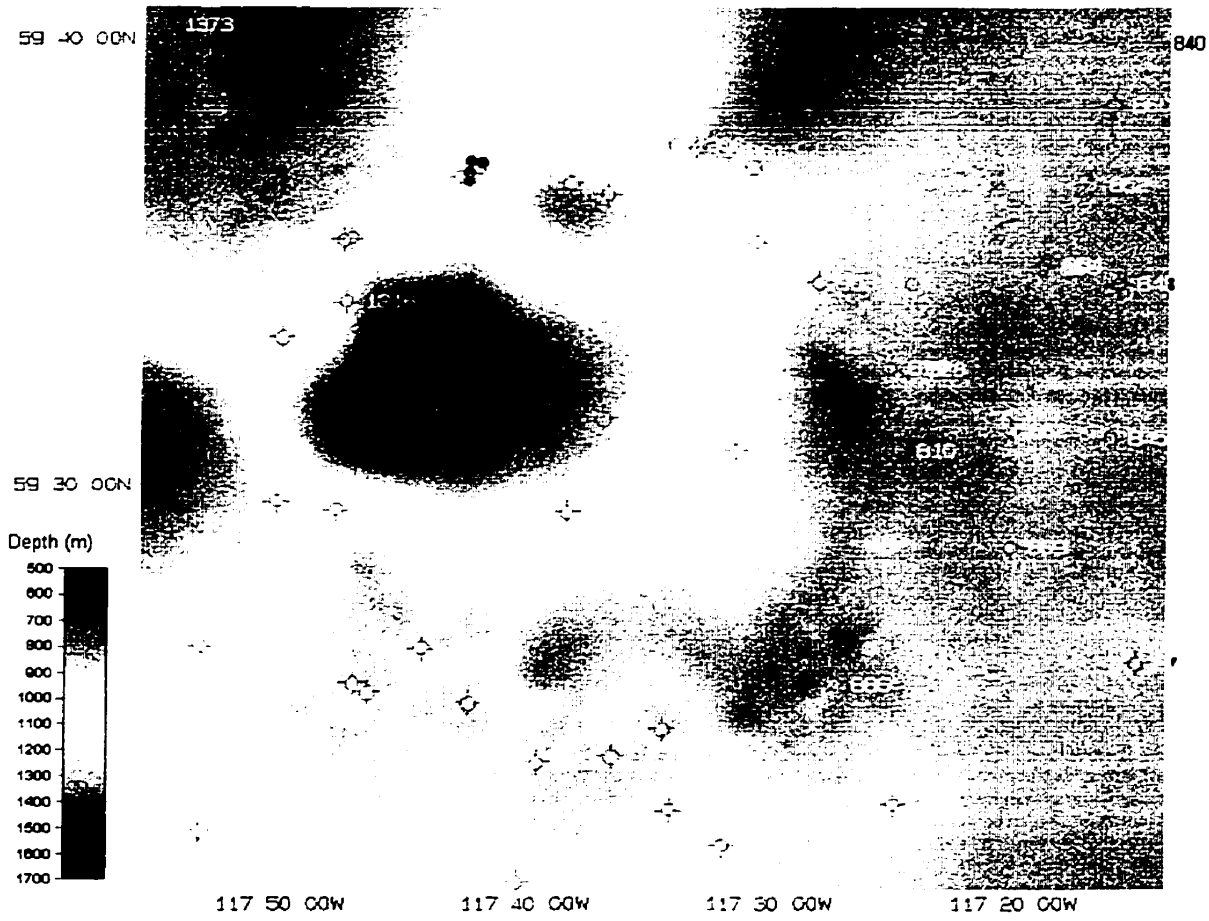

Figure 4.2.13 Slave Point depth structure as calculated using Petrosys. Depths are given below KB.

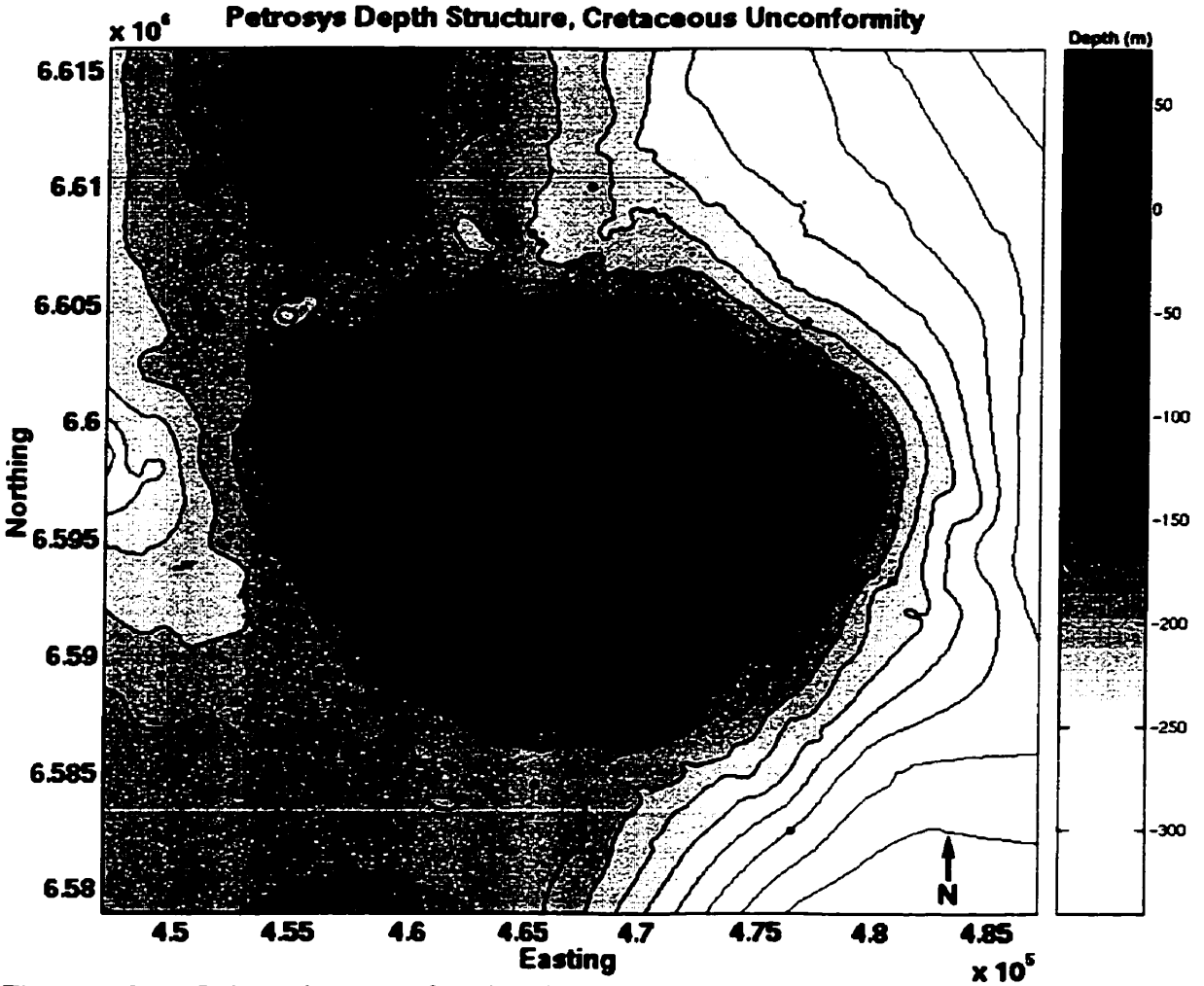

Figure 4.2.14 Paleozoic unconformity depth structure as calculated using Petrosys. All depths are referenced to sea level (light areas are structural highs).

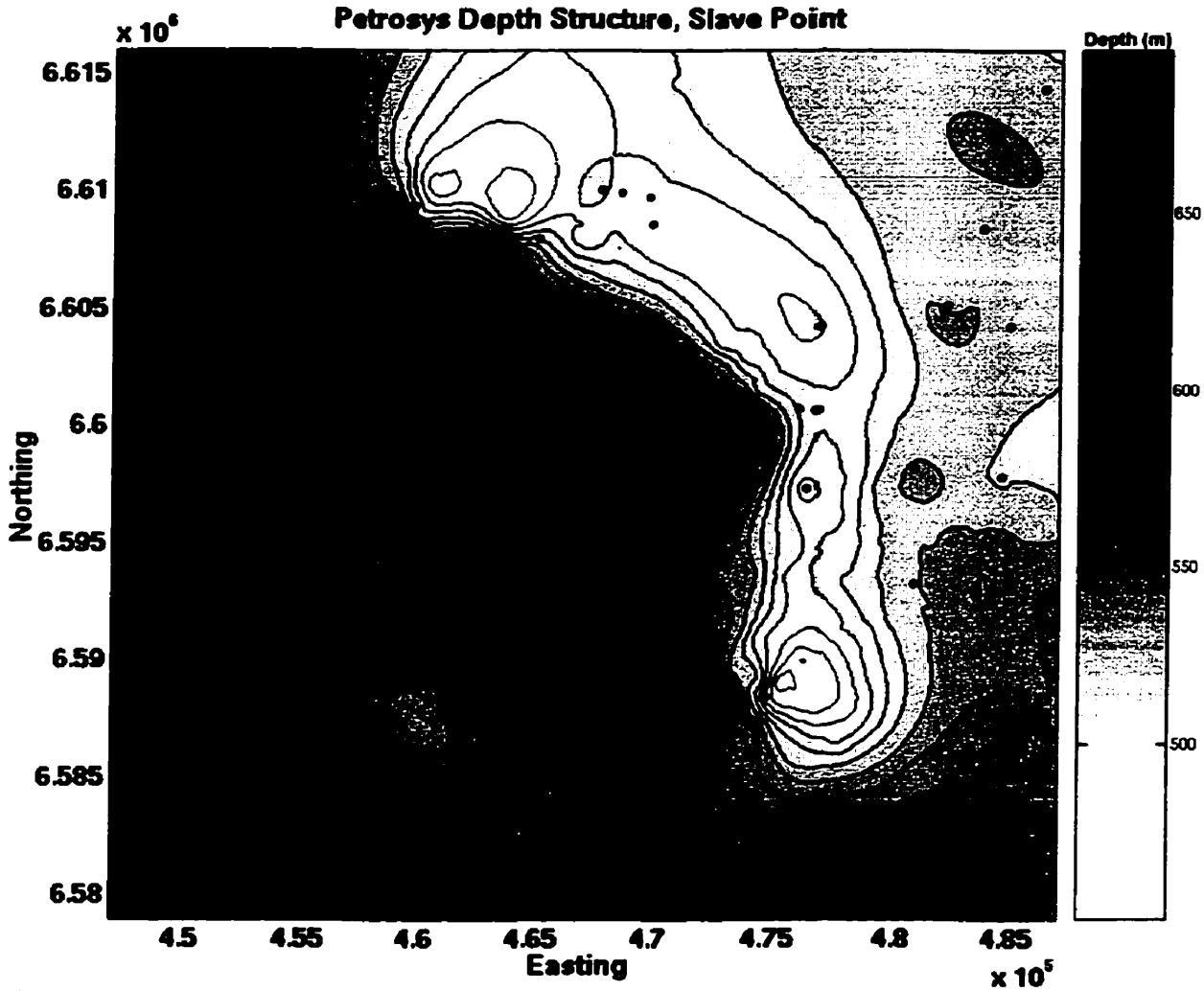

Figure 4.2.15 Slave Point depth structure as calculated using Petrosys. All depths are referenced to sea level (light areas are structural highs).

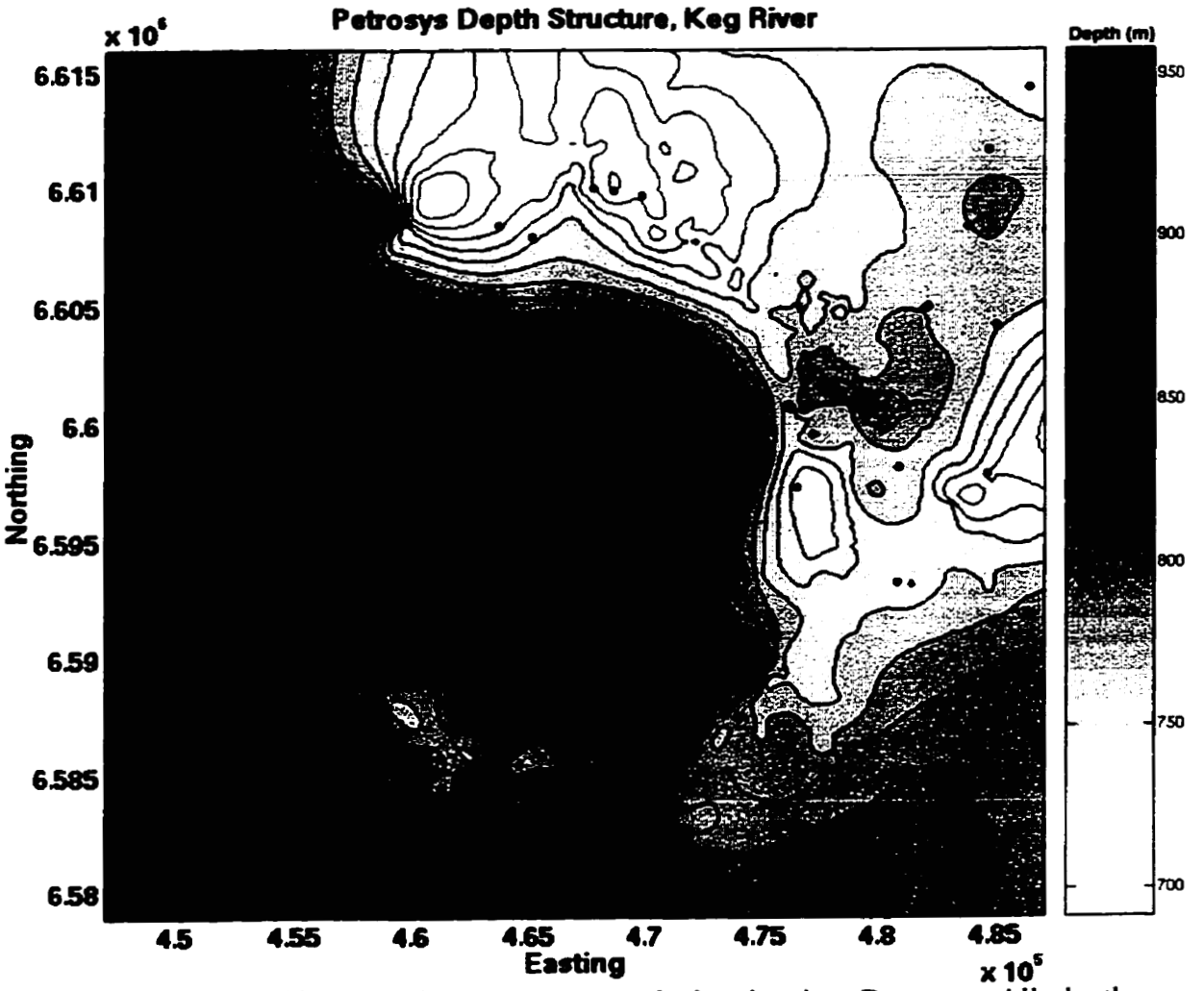

Figure 4.2.16 Keg River depth structure as calculated using Petrosys. All depths are referenced to sea level (light areas are structural highs).

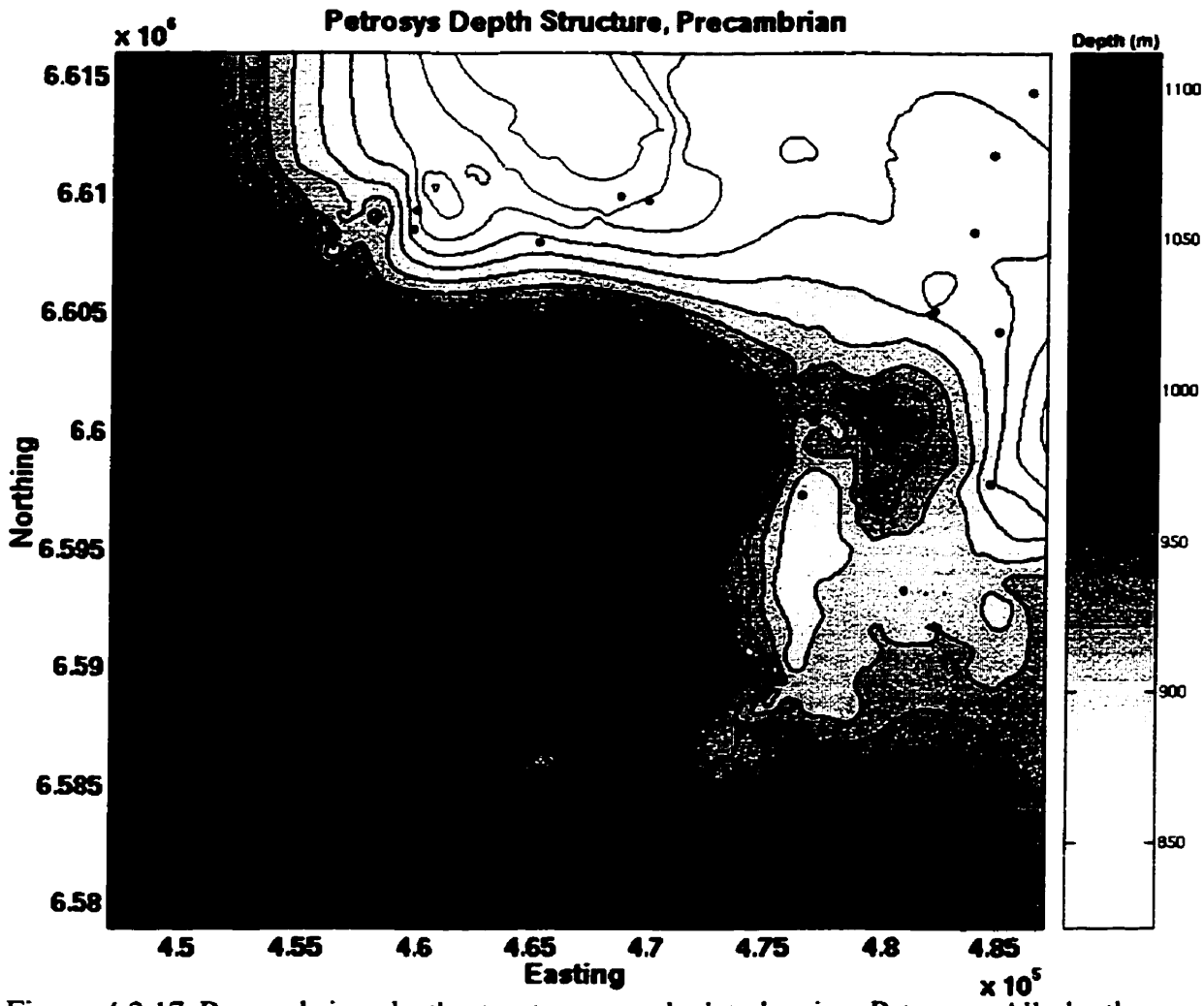

Figure 4.2.17 Precambrian depth structure as calculated using Petrosys. All depths are referenced to sea level (light areas are structural highs).

Figure 4.2.18 The input seismic data for the Slave Point horizon is plotted with well locations (black squares) using Geostat. Notice the circular appearance of the seismic structure.

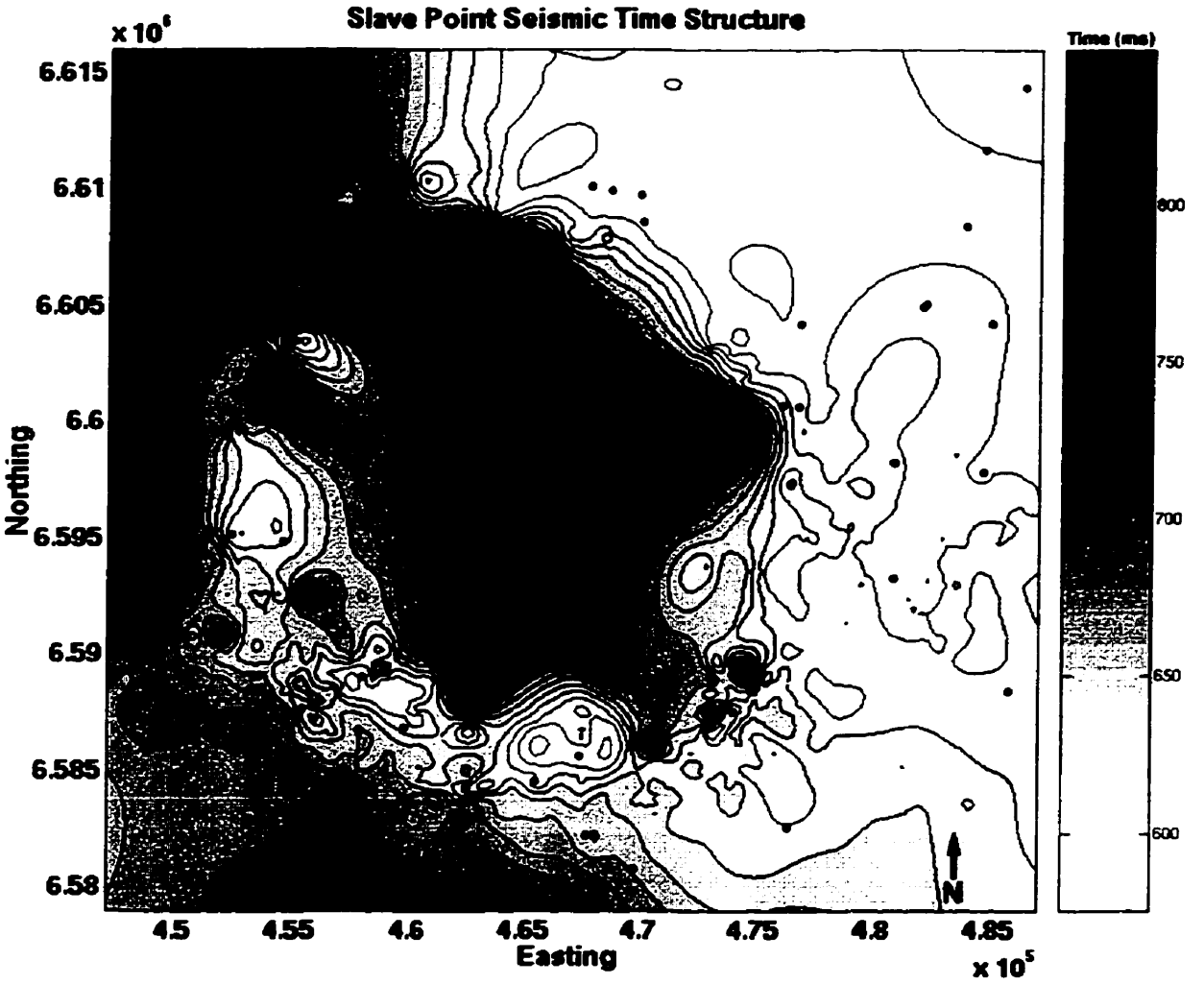

Figure 4.2.19 Slave Point time structure plotted using Matlab. Well locations are indicated by circles.

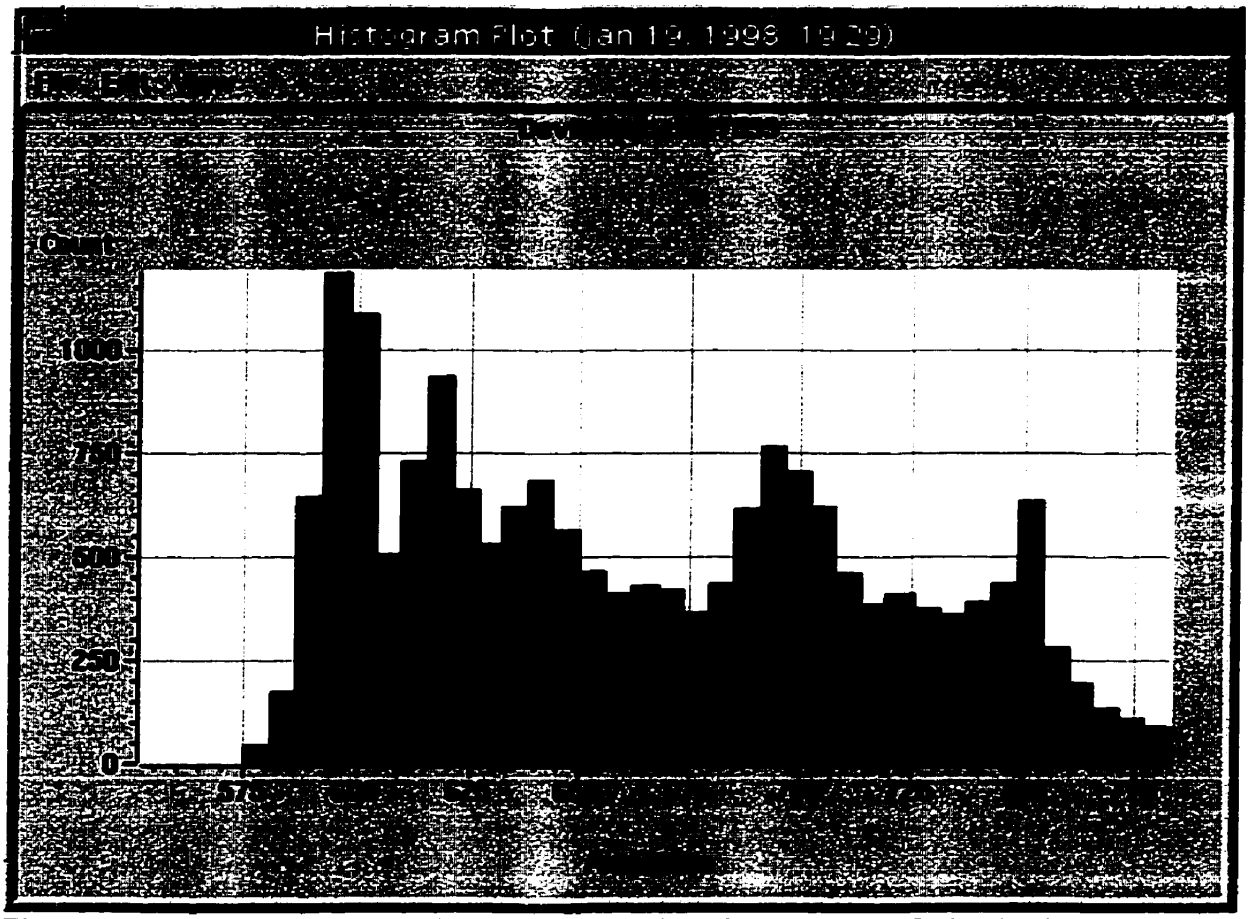

Figure 4.2.20 The histogram of input seismic data for the Slave Point horizon shows at least three distinct groups about which the travel times are scattered. The 600 ms group corresponds to highs located around the rim, the 700 ms group corresponds to the regional values, and the 750 ms group corresponds to the central low region.

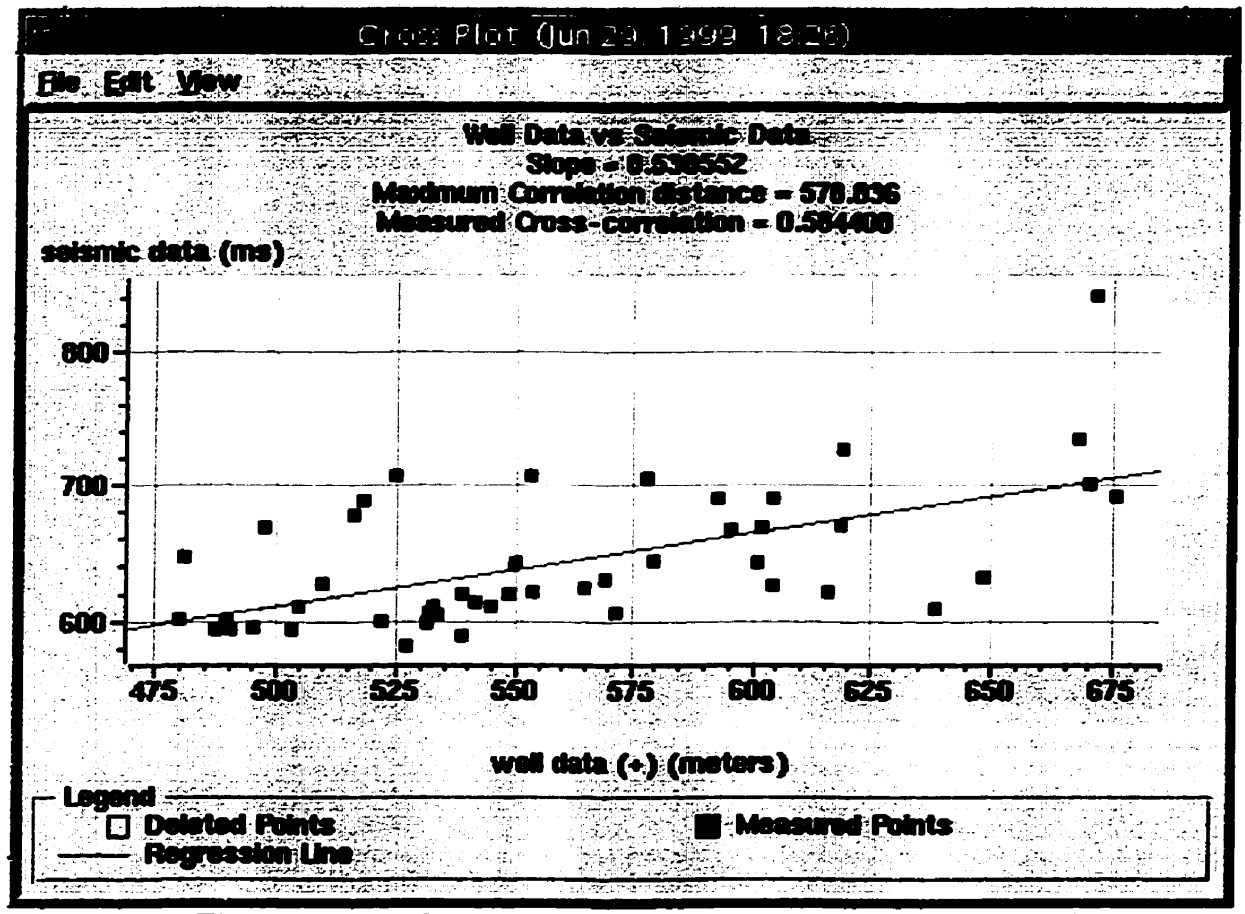

Figure 4.2.21 The cross-plot of the dense seismic data vs the sparse well data for the Slave Point horizon can be described by a linear regression line. The slope of this line corresponds to an average velocity function of 5386 m/s that can be used to perform a brute time-to-depth conversion.

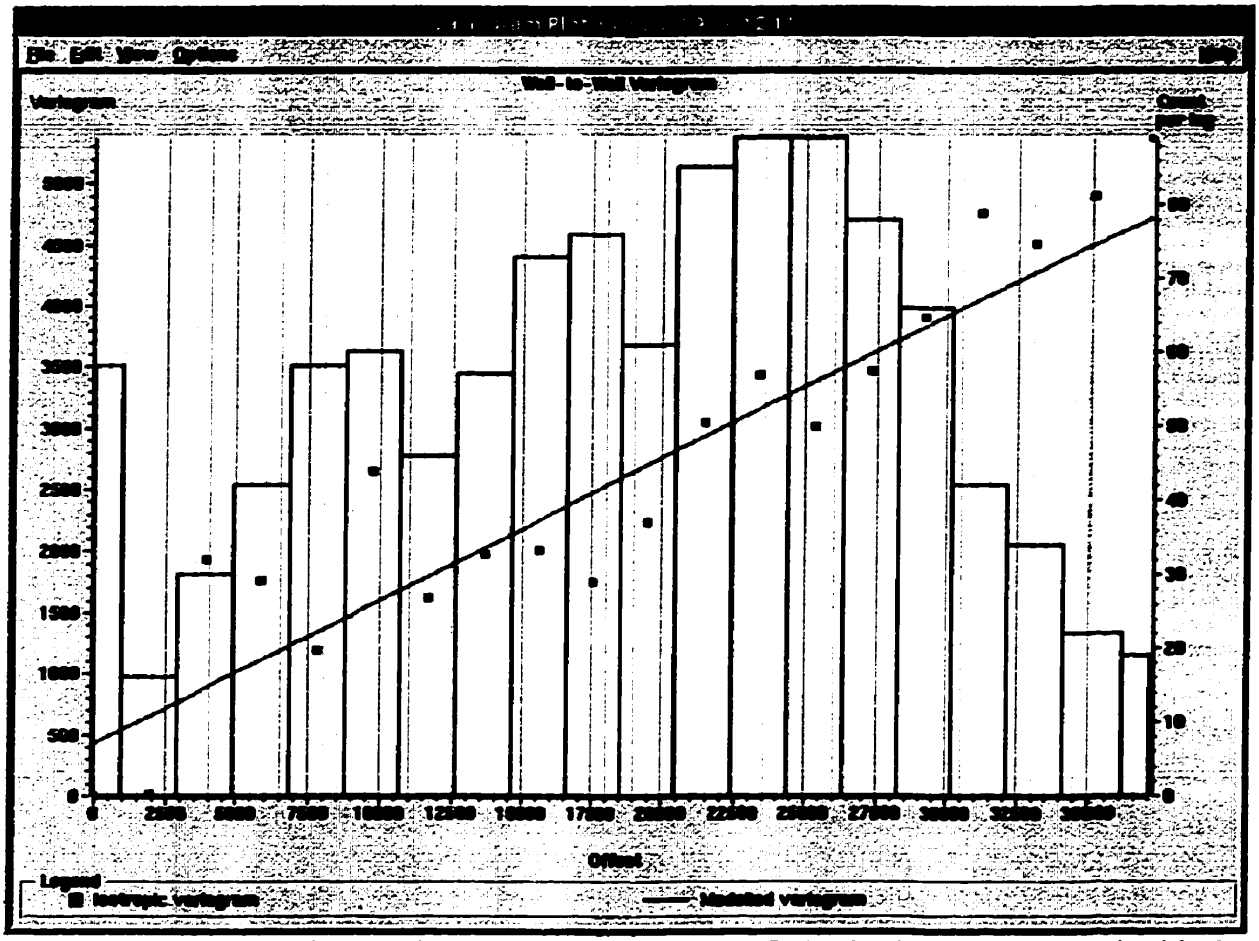

Figure 4.2.22 The well-to-well variogram for the Slave Point horizon is modelled with the variogram shown as a solid line. Shown behind the curve is a histogram representing the number wells used to calculate the variogram at each of the 20 offsets.

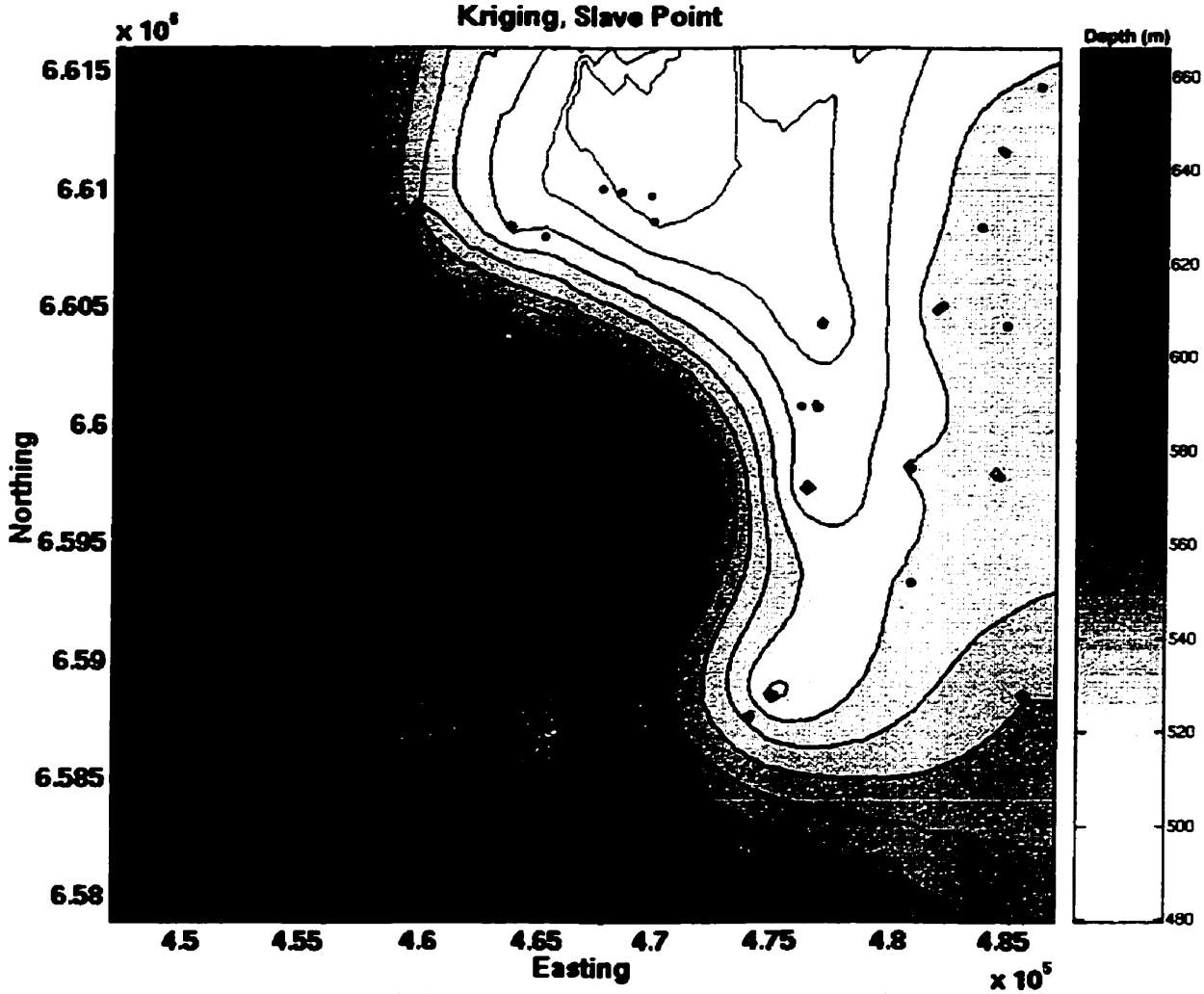

Figure 4.2.23 The kriged well data of the Slave Point horizon begins to show the shape of the structure. Since kriging depends only on the sparse well information, the resultant map is quite smooth. Well depths are given as values below sea level (light areas represent structural highs). Well locations are shown as black dots.

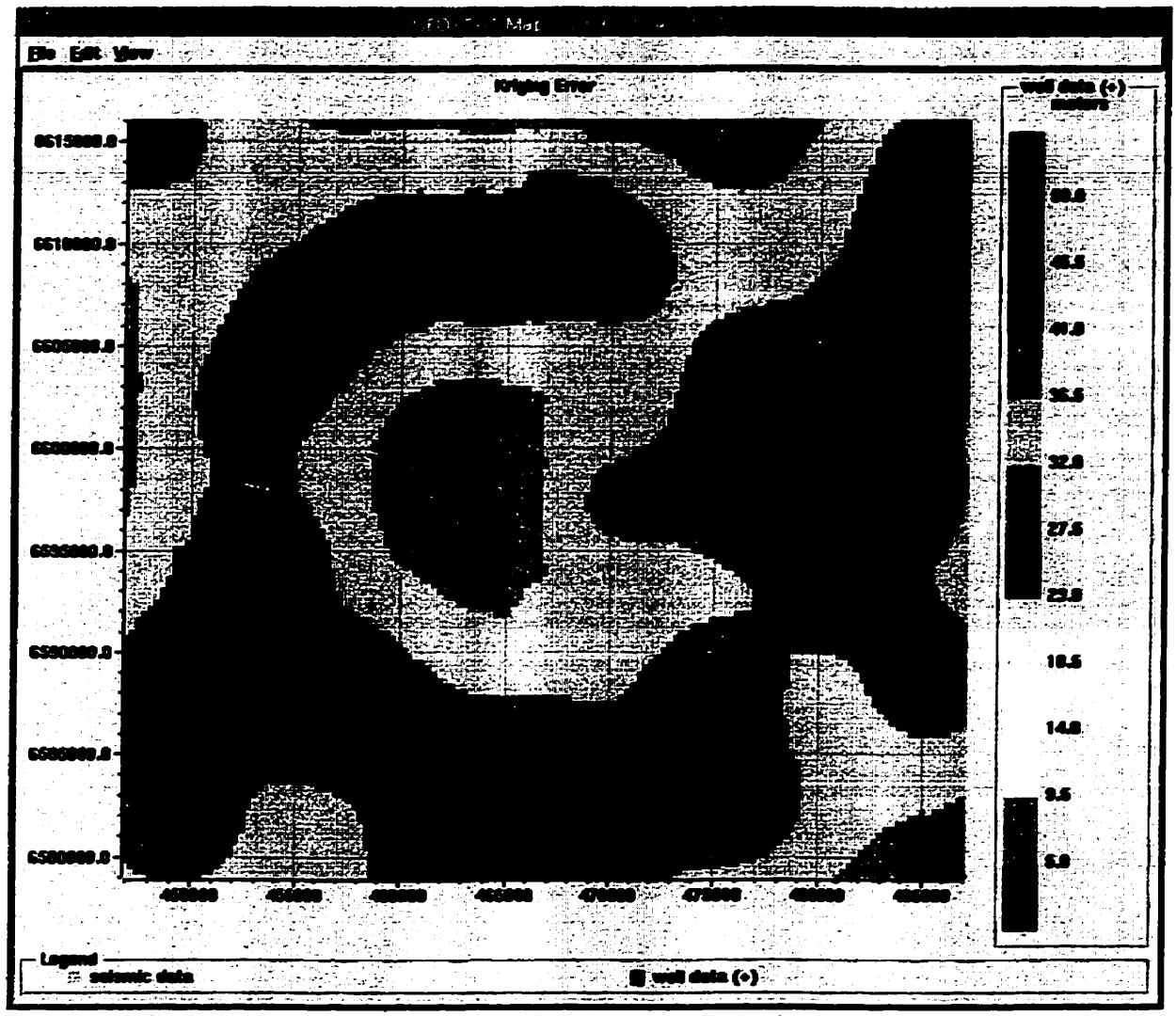

Figure 4.2.24 Kriging error as calculated for the Slave Point horizon. Errors are small close to the wells and increase away from the wells to a maximum of about ±40 m. Within the area of interest, the expected errors are quite reasonable at about ±30 m.

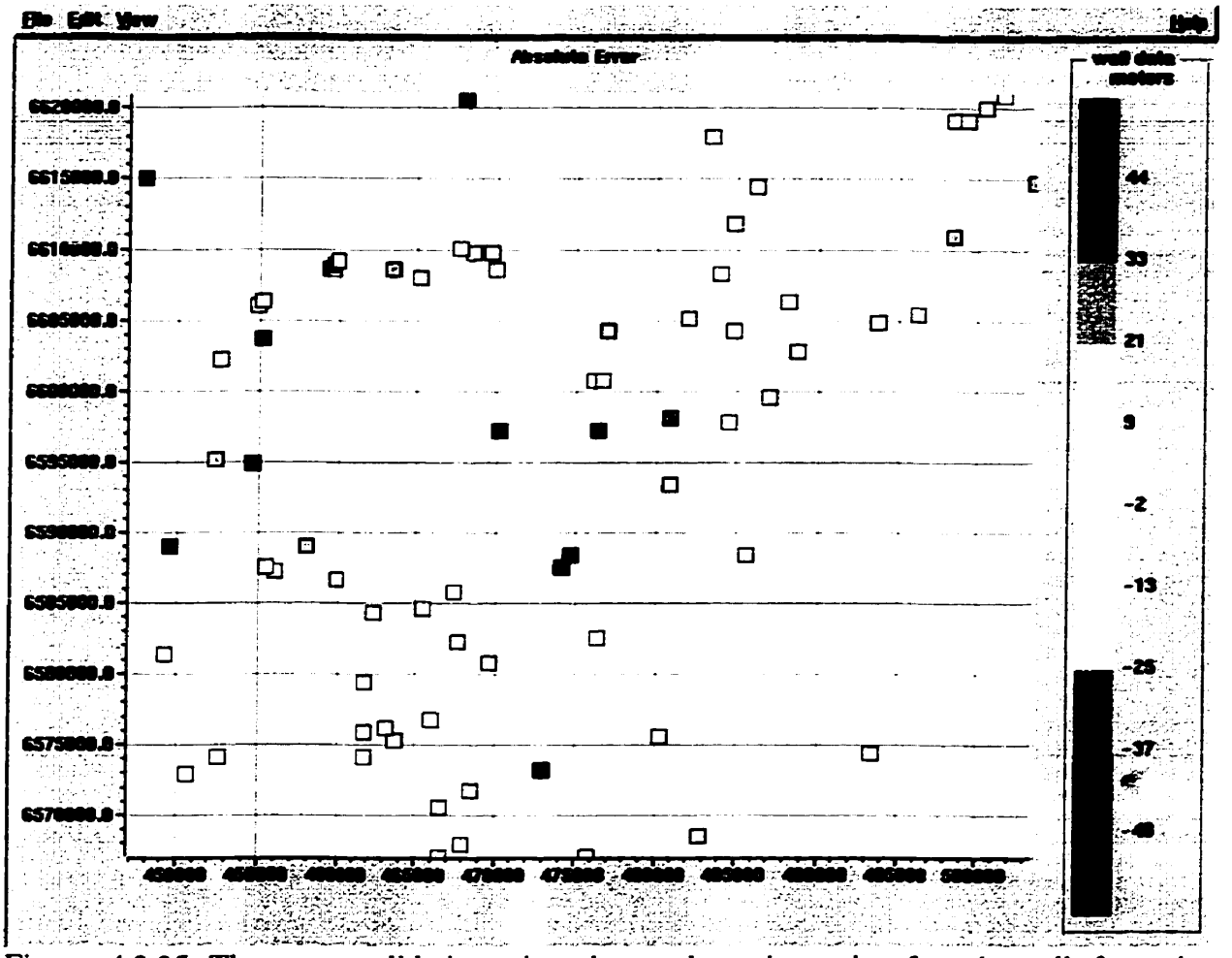

Figure 4.2.25 The cross-validation plot shows the mismatch of each well from its prediction (where the well is not used).

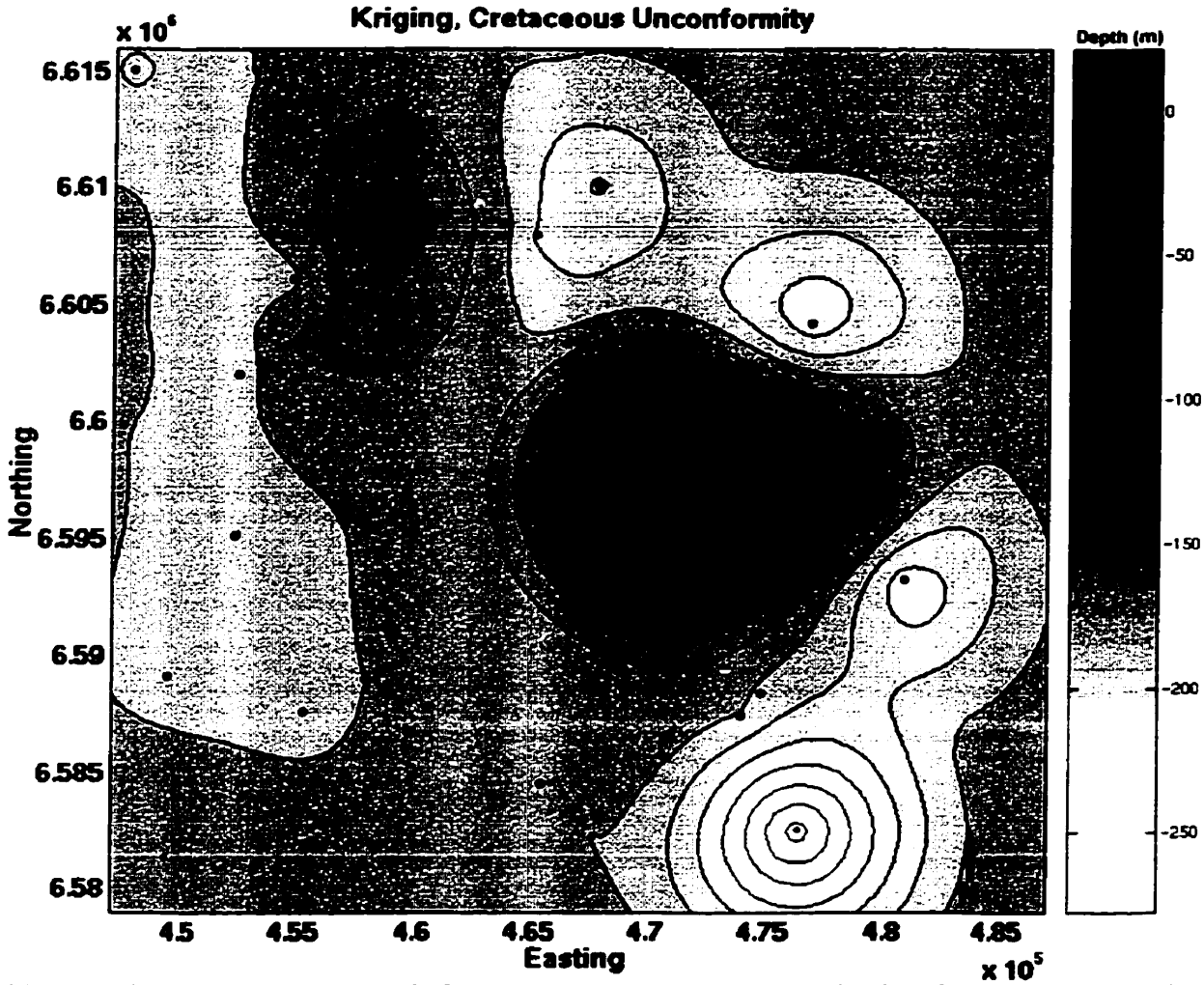

Figure 4.2.26 The kriging result for the Cretaceous unconformity is relatively flat showing some evidence of structure related to the rim. The central region appears as a significant low in an area with uncertain well picks. Well depths are given as values below sea level (light areas represent structural highs). Well locations are shown as black dots.

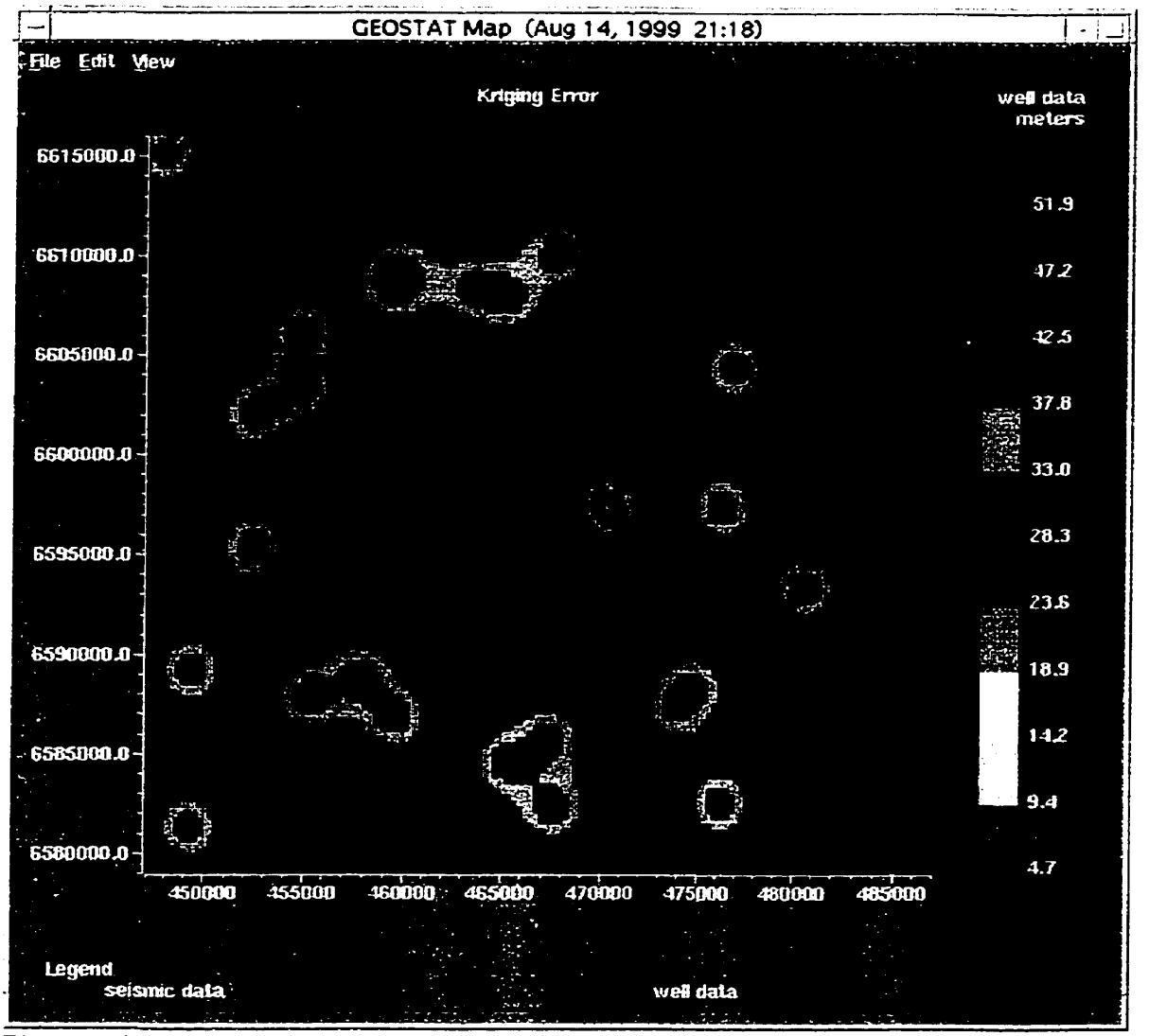

Figure 4.2.27 The expected error in the kriging result for the Cretaceous unconformity is as high as ±55 m. Within the area of interest (rim region) the error is only slightly smaller until very near to the well locations.

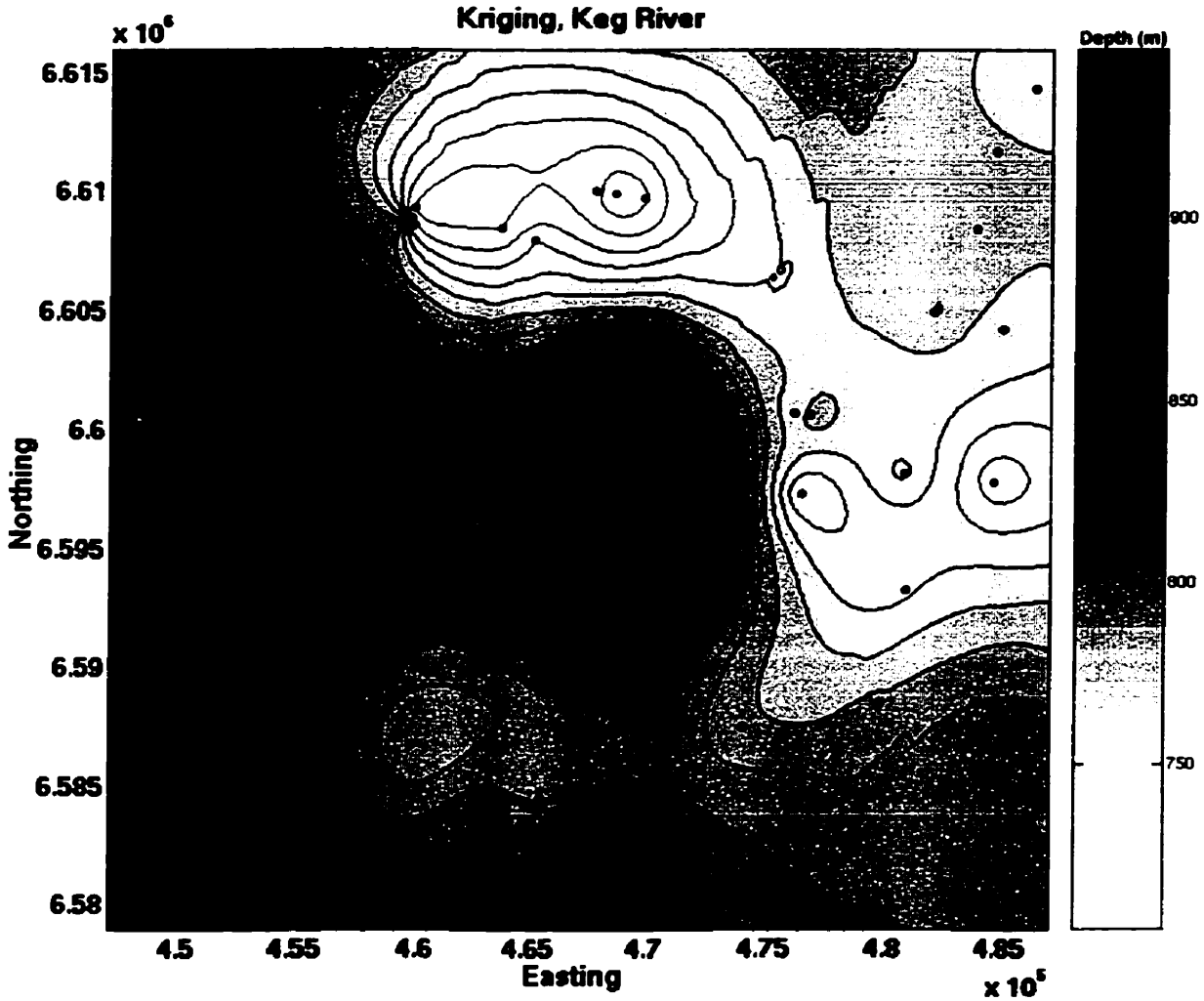

Figure 4.2.28 The Kriging result for the Keg River horizon is similar in many respects to the Slave Point kriging result shown in Figure 4.2.23. Overall, the structure is smooth showing evidence of rim structure. Well depths are given as values below sea level (light areas represent structural highs). Well locations are shown as black dots.

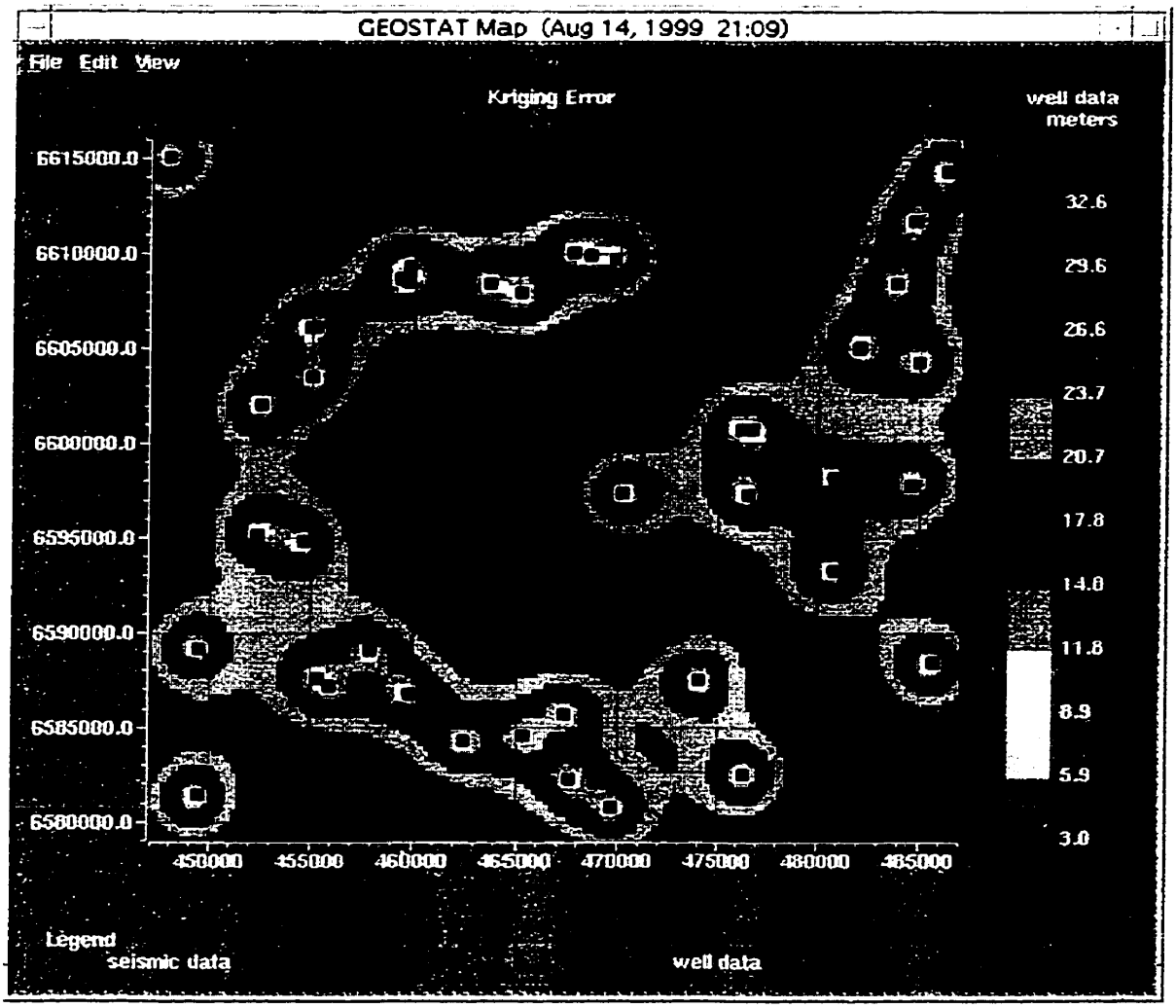

Figure 4.2.29 The expected error for the Keg River kriging result is good with values of ±10 m to ±30 m within the area of interest.

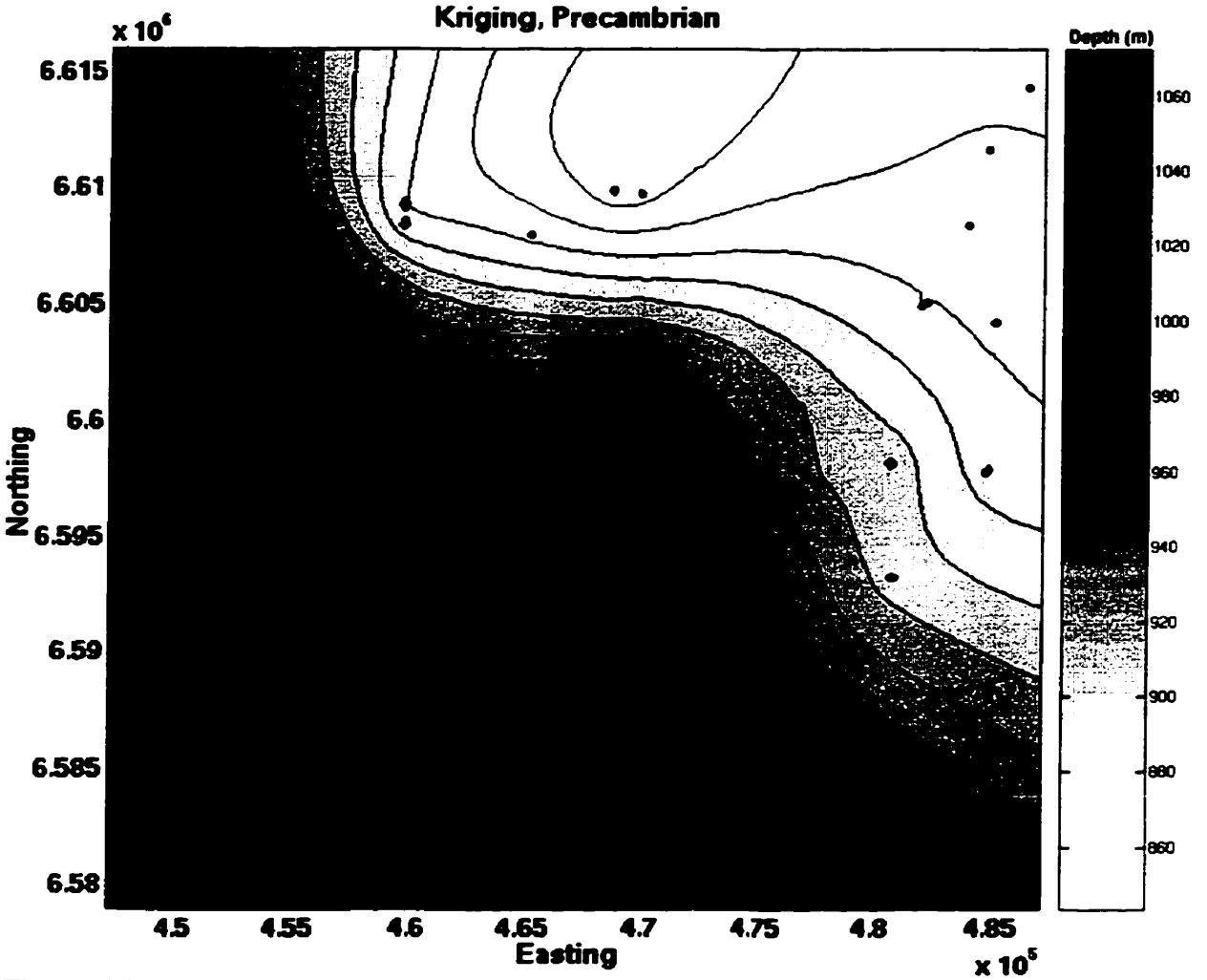

Figure 4.2.30 The Precambrian kriging result shows less structure than Figure 4.2.23 due, in part, to the fewer number of wells used in the calculation. The structure is smooth with the major trend being the dip to the SW. Well depths are given as values below sea level (light areas represent structural highs). Well locations are shown as black dots.

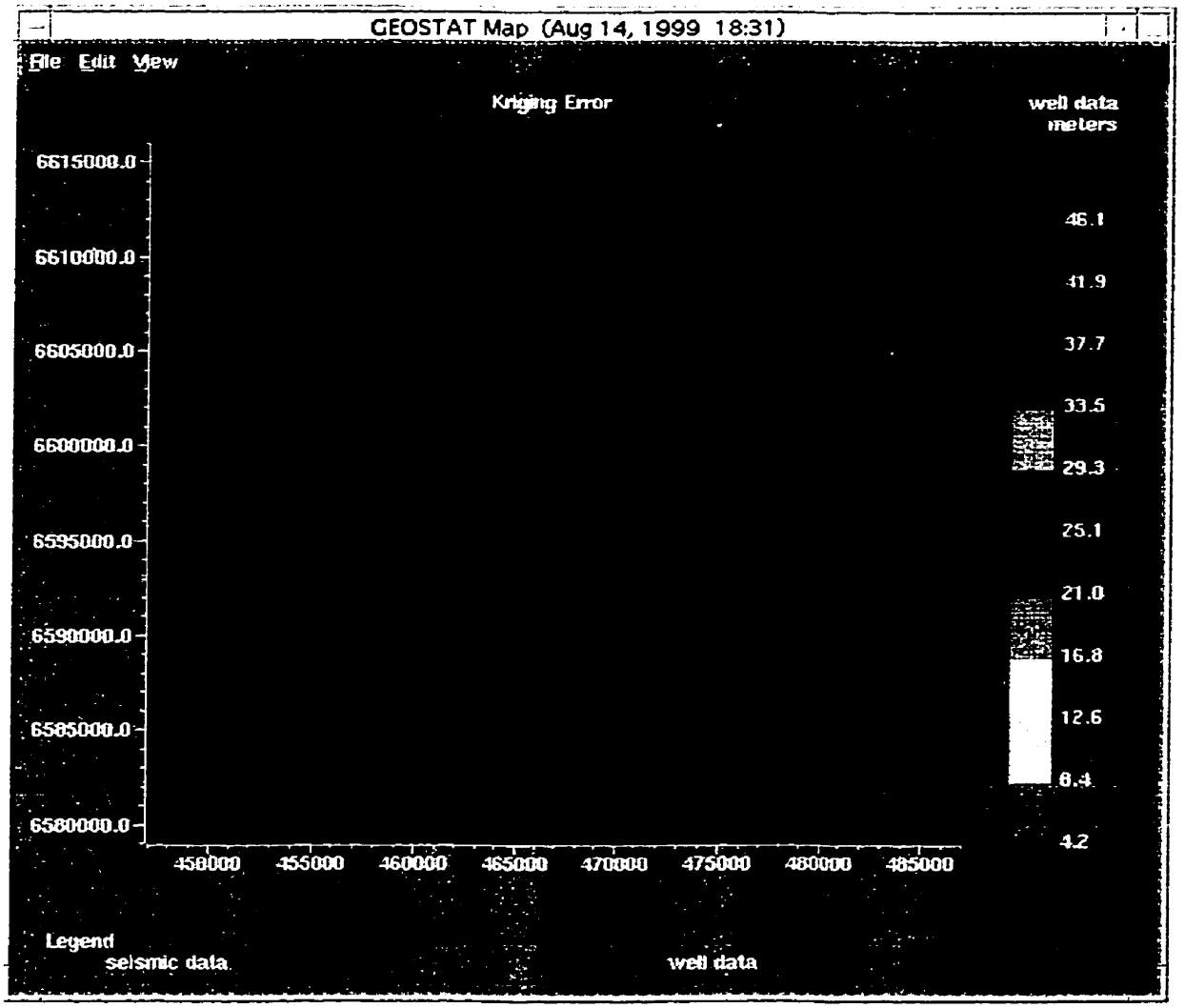

Figure 4.2.31 The expected error for the Precambrian result is high with values between about ±35 m and ±45 throughout most of the area.

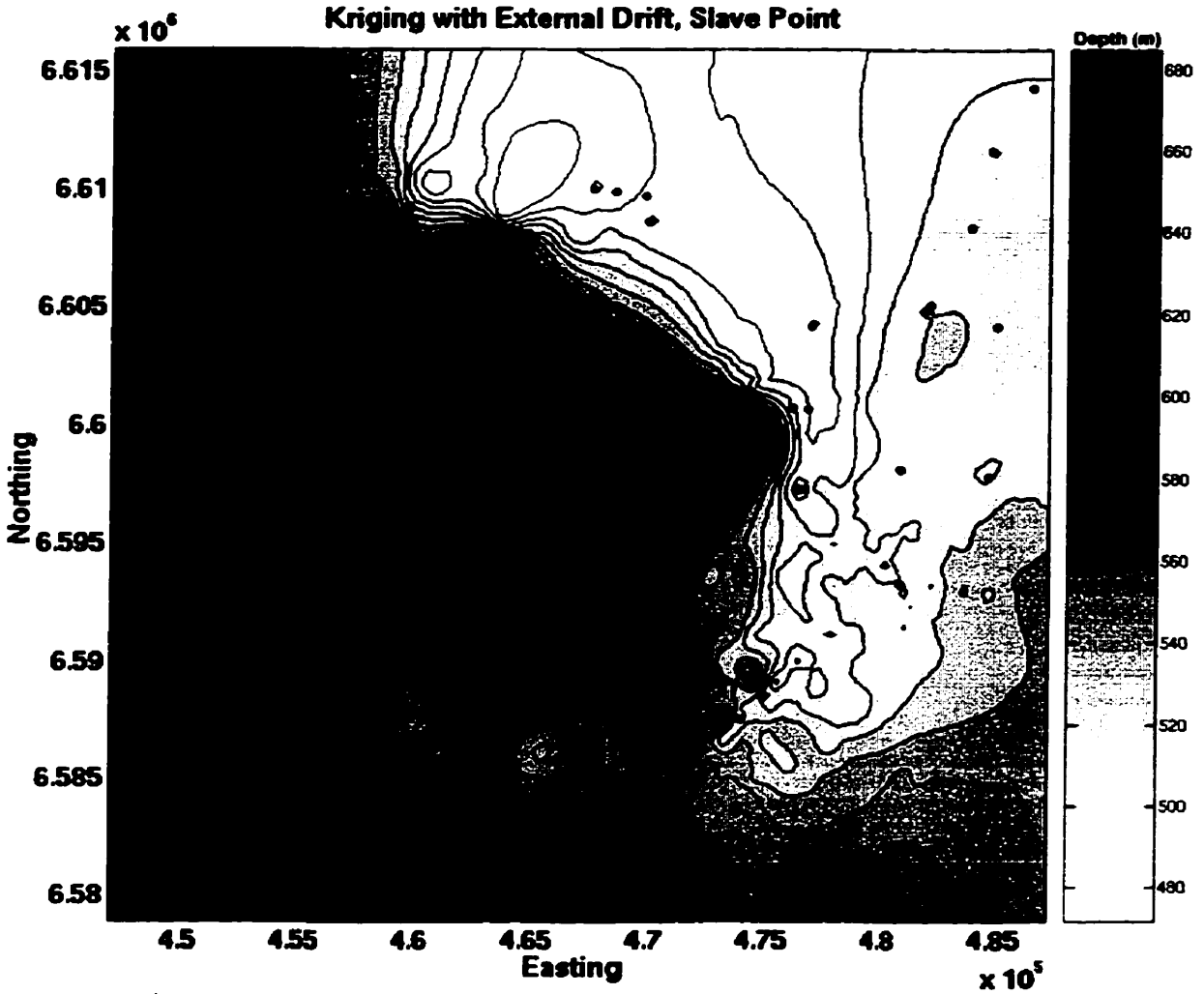

Figure 4.2.32 Using the geostatistical technique of kriging with external drift, a noticeably different depth structure is produced. This technique incorporates the trend from the seismic data to help define the structural highs associated with this dataset. Well depths are given as values below sea level (light areas represent structural highs). Well locations are shown as black dots.

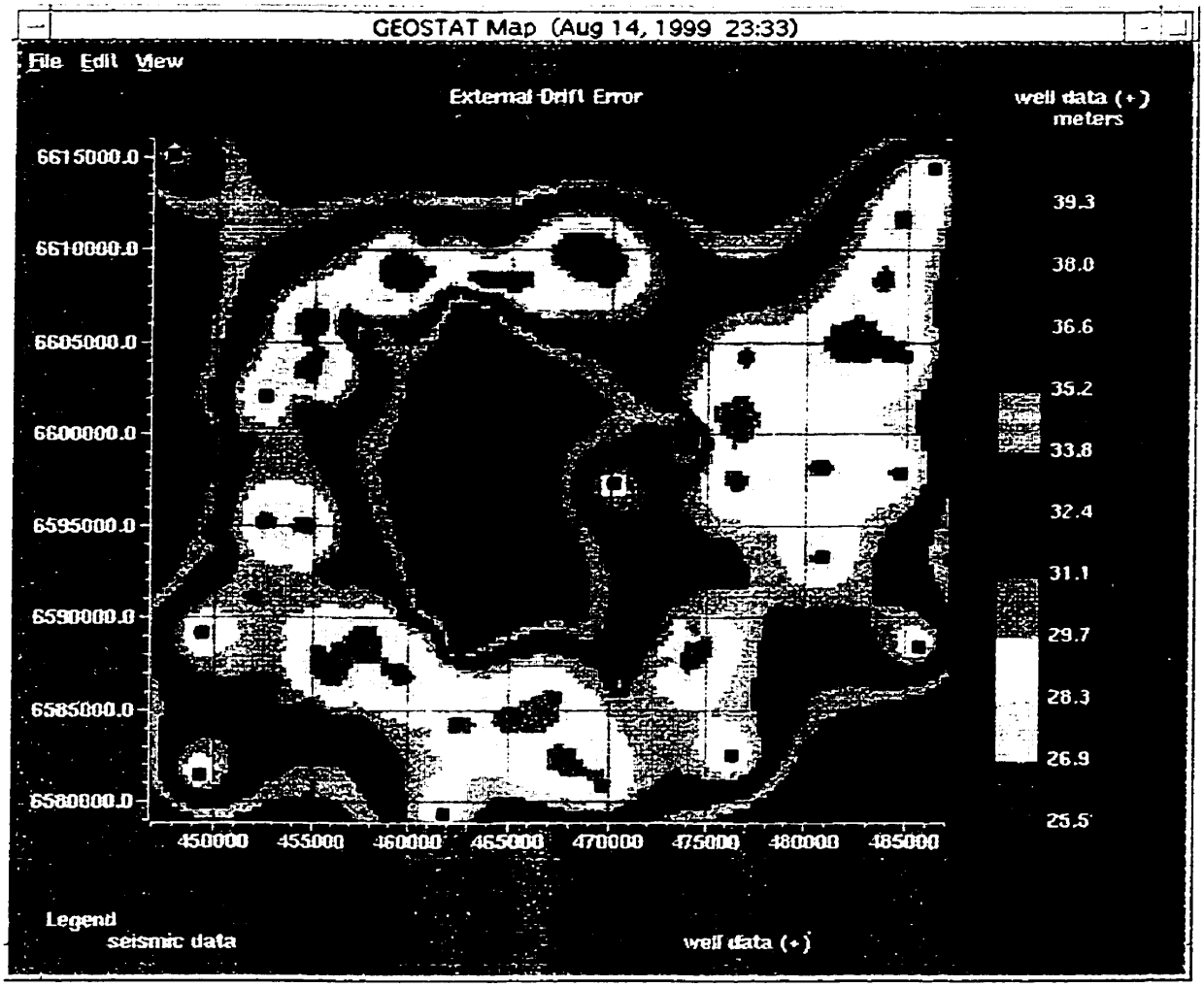

Figure 4.2.33 The kriging with external drift error ranges from a few meters close to the well to more than 40 m at the limits of the dataset. Within the area of interest, errors are generally less than about ±35 m. Corrected for anisotropic effects using an anisotropy factor of 0.8 at a principal angle of 160°.

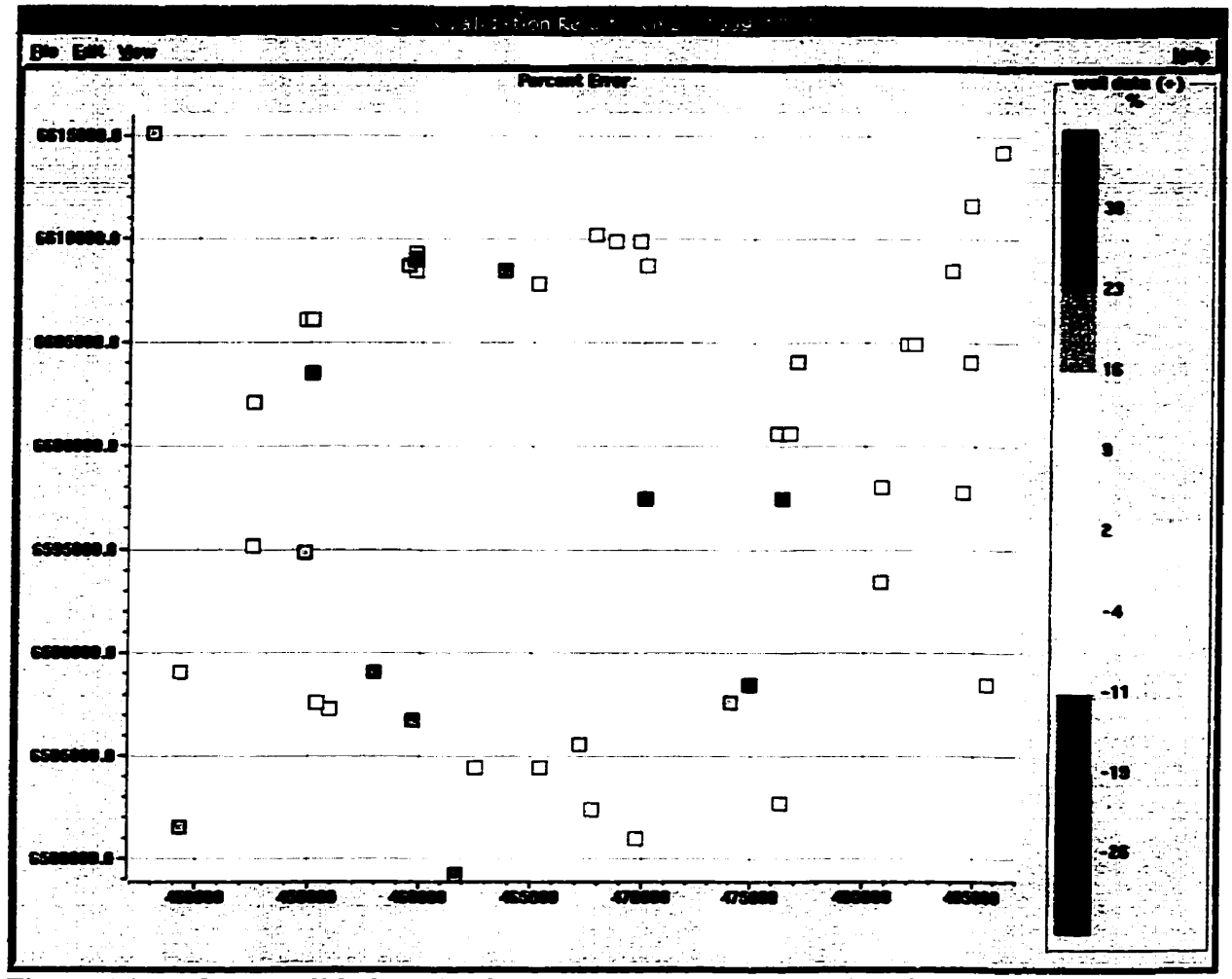

Figure 4.2.34 Cross-validation plot for the kriging with external drift calculation shows the effect of removing one well at time from the calculation. Notice that the error be as much as ±30% at some well locations but is generally less than about ±10%.

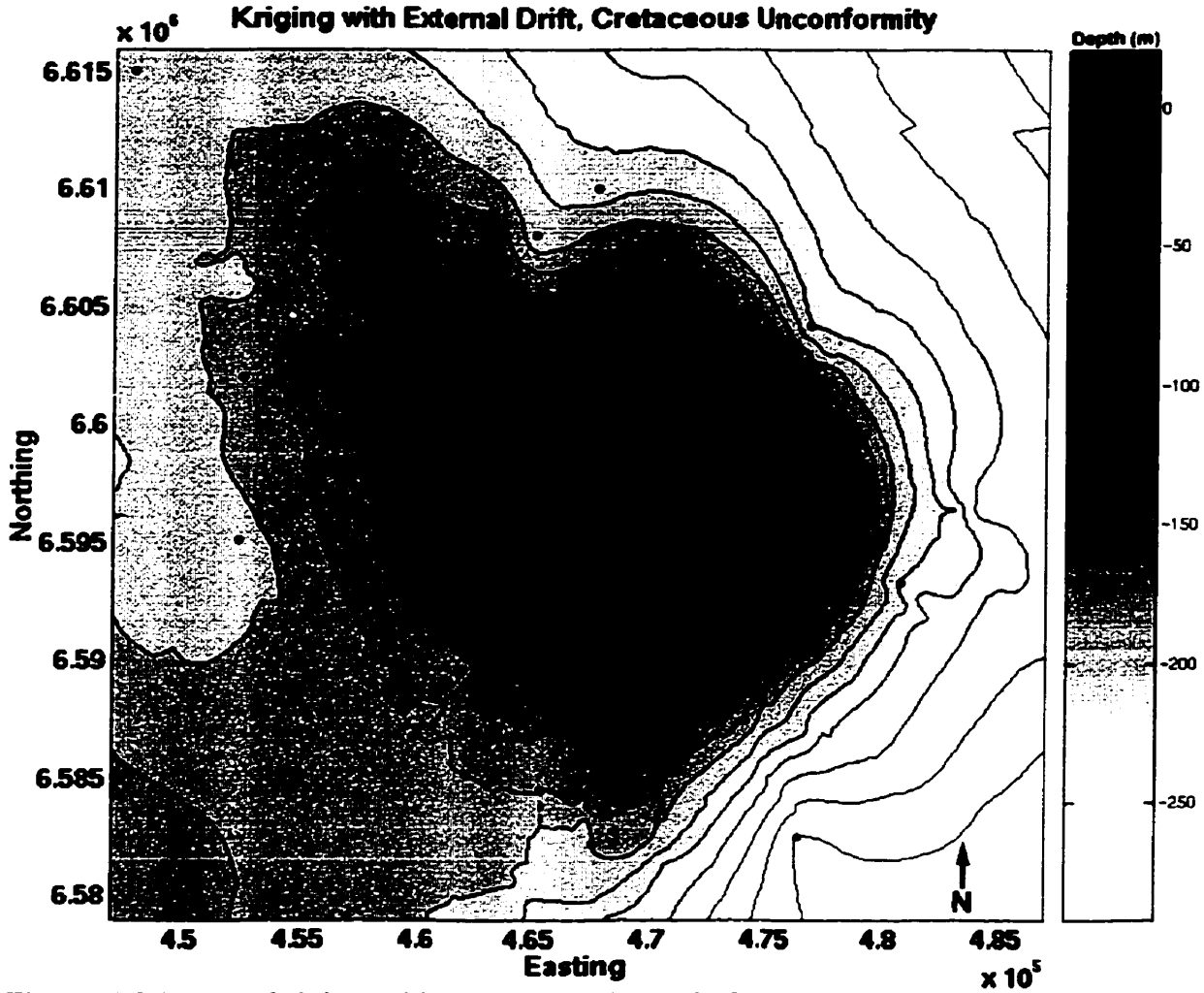

Figure 4.2.35 The kriging with external drift result for the Cretaceous unconformity is observed to be quite smooth with a central low region. Well depths are given as values below sea level (light areas represent structural highs). Well locations are shown as black dots.

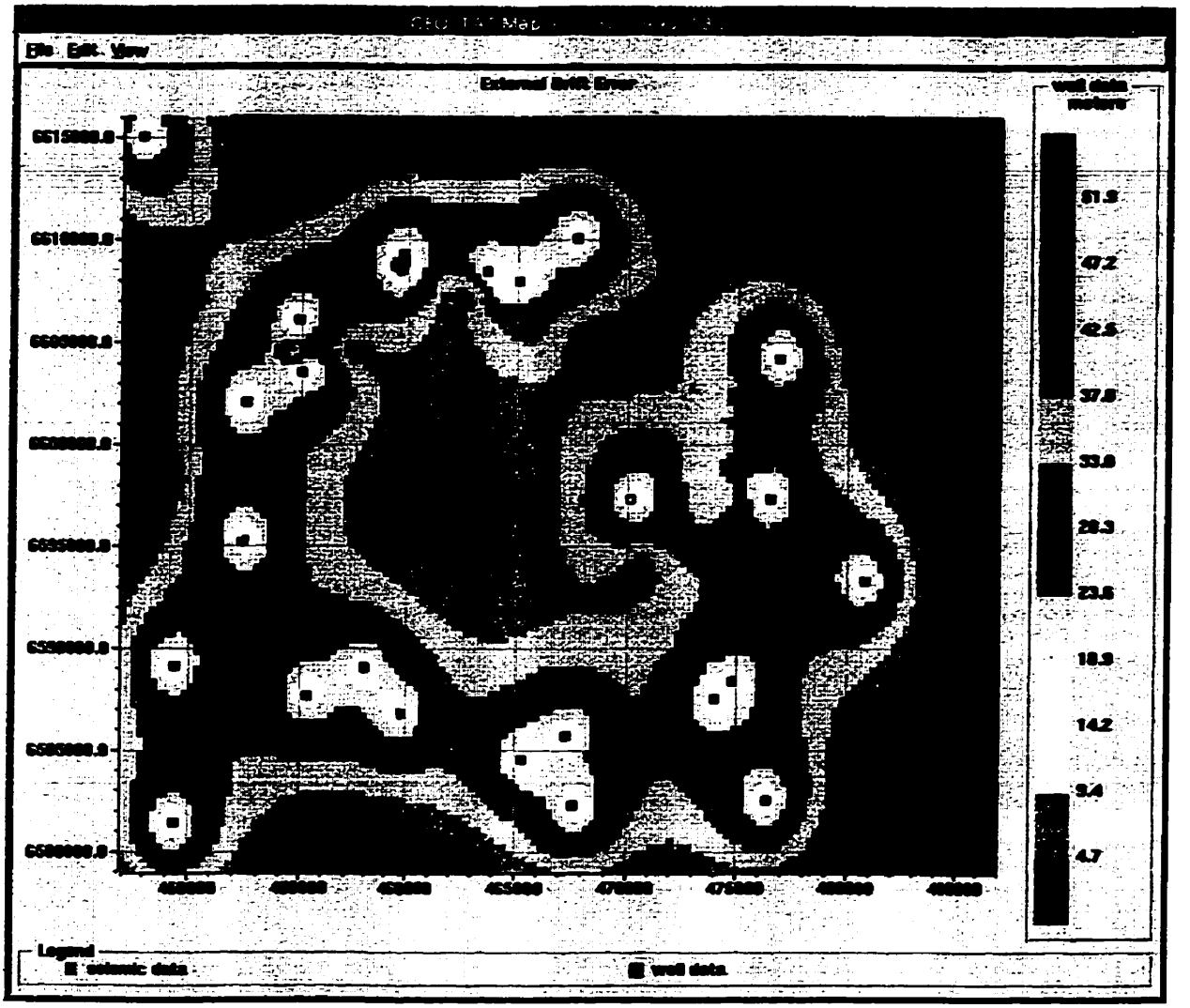

Figure 4.2.36 The kriging with external drift error is generally less than about ±40 m throughout most of the region of interest.

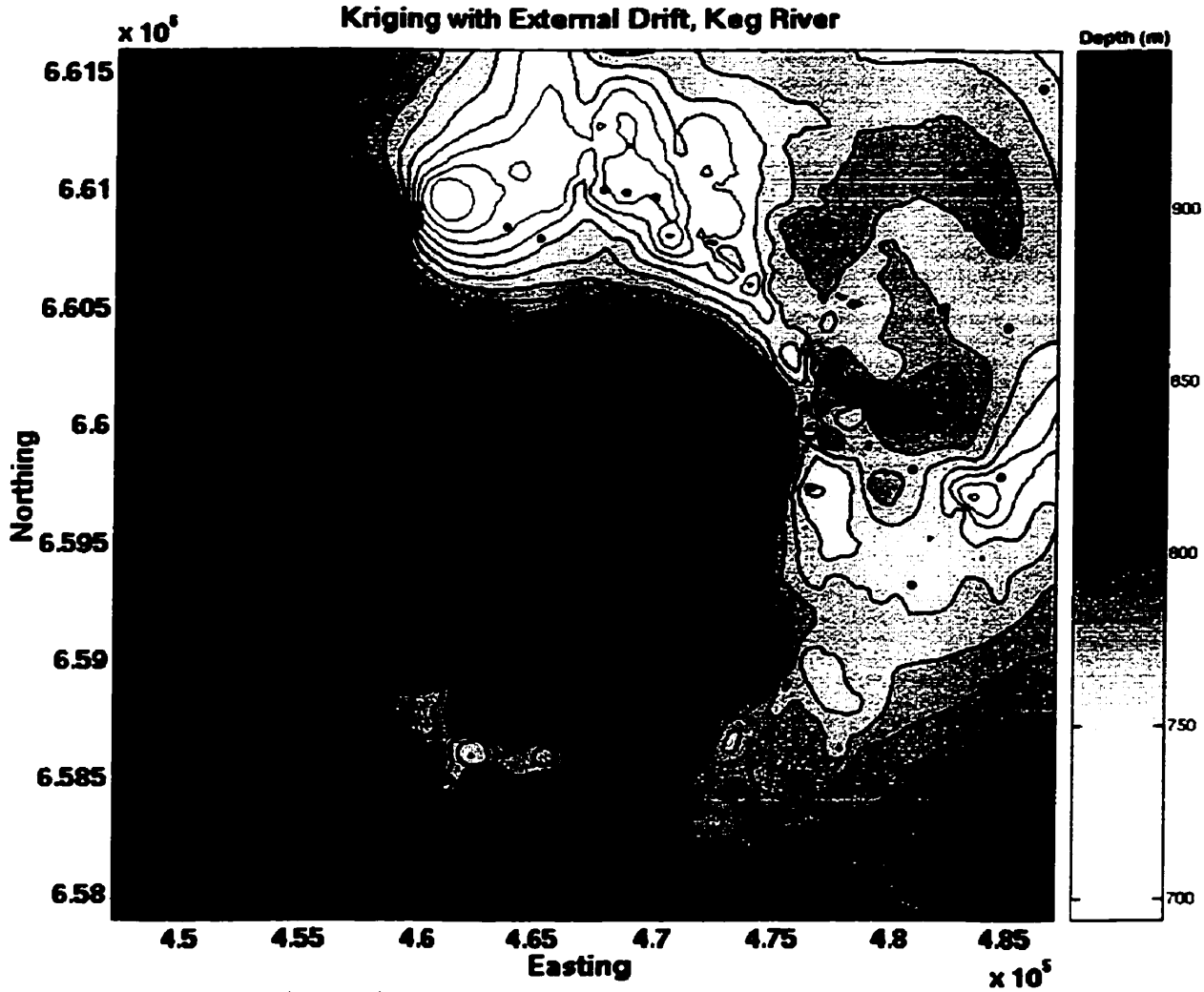

Figure 4.2.37 The anisotropic kriging with external drift result shows evidence of circular rim structure.Well depths are given as values below sea level (light areas represent structural highs). Well locations are shown as black dots.

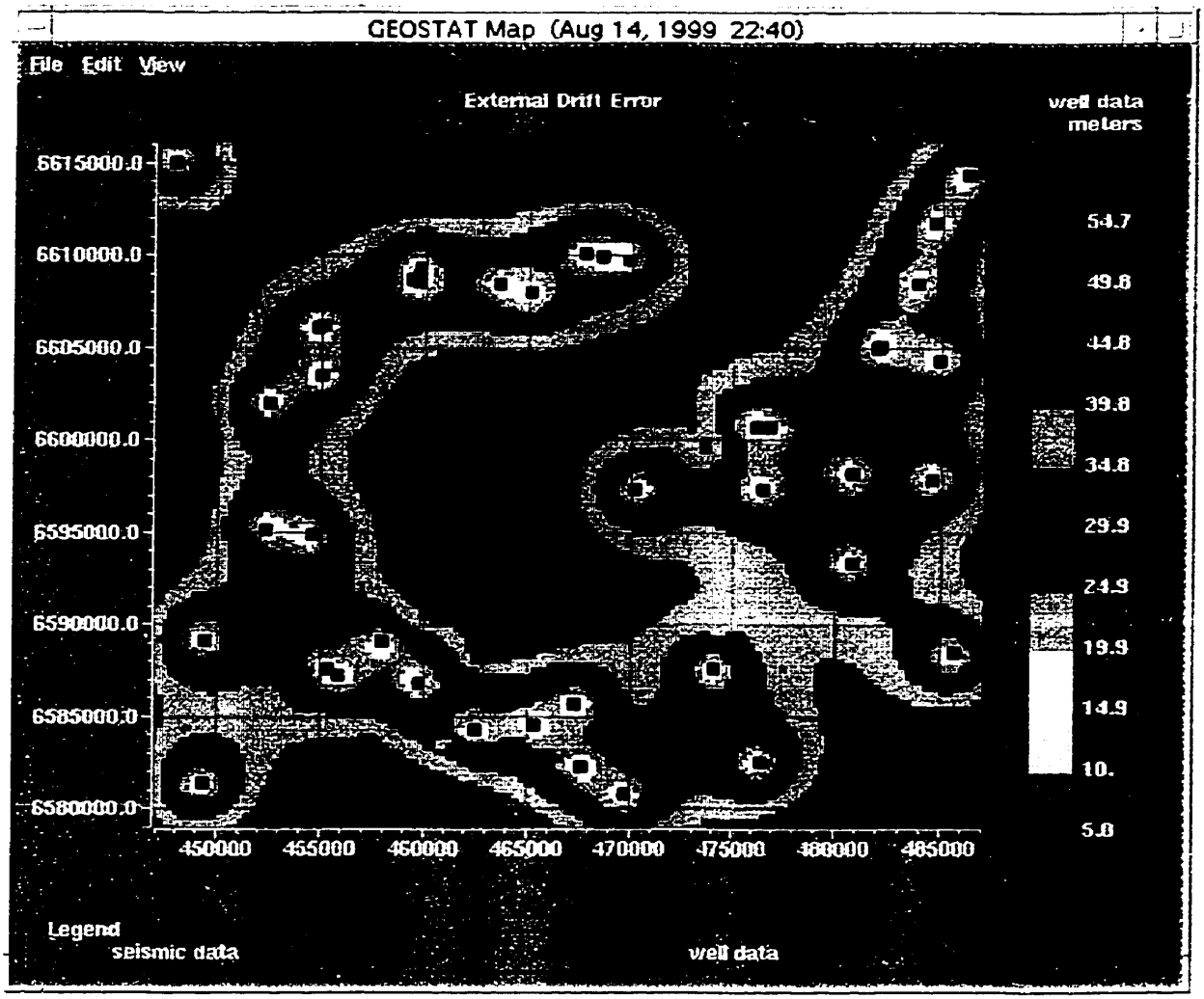

Figure 4.2.38 The expected error associated with the kriging with external drift result from the Keg River horizon is generally less than about ±35m within the area of interest.

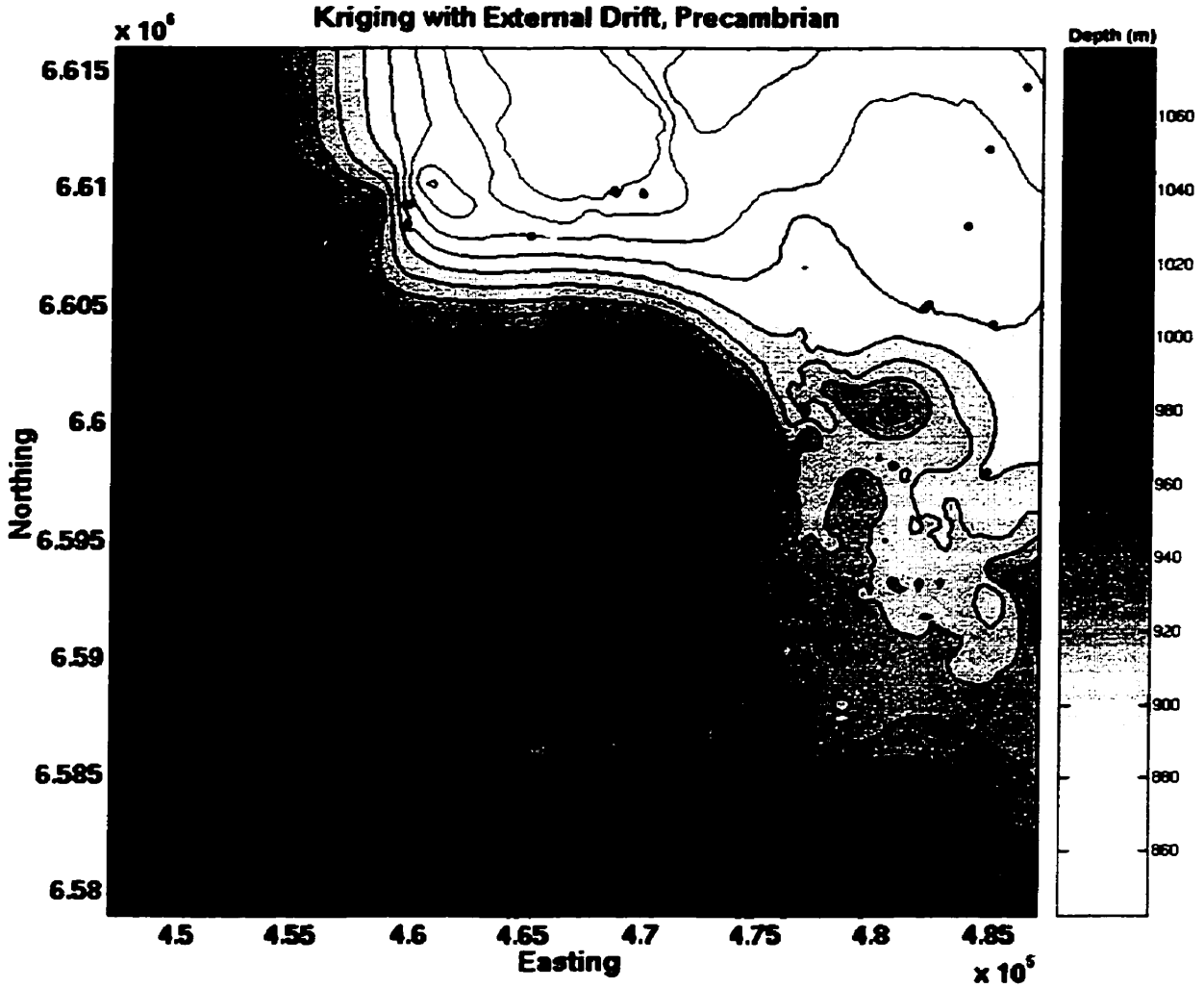

Figure 4.2.39 The anisotropic kriging with external drift result for the Precambrian horizon shows structure associated with the rim of the crater. Well depths are given as values below sea level (light areas represent structural highs). Well locations are shown as black dots.

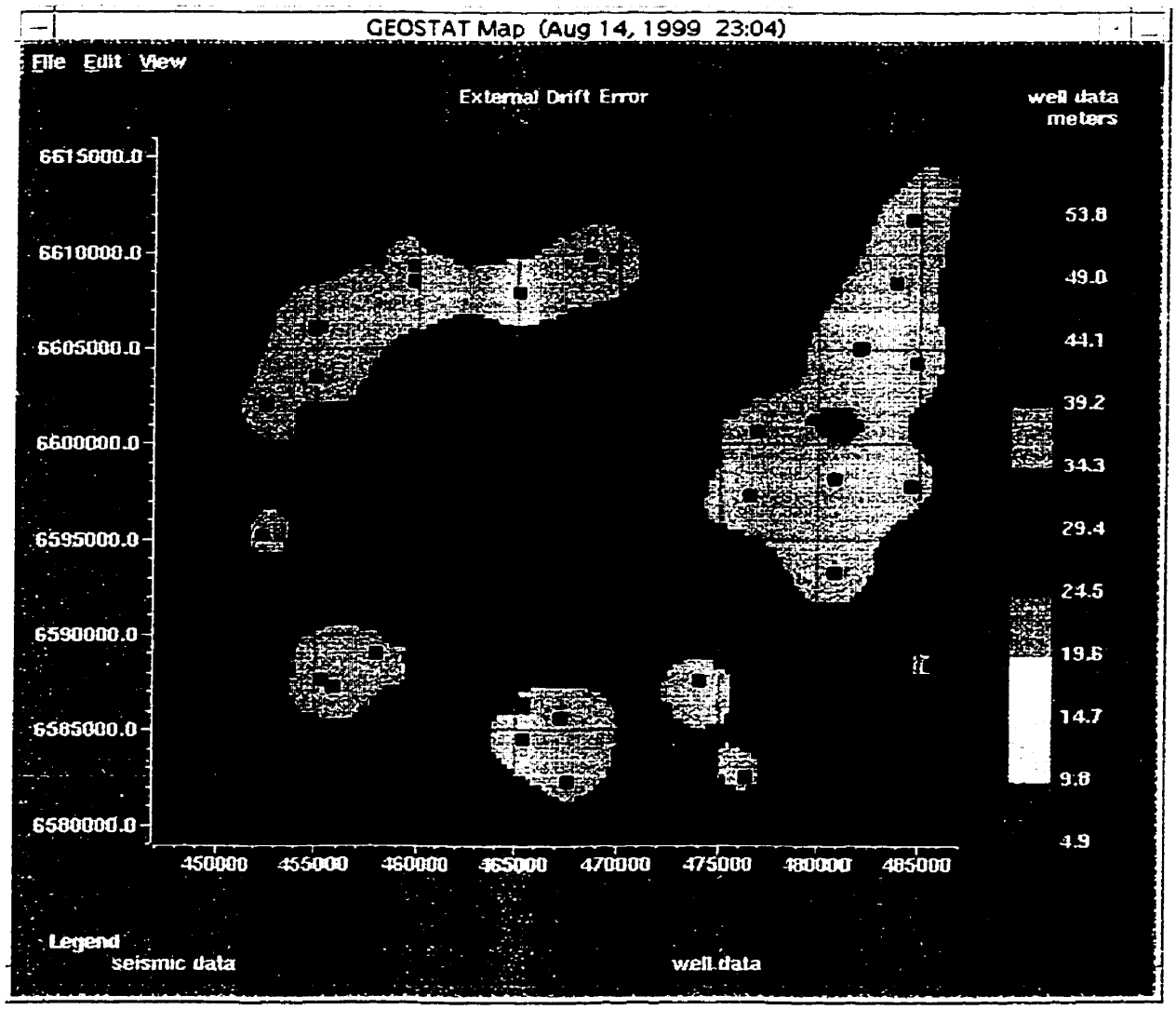

Figure 4.2.40 The expected error for the anisotropic kriging with external drift calculation for the Precambrian horizon is reasonable at less than about ±35m throughout most of the area of interest.

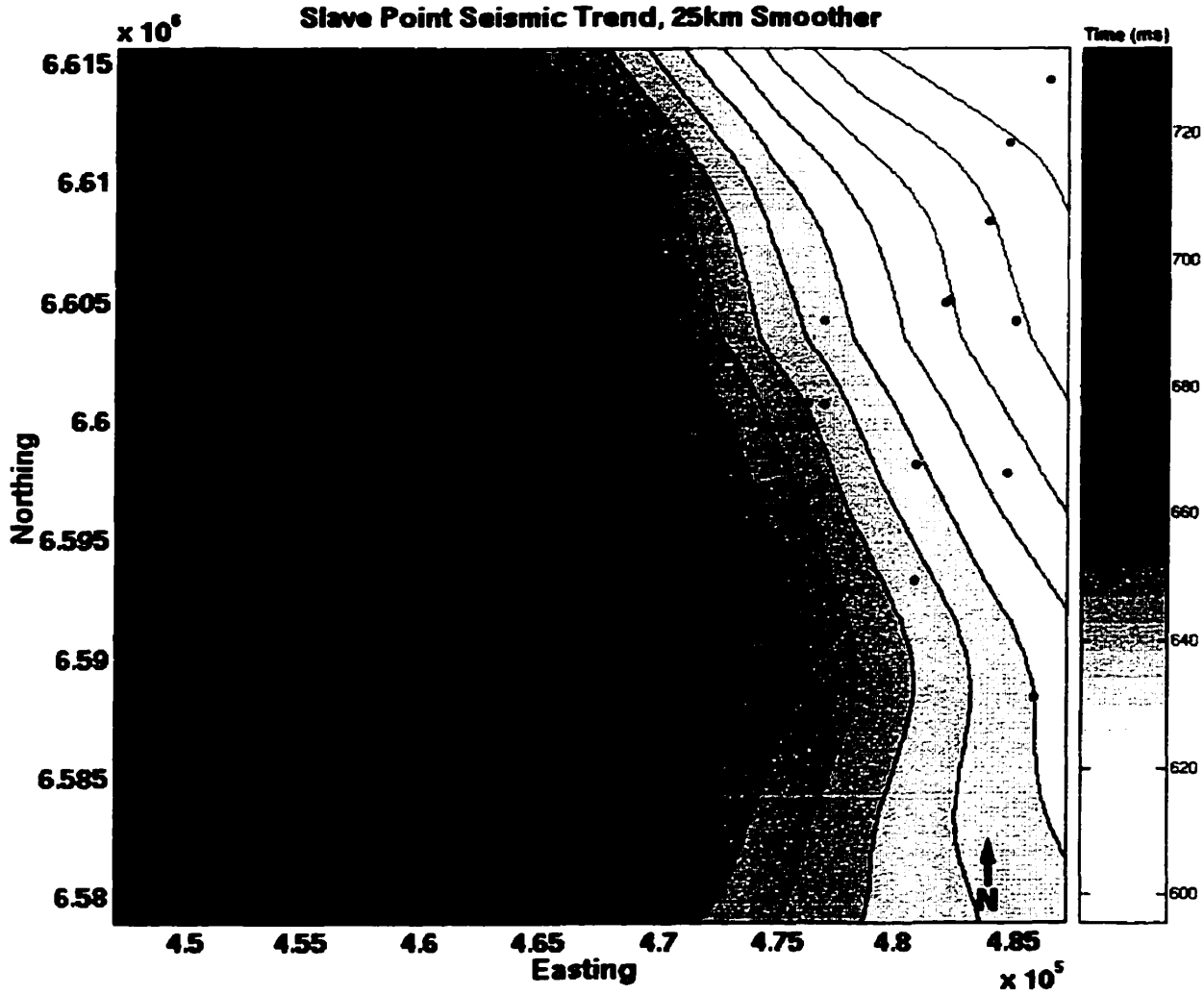

Figure 4.2.41 The trend in the seismic data as computed using a 25 km smoothing filter. The trend includes the influence of the unconformity dip and regional dip.

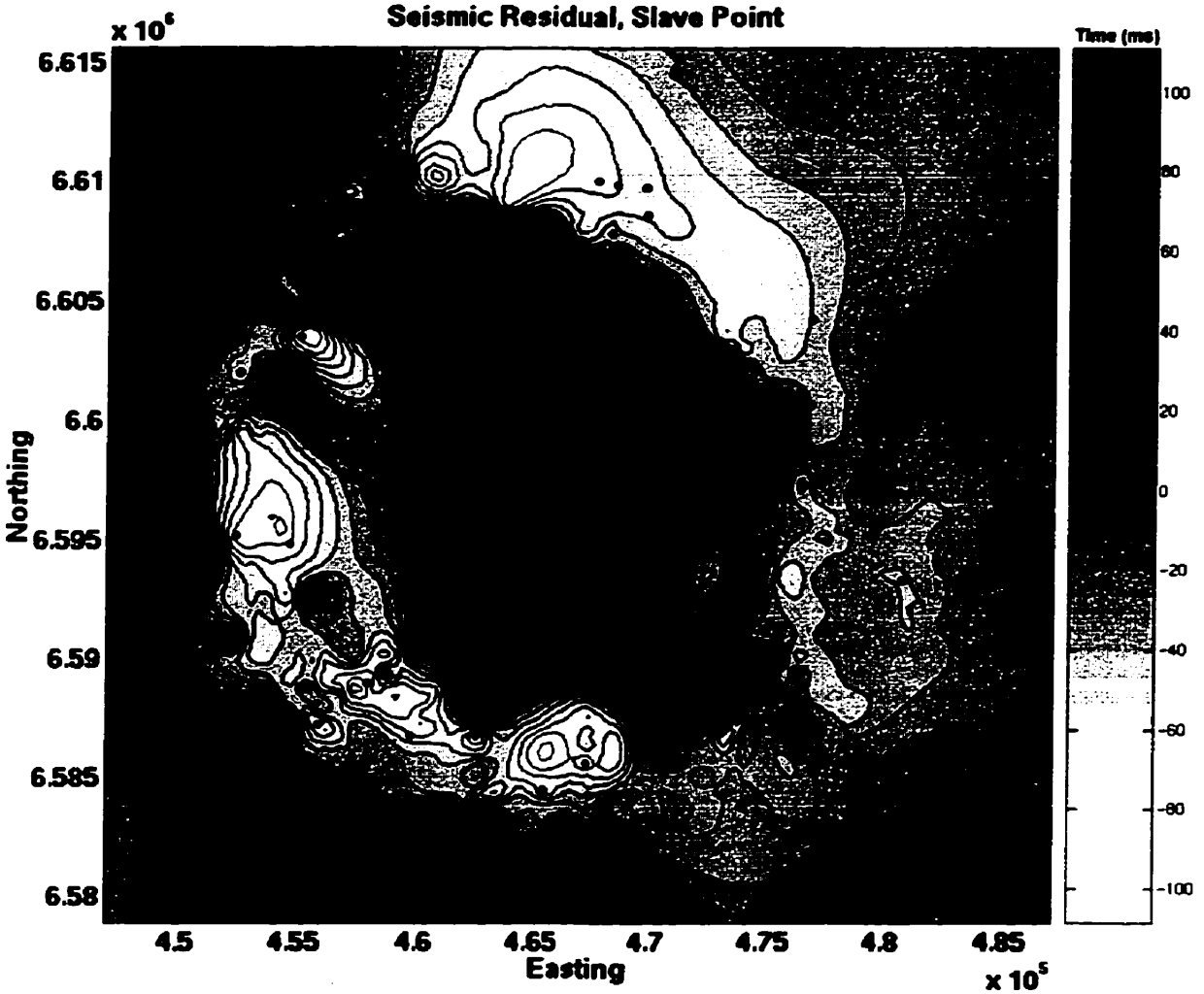

Figure 4.2.42 The 'residual' Slave Point time structure after the trend in figure 4.2.44 is removed. Well depths are given as values below sea level (light colours represent highs). Well locations are shown as black dots.

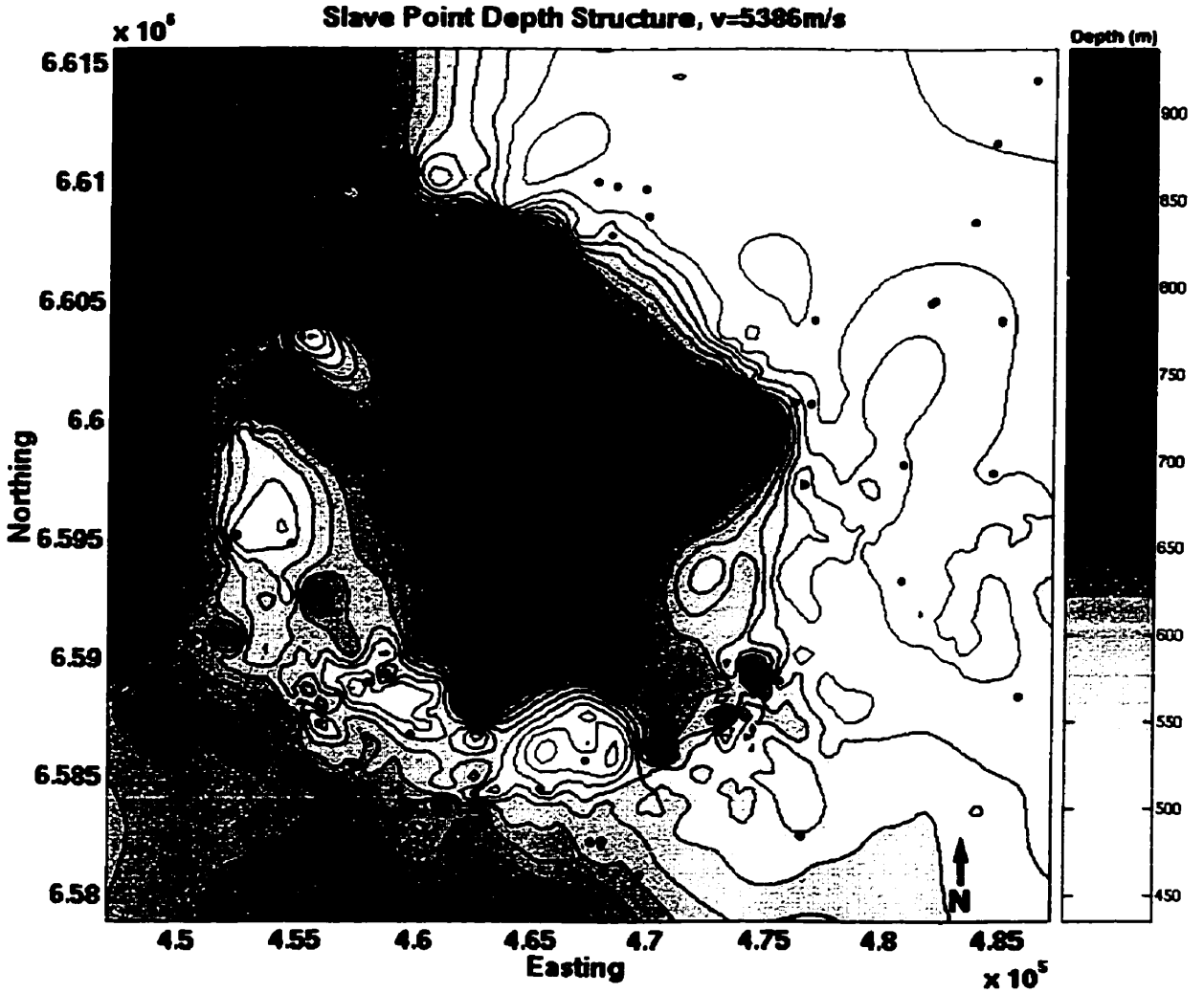

Figure 4.2.43 Depth to the Slave Point as calculated by applying the time-to-depth conversion factor shown in figure 4.2.21. Well depths are given as values below sea level (light colours represent structural highs). Well locations are shown as black dots.

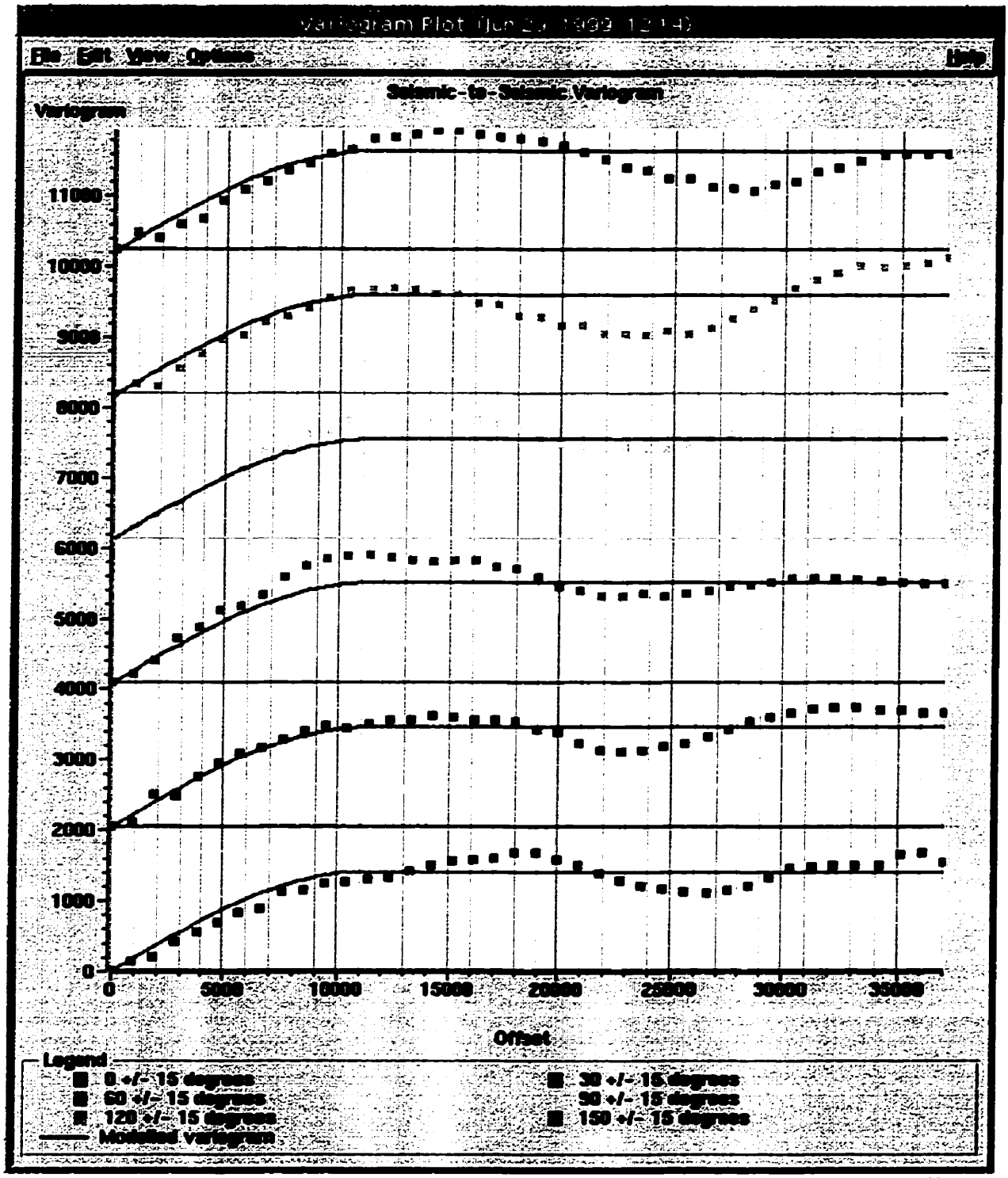

Figure 4.2.44 The seismic-to-seismic variogram can be calculated for six different azimuthal angles (directions) measured clockwise from North. The modelled variogram is shown as a solid line.

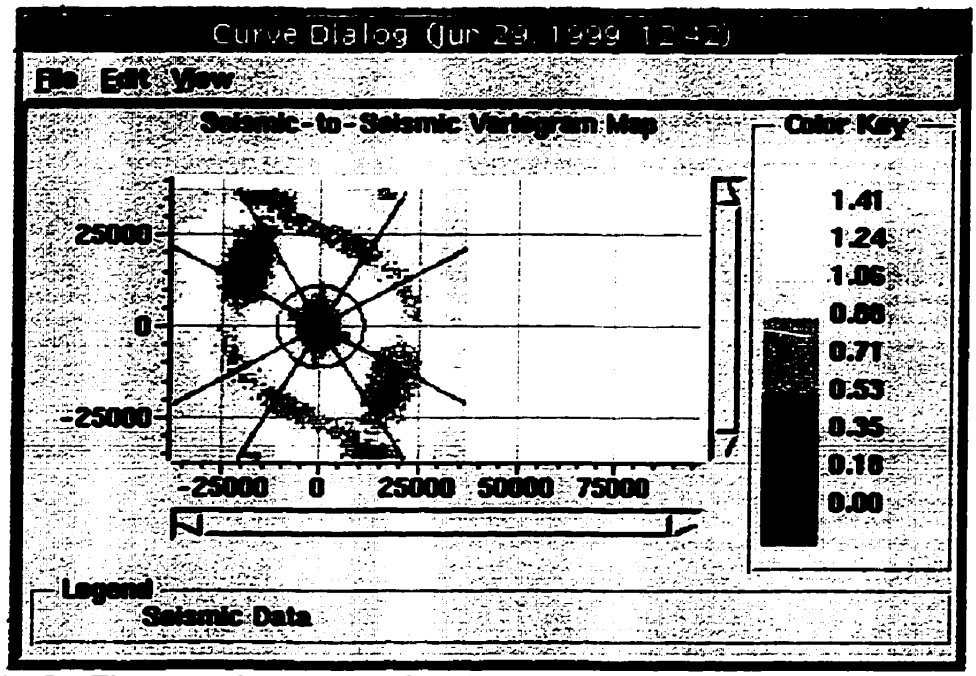

Figure 4.2.45a The covariance map for the seismic-to-seismic variogram exhibits the elliptical appearance of an anisotropic dataset.

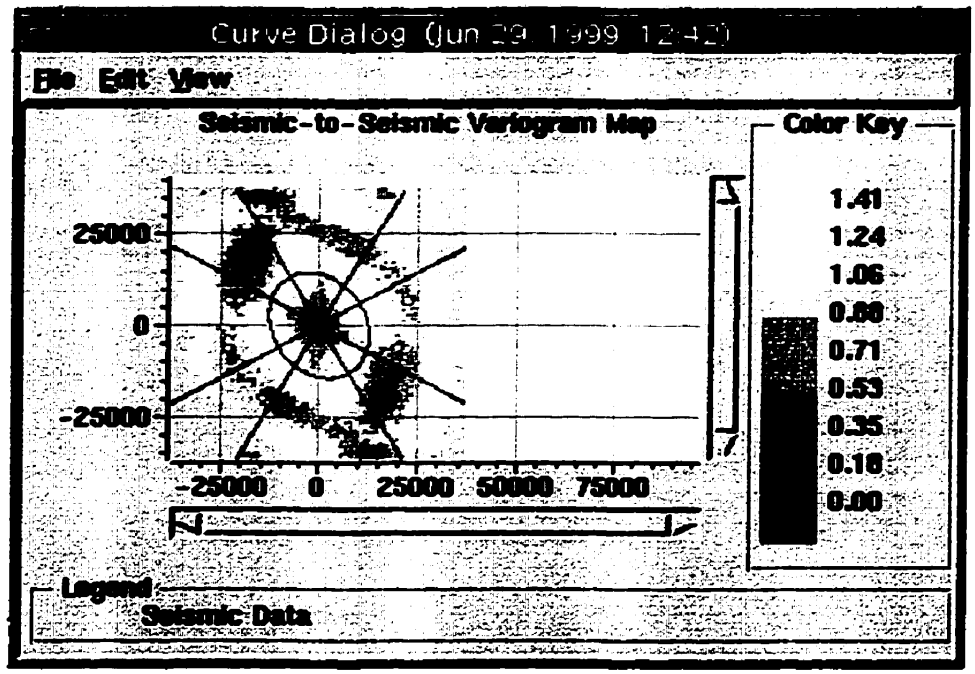

Figure 4.2.45b By increasing the range and setting the anisotropy factor to 0.8 at a principal direction of 150° the seismic-to-seismic variogram can be better modelled.

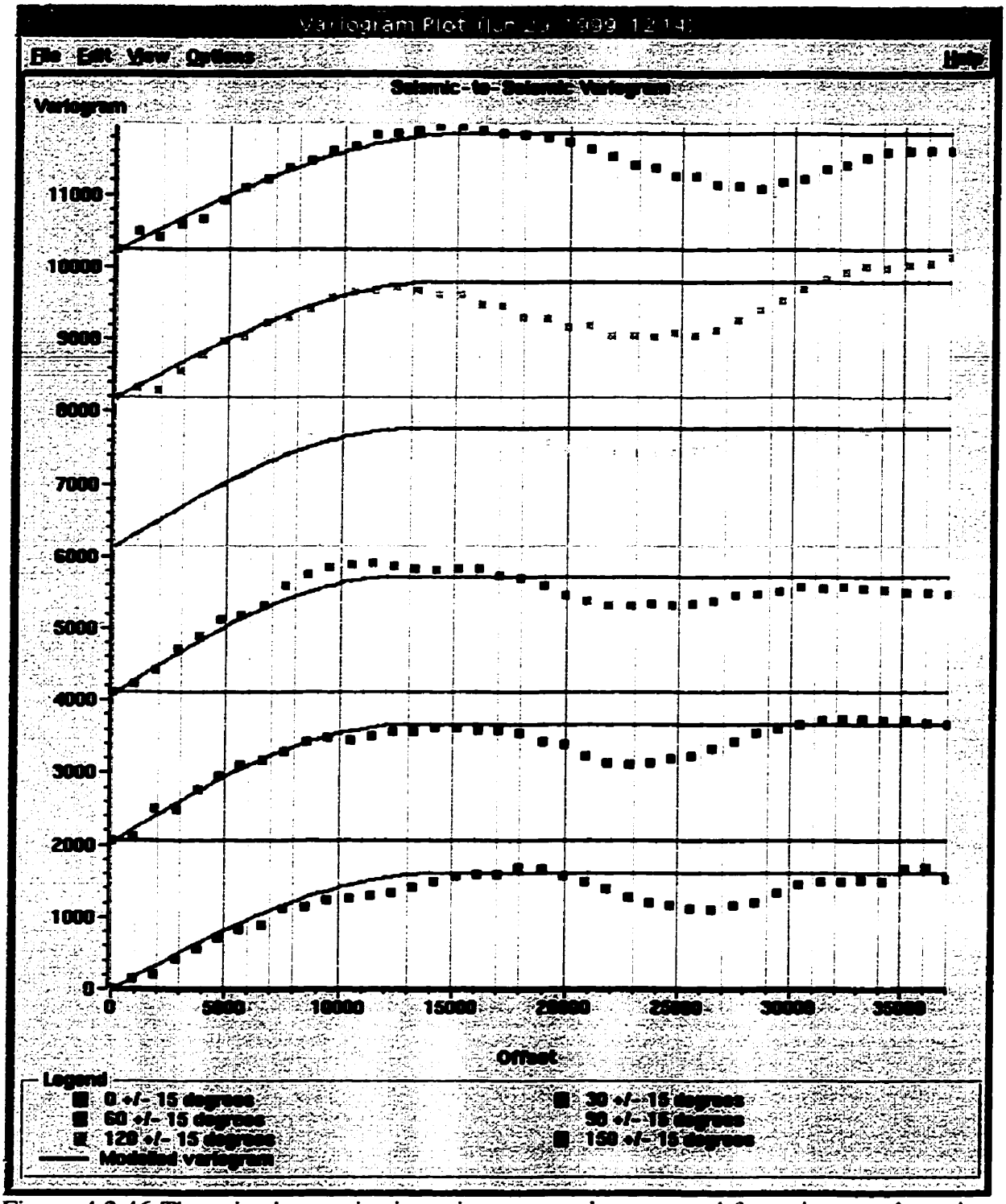

Figure 4.2.46 The seismic-to-seismic variogram can be corrected for anisotropy by using an anisotropy factor of 0.8 at a principal direction of 150°. The modelled variogram is shown as a solid line.

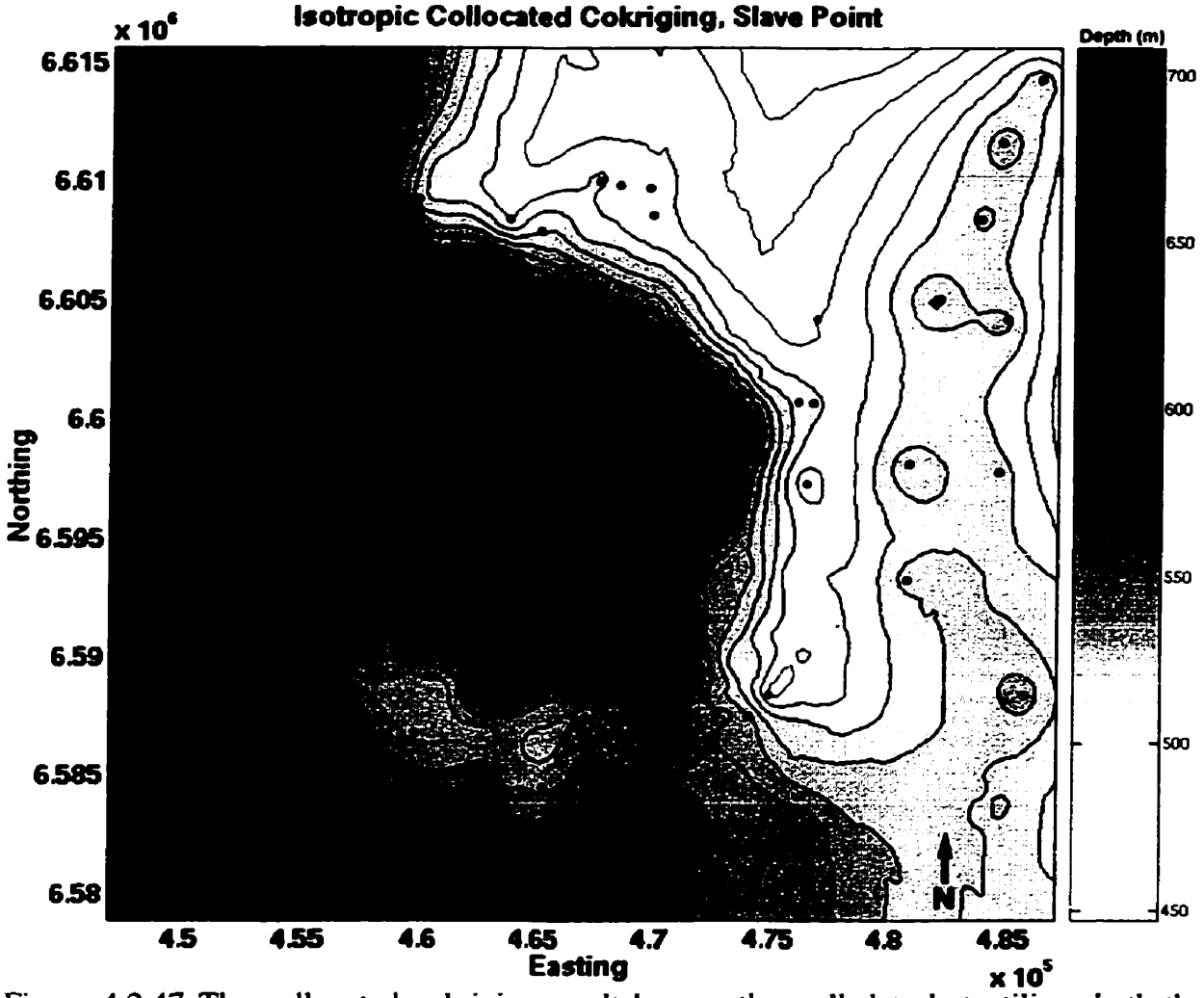

Figure 4.2.47 The collocated cokriging result honors the well data but utilizes both the seismic data and the variograms to interpolate between the wells. Well depths are given as values below sea level (light colours represent structural highs). Well locations are shown as black dots.

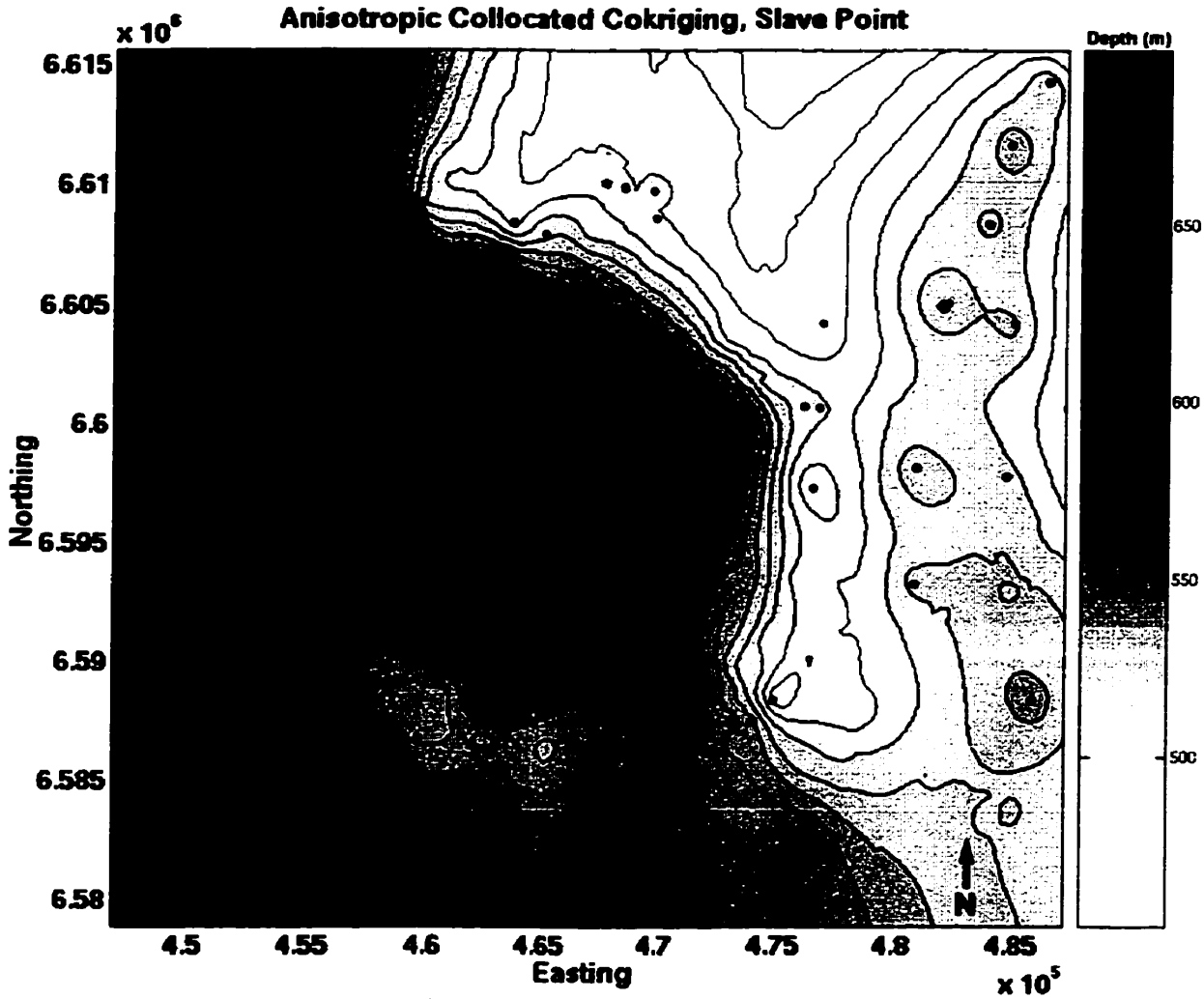

Figure 4.2.48 The collocated cokriging result has been computed using an anisotropy factor of 0.8 at a principal direction of 150°. Well depths are given as values below sea level (light colours represent structural highs). Well locations are shown as black dots.

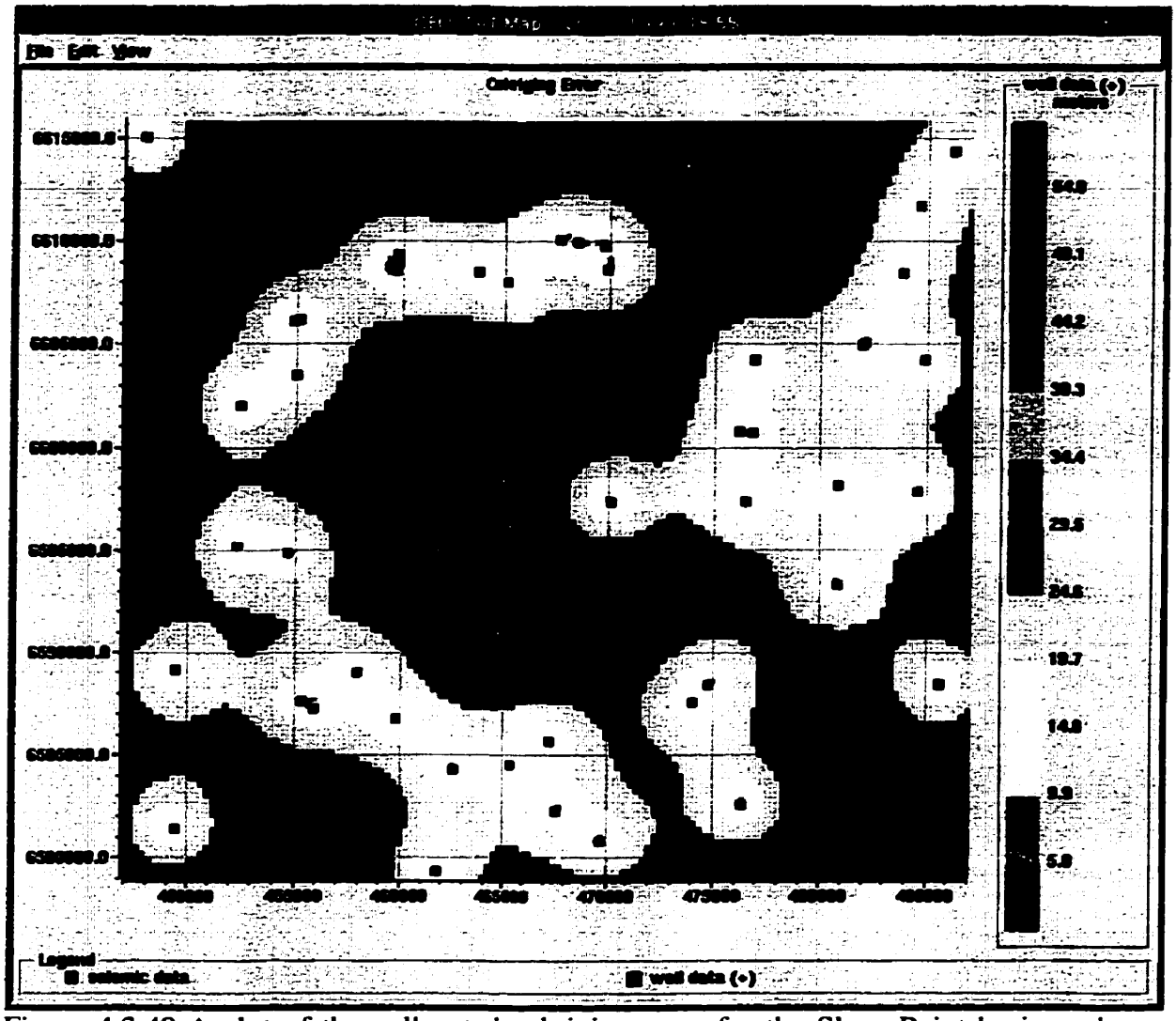

Figure 4.2.49 A plot of the collocated cokriging error for the Slave Point horizon shows that the error is small close to the wells and larger away from them.

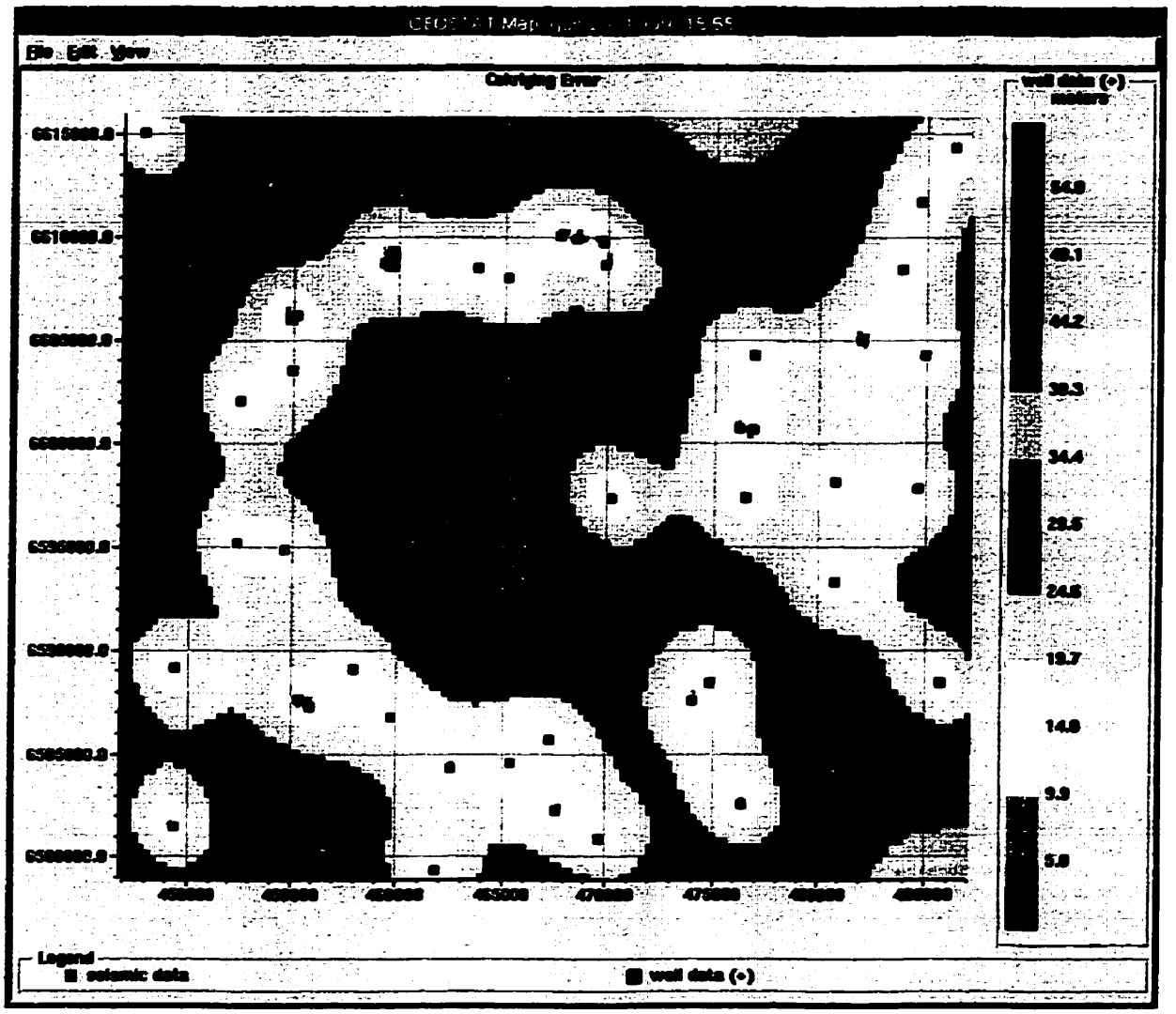

Figure 4.2.50 The collocated cokriging error associated with figure 4.2.51 is comparable to that in the absence of anisotropy corrections (Figure 4.2.52).

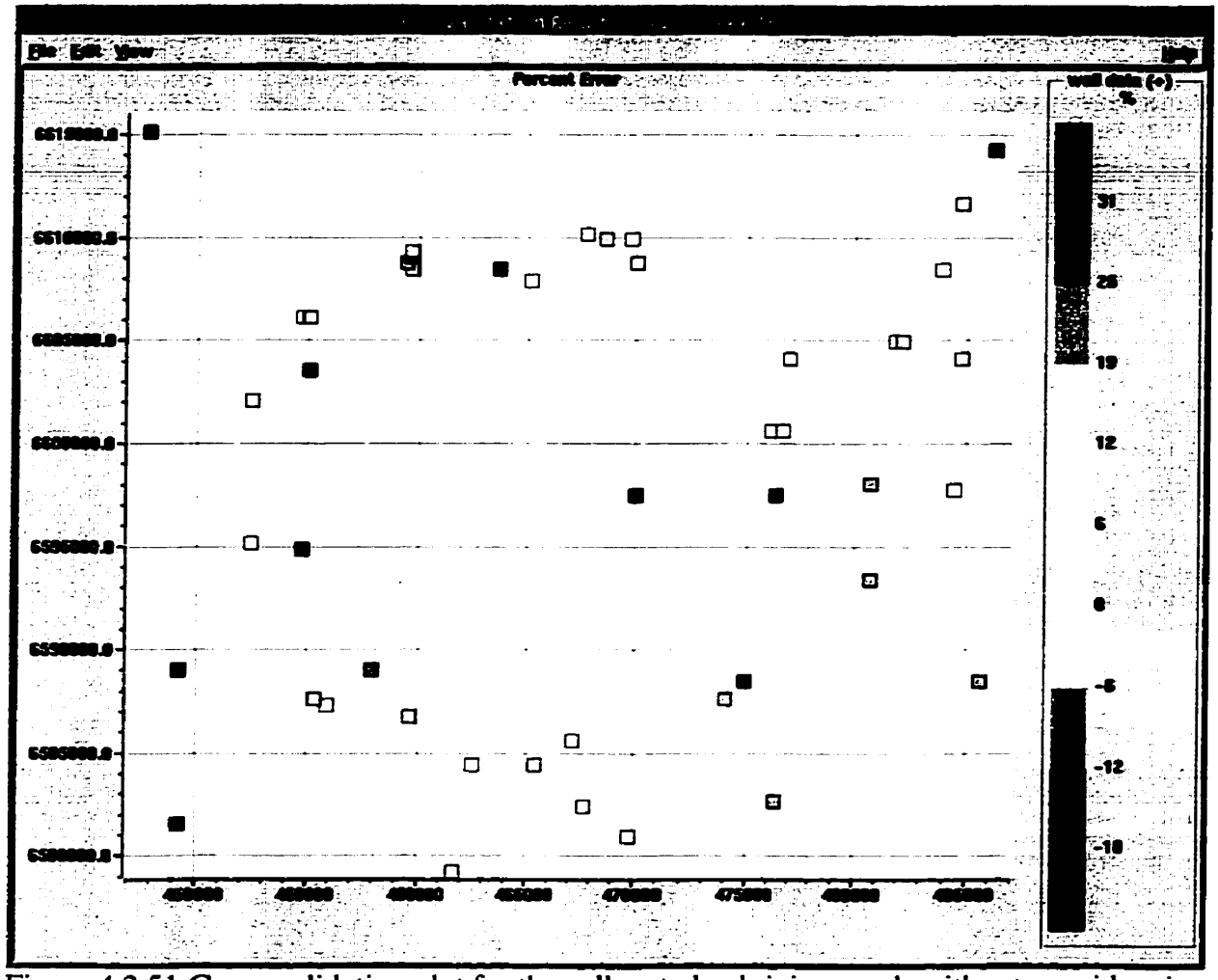

Figure 4.2.51 Cross-validation plot for the collocated cokriging result without consideration of anisotropy.

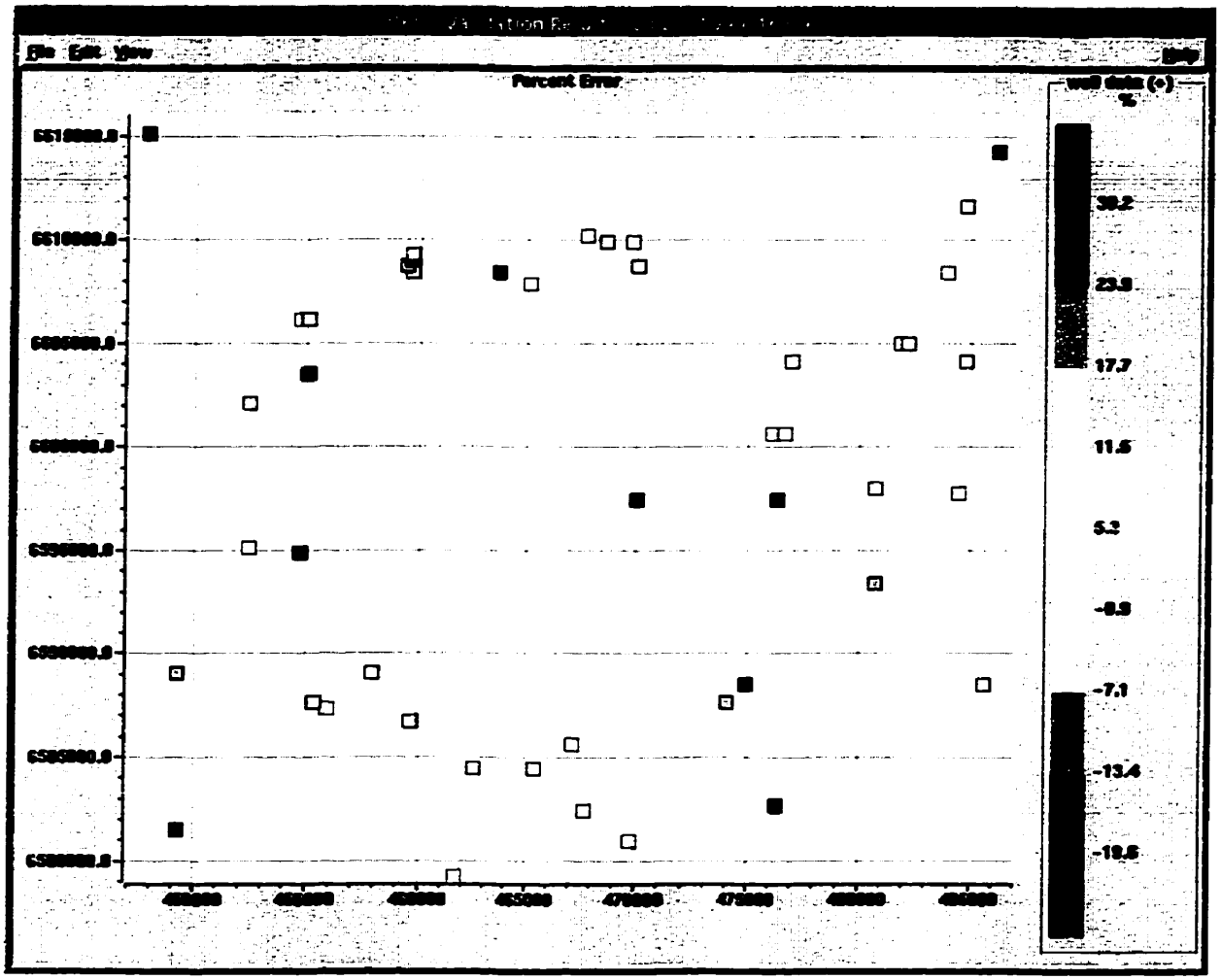

Figure 4.2.52 Cross-validation plot for the collocated cokriging result adjusted for anisotropy.

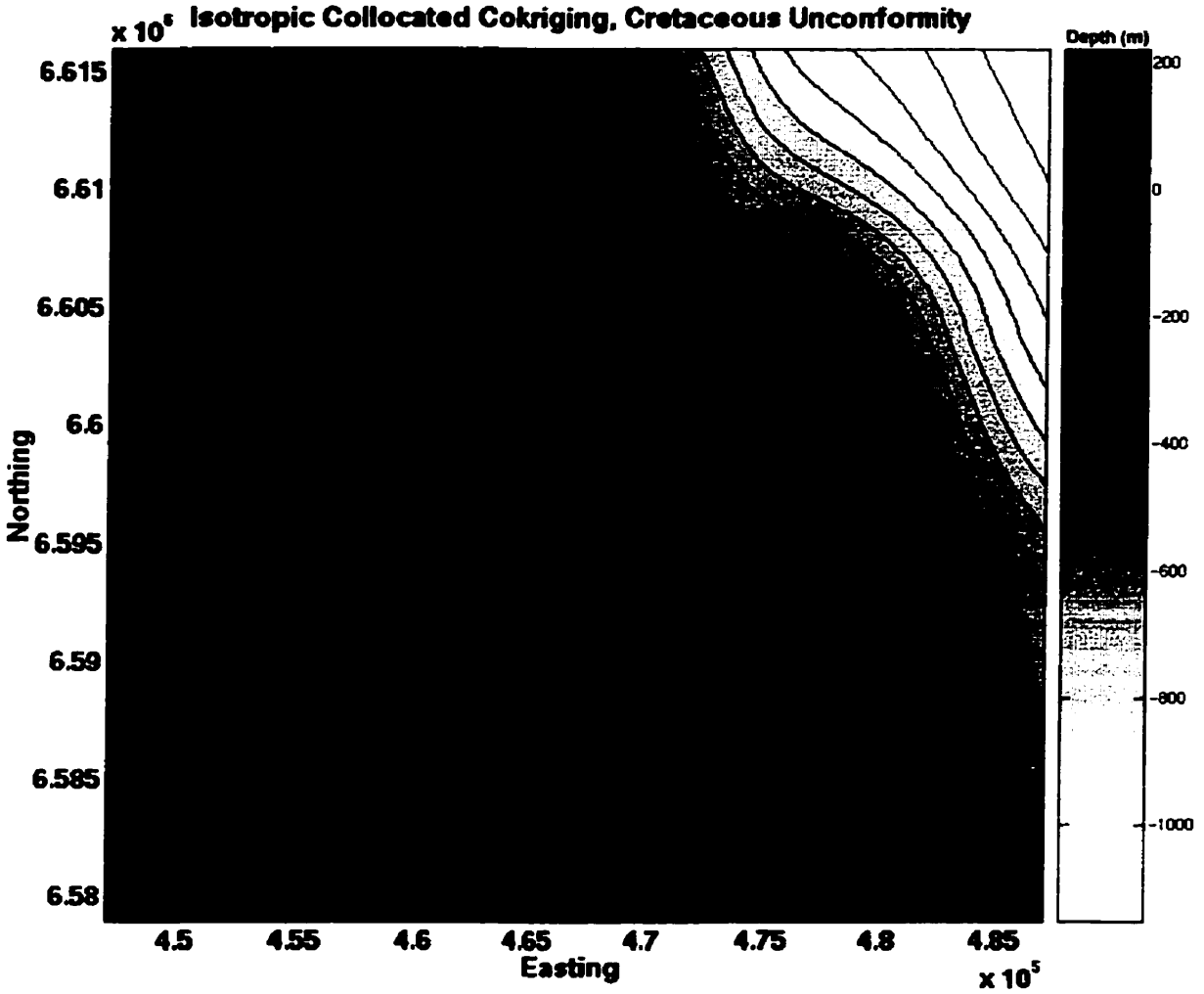

Figure 4.2.53 The isotropic collocated cokriging result for the Cretaceous unconformity honors both the well data and the seismic data and is observed to be smooth.Well depths are given as values below sea level (light colours represent structural highs). Well locations are shown as black dots.

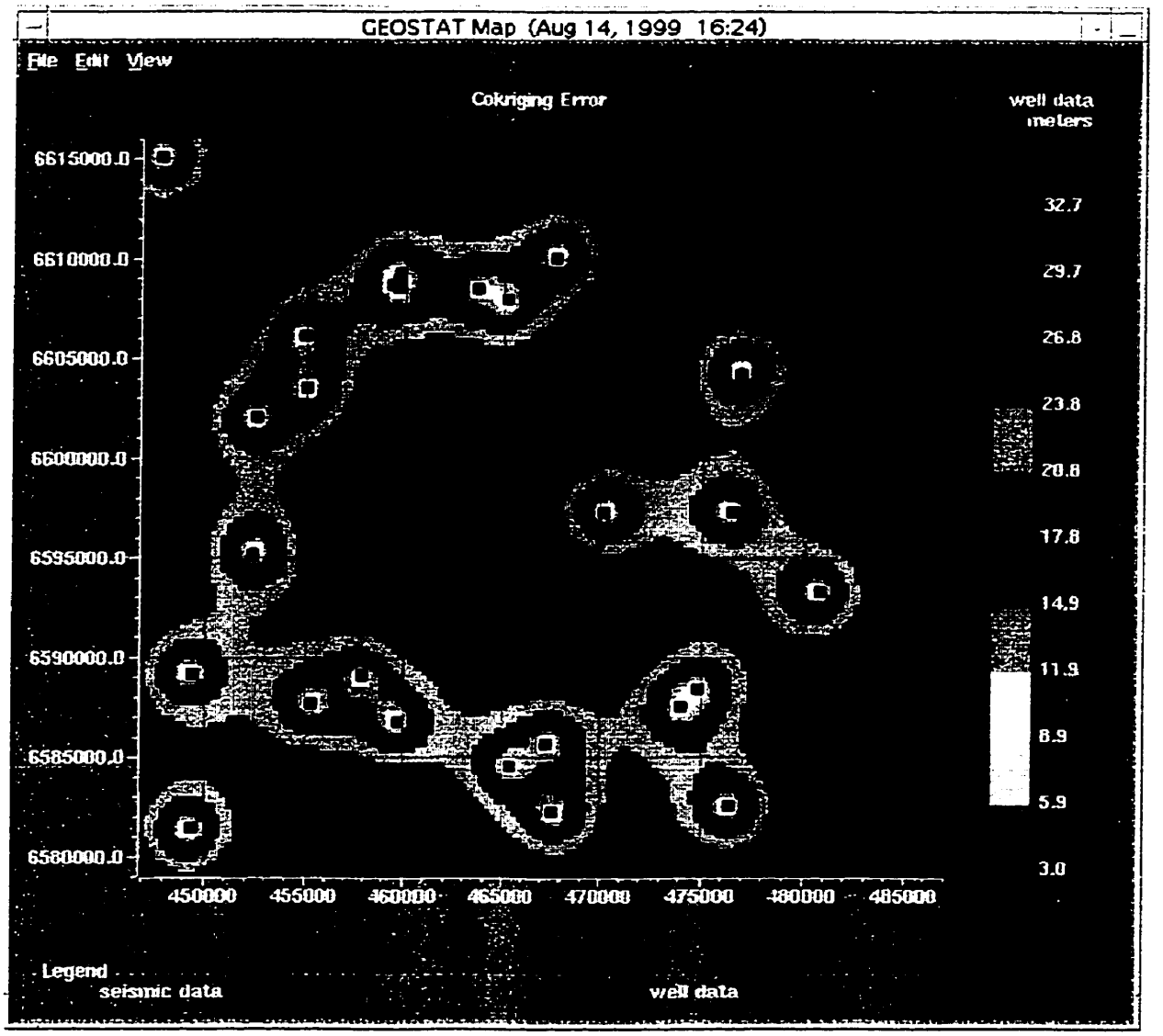

Figure 4.2.54 The Cretaceous unconformity collocated cokriging error is generally less than about ±30 m within the area surrounding the rim of the crater.

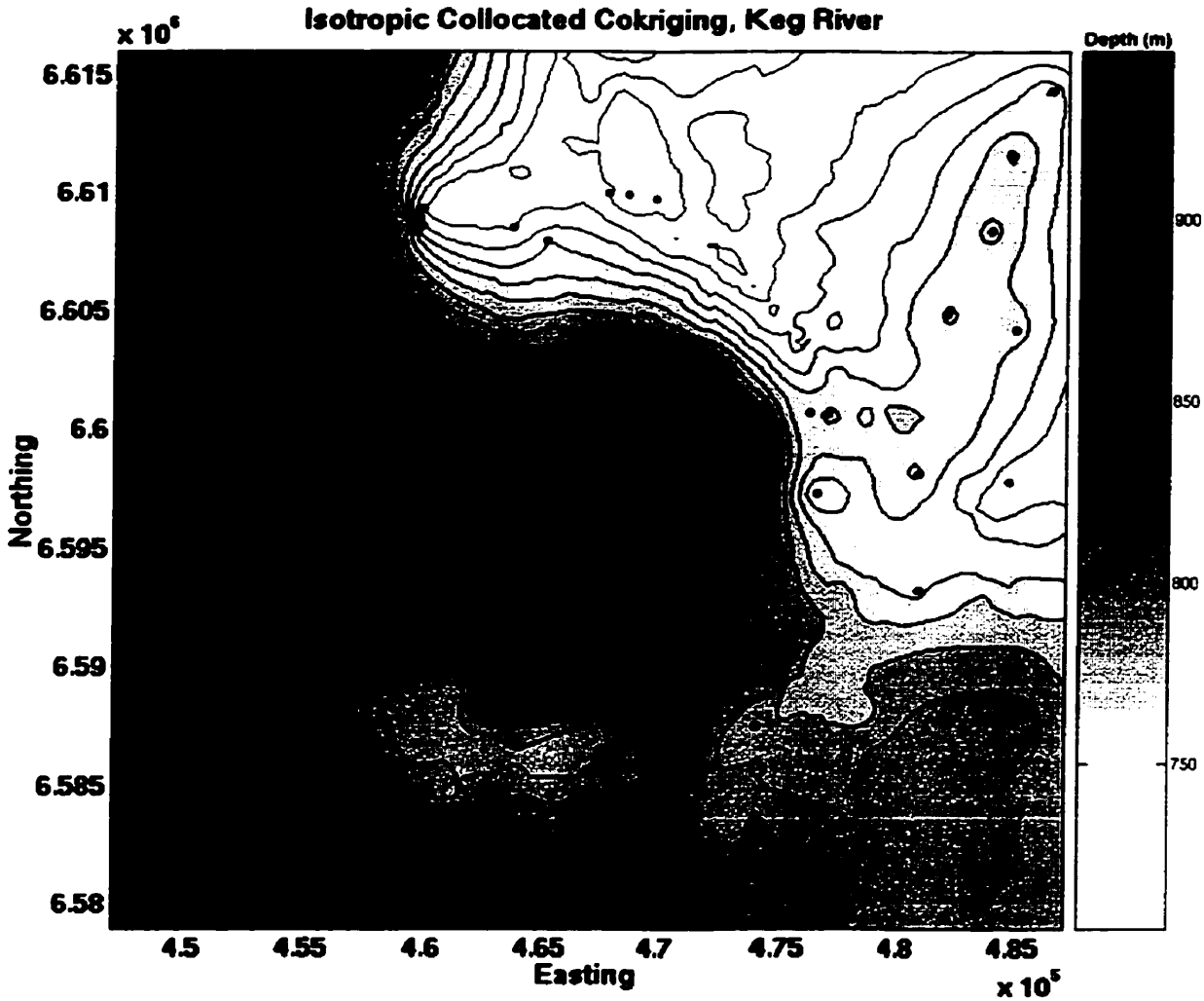

Figure 4.2.55 The Keg River isotropic collocated cokriging result shows evidence of the circular nature of the crater. Well depths are given as values below sea level (light colours represent structural highs). Well locations are shown as black dots.

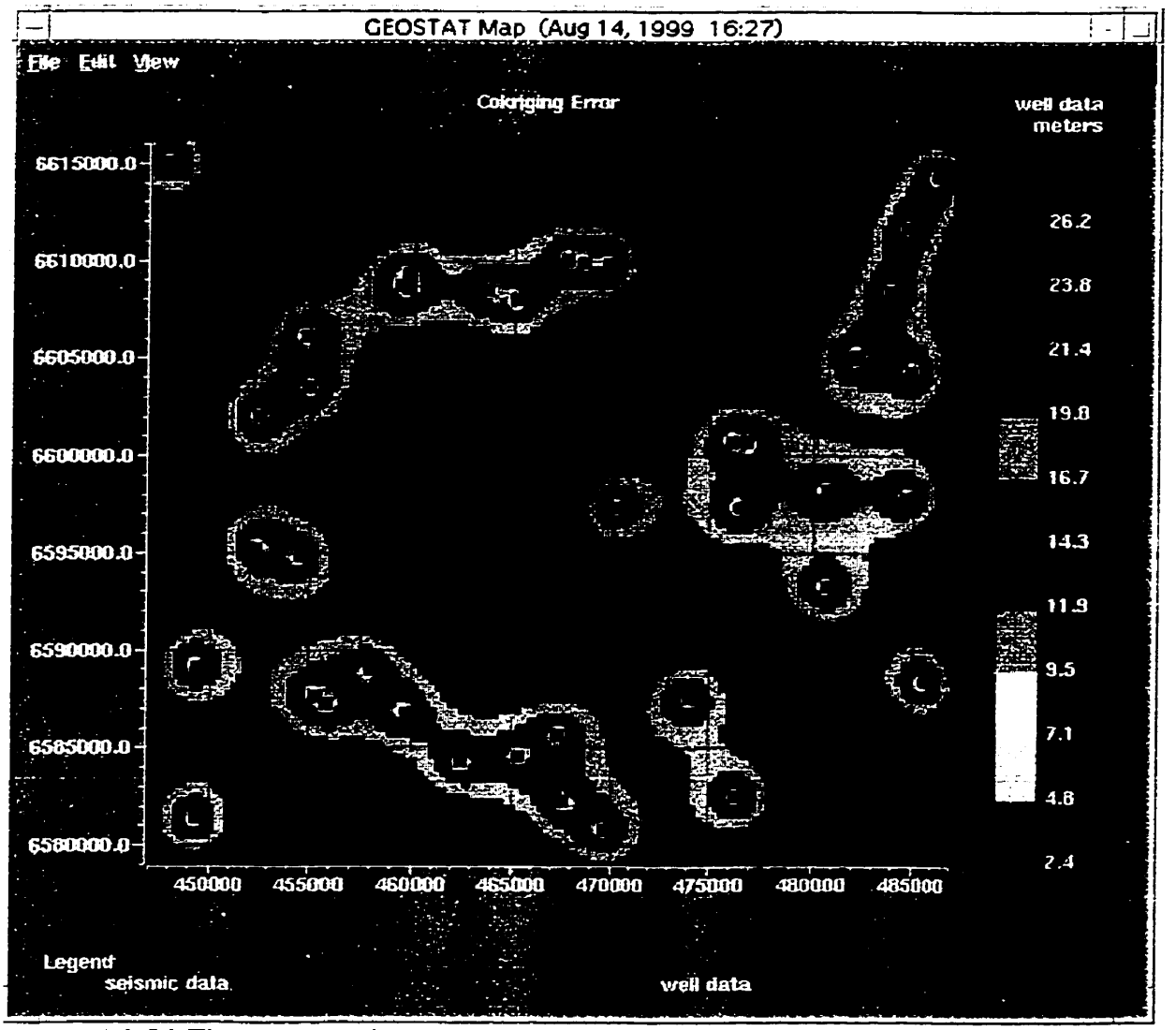

Figure 4.2.56 The collocated cokriging error for the Keg River horizon is generally less than about ±26 m within the area surrounding the rim of the crater.

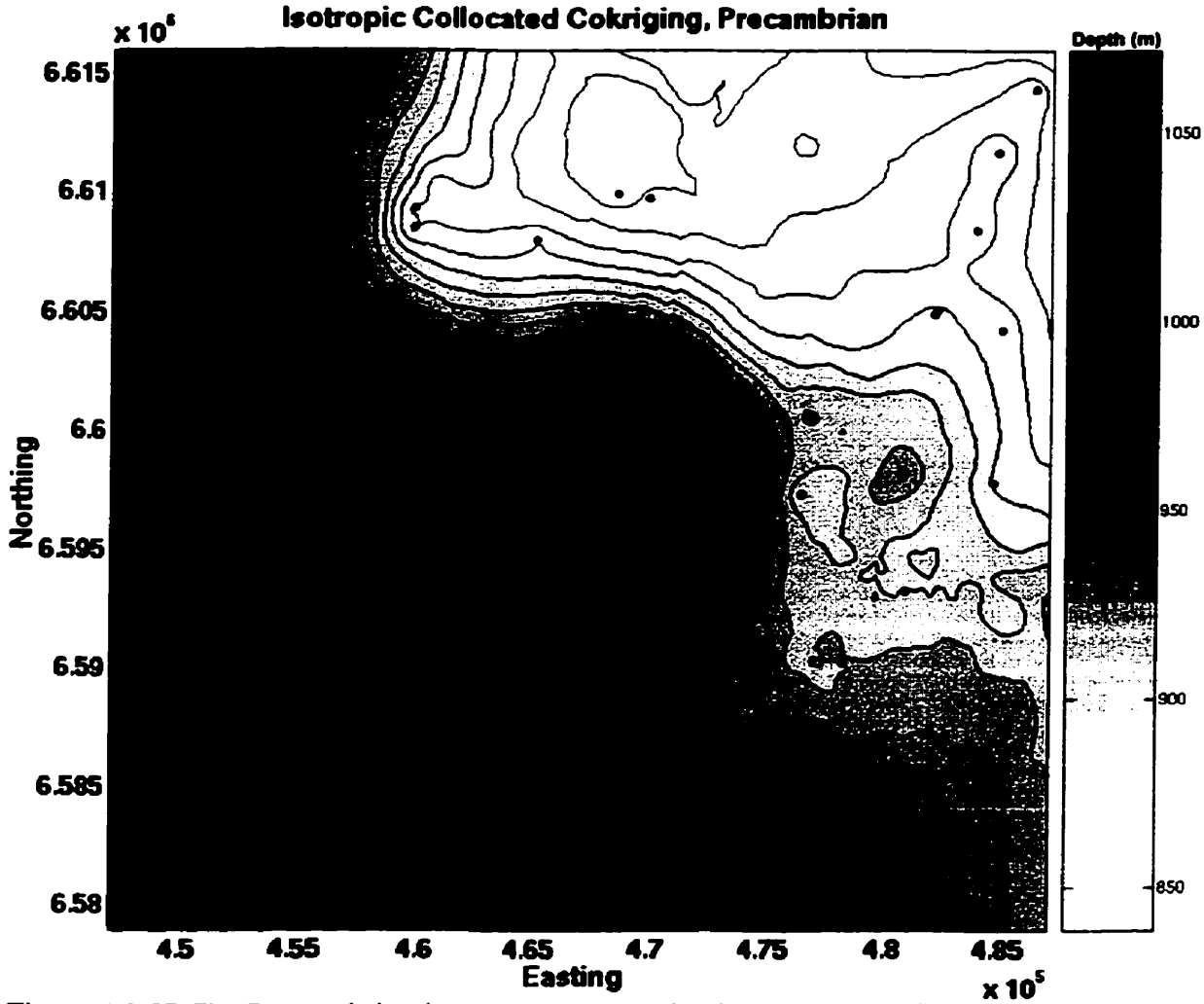

Figure 4.2.57 The Precambrian isotropic collocated cokriging result shows evidence of the circular nature of the Steen River structure. Well depths are given as values below sea level (light colours represent structural highs). Well locations are shown as black dots.

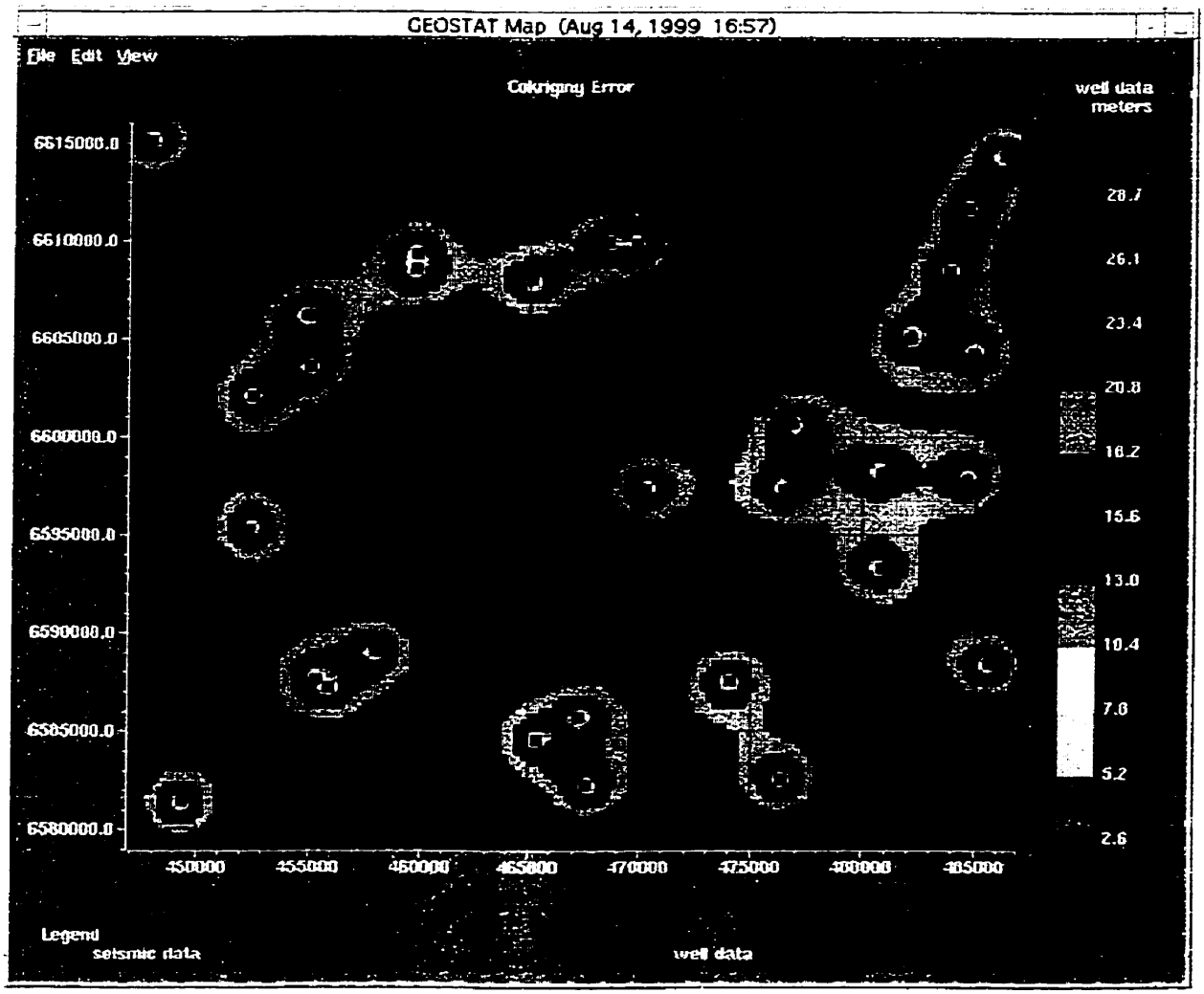

Figure 4.2.58 The Precambrian collocated cokriging error is generally less than about ±28 m within the area surrounding the rim of the crater.

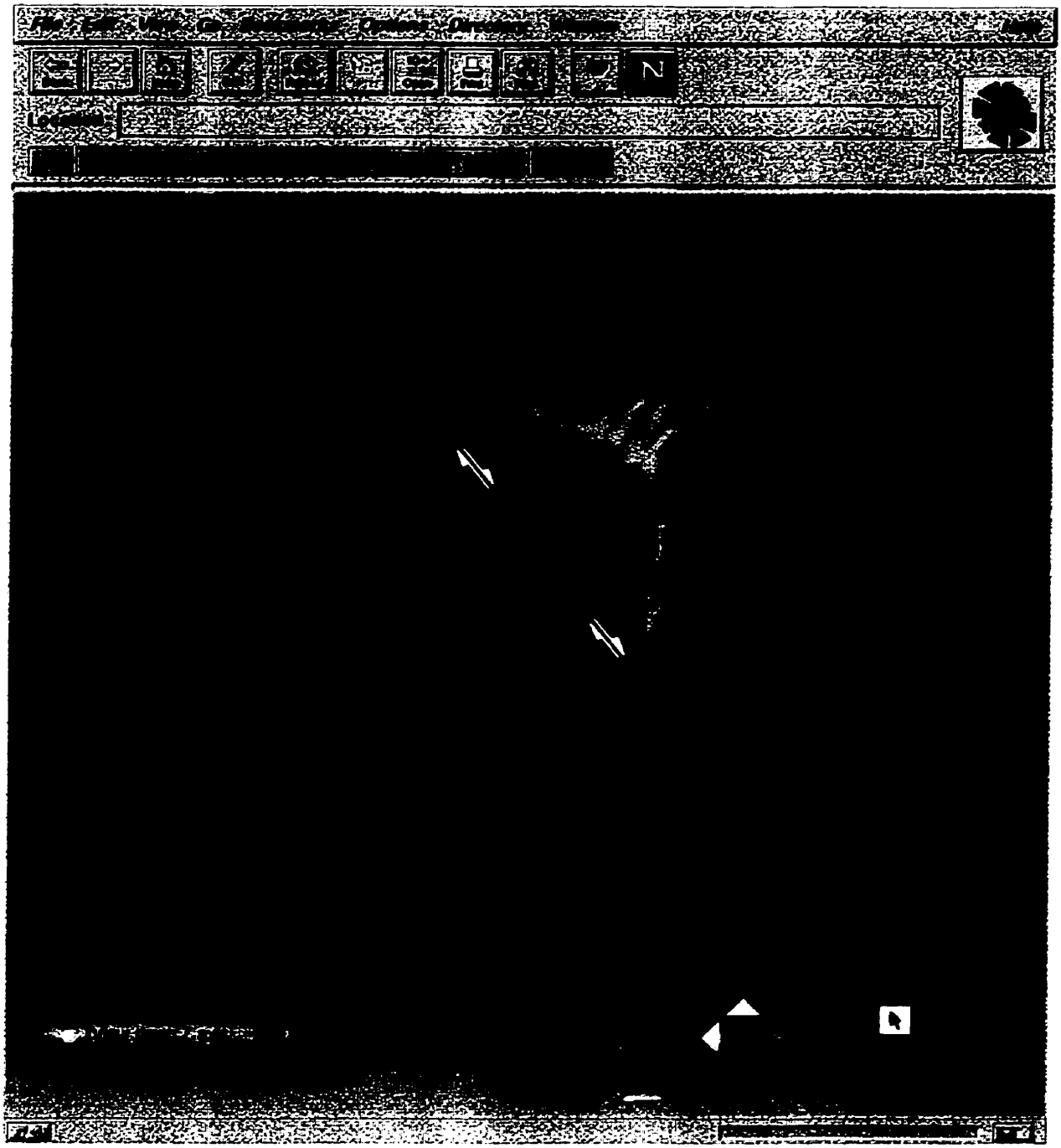

Figure 4.2.59 The above image is a screengrab of the CosmoPlayer VRML plug-in for Netscape. This world was rendered on an SGI Octane. The control panel at the bottom of the display is used to control motion during a real-time fly-through. Note the apparent faults as marked by the white arrows.

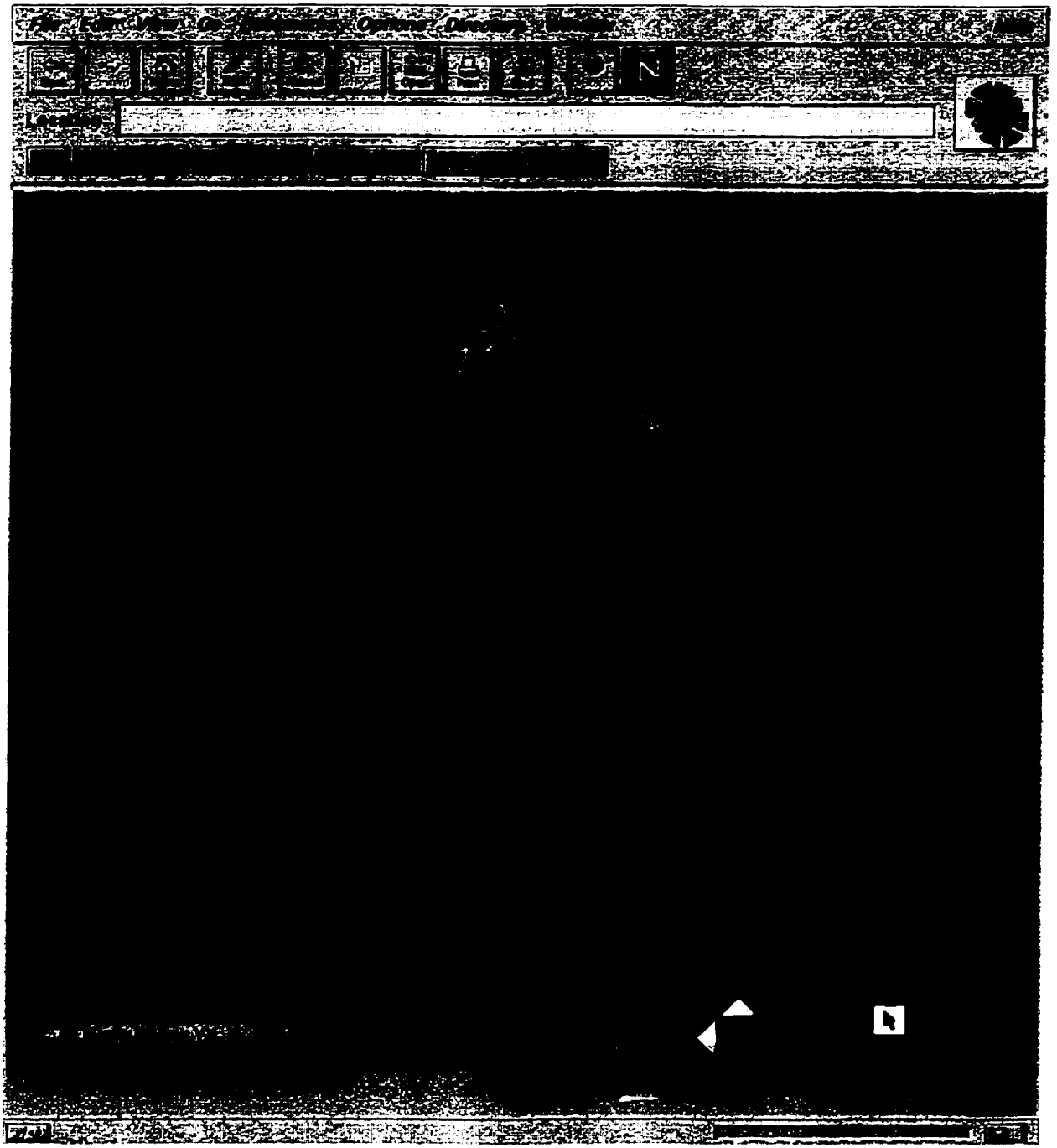

Figure 4.2.60 This image shows a slightly different view than that in Figure 4.2.62. The control panel at the bottom of the display is used to control motion during a real-time fly-through.

Chapter 5

SUMMARY

The slightly elliptical Puffin structure, located on the Ashmore Platform in the Timor Sea, is observed to have many of the characteristics of a simple impact crater. The measured diameter of the structure is nearly 2.0 km while the depth is approximately 150 m. The seismic data shows an elliptical feature (2.0 km by 1.8 km) with a flat floor, a raised rim, and a possible low-lying bench. The age of the Puffin structure is estimated to be approximately 15 MY.

At 1300 m in diameter the Muskingum structure is thought to be the result of a meteorite impact approximately 503±2 MY ago. The seismic data provides evidence for extensive rim faulting, a small central mound, slight rim uplift, and possible breccia infill. The central mound is a possible indicator of impact and might be a precursor to the wholesale stratigraphic uplift observed in larger, complex craters. Using the observed thickness of the inferred breccia, the Muskingum structure is estimated to have had an original diameter of 1450 m and a depth to the top of the breccia lens of 300 m. The transient cavity is estimated to have been approximately 1215 m in diameter by about 450 m deep.

The appearance of the Hotchkiss structure on seismic data closely resembles a complex impact structure. The disturbed area is nearly 3.5 km across and is punctuated by an erosional unconformity separating the disturbed carbonates from the overlying undisturbed sandstones. Observed on the seismic data is a central uplift, rim faults, an annular trough, and a possible breccia infill. The structure is estimated to have had an original diameter of 4.5 km and experienced approximately 500 m of subsequent erosion.

The 95±7 MY old Steen River structure is the only confirmed impact structure examined in this thesis. The structure has a diameter of 24 km and is observed to disturb

rocks at depths greater than several kilometers below the current surface of the crater. Using the geostatistical methods of kriging and cokriging, depth structure maps have been created from well and seismic data. The depth structure of the gas-producing Slave Point Formation shows the rim uplift, evidence for slump blocks, and a right-lateral fault through the center of the structure.

The methods of seismic interpretation can aid in the identification of buried impact structures. Many diagnostic impact features are well imaged by seismic methods allowing comparison with crater scaling relations. The interpretation of seismic data in the hopes of identifying new examples of impact structures will probably become more commonplace as the number of candidate targets shrinks.

Chapter 6

FUTURE WORK

6.1 Physical and Numerical Modeling

The physical modeling of impact structures began in 1891 when G.K. Gilbert examined the characteristics of low-velocity impacts in various powders and slurries. Hypervelocity modeling first became possible with the introduction of high-speed gas guns after the second world war. Using a hypervelocity test facility such as the Johnson Space Center Vertical Gun Range it would be possible to perform physical modelling experiments exploring the seismic characteristics of impact structures. Several stratified epoxy-impregnated sand models could be subjected to impacts by various projectiles at several angles of incidence. Subsequent baking of the models would preserve their morphology and allow them to be shipped back to Calgary for analysis using the 3-D seismic modeling facility located in the Department of Geology and Geophysics at the University of Calgary.

The seismic characteristics of impact craters could also be studied with numerical models. Using the information gleaned from this study, generalized stratigraphic models of both simple and complex craters can be created. Synthetic seismic datasets could then be made using software such as the GX-III software from GX Technology.

6.2 Examination of other circular features

Undoubtedly there exist many more examples of buried impact structures within the Western Canadian Sedimentary Basin and around the world. Those that show no surface expression will likely be found using the geophysical exploration techniques of seismic imaging, gravity, and high-resolution aeromagnetics. Due to this, it can be expected that many new discoveries will be made in areas with active geophysical exploration programs such as the WCSB, Texas, and the Middle East.

Chapter 7

APPENDIX

7.1 Appendix A - Known Terrestrial Impact Structures

Name	Latitude	Longitude	Diameter (km)	Age (Ma)
Acraman, Australia	32°1'S	135°27'E	160	570
Ames, Oklahoma	36°15'N	98°10'W	16	470 ± 30
Amguid, Algeria	26°5'N	4°23'E	0.45	0.1
Aorounga, Chad	19°6'N	19°15'E	17	200
Aouelloul, Mauritania	20°15'N	12°41'W	0.39	3.1 ± 0.3
Araguainha Dome, Brazil	16°46'N	52°59'W	40	249 ± 19
Avak, Alaska	71°15'N	156°38'W	12	100 ± 5
Azuara, Spain	41°10'N	0°55'W	30	130
B.P. Structure, Libya	25°19'N	24°20'E	2.8	120
Barringer, Arizona	35°2'N	111°1'W	1.186	0.049
Beaverhead, Montana	44°36'N	113°0'W	60	600
Bee Bluff	29°2'N	99°51'W	2.4	40
Beyenchime-Salaatin, Russia	71°50'N	123°30'E	8	65
Bigach, Kazakhstan	48°30'N	82°0'E	7	6 ± 3
Boltysh, Ukraine	48°45'N	32°10'E	25	88 ± 3
Bosumtwi, Ghana	6°32'N	1°25'W	10.5	1.3 ± 0.2
Boxhole, North Territory, Australia	22°37'S	135°12'E	0.17	0.03
Brent, Ontario	46°5'N	78°29'W	3.8	450 ± 30
Campo Del Cielo, Argentina	27°38'N	61°42'W	0.05	0
Carswell, Saskatchewan	58°27'N	109°30'W	39	115 ± 10
Charlevoix, Quebec	47 32N	70 18W	54	357±15
Chesapeake Bay, Virginia	37 15N	76 5W	85	35.5±0.6
Chicxulub, Mexico	21 20N	89 30W	170	64.98±0.05
Chiyli, Kazakhstan	49 10N	57 51E	5.5	46±7
Clearwater East, Quebec	56 5N	74 7W	22	290±20
Clearwater West, Quebec	56 13N	74 30W	32	290±20
Connolly Basin, Australia	23 32S	124 45E	9	60
Crooked Creek, Missouri	37 50N	91 23W	7	320±80
Dalgaranga, West Australia	27 45S	117 5W	0.021	0.03
Decaturville, Missouri	37 54N	92 43W	6	300
Deep Bay, Saskatchewan	56 24N	102 59W	13	100±50
Dellen, Sweden	61 55N	16 39E	15	110.0±2.7
Des Plaines, Illinois	42 3N	87 52W	8	280
Dobele, Latvia	56 35N	23 15E	4.5	300±35
Eagle Butte, Alberta	49 42N	110 35W	19	65
El'Gygytgyn, Russia	67 30N	172 5E	18	3.5±0.5

Flynn Creek, Tennessee	36 17N	85 40W	3.55	360±20
Garnos, Norway	60 39N	9 0E	5	500±10
Glasford, Illinois	40 36N	89 47W	4	430
Glover Bluff, Wisconsin	43 58N	89 32W	3	500
Goat Paddock, Western Australia	18 20S	126 40E	5.1	50
Gosses Bluff, North Territory, Australia	23 50S	132 19E	22	142.5±0.5
Gow Lake, Canada	56 27N	104 29W	4	250
Goyder, Northern Territory, Australia	13 29S	135 2E	3	>136
Granby, Sweden	58 25N	15 56E	3	470
Gusev, Russia	48 21N	40 14E	3.5	65
Gweni-Fada, Chad	17°25'N	21°45'E	14	<345
Haughton, NWT, Canada	75°22'N	89°41'W	20.5	21.5±1.0
Haviland, Kansas	37°35'N	99°10'W	0.015	0
Henbury, North Territory, Australia	24°35'S	133°9'E	0.157	0.01
Holleford, Ontario	44°28'N	76°38'W	2.35	550±100
Ile Rouleau, Quebec	50°41'N	73°53'W	4	300
Ilumetsa, Estonia	57°58'N	25°25'E	0.08	0
Ilyinets, Ukraine	49°6'N	29°12'E	4.5	395±5
Iso-Naakkima, Finland	62°11'N	27°9'E	3	>1000
Janisjarvi, Russia	61°58'N	30°55'E	14	698±22
Kaalijarvi, Estonia	58°24'N	22°40'E	0.11	0
Kalkkop, South Africa	32°43'S	24°34'E	0.64	<1.8
Kaluga, Russia	54°30'N	36°15'E	15	380±10
Kamensk, Russia	48°20'N	40°15'E	25	65.00±2.00
Kara, Russia	69°5'N	64°18'E	65	73.00±3.00
Kara-Kul, Tajikistan	39°1'N	73°27'E	52	25
Kardla, Estonia	58°59'N	22°40'E	4	455
Karla, Russia	54°54'N	48°0'E	12	10
Kelly West, Northern Territory, Australia	19°56'S	133°57'E	10	550
Kentland, Indiana	40°45'N	87°24'W	13	300
Kursk, Russia	51°40'N	36°0'E	5.5	250±80
Lac Couture, Quebec	60°8'N	75°20'W	8	430±25
Lac La Moinerie, Quebec	57°26'N	66°37'W	8	400±50
Lappajarvi, Finland	63°9'N	23°42'E	17	77.30±0.40
Lawn Hill, Queensland	18°40'S	138°39'E	18	515
Liverpool, Northern Territory, Australia	12°24'S	134°3'E	1.6	150±70
Lockne, Sweden	63°0'N	14°48'E	7	540±10
Logancha, Russia	65°30'N	95°48'E	20	25±20
Logoisk, Belarus	54°12'N	27°48'E	17	40±5
Lonar, India	19°59'N	76°31'E	1.83	0.052±0.010
Lumparn, Finland	60°12'N	20°6'E	9	1000
Macha, Russia	59°59'N	118°0'E	0.3	0.01
Manicouagan, Canada	51°23'N	68°42W	100	212±1
Manson, Iowa	42°35N	94°31W	35	65.7±1.0
Marquez, Texas	31°17N	96°18W	22	58±2
Middlesboro, Kentucky	36°37N	83°44W	6	300
Mien, Sweden	56°25N	14°52E	9	121.0±2.3
Misarai, Lithuania	54°0N	23°54E	5	395±145

Mishina Gora, Russia	58°40N	28°0	4	360
Mistastin, Canada	55°53N	63°18W	28	38±4
Mjolnir, Norway	73°48N	29°40E	40	143±20
Montagnais, Canada	42°53N	64°13W	45	50.50±0.76
Monturaqui, Chile	23°53S	68°17W	0.46	1
Morasko, Poland	52°29N	16°54E	0.1	0.01
New Quebec, Canada	61°17N	73°40W	3.44	1.4±0.1
Newporte, North Dakota	48°58N	101°58W	3	<500
Nicholson Lake, Canada	62°40N	102°41W	12.5	400
Oasis, Libya	24°35N	24°24E	11.5	120
Obolon, Ukraine	49°30N	32°55E	15	215±25
Odessa, Texas	31°45N	102°29W	0.168	0.05
Ouarkziz, Algeria	29°0N	7°33W	3.5	70
Piccaninny, Western Australia	17°32S	128°25E	7	360
Pilot Lake, Canada	60°17N	111°1W	5.8	445±2
Popigai, Russia	71°30N	111°0E	100	35±5
Presqu'ile, Canada	49°43N	78°48W	12	500
Pretoria Salt Pan, South Africa	25°24S	28°5E	1.13	0.2
Puchezh-Katunki, Russia	57°6N	43°35E	80	220±10
Ragozinka, Russia	58°18N	62°0E	9	55 5
Red Wing, North Dakota	47°36N	103°33W	9	200±25
Riachao Ring, Brazil	7°43S	46°39W	4.5	200
Ries, Germany	48°53N	10°37E	24	14.8±1.0
Rio Cuarto, Argentina	30°52S	64°14W	4.5	0.1
Rochechouart, France	45°50N	0°56E	23	186±8
Roter Kamm, Namibia	27°46S	16°18E	2.5	5.0±0.3
Rotmistrovka, Ukraine	49°0N	32°0E	2.7	140±20
Saaksjarvi, Finland	61°24N	22°24E	5	514±12
Saint Martin, Canada	51°47N	98°32W	40	220±32
Serpent Mound, Ohio	39°2N	83°24W	6.4	320
Serra da Cangalha, Brazil	8°5S	46°52W	12	300
Shunak, Kazakhstan	47°12N	72°42E	3.1	12±5
Sierra Madera, Texas	30°36N	102°55W	13	100
Sikhote Alin, Russia	46°7N	134°40E	0.027	0.00
Siljan, Sweden	61°2N	14°52E	55	368.0±1.1
Slate Islands, Canada	48°40N	87°0W	30	350
Sobolev, Russia	46°18N	138°52E	0.053	0.00
Soderfjarden, Finland	63°0N	21°35E	6	550
Spider, Western Australia	16°44S	126°5E	13	570
Steen River, Canada	59°31N	117°37W	25	95±7
Steinheim, Germany	48°40N	10°4E	3.8	14.8±0.7
Strangways, Australia	15°12S	133°35E	25	470
Sudbury, Canada	46°36N	81°11W	200	1850±3
Suvasvesi N, Finland	62°42N	28°0E	4	<1000
Tabun-Khara-Obo, Mongolia	44°6N	109°36E	1.3	3
Talemzane, Algeria	33°19N	4°2E	1.75	3
Teague, Australia	25°52S	120°53E	30	1685±5

Tenoumer, Mauritania	22°55N	10°24W	1.9	2.5±0.5
Ternovka, Ukraine	48°1N	33°5E	12	280±10
Tin Bider, Algeria	27°36N	5°7E	6	70
Tookoonooka, Australia	27°0S	143°0E	55	128±5
Tvaren, Sweden	58°46N	17°25E	2	0.00
Upheaval Dome, Utah	38°26N	109°54W	5	65.00
Ust-Kara, Russia	69°18N	65°18E	25	73±3
Vargeao Dome, Brazil	26°50S	52°7W	12	70
Veevers, Australia	22°58S	125°22E	0.08	1.0
Vepriaj, Lithuania	55°6N	24°36E	8	160±30
Vredefort, South Africa	27°0S	27°30E	140	1970±100
Wabar, Saudi Arabia	21°30N	50°28E	0.097	0.01
Wanapitei Lake, Canada	46°45N	80°45W	7.5	37±2
Wells Creek, Tennessee	36°23N	87°40W	14	200±100
West Hawk Lake, Canada	49°46N	95°11W	3.15	100±50
Wolfe Creek, Australia	19°18S	127°46E	0.875	0.3
Zapadnaya, Ukraine	49°44N	29°0E	4	115±10
Zeleny Gai, Ukraine	48°42N	32°54E	2.5	120±20
Zhamanshin, Kazakhstan	48°24N	60°58E	13.5	0.9±0.01

BIBLIOGRAPHY

Aki, Richards, 1980, *Quantitative Seismology: Theory and Methods.* San Francisco, CA: W.H. Freeman and Company, pp. 931.

Apthorpe, M., 1988, *Cainozoic depositional history of the North West Shelf*: Proc. of the North West Shelf symposium, Perth, W.A., 55-84.

Bradshaw, M.T., et al., 1988, *Paleogeographic evolution of the North West Shelf region*: Proc. of the North West Shelf symposium, Perth, W.A., 29-54.

Dence, M.R., 1965, *The extraterrestrial origin of Canadian craters.* NY Acad. Sci. Ann., **123**, 941-969.

French, B.M., 1998, *Traces of Catastrophe: A Handbook of Shock-Metamorphic Effects in Terrestrial Meteorite Impact Structures.* LPI Contribution No. 954, Lunar and Planetary Institute, Houston, pp. 120.

Gault, D.E., Quaide, W.L., and Oberbeck, V.R., 1968, *Impact cratering mechanics and structures.* in French, B.M, and Short, N.M (eds.), *Shock Metamorphism of natural materials.* Mono Book Co., Baltimore, Md., pp. 87-99.

Gault, D.E., and Wedekind, J.A., 1978, *Experimental studies of oblique impact*: Proc. Lunar Planet. Sci. Conf., **9**, 3843-3875.

Geological Survey of Canada Website, 1997, *Database of terrestrial impact structures.* http://gdcinfo.agg.emr.ca/toc.html?/crater/world_craters.html

Grieve, R.A.F., Robertson, P.B., and Dence, M.R., 1981, *Constraints on the formation of ring impact structures, based on terrestrial data.* In Multiring Basins (eds. P.H. Schultz and R.B. Merrill). Proc. Lunar Planet. Sci. Conf. 12A, pp. 37-57.

Grieve, R.A.F., and Pilkington, M., 1996, The signature of terrestrial impacts. AGSO J. Austral. Geol. & Geophys., **16**, 399-420.

Grieve, R.A.F., 1991, *Terrestrial Impact: The record in the rocks.* Meteoritics, **26**, 175-194.

Grieve, R.A.F., and Masaytis, V.L., 1994, *The economic potential of terrestrial impact craters*: Internat. Geol. Rev., **36**, 105-151.

Hansen, M.C., 1997a, *The Geology of Ohio – the Ordovician*: Ohio Division of Geological Survey, Ohio Geology, Fall 1997, 1-6.

Hansen, M.C., 1997b, *The Geology of Ohio – the Cambrian*: Ohio Division of Geological Survey, Ohio Geology, Winter 1997, 1-5.

Hildebrand, A.R. et al., 1998, *Mapping Chicxulub crater structure with gravity and seismic reflection data.* In: Grady, M.M., Hutchison, R., McCall, G.J.H., and Rothery, D.A.

(eds) Meteorites: Flux with Time and Impact Effects. Geological Society, London, Special Publications, **140**, 155-176.

Isaaks, E.H., and Srivastava, R.M., 1989, *An Introduction to Applied Geostatistics*. New York, NY: Oxford University Press, pp. 561.

Isaac, J.H., and Stewart, R.R., 1993, *3-D seismic expression of a cryptoexplosion structure*. Can. J. Expl. Geophys., Vol. 29, No. 2, 429-439.

Janse, A.J.A., 1985, *Kimberlites – where and when*: in Kimberlite occurrence and origin: A basis for conceptual models in exploration, 19-62.

Jenyon, M.K., and Fitch, A.A., 1985, *Seismic reflection interpretation*. Berlin: Borntraeger, pp. 318.

Masaytis, V.L., 1989, *The economic geology of impact craters*: Internat. Geol. Rev., **31**, 922-933.

Melosh, H.J., 1989, *Impact Cratering: A Geologic Process*. New York, NY: Oxford University Press, pp. 245.

Mitchell, R.H. *Kimberlites: Mineralogy, geochemistry, and petrology*: New York, NY: Plenum Press, 1986.

Mory, A.J., 1988, *Regional geology of the offshore Bonaparte Basin*: Proc. of the northwest shelf symposium, Perth, W.A., 287-309.

Oberbeck, V.R., and Quaide, W.L., 1968, *Thickness determinations of the lunar surface layer from impact craters*. J. Geophys. Res., 73, 5247-5270.

Purcell, P.G., and Purcell, R.R., *The North West Shelf, Australia – An introduction*: Proc. of the North West Shelf symposium, Perth, W.A., 3-15.

Robertson, G.A., 1997, *The Steen River structure, Alberta, Canada: Subsurface identification and hydrocarbon occurences*: Oklahoma Geological Survey Circular 100, pp. 385-390.

Schultz, P.H., and Gault, D.E., 1985, *Clustered impacts: Experiments and implications*. J. Geophys. Res. 90, 3701-3732.

Smith, C., *Theory and the art of communications design*. State of the University Press, 1997.

Westbroek, H.-H., 1997, *Seismic interpretation of two possible meteorite impact craters: White Valley, Saskatchewan and Purple Springs, Alberta*. M.Sc. Thesis, University of Calgary, 145 pp.

Winzer, S.R., 1972, *The Steen River astrobleme, Alberta, Canada*: 24th Inter. Geol. Cong., Sect. 15, pp. 148-156.

INDEX

B

breccia 5, 16

C

Coesite 3
contact stage 15
crypto-explosion structures 9

D

depth-to-diameter ratio 16, 27, 49, 72

E

elliptical crater 26
excavation stage 15, 16

G

geostatistics
  cokriging 92, 141, 143, 156
  kriging 90, 156

H

Hotchkiss structure
  geologic setting 65
  interpretation 68
  pre-erosion depth 71
  rim height 72
  stratigraphic column 77
  stratigraphic uplift 70
  transient cavity dimensions 72

K

kimberlite pipes 9

L

longitudinal stress 12, 13

M

Muskingum structure
  breccia 48
  central mound 48, 50, 51
  depth-to-diameter ratio 49
  geological setting 46
  rim height 49
  summary of dimensions 51
  transient cavity diameter 50

O

obliquity of impact 16, 17, 26

P

perpendicular stress 13
physical modeling 157
Poisson's ratio 12
Puffin structure
  age estimates 25
  geological setting 23
  morphometry 25
  summary of dimensions 28

S

salt dissolution 9
scaling relations 20
shattercones 3
stages of impact
  contact 15
  excavation 15
  modification 15
Steen River
  Cokriging 91
  hydrocarbon production (table) 85
  kriging 90
  Kriging with External Drift 90
  T-D conversion, GeoStat 89
  T-D conversions, Petrosys 87
Steinham Basin 3
Stishovite 3
structured targets
  central mound 18
  effects of layering 18